LEIBNIZ-INSTITUT FÜR ATMOSPHÄREN PHYSIK IAP

INAUGURAL-DISSERTATION

am Leibniz-Institut für Atmosphärenphysik in Kühlungsborn
zur Erlangung der Doktorwürde
der Mathematisch-Naturwissenschaftlichen Fakultät
der Universität Rostock

Lidar Investigations of the Mesopause Region: Temperature Structure and Variability

von
Cord Fricke-Begemann

Abstract: This work presents a comprehensive study of the temperature structure of the Earth's middle atmosphere. Temperature profiles in the mesopause region (80 to 105 km) are derived by means of a groundbased potassium resonance lidar and used to characterize the mean state of the atmosphere at different latitudes as well as seasonal and diurnal variations. One objective of this work was a further development of the lidar system used, including the tunable all solid-state laser emitter. Previously, the measurements were restricted to nighttime and thus it was a major challenge to enable observations in full daylight. To this end a unique FADOF (Faraday Anomalous Dispersion Optical Filter) was developed which provides a high signal transmission and background suppression while it avoids erroneous influences on the measurement.

Climatological results are derived from three years of nighttime measurements at Kühlungsborn (54°N). The seasonal variations of potassium density and temperature are analysed. In addition, observations were carried out during four campaigns at Tenerife (28°N) and main features of the seasonal variation at this latitude are revealed. The density of metal atoms exhibits a semiannual variation, which is presumably present at all latitudes and distinguishes potassium from other mesospheric metals. The temperature analyses confirm the concept of a global two-level behaviour of the mesopause. Even at the low latitude of 28°N the lowest temperatures occur only at two distinct altitude levels, which are nearly identical to midlatitudes. At 28°N the low-level state of the mesopause occurred for about one month near summer solstice, whereas it exists for four months at 54°N.

Temperature variations on the time scale of hours are used to study wave and tidal perturbations of the mesopause region. Detailed analyses show that accurate results on tides can only be derived from data sets which cover nearly complete diurnal cycles. Two continuous observations over several days are presented which have become possible with the achieved daytime capability. While a diurnal temperature oscillation was significantly present at 54°N it was not detectable at 28°N. The prevailing tidal component under winter conditions is a semidiurnal oscillation with amplitudes up to 15 K. Comparisons with current models show that especially this component is regularly underestimated. Strong amplitude variations of the tides are present on short time scales which are possibly induced by interactions with planetary waves.

Postal address:
Schloss-Str. 6
18225 Kühlungsborn
Germany

IAP Kühlungsborn
August 2004
IAP Nr. 10/2004
ISSN 1615-8083

Zusammenfassung

Die Kenntnis der Lufttemperatur ist von grundlegender Bedeutung für die Erforschung der Erdatmosphäre. Das Temperaturprofil in der Mesopausenregion (80–105 km Höhe) kann mit Hilfe eines Lidars (eines "Laser-Radars") gemessen werden, das mit Resonanzstreuung an Metallatomen arbeitet.

Teil der vorliegende Arbeit ist die Weiterentwicklung des verwendeten Kalium-Lidars. Schwerpunkte bilden dabei der Festkörperlaser und die Neuentwicklung eines optischen Filters, der die Temperaturmessung auch bei vollem Tageslicht ermöglicht. Temperaturmessungen wurden am Leibniz-Institut für Atmosphärenphysik in Kühlungsborn (54°N) durchgeführt und außerdem mit einem transportablen System auf Teneriffa (28°N) und Spitzbergen (78°N).

Die Lidarmessungen an den verschiedenen Breiten konnten das saisonale Zwei-Niveau-Verhalten der Mesopause als ein globales Phänomen etablieren. Die Mesopause, d. h. das Temperaturminimum in diesem Höhenbereich, tritt im Laufe des Jahres ausschließlich in zwei bestimmten Höhenniveaus auf, die nur eine geringe Abhängigkeit von der geographischen Breite aufweisen. Die niedrigsten Temperaturen stellen sich dabei stets im Sommer ein.

Erste kontinuierliche Messungen kompletter Tagesgänge zeigen deutliche Variationen der Temperatur durch Wellen verschiedener Typen. Eine wichtige Rolle spielen dabei ganz-, halb- und dritteltägige Gezeiten. Besonders stark ist die halbtägige Gezeit ausgeprägt, die Amplituden von mehr als 15 Kelvin erreichen kann.

LEIBNIZ-INSTITUT FÜR ATMOSPHÄREN PHYSIK IAP

Lidar Investigations of the Mesopause Region: Temperature Structure and Variability

von
Cord Fricke-Begemann

Dieser Forschungsbericht wurde als Disseration von der
Mathematisch-Naturwissenschaftlichen Fakultät der Universität Rostock
angenommen.

Gutachter: Prof. Dr. Ulf von Zahn (Universität Rostock)
Prof. Dr. Adolf Ebel (Universität zu Köln)
Prof. Dr. Chiao-Yao She (Colorado State University, Fort Collins, USA)

Verteidigt am 2. Juli 2004

Contents

1 Introduction **1**

2 Lidar Measurements **5**
2.1 Scattering of Light 5
2.2 The Lidar Backscatter Signal 6
2.3 Temperature Measurements 9
2.3.1 Doppler Broadening 9
2.3.2 The Potassium D_1 Resonance Line 10
2.3.3 Deviations From the Linear Lidar Equation 11

3 The Potassium Lidar **13**
3.1 Transmitter Unit 14
3.1.1 The Alexandrite Laser 15
3.1.2 Resonator Modes and Injection Seeding 18
3.1.3 Lidar Operation 22
3.1.4 Achievements 23
3.2 Receiver Unit for Nighttime Operation 25
3.2.1 Telescopes 25
3.2.2 Detection Bench 25
3.2.3 Electronics 26
3.2.4 Temperature Retrieval 26
3.3 Daylight Upgrade of the Lidar Receiver 29
3.3.1 Spectral Filtering Technique 29
3.3.2 Frequency Response and Effective Transmission 35
3.3.3 Reduction of the Field of View 39
3.3.4 Saturation 40
3.3.5 Avalanche Photodiode 43
3.3.6 Achieved Daylight Capability 44
3.4 Discussion and Outlook 46

4 Climatology **51**
4.1 Potassium Lidar Database 51
4.2 The Mesospheric Potassium Layer 54
4.2.1 Midlatitude Potassium Layer: Kühlungsborn (54°N) 54
4.2.2 Low Latitude Potassium Layer: Tenerife (28°N) 55
4.2.3 Discussion 57
4.3 The Temperature Structure of the Mesopause Region 60
4.3.1 Midlatitude Temperature Structure: Kühlungsborn (54°N) 61
4.3.2 Low Latitude Temperature Structure: Tenerife (28°N) 63

4.3.3 Discussion: Low Latitude Temperatures . . . 65
4.3.4 Discussion: The Two-Level Mesopause . . . 67
4.3.5 Concluding Remarks . . . 71

5 Diurnal Temperature Variations 73
5.1 Tidal Analysis of Nighttime Measurements . . . 75
5.1.1 Derivation of Tidal Parameters . . . 75
5.1.2 Tidal Parameters at Tenerife for Different Seasons . . . 77
5.1.3 Tidal Parameters at Kühlungsborn in Winter . . . 78
5.1.4 Discussion . . . 79
5.2 Combination with WINDII Measurements . . . 80
5.2.1 Approach to Diurnal Tidal Components . . . 82
5.2.2 Discussion . . . 85
5.3 Daytime Lidar Measurements . . . 86
5.3.1 Measurements at Tenerife, November 2000 . . . 86
5.3.2 Measurements at Kühlungsborn, February 2003 . . . 91
5.3.3 Measurements at Kühlungsborn, June 2003 . . . 94
5.3.4 Discussion of Spectral Analyses . . . 95
5.3.5 Conclusions of Spectral Analyses . . . 96
5.4 Discussion of Tidal Analyses . . . 97
5.4.1 Results . . . 97
5.4.2 Lidar Measurements at Other Latitudes . . . 99
5.4.3 Bias of Nighttime Mean Temperatures . . . 101
5.4.4 Other Observations . . . 102
5.4.5 Model Predictions . . . 103
5.5 Conclusions . . . 106

6 Summary 107

A Atomic Data on Potassium 111

B U. S. Standard Atmosphere, 1976 113

C Data Analysis 115
C.1 Harmonic Analysis . . . 116
C.2 Spectral Analysis . . . 119

D Monthly Observation Statistics 125

Bibliography 129

List of Figures 139

List of Tables 141

Chapter 1

Introduction

The Earth's Atmosphere

The Earth's middle atmosphere and its temperature structure are the primary subject of this work. The middle atmosphere has become a topic of research approximately one hundred years ago, with the surprising discovery by Teisserenc de Bort and Aßmann in 1902 that the temperature decrease with height does not continue to outer space but ends at about $8-11$ km. A correct approximation of the temperature profile was not established until the 1960s. The nomenclature which is now convention divides the atmosphere on the basis of its vertical temperature gradient into troposphere (up to $8-15$ km), stratosphere (up to $\sim$50 km), mesosphere (up to $\sim$100 km) and thermosphere. A number of known physical and chemical characteristics distinguish these layers. However, many fundamental phenomena and processes of the middle atmosphere, comprising both the stratosphere and the mesosphere, are not understood and form topics of current research.

The boundaries between these layers (tropo-, strato- and mesopause) are far from impermeable. Studies over the past decade have shown that strong chemical, dynamical and radiative coupling exists between them (e. g. *Summers*, 1999; *Brasseur et al.*, 2000; *Baldwin and Dunkerton*, 2001; *Becker and Schmitz*, 2003). With recent interest in long-term climate and temperature trends it has become increasingly evident that the global atmosphere must be considered as an integrated system to clarify the relative roles of natural and anthropogenic effects on the Earth's climate. For example, increasing levels of carbon dioxide (associated with global warming in the troposphere) lead to global cooling in the middle atmosphere. While tropospheric temperature is predicted to increase by $1-4$ K in a doubled CO_2 scenario, efficient radiative cooling is expected from model calculations to cool the middle atmosphere by $10-20$ K. Such a large temperature change would induce significant changes in the middle atmosphere circulation. This, in turn, would affect tropospheric climate because stratospheric dynamics provide the upper boundary mechanical forcing of tropospheric wave patterns. On the other hand, dissipation of gravity and planetary waves, both generated in the troposphere, provide momentum drag on the circulation of the middle atmosphere. The large temperature change predicted for the upper mesosphere has led to the proposal of using it as a precursor of climate trends (see review by *Beig et al.*, 2003). To detect and assess such trends one needs both accurate temperature measurements and thorough understanding of the processes governing the mesospheric energy budget.

A gravitationally bound atmosphere is in hydrostatic equilibrium. Solar radiation and the radiative properties of the atmospheric constituents provide the boundary conditions for a first-order description of the vertical thermal structure. An atmosphere controlled by sunlight can scarcely be rotationally symmetric. Nevertheless, it is useful to think of a mean planetary atmosphere, with diurnal and latitudinal variations occurring about the mean.

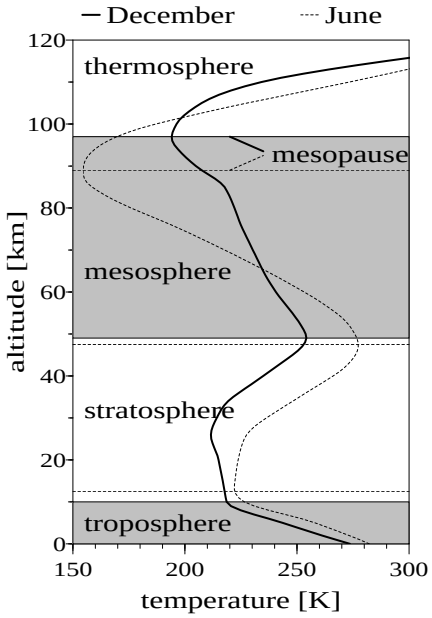

Figure 1.1: Model of the atmospheric temperature at 55°N for winter (solid) and summer (dotted).

Typical midlatitude temperature profiles of the Earth's atmosphere are shown in Figure 1.1 for June and December. They are taken from CIRA-86 (COSPAR International Reference Atmosphere 1986, *Fleming et al.*, 1990), which is based on measurements and theoretical approximations. The tropospheric temperature is governed by H_2O due to radiative and convective exchange. In the stratosphere trace amounts of O_3 are formed by sunlight, and the high efficiency of O_3 to absorb ultraviolet radiation causes a temperature inversion above the tropopause. In the mesosphere, the decrease in O_3 production in combination with the increased rate of cooling to space by CO_2 leads to the re-establishment of a declining temperature. Finally, above the mesopause, heating by O_2 photolysis and ionization, together with the lack of efficient infrared emission, increases the thermosphere temperatures to about 1000 K. Detailed discussions of the main processes are found in the literature (e. g. *Chamberlain and Hunten*, 1987; *Goody and Yung*, 1989).

The upper mesosphere exhibits a counter-intuitive seasonal behaviour in Figure 1.1, with lower temperatures observed in summer than in winter. This effect is strongest around the mesopause (the temperature minimum between mesosphere and thermosphere) which is located at a lower height in summer than in winter. The odd seasonal variation increases towards the polar regions, which are sunlit the whole day in summer. It illustrates that this region of the atmosphere is far from a purely radiative equilibrium. From the appearance of noctilucent clouds near 83 km (e. g. *Gadsden and Schröder*, 1989), it has long been expected that this region is colder in summer than in winter. In the thin and relatively dry air, temperatures near 150 K (below -120°C) are required for the formation of ice particles, which constitute the visible noctilucent clouds and contribute to the appearance of polar mesospheric summer echoes observed by radar.

The cold summer mesopause is known to be the result of a dynamical effect. In the upper mesosphere the breaking of gravity waves (see below) deposits momentum which induces a drag on the mean flow, causing a meridional drift from the summer to the winter pole. This meridional motion gives rise to vertical motion through mass continuity. Adiabatic cooling in summer and heating in winter cause the temperatures in the mesosphere to deviate by up to 60–90 K from a radiatively-determined equilibrium. Through this mechanism the polar summer mesopause becomes the coldest region in the Earth's atmosphere.

The major radiative, dynamical and chemical processes that govern the energy balance in the mesosphere are thought to be qualitatively known. However, we still do not have a quantitative global understanding of the magnitude and relative importance of these processes and their overall role in determining the structure and variability of the mesosphere (e. g. *Roble*, 1995; *Mlynczak*, 2000). Especially in the mesopause region, the energy budget is complex as it consists of several terms which are larger in magnitude than their sum. In addition to radiative and dynamical processes, exothermal chemical reactions involving the odd-oxygen and odd-hydrogen species (such as O, O_3, H, and OH) contribute to mesospheric heating, though the

chemical energy is partly radiated away as observable airglow. Turbulent dissipation of wave energy is another process which can, at least locally, cause large heating rates (*Ebel*, 1984; *Lübken*, 1997).

The atmosphere is permanently perturbed by waves, periodic oscillations in temperature, wind, pressure and density. They are classified by their physical properties as (a) acoustic waves with periods of seconds and below, (b) gravity waves with periods of minutes to hours and (c) planetary waves of the global atmosphere with periods of days. Instead of attaining a static equilibrium, the mean state of the atmosphere is a notional mean which is characterized by the waves occurring about it. Through non-linear interactions waves can continually exchange energy and momentum with the mean flow and thus influence large scale circulation patterns (e. g. *Holton and Alexander*, 2000). Waves are intensely studied as a major component of the atmosphere that provides coupling between the layers. On the other hand, where the mean state is of interest, it is necessary to average out wave perturbations. In particular, tidal waves which are periodic with the solar day, have a large potential to bias nighttime (and daytime) measurements and obscure the real mean state of the atmosphere.

Temperature Measurements

The energy budget governs the thermal structure, the dynamics and the chemical composition of the atmosphere. Therefore, its understanding yields a fundamental scientific problem. Until today, though, no extensive temperature data set exists from which the mesospheric energy budget can be determined.

The mesopause region is not easily accessible for measurements. *In-situ* measurements can only be done by means of rockets and are therefore expensive and rare. Passive rocket experiments with falling spheres tracked from the ground have been performed more frequently over the decades, but they still only provide snapshots of the momentary state of the atmosphere and are restricted to a few launch sites. Their vertical resolution is not ideal and the altitude range does not cover the full mesopause region, being mostly limited to below 90 km.

With the progress of laser technology, *lidar* instruments became more frequently used as they can measure atmospheric parameters continuously with high vertical and temporal resolution (see Chapter 3). Hence, they can be employed to study both the climatological structure and the wave perturbations. Potassium resonance lidars are used in this work to obtain temperature profiles of the mesopause region. In the altitude range of approximately 75 to 110 km exist layers of metal atoms, which are used as tracers to determine air temperatures with high accuracy (*Fricke and von Zahn*, 1985). These layers are permanent and believed to originate from extraterrestrial material. The average global mass accretion from small meteoroids was determined to be about 110 tons per day (*Love and Brownlee*, 1993). When meteoroids enter the atmosphere they can produce radar-detectable ionization trails and visible shooting stars in these altitudes. As they evaporate, they generate a strong local enhancement of metal atoms which has frequently been detected by resonance lidars (e. g. *von Zahn et al.*, 2002). Besides the temperature measurements, metal lidars can provide information on the composition and dynamics of the mesopause region.

Optical remote sensing of the mesopause region has long been limited to the period of darkness, due to the high solar background during daytime. This restriction has been a major challenge in lidar development over recent years. Hence, the upgrade of the potassium resonance lidars for long-term continuous day-and-night temperature measurements forms an

important part of this work.

Today, there is a variety of remote sensing techniques for temperature measurements in the mesosphere. So-called Rayleigh lidars can derive the temperature from the troposphere to the mesosphere, up to heights of about 90 km. Passive instruments analysing the airglow emissions, like OH-spectrometers, can be operated continuously at relatively low expense and have been widely applied. A major disadvantage of these techniques is the absence of height information, thus the accurately measured temperature value cannot be closely assigned to one altitude. The relatively new method of deriving temperatures from meteor radar observations has the advantage of being independent of weather conditions and time of day, but it cannot derive vertical profiles and needs a long integration time and some *a-priori* information about the state of the atmosphere. In contrast to groundbased observations, a spaceborne instrument can provide near-global mapping at the expense of local time coverage and usually with poorer resolution and accuracy. Thus, the different observation techniques complement each other as they all have specific advantages, difficulties and shortcomings. For example, they can be combined to provide daytime and nighttime temperatures or, ideally on a single day, a groundbased lidar can measure the local time variation, while a satellite covers the horizontal dependence.

Objectives and Structure of This Work

This study has been carried out at the Leibniz-Institute of Atmospheric Physics in Kühlungsborn, Germany, and concentrates on lidar measurements of the temperature in the mesopause region. The objectives of the work to this thesis included (a) the setup of a new lidar system and its technical development for daylight capability, (b) measurements of the temperature structure at different latitudes and (c) analyses of the data with respect to the mean temperature structure as well as seasonal and diurnal variations.

The structure of this thesis is organized as follows. Chapter 2 describes the principles of the lidar observation method and temperature calculation. Chapter 3 deals with the technical details of the instruments including major developments of the laser and of the receiver system. Chapter 4 presents the data set obtained over the last few years and investigates seasonal and latitudinal variations of the potassium layer and the temperatures in the mesopause region. Chapter 5 addresses the effects of tides and waves on the temperature structure, and finally, Chapter 6 provides a short summary of the results.

In this work the *mesopause region* is referred to as the altitude range from 80 to 105 km, wherein the mesopause altitude varies. Altitudes in this region cannot generally be attributed to either the mesosphere or the thermosphere. Alternatively, the term *mesosphere/lower thermosphere* (MLT) is often used in the literature. Also convenient is the simplifying use of *mesospheric*, especially for the metal layers, even under conditions when they are mainly located in the lower thermosphere.

This work discusses observations at different latitudes which are classified into *low, mid* and *polar latitudes.* Latitudes below 30° are referred to as low latitudes and comprise both the tropics ($< 23.5°$) and the subtropics. Midlatitudes denote the temperate zone ($30° - 66.5°$) while polar latitudes refer to the Arctic or Antarctic.

Chapter 2

The Principle of Lidar Measurements

This chapter gives an introduction to the physical principles of atmospheric lidar measurements. It also discusses the derivation of air temperatures and potassium densities from lidar observations. The most important mathematical methods used in this work to evaluate the measurements are summarized in Appendix C and discussed with respect to their practical application. Except for one novel method used to combine two data sets (the *consistency test*), they have been discussed in detail in the literature.

The acronym LIDAR (light detection and ranging) has been introduced in relation to radar as both devices have the same operation principle. A lidar is an active remote sensing instrument which sends out a pulsed laser beam and receives the light scattered back from the atmosphere. At which distance the scattering process has occurred is calculated from the time elapsed between emission and detection of the light. A variety of information about the scattering medium can be derived from the intensity, spectral composition and polarization of the scattered light, depending on the properties of the emitted light. As the scattering and absorption of the laser beam is proportional to the density of the scatterers and absorbers, lidars have often been used to measure concentrations of aerosols, trace gases and atmospheric pollutants.

2.1 Scattering of Light

Light is scattered in the atmosphere by various processes. When a plane wave encounters an ensemble of targets with the total cross-section σ, the intensity of light dI scattered into a solid angle $d\Omega$ in the direction ϑ is given by

$$\left.\frac{dI}{d\Omega}\right|_{\vartheta} = \frac{I_0}{A}\left.\frac{d\sigma}{d\Omega}\right|_{\vartheta} N\,, \tag{2.1}$$

where I_0 is the illumination intensity, $\frac{d\sigma}{d\Omega}$ is the differential scatter cross-section, and N is the number of scattering elements in the illuminated volume V of length l and area A. Using the local number density of the scatterers $\rho = N/(A \cdot l)$, Eq. 2.1 becomes

$$\left.\frac{dI}{d\Omega}\right|_{\vartheta} = I_0\, l\, \rho \left.\frac{d\sigma}{d\Omega}\right|_{\vartheta}. \tag{2.2}$$

In the case of the lidar, $d\Omega$ is very small and only backscattered light is observed ($\vartheta \approx 180°$). The differential cross-section is often replaced by the volume backscatter coefficient

$$\beta = \rho \cdot \left.\frac{d\sigma}{d\Omega}\right|_{180°}. \tag{2.3}$$

This can be rewritten as $dI = I_0\, \beta\, l\, d\Omega$ and expanded to derive the lidar equation (see next section).

Elastic scattering processes in the atmosphere are attributed to different processes which can be classified into three categories:

Rayleigh scattering[1] comprises non-resonant scattering by air particles with dimensions much smaller than the wavelength of the light, mainly the molecules N_2 and O_2 (e. g. review by *She*, 2001). Its intensity is related by λ^{-4} to the wavelength. For $\lambda = 770\,\mathrm{nm}$ the average molecular backscatter cross-section is $\frac{d\sigma_{\mathrm{Ray}}}{d\Omega} = 1.373 \cdot 10^{-32}\,\frac{\mathrm{m}^2}{\mathrm{sr}}$ (*Bucholtz*, 1995) as long as the mean composition of the atmosphere is unchanged (up to $\sim$100 km). When molecular anisotropy is neglected, the differential cross-section is related to the total cross-section σ_{Ray} via the phase function by $\left.\frac{d\sigma_{\mathrm{Ray}}}{d\Omega}\right|_{\vartheta} = \frac{\sigma_{\mathrm{Ray}}}{4\pi}\frac{3}{4}(1+\cos^2\vartheta)$.

Mie scattering[2] refers to scattering by aerosols with a size similar to the wavelength. The backscatter cross-section σ_{Mie} increases strongly with the particle size, but it is also dependent on shape and material. Information about the size distribution of atmospheric aerosol can be derived from the wavelength dependence of the backscatter coefficient (e. g. *Müller and Quenzel*, 1985). For very small particles (below about 100 nm), the Mie cross-section converges towards the Rayleigh value. For larger particles, Mie scattering increases more slowly with decreasing wavelength (typically about λ^{-1} to λ^{-2}).

Resonance scattering can occur by resonant absorption and elastic re-emission if the wavelength emitted coincides exactly with a transition line of an atmospheric constituent. As the cross-sections can be very large (15 or more orders of magnitude larger than σ_{Ray}), they can be used to quantify the occurrence of trace gases as in the case of the mesospheric metal atoms.

The total backscatter cross-section of a volume of air is the sum of the above processes and can be expressed as

$$\begin{aligned} \beta &= \beta_{\mathrm{Ray}} + \beta_{\mathrm{Mie}} + \beta_{\mathrm{Res}} \\ &= \rho_{\mathrm{air}} \left.\frac{d\sigma_{\mathrm{Ray}}}{d\Omega}\right|_{180^\circ} + \beta_{\mathrm{Mie}} + \rho_{\mathrm{K}} \left.\frac{d\sigma_{\mathrm{K}}}{d\Omega}\right|_{180^\circ} . \end{aligned} \tag{2.4}$$

The second line of Eq. 2.4 assumes, that resonance scattering is completely due to K atoms. Resonance scattering has by far the highest wavelength dependence and, thus, if λ is varied slightly (by about 1:10^6) only β_{Res} will change significantly while β_{Ray} and β_{Mie} stay constant. By this wavelength dependence, it is possible to distinguish between the contributions from different scattering processes.

2.2 The Lidar Backscatter Signal

A lidar measures the intensity of light scattered in the atmosphere. The detected intensity at the time t after a laser pulse was sent out, is assigned to a distance of $r = 2ct$ from the instrument (c, speed of light). The altitude where the scattering process took place is given by $z = z_0 + r$ for a vertically pointing lidar located at an altitude z_0. The detected light intensity from a distance

[1] Referring to the work of Lord Rayleigh (John William Strutt, 1842–1919). The definition usually includes both elastic Cabannes and rotational Raman scattering (*Young*, 1981).

[2] Named after Gustav Mie (1868–1957), who calculated the scattering by spherical particles.

r_i is integrated over an interval dr which is typically 200 m for the lidars used in this study. The corresponding time intervals are dt_z =1.334 µs. For elastic scattering processes, the measured intensity I from the distance interval $[r_i \pm dr/2]$ at the laser wavelength λ is described by the linear *lidar equation*:

$$I(\lambda, r_i) = I_0(\lambda)\ \beta(\lambda, r_i)\ dr\ \eta(\lambda)\ T^2(\lambda, r_i)\ \frac{A}{r_i^2}\ o(r_i) + U(r_i)\,. \tag{2.5}$$

The terms are defined as follows:

$I_0(\lambda)$: Intensity of laser pulse emitted into the atmosphere (e. g. energy, number of photons).

$\beta(\lambda, r_i)$: Total volume backscatter coefficient.

$\eta(\lambda)$: Overall efficiency of the receiver, including insertion losses of the fiber cable, transmission of optics and wavelength selective filters, and detection efficiency of the detector.

$T(\lambda, r_i)$: Transmission of the atmosphere between the location of the lidar and the scattering volume r_i. In the lidar equation, T appears squared as the stretch is passed twice. It is given by the effective extinction coefficient α as

$$T(\lambda, r_i) = \exp\left(-\int_0^{r_i} \alpha(\lambda, r)\, dr\right)\,. \tag{2.6}$$

A : Effective area of the receiving telescope occupying a solid angle of $d\Omega = A/r_i^2$ (in sr) when seen from the location of scattering.

$o(r_i)$: Overlap function between the laser beam and the telescope's field of view. For our K-lidars, full overlap ($o = 1$) is achieved above 20 km. In the case of partial overlap the energy distribution over the radius of the laser beam has to be taken into account.

$U(r_i)$: Non-backscatter signal, may consist of continuous background radiation U_b and electronic noise U_e of the detector, which can be induced partly by the signal from lower distances:

$$U(r_i) = \int U_b(\lambda)\ \eta(\lambda)\ d\lambda + U_e(r_i)\,. \tag{2.7}$$

The description of the detected signal in the form of Eq. 2.4 and 2.5 is simplified and may not be valid in all cases. It excludes non-linear and secondary effects which may occur for various reasons. The most important of these effects are summarized in Section 2.3.3. Usually it is possible to avoid them, but otherwise, they have to be included in the data evaluation.

Some of the above parameters, like the tropospheric transmission, are not known well enough to calculate the volume backscatter coefficient $\beta(r_i)$ directly. For mesospheric applications, the evaluation is restricted in practise to relative calculations between heights where the transmission losses are negligible and overlap does not change. Then, the lidar equation (2.5) can be simplified to

$$I(\lambda, r_i) = const \cdot \frac{\beta(\lambda, r_i)}{r_i^2} + U(r_i)\,. \tag{2.8}$$

Furthermore, it is usually possible to achieve an altitude independent background (or have its characteristics known). Then U can be determined at altitudes where $\beta = 0$ (e. g. above

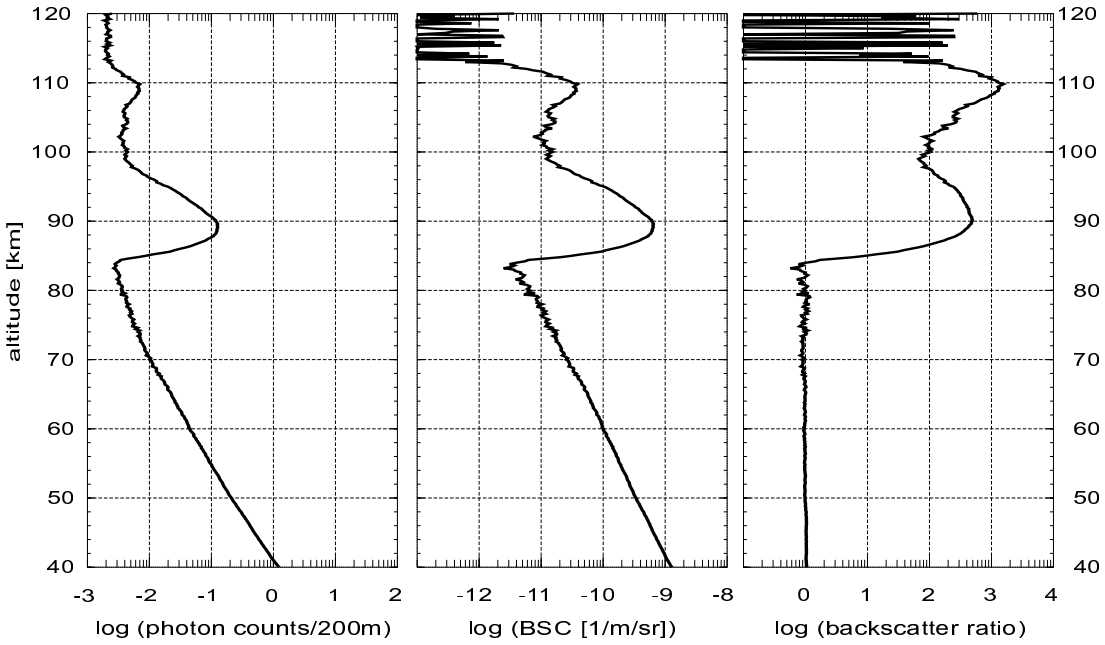

Figure 2.1: Lidar return averaged over 1 h or 100,000 laser pulses. Left: detected $I(z)$ in photon counts per laser pulse and 200-m altitude range. Middle: backscatter coefficient $\beta(z)$. Right: backscatter ratio $R(z)$. Measured on June 3rd, 2003, with the K-lidar in Kühlungsborn.

120 km) and can be subtracted from the signal. Afterwards the range correction is applied to calculate the corrected signal $\hat{I}(r_i) = (I(r_i) - U)\, r_i^2$, which is directly proportional to the volume backscatter coefficient $\beta(\lambda)$ for the wavelength considered.

If the backscatter coefficient is known in one altitude r_0 it can be calculated for any other. In practice r_0 is chosen to be an altitude (e. g. 40 km) where the backscatter signal is strong and known to be the result of Rayleigh scattering only, except after extraordinary volcano eruptions. The air density is taken from a model atmosphere (e. g. CIRA, MSIS) to calculate $\beta(r_0) = \beta_{\mathrm{Ray}}(r_0) \sim \rho_{\mathrm{air}}(r_0)$, from which the volume backscatter coefficient can be derived as

$$\beta(r_i) = \beta_{\mathrm{Ray}}(r_0) \cdot \hat{I}(r_i)/\hat{I}(r_0)\,. \tag{2.9}$$

Using this method of relative measurements, the density of potassium atoms or the backscatter coefficient of noctilucent clouds is determined. Usually the portion of the signal β_{Ray} which is due to Rayleigh scattering is calculated[3] and subtracted from the backscatter coefficient to evaluate the additional $\beta_{\mathrm{add}} = \beta - \beta_{\mathrm{Ray}}$. Alternatively, the backscatter ratio $R = \beta/\beta_{\mathrm{Ray}}$ can be used. $R-1$ is proportional to the mixing ratio of a scattering species.

An example for the lidar return signal is shown in Figure 2.1, obtained with the stationary K-lidar described in Chapter 3. As always in this work, the lidar pointed vertically and altitudes are given with respect to sea-level. The measured return signal from above 40 km is given as mean photon counts per laser pulse. Less than one photon is detected per pulse in each altitude interval ($1/dt_z \approx 0.75$ MHz). The signal consists of the exponentially decreasing Rayleigh

[3]To calculate β_{Ray} the receiver bandwidth has to be considered. For the IAP K-lidars, it is narrow enough to strongly suppress the shifted rotational Raman lines and, hence, the Rayleigh signal can be assumed to originate purely from the Cabannes line (*She*, 2001).

scattering in the lower part and is dominated by the potassium resonance signal between 85 and 115 km. Above the potassium layer a background of $2{\times}10^{-3}/dt_z$ can be seen. In this case (June 3rd, 2003) the layer exhibited two maxima near 90 and 110 km. The backscatter coefficient shown in the middle panel corresponds to a potassium density of $\rho_K = 20$ atoms/cm^3 at 90 km. The backscatter ratio (right panel) equals one in the lower part where $\beta = \beta_{Ray}$. The dominance of the upper peak shows that the potassium mixing ratio ρ_K/ρ_{air} is higher at 110 km than at 90 km.

2.3 Temperature Measurements

Atmospheric temperatures can be derived from lidar measurements by various techniques (e. g. Rayleigh lidar, Raman lidar) but until now the complete mesopause region is accessible only by metal resonance lidars which employ the mesospheric atom layers. First temperature estimations were obtained by *Blamont et al.* (1972) using absorption cells. *Fricke and von Zahn* (1985) developed a method to derive accurate air temperature profiles by probing the sodium layer with a narrow-band laser. The potassium lidar technique used in this work was introduced by *von Zahn and Höffner* (1996) to measure the air temperature in the mesospheric potassium layer by determining the Doppler width of the potassium D_1 resonance line. The spectral shape of the line is given by the atoms' mean thermal movement, which is governed by the ambient temperature. Before taking the K(D_1) hyperfine structure into account, the broadening of a single resonance line is considered below.

2.3.1 Doppler Broadening

Generally, an ensemble of atoms at rest would have a Lorentzian-line profile due to the finite duration of the oscillation of the absorbing and re-emitting atoms. The natural linewidth is given by the lifetime τ of the excited state as $\delta\nu_N = (2\pi\tau)^{-1}$. For the K($D_1$) transition with a lifetime of 26.2 ns, the natural linewidth is about 6 MHz.

This linewidth is not observed in the atmosphere as all atoms are in thermal motion and their apparent resonance frequency is shifted from the intrinsic frequency. When a frequency ν_0 is emitted from the ground, the atoms *see* the frequency $\nu = \nu_0\sqrt{\frac{c-w}{c+w}} \approx \nu_0(1-w/c)$ due to the optical (linearized) *Doppler effect*. Here, w is the vertical (or radial for non-vertical observations) component of the relative velocity between the atom and the observer (positive away from the ground). For the K(D_1) transition at 770 nm, a radial velocity of 1 m/s produces a shift of about 1.3 MHz.

At thermal equilibrium, atoms (and molecules) follow a Maxwellian speed distribution. At a temperature T, the number of atoms $n(w)$ per unit volume with a vertical velocity component between w and $w+dw$ is

$$n(w)dw = \frac{\rho}{w_p\sqrt{\pi}} e^{-(w/w_p)^2} dw\,, \tag{2.10}$$

where ρ is the total density of atoms. The most probable speed w_p is calculated from the temperature, the mass of the atoms m and the Boltzmann constant k_B by $\frac{1}{2}mw_p^2 = k_B T$. The density of atoms whose resonance frequencies are shifted from ν_0 into the interval from ν to $\nu - d\nu$ is given by the relations above as

$$n(\nu)d\nu = \frac{c\rho}{w_p\nu_0\sqrt{\pi}} e^{-\left(\frac{c(\nu-\nu_0)}{w_p\nu_0}\right)^2} d\nu\,. \tag{2.11}$$

This represents a Gaussian distribution with the full half-width (FWHM) of

$$\delta\nu_D = 2\sqrt{\ln 2}\frac{w_p}{c}\nu_0 = \sqrt{8\ln 2\frac{k_B T}{mc^2}}\,\nu_0\,, \tag{2.12}$$

which is called the *Doppler width* and proportional to $\sqrt{T}$. Thus, we get

$$n(\nu)d\nu = 2\sqrt{\frac{ln2}{\pi}}\,\frac{\rho\,d\nu}{\delta\nu_D}\,\exp-\left(2\sqrt{\ln 2}\frac{\nu-\nu_0}{\delta\nu_D}\right)^2. \tag{2.13}$$

For potassium atoms at $T = 200\,\mathrm{K}$ the most probable speed is $w_p = 292\,\mathrm{m/s}$, and a single transition at the K(D_1) frequency has a Doppler width of $\delta\nu_D = 631\,\mathrm{MHz}$, or $\delta\lambda_D = 1.25\,\mathrm{pm}$.

The lidar measures, as a function of laser frequency, the effective volume backscatter coefficient $\beta(\nu)$ (Eq. 2.3) which is proportional to the density of atoms scattering at that frequency. For a finite laser bandwidth, β equals the integral over the laser lineshape function g, which is normalized to $\int g(\nu')d\nu' = 1$,

$$\beta(\nu) = \int g(\nu')n(\nu')d\nu'\;\left.\frac{d\sigma}{d\Omega}\right|_{180^\circ}. \tag{2.14}$$

As atomic resonance lines are always observed with Doppler broadening, the specific differential cross-section is often replaced by a temperature dependent *effective* backscatter cross-section σ_{eff} to separate the temperature effect from the density,

$$\sigma_{\mathrm{eff}}(\nu) \equiv \beta(\nu)/\rho\,, \tag{2.15}$$

where ρ denotes the total number density of atoms. Still, in some cases it is important to remember that it is not the cross-section that is reduced in the Doppler wings, but the number of scattering atoms.

These considerations have neglected the natural linewidth because it is significantly smaller than the Doppler width for mesospheric potassium. Nevertheless, for correct temperature calculations the natural linewidth and the laser bandwidth have to be taken into account to calculate the effective profile. This is a so-called Voigt profile, which is a convolution of Gaussian and Lorentzian profiles. There are other broadening mechanisms but they do not have to be considered here. For mesospheric conditions the collision frequency is much smaller (cf. Appendix B) than the natural linewidth and, thus, *pressure broadening* due to a reduced lifetime is negligible.

2.3.2 The Potassium D_1 Resonance Line

The influence of the nuclear spin of the potassium atom ($I = 3/2$) causes the K(D_1) fine structure line to split into four hyperfine components depending on the total angular momentum quantum numbers of the ground and excited state (F and $F' = 0$ or 1). The splitting amounts to 231 MHz (0.457 pm) for the lower ($4S_{1/2}$) and 28 MHz (0.055 pm) for the upper state ($4P_{1/2}$) of ^{39}K. The frequency offset between the transition pairs (F, F') is given in more detail in Appendix A. All transitions are of equal strength except for the weaker (1,1). The hyperfine structure and the line center are different between ^{39}K and the second stable isotope ^{41}K which has a natural abundance of 6.73%. The isotopic shift of the line center is 235 MHz (0.465 pm). No deviation from the universal isotopic composition has been found (*Humayun and Clayton,*

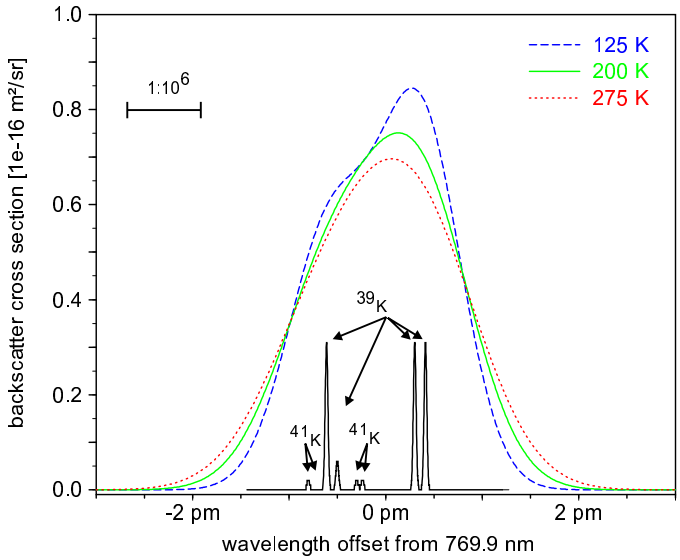

Figure 2.2: The effective backscatter cross-section of atmospheric potassium for temperatures of 125, 200 and 275 K. The individual hyperfine structure lines are indicated at the bottom with a linewidth of 20 MHz. A wavelength offset of 2 pm equals 1 GHz in frequency. Adapted from *von Zahn and Höffner* (1996).

1995a,b), even in extraterrestrial probes. Therefore, the observed ρ_K of mesospheric potassium appears as a superposition of the two isotope cross-sections with their natural abundance h_A. The effective backscatter cross-section is a superposition of the Doppler broadened lines:

$$\sigma_{\text{eff}}(T) = \sum_{i=1}^{4} \sum_{A=39,41} g_i \, h_A \, \sigma_{i,A}(T) \,, \tag{2.16}$$

where g_i are the individual weights of the four hyperfine structure transitions and A is the atomic mass. Figure 2.2 shows σ_{eff} for three different atmospheric temperatures (*von Zahn and Höffner*, 1996). The center wavelength is 769.9 nm in standard air and 770.109 nm in vacuum (cf. Appendix A). The width and the shape of the curve are temperature dependent. The FWHM of 936 MHz (1.85 pm) at 200 K increases with T by about 1 MHz/K. The maximum cross-section is 7.65×10^{-17} m^2/sr for $T = 200$ K.

Our lidar measurements use a continuous frequency scan to determine the frequency dependence of the backscatter coefficient. The measured $\beta(\lambda)$ is completely determined by four atmospheric properties: The mean β is proportional to the K density $\rho_K(z)$ and the frequency independent background is caused by Mie scattering provided that Rayleigh signal and background have been completely subtracted. The offset of the centroid wavelength from the atomic resonance line center is determined by the vertical (radial) wind component, and the width and shape of the curve are governed by the air temperature $T(z)$.

2.3.3 Deviations From the Linear Lidar Equation

As mentioned above, under certain conditions the linear description of the measured lidar return in the simplified form of Eq. 2.8 may not be valid. Such deviations must be considered in order to ensure correct temperature and density calculations.

The most frequent technical cause for non-linearity is the detector. Detectors may become saturated when the illuminance exceeds a certain limit, but the output signal can be corrected as long as the detector characteristic is known. Conditions where the detector exhibits gain changes due to the signal from lower altitudes should be avoided. In that case, η would not be constant and both the backscatter signal and the background would become impossible to determine.

In the mesosphere, high laser energy densities can cause the resonant scattering process to be saturated. The scattering brightness is limited, when the number of excited atoms becomes significant in relation to the number in the ground state. Saturation effects occur when the interaction of an atom with a photon is prevented or influenced by a previous scattering process during the same laser pulse, and they may appear in different ways. This effect can be important for both density and temperature measurements and will be discussed in detail in Section 3.3.4. In the mesopause region, the collision frequency is in the order of $10^4\,\mathrm{s}^{-1}$ (cf. Appendix B) and, thus, equilibrium conditions will have been restored at the following laser pulse which occurs after $\sim 0.03\,\mathrm{s}$.

The metal layer itself may cause highly frequency dependent extinction of the laser beam and the backscattered light. While this effect is negligible for potassium (below 0.1%), it is significant for the sodium layer due to the higher densities and has an influence of 2–8 K on temperatures derived with Na-lidars (*Yu and She*, 1993). Sufficiently large backscatter coefficients that would cause multiple scattering of a single photon, as in tropospheric clouds, do not occur in the middle atmosphere.

In contrast to sodium and iron resonance lidars, the influence of the Earth's magnetic and electric fields are negligible for our potassium lidar due to the different atomic properties. For the linearly polarized light used, the Hanle effect does not change the transition propabilities (*Zimmermann*, 1975; *von Zahn and Höffner*, 1996) for potassium and, hence, the cross-section is independent of the geomagnetic field. The Zeeman splitting is below 1 MHz for a realistic field of 0.5 G. The linear Stark effect does lead to an additional splitting of the $K(D_2)$ line but not of the $K(D_1)$ line used, and the quadratic effect results in a line shift below 1 MHz unless electric fields above $10^5\,\mathrm{Vm}^{-1}$ would occur.

Chapter 3

The Potassium Temperature Lidar

The various types of lidar instruments are classified according to the atmospheric parameter measured and the scattering process or atmospheric constituent used. The potassium resonance temperature lidars (K-lidars) of the Leibniz-Institute of Atmospheric Physics (IAP) were developed primarily for the purpose of measuring the temperature in the mesopause region by probing the spectral shape and width of the resonance line of mesospheric K atoms. Potassium densities and aerosol backscatter coefficients are also derived from the measurements. The retrieval of atmospheric parameters from the received signal has been discussed in Section 2.2. This chapter provides a technical description of the lidar, discusses the improvements made during this thesis work and gives an assessment of the current instrument performance.

Lidars consist of a transmitter and a receiver unit. The schematic of the IAP K-lidars is shown in Figure 3.1. The transmitter unit includes an alexandrite power laser, a seeding laser, which is stabilized to a potassium vapour cell and a spectrum analyser for measuring the frequency of the laser pulses. A telescope mirror collects the backscattered light from the atmosphere and focusses it into a fiber cable. On the detection bench the light is then filtered and converted to electronic signals for registration. The constituents are described in detail in the following sections.

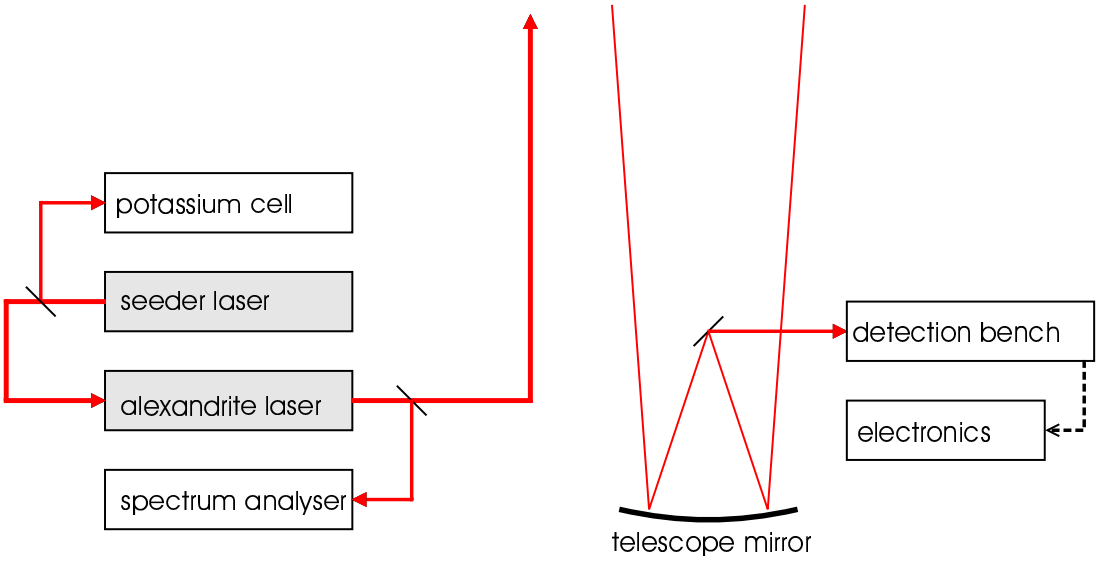

Figure 3.1: Schematic of the IAP K-lidar setup. The transmitter unit is shown to the left and the receiver to the right.

The potassium lidar principle has been developed at Bonn University in the 1990s for mesopause temperature measurements. The first instrument was installed in a standard transport container for easy transportation to various locations and has been operational since 1995. During a shipborne campaign in 1996 and a first year of observations in Kühlungsborn, valuable results were obtained and the principle of operation of the instrument proved to be appropriate for reliable nighttime temperature measurements. To enable necessary further developments of the system, while keeping the lidar in operation, it was decided to build a second (stationary) system in the IAP building in Kühlungsborn. Thereby, it became possible to continue the measurements at Kühlungsborn with the advantage of common-volume observations with the other lidars and to operate the transportable lidar at remote locations. In particular, it was deemed desirable to extend the observations to other latitudes to complete the global picture of the mesosphere.

The instrument development focussed on two aspects: firstly, the laser had to be improved and made more stable and user friendly to enable long-term operation by non-scientific staff. Measurements with continuous high accuracy are necessary to identify interannual variations and trends in the mesopause region. Secondly, the lidar had to be prepared for daytime observations to analyse, for example, tides and systematic differences between day- and nighttime. Apart from some improvements of the laser, major upgrades of the receiver were necessary to achieve daylight capability.

3.1 Transmitter Unit

The heart of a lidar system is the power laser which produces a continuous series of light pulses which are emitted into the atmosphere. For the IAP K-lidars this is provided by a solid-state alexandrite ringlaser which is seeded and Q-switched to achieve narrow-band pulses. A number of additional components are necessary to control and analyse the performance of the power laser.

Selection of the Lidar Type

For the objective of this work, it is desired to derive temperatures with an uncertainty of less than ±5 K at a resolution of about 1 h and 1 km over the whole mesopause region. Lidar temperature soundings of this region are possible by using the metal atoms in the layers at about 80–110 km as a tracer and measuring the thermally induced Doppler broadening of an atomic resonance line. Since the work of *Fricke and von Zahn* (1985), this has been successfully done by probing the D_2 transition of sodium at 589 nm with a narrow-band dye laser. However, it is preferable to use solid-state lasers to achieve higher output power and smaller spectral bandwidth, in addition to a more compact setup and reduced maintenance effort, which is especially important for a transportable system and long-term operation at remote sites or automatic systems. A tuneable high power narrow-band solid-state laser which operates at 589 nm has only recently become available (*She et al.*, 2002c). Light at this wavelength can be generated by frequency mixing of two infrared lasers (*Jeys et al.*, 1989; *Vance et al.*, 1998) or a two-step non-linear conversion of the near infrared output of an alexandrite laser (*Schmitz et al.*, 1995).

To avoid the problematic conversion processes, *Höffner and von Zahn* (1995) developed the alternative approach to use potassium atoms instead of sodium. The K density in the mesosphere was known to be smaller by more than one order of magnitude (*Megie et al.*, 1978), but

this is balanced by some technical advantages. The K(D_1) line at 770 nm is directly accessible by high power alexandrite lasers, whereas the stronger K(D_2) resonance line at 766 nm (see Appendix A) lies within an O_2 absorption band and cannot be used (proposed by *Papen et al.*, 1995). A narrow-band transmitter had been developed since 1991 in collaboration between Bonn University and a manufacturer of alexandrite lasers (Light Age, Inc., Somerset, USA), using a ring resonator with injection seeding (*Schmitz*, 1994). Temperature measurements have been carried out successfully with this laser system since 1995 (*von Zahn and Höffner*, 1996; *von Zahn et al.*, 1996).

When it was initiated at the IAP in 1997 to build a second (yet stationary) lidar for mesopause temperature measurements, the same principle was adopted so that developments from one system can be applied easily to the other. Although the alexandrite laser had proven to be suitable for K-lidar measurements, a number of improvements were necessary, especially, for the achievement of daylight capability. To this end a new laser setup was developed as part of this thesis.

The necessary improvements concern both the value and the stability of several laser parameters (pulse duration, pulse energy, repetition rate, beam divergence and beam direction). For reliable and easy operation the transmitter needed to be advanced, away from an expert system which could only be operated by a well trained scientist, who was fully occupied during the operation. Additionally, the time needed for preparation and maintenance work had to be restricted. The frequency of system breakdowns due to damaged optics or other failures of the alexandrite power laser or the seeding laser had to be reduced and the regular lifetime of the laser components enhanced.

The laser development was based on a commercially available laser system (Light Age, Inc. PAL-101PRO) and was undertaken in close co-operation with J. Höffner. Technical details of the laser development are considered confidential and are described in an internal IAP report. They are intended for publication in collaboration with the manufacturer. This work concentrates on a qualitative discussion and the improvements achieved. A detailed analysis of a similar laser system is also available in the open literature (*Wulfmeyer*, 1998).

3.1.1 The Alexandrite Laser

Among the first tunable solid-state lasers was the alexandrite laser (*Walling et al.*, 1979). The laser material alexandrite ($Cr^{3+}:BeAl_2O_4$) is similar to ruby ($Cr^{3+}:Al_2O_3$), which can be used to build a three-level laser. Alexandrite lasers can be operated on a vibronic transition where the lower laser level of the chromium ions is vibrationally broadened, thereby resembling a four-level laser. This makes it easier to reach the lasing threshold and allows laser operation continuously over the range of about 700–820 nm. The properties of alexandrite are described elsewhere (e. g. *Walling*, 1987; *Koechner*, 1992; *Duarte*, 1995). Two broad absorption bands, centered at 420 and 560 nm, allow effective pumping with flashlamps. Due to an upper reservoir level which lies energetically about 800 cm^{-1} below the upper laser level, alexandrite has a relatively long fluorescence lifetime of more than 100 µs. This facilitates flashlamp pumping and Q-switch operation. The cross-section for stimulated emission peaks near 750 nm for a crystal temperature of 70°C. Alexandrite is a birefringent material with biaxial properties, where the laser light is always linearly polarized. Due to the relatively low gain of alexandrite, optical components inside the resonator must be selected carefully in order to minimize losses.

In the ring resonator (Figure 3.2), two laser rods are mounted in pump chambers with two flashlamps each, which are situated at the outer focal lines of a double-elliptic reflector. The

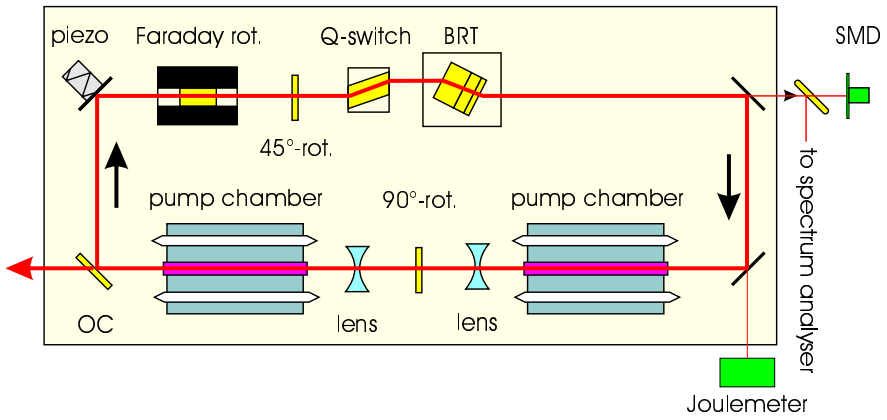

Figure 3.2: Schematic of the IAP alexandrite laser setup (OC, output coupler; BRT, birefringent tuner; SMD, single-mode diode). The arrows give the direction of beam propagation. Mirrors are not labelled.

light from the flashlamps is efficiently focussed onto the rod which is situated at the common inner focal point in a glass tube. Through this flow tube the rod temperature is kept constant by a thermally stabilized water cycle. The power supplies nominally allow a pulse repetition rate of up to 60 Hz, but due to the electronics, it is restricted to 40 Hz.

Thermal Lensing

The pumping energy absorbed causes a warming of the laser rod. The rod is cooled at the surface by the water, leading to a radial temperature distribution that is parabolic to a first-order approximation, inducing a rod-end curvature. At pulse repetition rates above 10 Hz a nearly stationary state is reached which depends on the mean pumping power. The resulting refractive index also becomes parabolic and together with the curved rod-end geometry the rod acts as a thick lens with a certain focal length. For the system used, the focal length was measured and found to be in good agreement with the more refined measurements by *Wulfmeyer* (1998). The rods possess an astigmatism which is due to the different characteristics of the crystal axes. It is corrected by the rod in the second pump chamber which is rotated by 90°, implying the need for the same rotation of the polarization axis of the beam between the pump chambers. In order to achieve stable modes in the resonator, the thermal lensing of the rods must be compensated partly by the use of diverging lenses.

It is desirable to operate the laser with low pumping energy by minimizing the resonator losses and optimizing the optical alignment. Thereby, the thermal lensing fluctuations and pointing instabilities are reduced and the lifetime of the flashlamps is significantly enhanced.

Operation Principle of the Laser

The general setup of the IAP alexandrite laser is shown in Figure 3.2. The beam circulates clockwise through the ring and leaves the resonator to the left. Side beams are used to monitor the laser performance (Section 3.1.3). Since two beam directions are possible in a ring resonator, an *optical diode* is employed to achieve unidirectional operation. It consists of a Faraday rotator which rotates the polarization axis by 45° depending on the beam direction and a quartz rotator where the direction of rotation is independent from the beam direction. In

reverse direction, the polarization experiences no net rotation and is not amplified significantly in the laser rod (about 10% of the other orientation). Instead, it is suppressed by high losses at the other optics which are aligned under the Brewster angle. Therefore, the polarization is parallel to the plane of incidence at the right pump chamber and perpendicular at the left.

For operation off the gain maximum, broad-band spectral filtering is achieved by a *birefringent tuner* (BRT), also called a *Lyot-filter*. As described by *Preuss and Gole* (1980), it consists of a series of birefringent plates which are rotated to tune the transmission peak to the desired wavelength.

In normal operation, a laser pulse would build up by spontaneous emission as soon as a net amplification in the resonator is reached, i. e. when the gain in the rods exceeds the losses during one round-trip. This occurs before the complete energy from the flashlamp pulse is stored in the rod and may result in multiple laser pulses which must be prevented for lidar applications. Also, narrow-band pulses can be achieved only if the laser pulse builds up when the resonator provides constructive interference for the desired wavelength (see below). Thus, a *Q-switch* is used to reduce the resonator quality until the fluorescence maximum is reached and the resonance conditions are satisfied. At this moment, it switches quickly to high quality and allows a laser pulse to emerge. The Q-switch consists of a Pockels-cell, which uses the linear electro-optical effect to change the beam polarization and induce losses and suppress amplification.

New Resonator Setup and Pulse Length

The performance of the commercially produced laser is not sufficient for temperature soundings. The advanced version developed at Bonn University and used in the first generation potassium lidar (*BU setup*) was not fully satisfying either. To further improve the performance and reliability of the alexandrite laser a number of changes were applied to the resonator setup at the IAP. The present setup which was developed during this work is referred to as the *IAP setup*. The technical changes are described in more detail in the internal report.

For a beam width of 1 mm, an output pulse energy of 200 mJ and a pulse length of 200 ns, the mean power density is about 1 MW/mm^2. If the reflectivity of the output coupler is 75% the power density inside the resonator is 4 times higher and close to the typical damage threshold of optical surfaces (10 MW/mm^2). Thus, to reduce the risk of damage to the optics, a larger beam diameter is appreciated.

The beam propagation in the resonator can be simulated using the *ABCD* matrix technique for Gaussian optics (*Kogelnik and Li*, 1966; *Magni*, 1986). Calculations for the BU setup have shown that the beam waist was smaller than 1 mm (*Schmitz*, 1994). For the IAP setup of the resonator, similar calculations show that it was increased by more than 30% (*Höffner*, private communication) which reduces the energy density by 50%.

A long duration of the laser pulses is crucial for two reasons. For the lidar measurements it is important to avoid saturation effects which depend on the temporal and spatial energy density. Thus, longer pulses allow a lower beam divergence which is necessary for daytime lidar operation. Also, increasing the pulse length will again reduce the energy density in and outside the laser resonator and therefore the risk of damage to the optics. As the fluorescence lifetime of the upper laser level of alexandrite is very long, it does not limit the pulse length. In order to enable a lidar range resolution of 200 m the geometric length of the laser pulses should not exceed this limit. Hence, the aim was to extend the FWHM value (t_p) of the near Gaussian pulses to 200–300 ns.

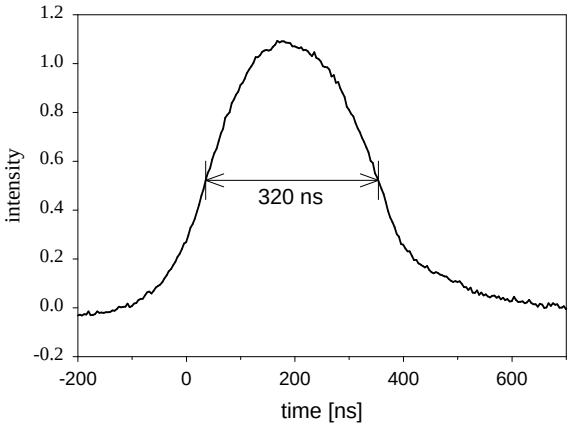

Figure 3.3: Temporal intensity profile of a single laser pulse measured with a fast photodiode (arbitrary units). The FWHM length of this pulse was 320 ns, the output energy was about 150 mJ.

The laser pulse length of the commercial alexandrite laser PAL-101PRO was not specified by the manufacturer and was found to be below 100 ns for Q-switch operation. *Schmitz* (1994) reported a pulse length of 115 ns for the BU laser setup. With the IAP setup much longer pulses were achieved. The example of Figure 3.3 shows a pulse length of $t_p = 320$ ns which is only slightly above the typical value for an energy of 150 mJ. For pulse energies up to 200 mJ, a mean value of 250 ns is obtained with the new laser setup. With increasing pulse energy the pulse length decreases due to enhanced gain in the laser rod.

3.1.2 Resonator Modes and Injection Seeding

In a laser resonator a number of transverse electro-magnetic (TEM) and longitudinal modes may be formed, all having individual frequencies. In normal operation the lasing process can occur in all stable modes which have frequencies within the gain curve. For measuring the atmospheric Doppler broadening the frequency spectrum should be as narrow as possible to avoid uncertainties due to the convolution of the laser spectrum and the backscatter cross-section (Eq. 2.14). The fundamental TEM mode (TEM_{00}) has a Gaussian energy distribution and the lowest divergence. Therefore, it is desired to operate the laser in TEM_{00} and single longitudinal mode.

For each longitudinal mode the optical path length L must be an integer multiple of the wavelength for positive interference to occur. The frequency spacing between adjacent modes is given as $\Delta\nu_L = c/L$, which is the reciprocal of the round-trip time of a light pulse through the resonator. For a 2-m resonator the mode spacing is $\Delta\nu_L = 150$ MHz. When the laser emits in two longitudinal modes they are clearly detected by the spectrum analyser and a corresponding mode beating of $\sim$7 ns can be observed in the temporal development of the laser pulse intensity when measured with a fast photodiode. The spacing of two transversal modes TEM_{mn} is $\Delta\nu_{mn} = c/(4L)$ in a ring resonator (*Wulfmeyer*, 1995, p. 90). Accordingly, slower mode beating can be observed when the laser is allowed to form other modes in addition to TEM_{00}. Higher transversal modes can be identified visually when the beam is widened and projected onto a screen, where each mode produces a specific pattern. Higher modes have a larger beam diameter and suffer higher refraction losses at small apertures in the laser. The IAP laser is observed

to operate in TEM_{00} mode for more than 99% of the pulses.

The transmission curve of the birefringent tuner is relatively broad and allows amplification of several longitudinal modes. Narrow-band operation of an alexandrite laser was demonstrated by *Schwemmer et al.* (1991) who used *injection seeding* by a diode laser with a bandwidth which covers two or three longitudinal modes. The continuous-wave (cw) beam of the seeding laser is coupled into the resonator so that some light intensity at the desired frequencies is always present. When the Q-switch enables the building up of a laser pulse the stimulated emission at the seeding frequencies dominates spontaneous emission at other frequencies. Thus, only the seeded modes are present in the laser pulse.

In order to achieve single longitudinal mode (SLM) operation the alexandrite laser is injection seeded by a cw diode laser with a bandwidth which is smaller than the longitudinal mode spacing. In this case SLM operation can be achieved if the seeding frequency matches a resonator mode. As this condition is not always fulfilled, a *mode matching* technique has to be applied, to ensure that one resonator mode matches the seeding frequency at the time when the laser is fired.

Mode Matching

The different possibilities of mode matching have been analysed by *Schmitz* (1994) for an alexandrite laser. Active stabilization of the resonator to the seeder frequency would be complicated because the frequency is steadily changing during lidar operation. Furthermore, in environments with high noise or vibrations the stabilization would need to be extremely fast. Finally, during the pumping process, the refractive index of the laser rods changes and, thus, the optical length of the resonator. These conditions make active stabilization of the resonator impractical.

Instead, it is possible to use a fast resonance-detection technique. A photodiode behind a laser mirror (SMD in Figure 3.2) measures the light intensity in the resonator before the Q-switch is opened. The signal is a superposition of the fluorescence intensity originating from the spontaneous emission of the pumped laser rods and an interference signal from the seeding beam (Figure 3.4). The fluorescence intensity is proportional to the energy stored in the laser rods and thus its maximum is the best time for the laser pulse to build up. The continuous seeding light is amplified in the rods and produces self-interference after each circulation. Positive interference indicates times when the cavity is resonant with the injected beam. A detection of this interference can be used to obtain SLM operation by opening the Q-switch at this time, as has been described by *Henderson et al.* (1986). A dedicated electronic device detects the interference maxima and triggers the Q-switch to open at the first one after the fluorescence maximum is reached. This produces a SLM laser pulse at the seeded frequency. SLM laser operation is confirmed either by the absence of mode beating (Figure 3.3) or with the aid of the spectrum analyser (see Section 3.1.3).

Mode matching can be achieved in different ways. It is possible to passively wait for mode matching to occur by chance (*Schmitz et al.*, 1995), which is done in the commercial version. Unfortunately, the optical length has a turning point ($dL/dt = 0$) when the maximum energy is stored in the rod and thus the modulation is very weak during the period when mode matching is desired. If the laser pulse is delayed by more than about 20 µs after the maximum of the laser rod fluorescence has occurred, its energy will be significantly reduced. Like in the example shown in the left panel of Figure 3.4, for a large fraction of pulses no usable mode matching occurred near the fluorescence peak.

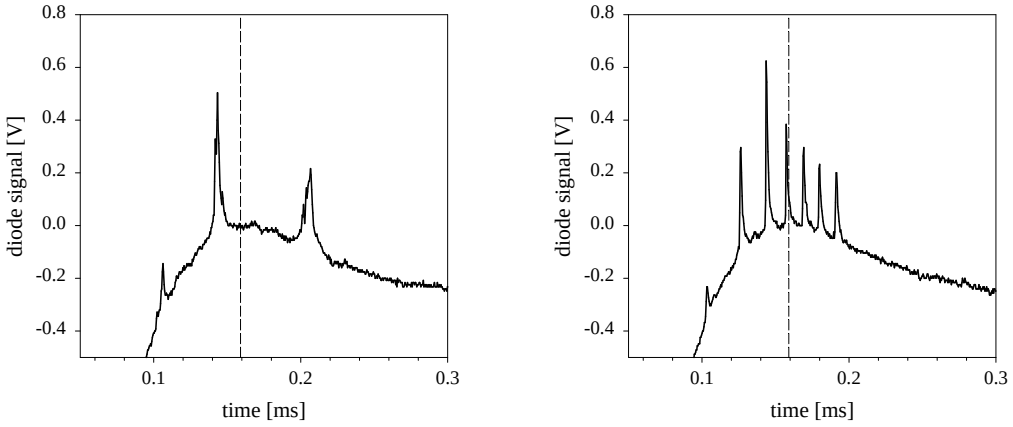

Figure 3.4: The seeding interference detected by the SMD photodiode. The maximum of the underlying fluorescence curve is marked by the vertical line. The sharp peaks are caused by positive interference of the seeder light. Left: original setup with passive mode matching. Right: active mode matching with the piezo-driven mirror.

This lack of modulation can be overcome by applying a fast jitter of at least $\pm\Delta\nu_L$ on the seeding frequency. This technique allows reliable SLM operation and has been used in the BU setup since 1995. However, the frequency jitter is also present in the alexandrite laser output and creates disturbance in lidar application.

Therefore, in the new IAP setup a different active mode matching technique is applied which was first demonstrated by *Henderson et al.* (1986) for a linear Nd:YAG laser. At the time of the fluorescence maximum, the resonator length is changed by a piezoelectric actuator which moves one laser mirror. The motion is perpendicular to the mirror surface and extends over a few µm which does not influence the resonator stability. To achieve a sufficiently fast movement with a single piezo for short intervals between the interferences, lightweight laser mirrors are used and appropriate driving electronics have been developed at the IAP. As demonstrated in Figure 3.4 an interference pattern is induced with a spacing of about 20 µs which is sufficient to always obtain a mode matching condition at the maximum of the fluorescence curve. Thereby, the temporal jitter of the Q-switch firing time is reduced to a range of 20 µs and, consequently, the energy stability is noticeably enhanced. The piezo produces a resonator tuning of only about 1 MHz during a laser pulse length of 200 ns and, thus, no significant spectral broadening is expected due to a change of the geometric resonator length during the pulse emission. However, a frequency variation within the duration of the laser pulse (a *chirp*) may alternatively be caused by electronically induced detuning of the resonator. This process cannot be avoided because the refractive index of the alexandrite rods depends on the degree of electronic excitation. The excitation changes rapidly during the laser pulse formation. Thereby, the optical resonator length and the resonance frequency change.

The new piezo setup enables stable SLM operation at exactly the desired frequency and could also be used for applications which need high pulse-to-pulse frequency stability. The active mode matching technique has been demonstrated before to allow reliable operation of a Nd:YAG laser in high noise environments (*Fry et al.*, 1991). Even vibrations of the laser table or laser mirrors, which might occur when the lidar was installed on a ship, do not disturb the SLM operation of our alexandrite laser.

The Seeding Laser

For injection seeding the power laser we employ a cw single-mode diode laser. Since 1997 an external cavity diode laser (ECDL) has been used (Toptica DL 100) in which a grating provides feedback into the laser diode. This grating acts as an external resonator and causes the diode to emit at a single frequency only. The frequency can be tuned over a range of about 6 GHz without mode hopping by tilting the grating. During lidar operation the K(D_1) resonance line is scanned by a continuous modulation of the ECDL frequency over a range of 1.64 GHz.

Due to the used cavity version with high thermal stability, the diode laser shows short-term frequency fluctuations of a few MHz only. This stability is sufficient to perform Doppler-free spectroscopy of potassium atoms as was done by *Lautenbach* (2001) for accurate calibration of the spectrum analyser. Thereby, the spectral width of the seeder has been estimated to be about 9 MHz (FWHM). When the laser is switched on it returns to the K(D_1) frequency with an accuracy of a few GHz and can be re-tuned easily to the resonance line.

As shown in the schematic of the seeder setup (Figure 3.5), the beam from the diode laser passes an optical isolator (Linos, 60 dB) to suppress backreflections onto the diode which could interfere with its performance. An anamorphotic prism pair forms a circular beam profile after the polarization is rotated to minimize losses. A beam splitter directs a fraction of the beam into a potassium vapour cell. The resonance signal from the vapour cell is detected by a photomultiplier and used to stabilize the frequency scan to the center of the resonance line with an accuracy of a few tens of MHz by means of a lock-in amplifier. This provides the frequency guidance for the lidar operation.

The main portion of the seeder light is passing through a laser modulator (Linos LM0202), which contains a Pockels-cell and can be switched electronically to couple the laser beam into one or another fiber cable. These polarization maintaining single-mode fiber cables guide the beam either to the alexandrite laser or to the spectrum analyser to measure the seeding laser spectrum directly. Attenuated by the various optical components, at least 10% of the output power of 20 mW are coupled into the ringlaser, an amount which is sufficient for reliable injection seeding. The coupling technique in the IAP setup is discussed in the internal report.

The laser modulator also serves to switch off the seeding beam when the laser pulse is sent out into the atmosphere. The continuous seeding beam could otherwise contribute significantly to the background because it produces a steady signal from the lower troposphere (see Section 3.2.4).

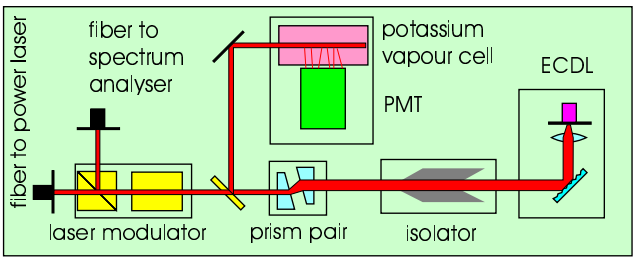

Figure 3.5: The seeding laser (ECDL, external cavity diode laser; PMT, photomultiplier tube). The main fraction of the beam is coupled into either of the two fiber cables.

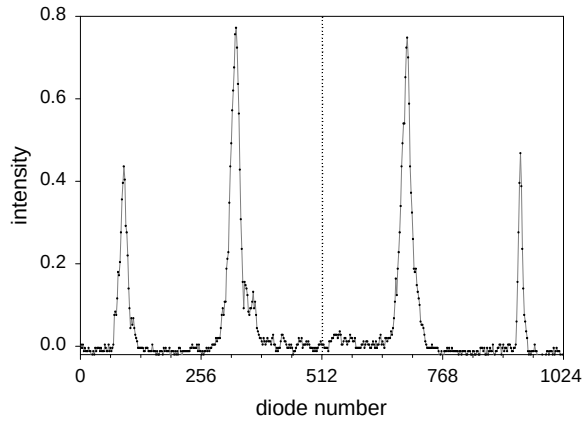

Figure 3.6: Frequency spectrum 'picture' of a single laser pulse obtained with the spectrum analyser. The diode array measures a cross-section of the interference ring pattern. The width of the peaks corresponds to about 40 MHz FWHM, which is the resolution of the spectrum analyser.

3.1.3 Lidar Operation

During the lidar measurements the laser operation needs to be monitored continuously. Although the laser mirrors have high reflectivity ($\geq$99.5%), a significant amount of laser energy is leaving the resonator there (up to 4 mJ for an output coupler reflectivity of 75% and an output energy of 200 mJ). These side beams (see Figure 3.2) are used to analyse the laser performance during operation. One side beam is directed on a Joulemeter to monitor the pulse energy, which is a fixed fraction of the main output. The second one passes an adjustable attenuator and is directed into the spectrum analyser. This is a stabilized plane Fabry-Perot etalon (Hovemere ltd.) with a nominal free spectral range of 1 GHz. The fringe pattern is imaged on a linear CCD array (1024 diodes) which is read out after each laser pulse to calculate the pulse frequency and its bandwidth in real-time. An example is shown in Figure 3.6. The resolution depends on the position on the array and the lowest detectable bandwidth ranges between 40 and 60 MHz. With a Doppler-free polarization spectroscopy experiment, *Lautenbach* (2001) determined the calibration of the spectrum analyser with an accuracy of 1 MHz. The long-term stability of the spectrum analyser is not sufficient to use it as an absolute frequency standard and therefore the seeding laser is stabilized to the vapour cell.

For temperature measurements, only the relative frequency of each outgoing laser pulse has to be known and can be measured with high accuracy by the spectrum analyser. Between the seeding laser and the power laser a frequency offset of up to 35 MHz is observed. Therefore, it is necessary to measure the frequency of the outgoing laser beam, whereas, it would not be sufficient for accurate temperature measurements to solely determine the seeding frequency. The observed shift is in the order of the spectral width of the laser pulses. Its cause is not clear but it might be a result of the chirp induced by the change of the refractive index.

By modulating the frequency of the seeding laser, the K(D_1) line is scanned with a period of about 2 s. With the spectrum analyser each laser pulse is evaluated and only if the pulse is found to be single-mode, the backscatter signal for the determined frequency is stored.

Our technique of a continuous frequency scan remains in contrast to techniques employed in sodium lidars which use only two or three fixed laser frequencies (*She et al.*, 1990; *She and Yu*, 1994; *Gardner et al.*, 2001) and derive the temperature from their intensity ratio. Our

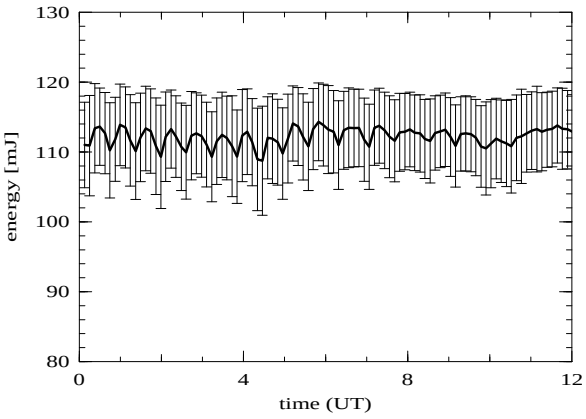

Figure 3.7: Laser pulse energy measured on February 25th, 2003. For every 5000 pulses both the mean and standard deviation are plotted. The average value of the standard deviations is below 6 mJ.

technique provides the possibility to compare the theoretical with the measured form of the σ_{eff} curve and calculate other parameters. This serves to ensure correct temperature calculations and has been done with the laser bandwidth, the spectrum analyser calibration, the isotopic composition and line shift of potassium, and frequency dependent saturation effects (*Höffner*, manuscript in preparation).

With this technique the laser bandwidth was determined to be about 12 MHz (FWHM). This value is clearly below the resolution of the devices available to us to measure the spectral width directly. It is in accordance with the Fourier limit that defines with $\Delta\nu = 1/(2t_{\text{p}})$ a minimum spectral width of 2 MHz for a pulse length of $t_{\text{p}} = 250$ ns.

The divergence of the laser beam in single mode operation was determined to be about 0.4 mrad (full angle) by measuring the beam diameter at a distance of 30 m. This divergence is in good agreement with the calculated resonator modes and results in a beam diameter of 40 m in 100 km altitude. When a smaller field of view of the receiving telescope is used, the divergence of the laser beam can be adapted by passing it through a beam-widening telescope. The beam steering mirror reflects the beam into the atmosphere and is exactly tilted by picomotors (NewFocus Inc.) to ensure that the beam direction matches the viewing direction of the telescope and overlap in the middle atmosphere is complete. The exact time at which the laser beam is sent out is registered by a photodiode.

3.1.4 Achievements

Compared with the former (BU) setup the beam divergence of the alexandrite laser in the IAP setup is reduced and its pointing stability appears to be higher. This is important for daylight operation when the field of view of the receiving telescopes must be small (cf. Section 3.3).

The continuously monitored laser pulse energy shows the inherent stability of the IAP system (Figure 3.7). For a period of 12 hours the laser did run unattended and the mean energy for each group of 5000 laser pulses is shown together with its standard deviation. The measured pulse-to-pulse variability of the laser energy is 5%. The periodic variation of the mean is about 1% and is mainly due to variations of the cooling water temperature. The temperature clearly shows 30-min oscillations until 06:00 UT which are induced by an Nd:YAG laser system operating simultaneously during that time. This demonstrates that a further enhanced stability

Table 3.1: Typical properties of the IAP alexandrite power lasers during K-lidar operation.

Laser medium	2 rods, $Cr^{3+} : BeAl_2O_4$
Geometry	ring resonator
Wavelength	770 nm, tunable
Spectral width	$\leq$20 MHz (FWHM)
Polarization	linear
Repetition rate	33 Hz
Pulse energy	150 mJ
Energy fluctuations	5% (1σ)
Pulse length	250 ns (FWHM)
Beam divergence	0.4 mrad (full angle)

of the alexandrite laser could be achieved by the introduction of an active control of the cooling water temperature.

The transmitter system has been substantially improved for long term operation. The thermal stability is much higher and the cooling system works reliably, thereby avoiding regular re-adjustments of the alexandrite laser. With the new setup the alignment has become easier and, hence, more reproducible. The increased pulse length and larger beam diameter reduce the risk of damage to the optical components. Due to reduced resonator losses weaker pumping is required and, thus, the lifetime of the flashlamps strongly enhanced by about a factor of four. In the current operation mode the lifetime of the Q-switch crystals is extended from a few months to several years. Operation in single longitudinal mode is achieved reliably.

Since the laser in the transportable lidar system was rebuilt almost identically to the stationary system in February 2001, it has been successfully in operation on the Arctic island of Spitsbergen without a significant failure of the alexandrite laser. The transmitter system in its current state is regarded appropriate for regular continuous long-term temperature measurements. The typical operation parameters of the alexandrite power lasers in the IAP setup are gathered in Table 3.1, being valid for both systems. Pulse energies up to 200 mJ are possible but only 150 mJ are regularly used to protect the optical components and avoid saturation effects.

The laser performance is not only clearly superior to the commercially available setup but it is also an improvement compared with our previous system and to the parameters achieved by *Wulfmeyer* (1998) for a similar high-performance alexandrite ringlaser. With one pump chamber only, he obtained pulses with 200 ns for only 50 mJ of output energy and the same beam divergence. The energy fluctuations of his laser were less than 8% and the linewidth was below 40 MHz.

The high efficiency of the IAP lasers with the new resonator setup is demonstrated by the required pump energy. To produce laser pulses with 150 mJ the flashlamps are operated at 1.76 kV instead of the formerly needed 2.1 kV at a similar repetition rate. This is a reduction of the pump energy by 30%. The slope efficiency of the laser is estimated to be 0.6% from the pumping energy needed to raise the output energy from 100 to 150 mJ. These numbers are obtained for seeded single mode operation.

Currently, both IAP K-lidar systems are operated in a semi-automatic mode. They can be operated by persons with limited training and students have been employed to perform atmospheric measurements. After the switch-on procedure remote computer control is provided for most important functions, which include online data visualization, prevention of system damages and the complete shutdown of the system.

3.2 Receiver Unit for Nighttime Operation

In this section the receiver unit of the IAP K-lidars is described, first, in the state it was used for nighttime observations. The necessary upgrade of the instrument for daytime operation is the subject of Section 3.3.

The light from the atmosphere is collected by a telescope mirror and transferred through a fiber cable to the *detection bench* where it is filtered and detected. The electronic signals produced are then registered and stored by computer.

A major difficulty for lidar investigations of the mesopause region is the weak signal. This is partly due to the distance term A/r^2 in the lidar equation (Eq. 2.5) which gives the solid angle covered by the receiving telescope of about 10^{-10} sr. Although a powerful laser source is used single photon events have to be registered in the received backscatter signal. The main implications are (a) that it is appropriate to take some efforts to maximize the signal and statistically enhance the results, and (b) that for daylight operation intense filtering is necessary to separate the backscatter signal from the solar background.

3.2.1 Telescopes

The IAP lidars employ parabolic telescope mirrors to receive the light from the atmosphere. The signal strength is proportional to the receiver area. Due to large telescopes being extremely costly a system of 8 smaller mirrors of 0.5 m diameter and 1.2 m focal length was installed at the IAP. This setup is very flexible as the individual mirrors can be grouped in various ways to distribute the area between the lidar systems. Seven of the mirrors could be used with the K-lidar and provide an area larger than one 1.3-m telescope.

In lidar application no image is produced by the telescope but the light is collected into a fiber which is placed at its focal point. With the relatively short focal lengths used, no additional optic is needed. For nighttime lidar operation fiber cables with relatively large aperture diameters (up to 1 mm) can be used and medium optical quality of the telescope is sufficient. Usually, a bundle of 7 fibers with 0.6 mm aperture each was employed which gives a full *field of view* (FOV) of 500 µrad with the focal length of 1.2 m. This is sufficient to cover the full laser beam and no beam-widening telescope had to be used. The transportable instrument is equipped with a high quality 0.8-m mirror and was operated at a FOV of 789 µrad.

3.2.2 Detection Bench

When the light enters the detection bench through the fiber cable bundle it encounters the chopper at first. This wheel with four fins rotates at 10,000 min^{-1} and modulates the light with a frequency of 667 Hz. The laser is synchronized to this wheel and fires when the fiber is covered by a fin. This serves to protect the sensitive detector from the high intensity of the light scattered back from the lower atmosphere. About 0.2 ms after the laser has fired, the fiber is uncovered and the signal originating from above 30 km can pass.

A lens forms a parallel beam which then passes the optical filter and is focussed on the detector. For nighttime operation interference filters with 1 nm bandwidth are used. They provide sufficient background reduction and a high transmission (about 70%). For daytime operation higher efforts are necessary and will be discussed in Section 3.3.

The signal is detected by a photon counting photomultiplier tube (PMT). The type used (Burle C31034-A02) has, at 15%, the highest quantum efficiency available at 770 nm and a

nominal low dark count rate of less than 100 Hz when cooled to below -30°C. To achieve this it is placed in a sealed air-cooled housing (Products for Research Inc. PC206CE). The PMT provides a linear response for count rates up to ∼10 MHz and has a projected sensitive photocathode area of 4 mm × 10 mm.

With a dichroitic beam splitting mirror in front of the interference filter other wavelengths can be separated from the beam. In this way the telescopes have been used simultaneously for other lidars what ensured common volume operation. This was important for the study of meteor trails, where beneath potassium also sodium, iron and calcium atoms and calcium ions have been observed (cf. *von Zahn et al.*, 1999, 2002).

3.2.3 Electronics

The synchronization of the various lidar components is governed by IAP-built electronics. In accordance with the laser repetition rate each lidar sounding is initialized at a time when the free running chopper wheel is in the desired position. With certain delays, the laser flashlamps, the Q-switch, the single mode electronics, and others are activated. When the laser pulse is detected to emerge the counter is started and the laser modulator is switched to block the seeding beam.

The photon count signal from the PMT is amplified and passed through a discriminator to achieve uniform pulses which are counted by a Joerger S3 model. The counter integrates the photon counts over 200-m range intervals (bins of dt_z =1.334 µs) and can be read out after each laser pulse. Due to frequent irregularities the CAMAC interface electronics have been replaced in 2003 by an advanced counter developed at the IAP (T. Köpnick and J. Höffner), which is operated at 50-m range intervals.

The photon count profiles are transferred to a computer which also reads the spectrum analyser's diode array. According to the spectral information (purity, wavelength) the photon counts are typically integrated over 4000 laser pulses (∼2 min) and then stored in a file. An example for the mean count rate has been shown in Figure 2.1 (p. 8). The storage of single lidar return profiles is possible but usable only for nighttime operation. The photon count signal from about 40 km height is used to continuously monitor the overlap between the laser beam and the telescope's FOV.

While the laser wavelength is continuously varied over the Doppler width of the K(D_1) resonance line, the photon counts are usually *binned* into 18 intervals of 0.18 pm width, i. e. they are sorted into the intervals and integrated separately. Number and width of these bins have been chosen to optimize the temperature calculation from the potassium backscatter signal. The resulting range of ±1.62 pm from the K(D_1) line center is the *lidar scan range* over which the laser wavelength is continuously tuned. To account for the lower resonance signal in the wings of the Doppler broadened line (∼10% of the signal at the line center) the seeding laser performs a sinusoidal scan causing a higher number of pulses at the outer than at the center wavelengths.

3.2.4 Temperature Retrieval

While the magnitude of the backscatter coefficient allows to calculate the potassium density, the atmospheric temperature is derived from its wavelength dependence (see Section 2.3.2). The spectral shape of the theoretical effective backscatter cross-section (Figure 2.2) is fitted to the backscatter coefficients $\beta(\lambda)$ measured for the 18 wavelengths bins. The numerical evaluation is carried out with a computer program developed at the IAP by J. Höffner. The systematic

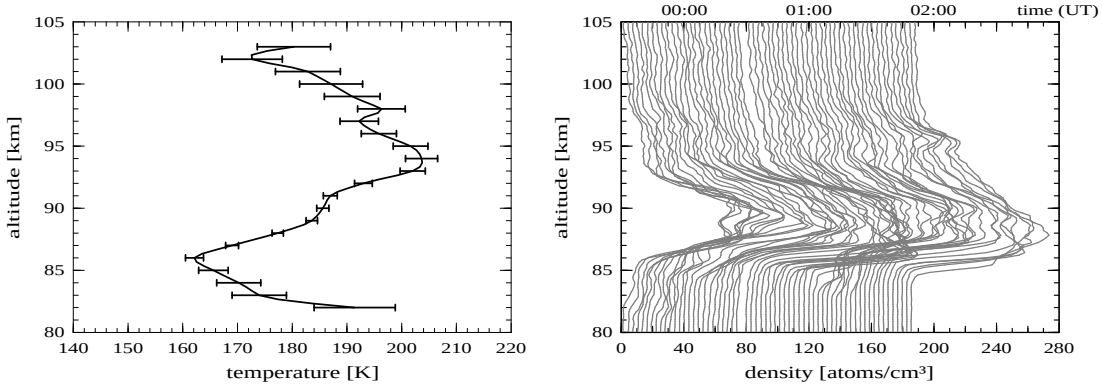

Figure 3.8: Example of a nighttime measurement from Kühlungsborn, August 12th/13th, 1997. Left: temperature profile at 0:00 UT after 1 h and 2 km integration. Right: K densities with 200 m and ∼2 min resolution; the individual profiles are plotted with an offset given by the time axis.

uncertainty of the fit has been estimated by *von Zahn and Höffner* (1996) to be about 3 K. It is due to uncertainties in the atomic constants, the laser bandwidth and saturation effects.

An example for a nighttime measurement is given in Figure 3.8. This temperature profile from the mid of August at Kühlungsborn is a typical summer profile with the absolute minimum at 86 km and a secondary minimum at 102 km. At the peak of the K layer near 90 km with a density of $\rho_K = 80\,\mathrm{cm}^{-3}$ the statistical temperature uncertainties are as low as ±1 K after one hour integration. Values with errors of less than ±10 K are calculated over a wide range of the layer with densities down to a few atoms per cm^3. Density profiles are given with a higher resolution (∼2 min) and show variations on shorter timescales. As ρ_K is derived from the photon counts integrated over all wavelengths its statistical uncertainty is lower.

The statistical temperature error depends on the uncertainties of the 18 $\beta(\lambda)$-values which are due to photon noise. It decreases with the accumulated number of counts but increases with the number of background counts. From a simulation of measurements (*Höffner*, manuscript in preparation) in the configuration described, the expected temperature uncertainty is shown in Figure 3.9 for each number of signal and background photon counts summed over the 18 wavelengths bins. For a signal-to-background ratio (SBR) of better than 100:1, the background becomes irrelevant. The values are given for a temperature of $T = 180$ K and increase slightly with T.

Under ideal conditions in moonless nights a background count rate of $1/4000/dt_z$ (one count per 4000 laser shots and 200-m altitude interval) can be achieved, which is due to PMT dark counts, starlight and nightglow of the atmosphere. In spite of the low densities of the alkali metals, their atomic resonance lines are quite prominent in the photochemical airglow due to their high reactivity with oxygen compounds (*Chamberlain and Hunten*, 1987, p. 286). A lidar return signal of $0.1/dt_z$ can be recorded from the peak of the potassium layer for relatively high K densities (compare Figure 2.1). After a 10^6-fold integration, typically over 2 km and 1 h (about 100,000 laser shots), these 10^5 counts allow temperature calculations with an accuracy of nearly ±1 K. Taking an error of 10 K as a threshold for reliable temperature measurements, results are expected over the range where the signal is above 5% ($10^{3.7}$ counts in Figure 3.9) at the edges of the potassium layer (in agreement with Figure 3.8).

For a constant SBR the uncertainty is inversely proportional to $\sqrt{S}$ and $\sqrt{B}$. A reduction

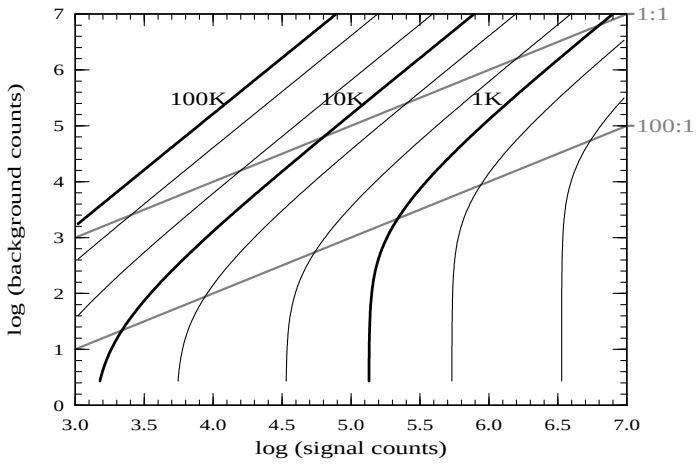

Figure 3.9: Isolines of simulated statistical uncertainty for an atmospheric temperature of 180 K, depending on the number of signal and background photon counts integrated over all wavelengths. The thin isolines represent 0.2, 0.5, 2, 5, 20, and 50 K errors, respectively. The grey lines mark constant signal-to-background ratios.

of the number of counts and integration time by a factor of 100 will increase the error only by a factor of 10. Thus, the temporal resolution can be largely enhanced when only the peak of the layer is considered. For an increased background under daylight conditions, a SBR of 1:1 may be obtained. After the same integration as before, 10^5 signal and background counts would provide an accuracy which is reduced to nearly ±10 K. Thus, the temperature calculation would be limited to the range with high K densities under daylight conditions.

Seeder Induced Background

A significant height-independent background signal can be caused by the cw beam of the seeding laser and can increase the uncertainty of the temperature calculation. The seeding beam circulates in the resonator and leaves the resonator along the same axis as the pulse from the power laser, and also the portion reflected by the output coupler when the seeder light enters the resonator is propagating into the atmosphere. Although it is of low power the continuous beam gives rise to a significant background signal. The lower troposphere, due to its high backscatter coefficient and low distance, causes a signal that adds to the pulsed laser returns from all altitudes. Since it is at the K(D_1) wavelength it cannot be rejected in the detector. In order to suppress this unwanted signal, the laser modulator has been integrated into the seeder setup (Figure 3.5) and switches off the seeding beam within 1 µs after the laser pulse is emitted.

The seeder induced background becomes obvious under certain weather conditions, as shown in Figure 3.10. During the observations of the Leonid meteor shower in 1999 the conditions were difficult due to haze and low clouds. While the potassium signal was reduced only by 35%, the same aerosols caused the background to increase nearly by a factor of 100 when the laser modulator was not used (∘). The average SBR dropped to about 1:1. By contrast, when the seeding beam was blocked (+) no significant background enhancement occurred and more accurate temperature calculations were possible. Under clear sky conditions the effect of blocking the seeding beam is notable at the upper edge of the layer, extending the altitude range usable for temperature calculation by several km.

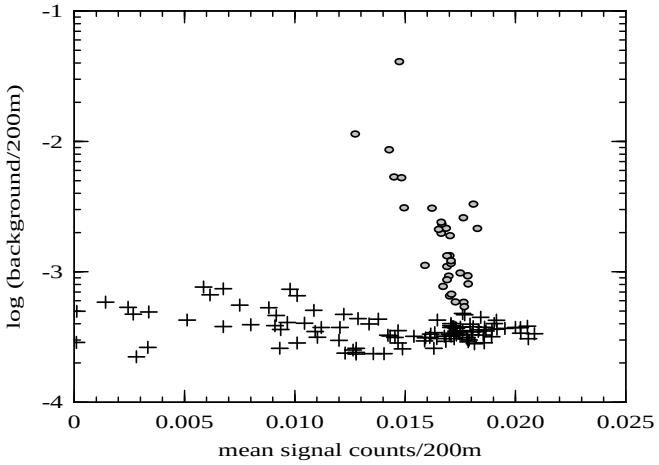

Figure 3.10: Relation between background and mean potassium signal (80–105 km) during hazy conditions in the night of November $15^{th}/16^{th}$, 1999, at Kühlungsborn. During the first hour the seeding beam was not blocked (∘); afterwards, it was blocked by the laser modulator (+).

3.3 Daylight Upgrade of the Lidar Receiver

For a long time lidar investigations of the mesosphere have been restricted to nighttime conditions. During daytime the sunlight produces a background which is about 6 orders of magnitude larger than the background caused by nightglow and starlight. With the lidar configuration described above the background would exceed the signal from the mesosphere by at least 3 orders of magnitude. This count rate would exceed the bandwidth of the detector and its noise would hinder the evaluation of the data, as is obvious from Figure 3.9 (SBR$<$1:1000).

In order to enable continuous measurements during day and night and measurements during polar summer conditions, the background has to be suppressed by at least additional 3 orders of magnitude. This would cause the lidar signal to exceed the background (SBR$>$1:1), so that after an integration time in the order of one hour, temperatures can be derived. Three different measures can be taken. Only their combination provides daylight capability and their effects on the temperature measurements have to be considered carefully. Spectral filtering should reduce the receiver bandwidth from about $\Delta\lambda = 1$ nm to $\Delta\lambda \leq 10$ pm. Spatial filtering can also suppress the background significantly and the usage of a more efficient detector will reduce the necessary integration time. The main results discussed here have already been published (*Fricke-Begemann et al.*, 2002a).

3.3.1 Spectral Filtering Technique

For nighttime lidar observations, conventional interference filters are completely sufficient, which can have a spectral bandwidth down to 0.3–1.0 nm. For efficient daylight rejection much smaller bandwidths of below 10 pm are required because the background is given by its integral (Eq. 2.7). The transmission passband should cover the full spectral width of the probed resonance line. The influence of a narrow filter curve is discussed below in detail (Section 3.3.2) but it is clear that a flat filter curve over the lidar scan range of 3.2 pm will minimize necessary corrections and avoid uncertainties caused by fluctuations of the filter curve. The second requirement to the optical filter is a high transmission over the passband and a good blocking

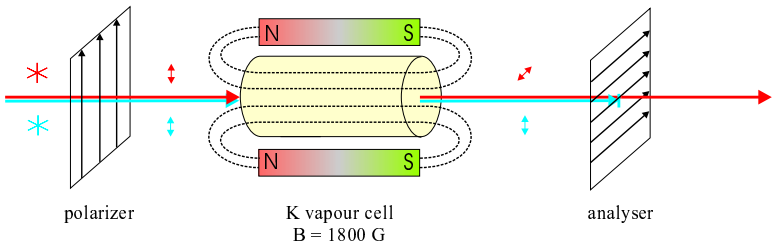

Figure 3.11: The principle setup of a Faraday anomalous dispersion optical filter (FADOF). The incoming beam is linearly polarized by a polarizer and passes through an atomic vapour cell in a longitudinal magnetic field. Only when the light interacts with the potassium vapour it can partially pass the analyser, otherwise it is efficiently blocked.

outside. The ideal filter would be described by an rectangular transmission curve with a width of about 5 pm.

The common narrow-band filter technology for lidar is the high-resolution Fabry-Perot etalon (e. g. *McKay*, 1999). Its disadvantage is the requirement of high optical quality of the incoming light. A narrow spectral bandwidth combined with a high peak transmission requires an extremely low beam divergence, i. e. large optical apertures, which make the technical realization of such a filter very expensive (∼100,000 EUR). To tune and lock an etalon on the lidar emitter wavelength, extensive mechanical and thermal stabilization is necessary. Reliable operation of such a filter requires a temperature-stable and vibration-free environment. This cannot always be guaranteed for a transportable lidar system operated under extreme climatical and operational conditions.

The Faraday Anomalous Dispersion Optical Filter (FADOF)

A more robust and cost-effective (∼15,000 EUR) technology is an atomic resonance filter. The *Faraday anomalous dispersion optical filter* (FADOF) has become important in free-space optical communication and remote sensing. The FADOF theory has been discussed thoroughly in the literature. First developed by *Yeh* (1982) it was improved by *Yin and Shay* (1991) to include hyperfine structure effects. *Dick and Shay* (1991) showed the first experimental realization of such a filter. For daytime operation of their sodium lidar, a FADOF has been developed by *Chen et al.* (1993, 1996). For potassium, the theory has also been discussed in detail (*Yin and Shay*, 1992; *Dressler et al.*, 1996) and an operational filter for solar remote sensing was developed by *Tomczyk et al.* (1995). Therefore, the following discussion focusses on the operation principle of the filter, which is shown in Figure 3.11.

A FADOF consists of an atomic vapour cell within a permanent magnetic field between crossed polarizers; the field is oriented parallel to the optical axis. The spectral portion of light whose state of polarization is not influenced by the atomic vapour is completely blocked by the second polarizer. The polarization axis of light close to an atomic resonance wavelength is rotated by an angle φ_{rot} due to the resonant Faraday effect, when travelling through the vapour cell. Hence, it can partly ($\sim \sin^2 \varphi_{rot}$) pass the analyser.

The effect can be explained considering the normal Zeeman effect. In an external magnetic field an atomic resonance line is split into three components: an unshifted π-polarized and two $\sigma^{\pm}$-polarized lines, which experience the Zeeman shift of $\pm\Delta\nu_Z$ (or $\Delta\lambda_Z$). In the direction of the magnetic field the parallel π-component is not active and the perpendicular

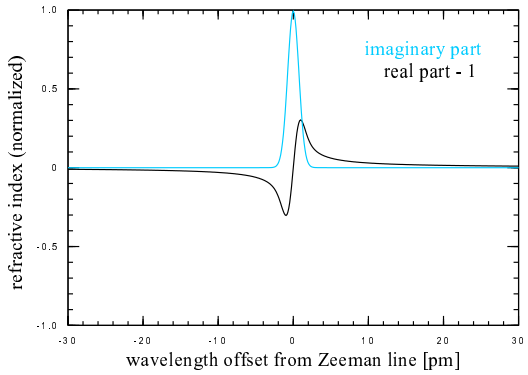

Figure 3.12: The refractive index curves of the atomic vapour for circularly polarized light around the corresponding Zeeman component. The curves are normalized to the imaginary part (grey). The anomalous dispersion of the real part (black) extends beyond the absorption region.

$\sigma^{\pm}$-components appear with opposite circular polarization. The refractive index $n = n_r + i \cdot n_i$ of the atomic vapour shows an anomalous dispersion in the vicinity of a resonance line as plotted in Figure 3.12. In the center the high imaginary part n_i causes nearly complete extinction but it decreases more rapidly than the deviation of the real part n_r. Thus, away from the extinction region the speed of propagation is changed. Anomalous dispersion occurs for both σ-components and the different circular components pass the vapour cell at different speeds. As the incoming linearly polarized light is a composite of two circularly polarized beams, their phases are shifted after passing the cell. Consequently, the plane of linear polarization of the composite is rotated by half the phase difference. Thus, the beam can partially pass the analyser. This effect of circular birefringence is known as the Faraday effect. Additionally, the inverse Zeeman effect or circular dichroism occurs: close to the Zeeman shifted wavelengths, one circular component is completely absorbed while 50% of the other passes the analyser, resulting in a total transmission of $\mathcal{T}(\Delta\lambda_Z) = 25\%$.

The above illustration is simplified, because for the K(D_1) transition, the anomalous Zeeman effect occurs and the hyperfine structure has to be taken into account. In strong external magnetic fields the coupling of nuclear and electronic momentum is subordinate and F (the total angular momentum) is no longer a well defined quantum number. The Zeeman effect of the hyperfine multiplet is transferred to the hyperfine splitting of the Zeeman multiplet (Paschen-Back effect of the hyperfine structure or Back-Goudsmith effect, *Windholz and Musso*, 1988). The transmission is calculated following the theory given in the literature cited above. The numerical algorithm is based on a program by S. Tomczyk (*private communication*) and for the dispersion curves tabulated approximations are used (*Beckers*, 1969; *Gray*, 1992, pp. 227ff).

FADOF Transmission Curve Calculation

The normal Zeeman splitting is determined by the applied magnetic field B as $\Delta\nu_Z = eB/4\pi m_e$. For a given $\Delta\nu_Z$, the refractive index at any wavelength is proportional to the number of atoms along the beam path. Thus, the rotation angle can be adjusted to $\varphi_{rot} = \pi/2$ at the center by the vapour pressure via the cell temperature θ_F. Consequently, $\mathcal{T}$ is nearly 99% at the line center if the Zeeman splitting is large enough. The calculated rotation and transmission curves for a K(D_1) FADOF are shown in Figure 3.13 for the parameters which have been realized in our

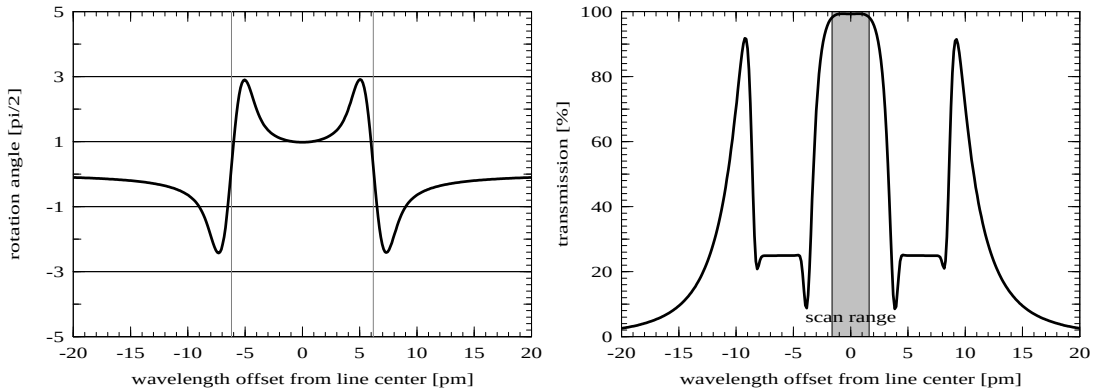

Figure 3.13: Calculated curves for a K(D_1) FADOF with $\theta_F = 124.8°$C, $B = 1800$ G and 22 mm optical pathlength. Left: rotation angle φ_{rot} of the plane of polarization. The vertical lines mark the Zeeman shift of $\Delta\lambda_Z = \pm 6.18$ pm. Right: theoretical transmission $\mathcal{T}$ for linearly polarized light. The grey area denotes the lidar scan range of ±1.62 pm.

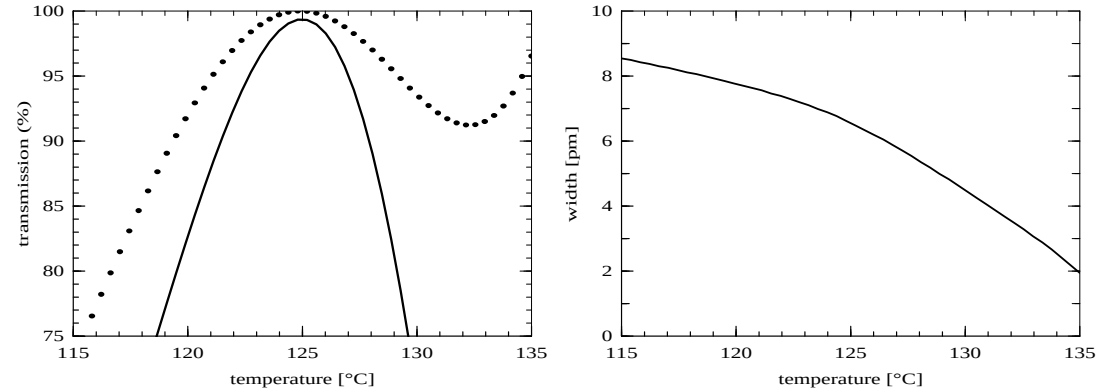

Figure 3.14: Calculated dependence of the FADOF transmission on the filter cell temperature θ_F. Left: transmission at the line center (solid), for a field of $B = 1800$ G. The integrated transmission (dotted) has been normalized. Right: FWHM width of the center transmission peak.

FADOF (see below). They are characteristic for a FADOF of any material and set of parameters (e. g. *Yeh*, 1982, for Cs). φ_{rot} is constant halfway between the two Zeeman lines, where their contributions overlap. This center naturally agrees with the center of the atomic resonance line. Thus, a flat and centered transmission curve is achieved which provides the best condition for spectral analysis of the atmospheric K(D_1) line. Around the Zeeman shifted absorption lines $\Delta\lambda_Z$, the transmission equals 25%. Away from the Zeeman lines, $\mathcal{T}$ becomes maximum where the rotation amounts to an odd multiple of $\pi/2$. For the parameters given ($B = 1800$ G, or 0.18 T, and 20 G/mm gradient along the pathlength of 22 mm), the transmission curve has a center peak of 6.7 pm FWHM and two side peaks of ∼4 pm FWHM about 10 pm off the center.

The dependence of the FADOF transmission curve on the cell temperature θ_F is shown in Figure 3.14 for an otherwise unchanged configuration. The theoretical transmission at the line center reaches more than 99% at a filter temperature of $\theta_F = 125°$C. For lidar application, the background signal is given by the integrated transmission $\int \mathcal{T}(\lambda) d\lambda$ (the *background equivalent bandwidth*) which peaks with a value of 14.7 pm at the same temperature. As it de-

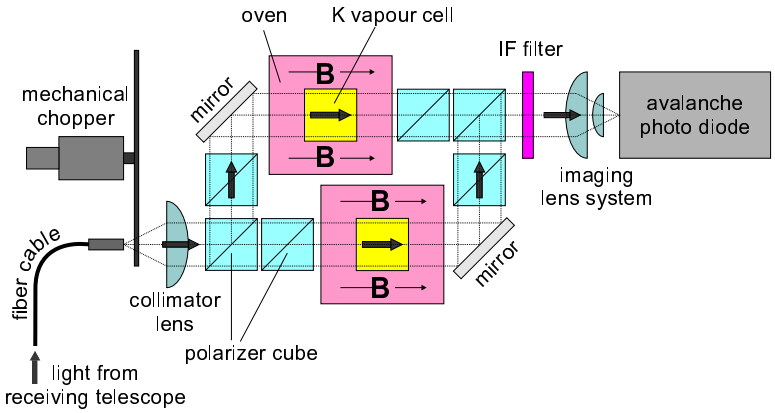

Figure 3.15: The twin FADOF system integrated in the IAP K-lidar detection bench (B, magnetic field). The magnets are integrated into the oven. From *Fricke-Begemann et al.* (2002a).

creases more slowly, the highest SBR is also reached for this θ_F. When θ_F is increased both the transmission and the width of the central peak (right panel) decrease. For lower temperatures, $\mathcal{T}(0\,\mathrm{pm})$ decreases and produces a dip on the curve as the maximum transmission ($\varphi_{\mathrm{rot}} = \pi/2$) is found to the sides of the center. These transmission peaks occur at the edges of the lidar scan range (±1.62 pm) for a 1.5°C lower θ_F. Thus, for a stable transmission curve a temperature stability with variations below ±1°C is required.

As shown by *Yeh* (1982) the FADOF has a very large acceptance angle and, therefore, the demands on the optical quality of the incoming light are low, especially when compared with an etalon. When the divergence of the light gets too large the blocking efficiency of the polarizers can be reduced.

Twin Filter Design

To realize the FADOF technology compact filter cells have been designed at the IAP (by J. Höffner and M. Alpers) which are easily positioned between the polarizers. These filter cells contain the heating, temperature probe, magnets, and potassium vapour cell in an isolated housing of 85 mm length and 96 mm diameter. Both the aperture and the pathlength of the vapour cell are 22 mm. To produce a strong, uniform, and stable magnetic field, a stack of permanent NdFeB ring-magnets encloses the vapour cell. The magnets are custom-built (Magnetfabrik Schramberg) to achieve, depending on the stack height, an axial field of nearly 2000 G which is homogeneous over the diameter of the vapour cell. The vapour cell is heated mainly at its windows to avoid condensation of potassium in the beam path. Its temperature is stabilized with a resolution of 0.1°C.

When the light enters the detection bench through the fiber cable, it is not polarized. As the FADOF works with polarized light and a high overall transmission is desired, a novel twin filter design was developed at the IAP consisting of two parallel FADOFs with orthogonal polarization (Figure 3.15). Using thin-film polarizer cubes the reflected and the transmitted beam of the first polarizer can be used. In the two filter cells the plane of polarization is rotated and the last polarizer merges the two beams again. The degree of background reduction depends on the extinction ratio of the polarizers. The reflected beam is insufficiently polarized (∼95%) and therefore additional polarizers are inserted behind the beamsplitter and the cells.

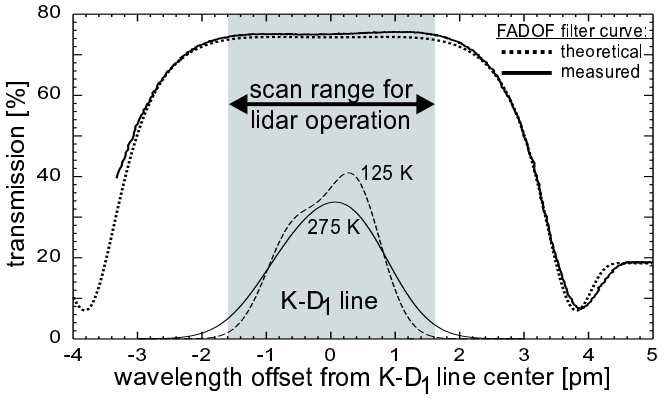

Figure 3.16: Measured transmission curve of the IAP twin FADOF (solid) compared with the theoretical curve (dotted) which is scaled to the same transmission. The grey area marks the lidar scan range and the effective K(D_1) cross-section is given for comparison. From *Fricke-Begemann et al.* (2002a).

Polarizers on the transverse branches (vertical in Figure 3.15) are rotated by 90° about the beam axis. With this setup extinction ratios of up to $1{:}10^4$ are reached and the remaining transmission was measured to be almost completely due to the filter cell influence.

The used fiber cables (CeramOptec Optran UV/WF), typically, have a numerical aperture of NA = 0.22. It defines the maximum entrance angle for the fiber in a medium with the refractive index n_0 as $\sin\alpha_{\max} = \mathrm{NA}/n_0$. When the emerging light is collimated with a lens of $f = 40\,\mathrm{mm}$, the beam has a diameter of $f \cdot 2\tan\alpha_{\max} + d_F = 18.6\,\mathrm{mm}$ for a fiber aperture of $d_F = 0.6\,\mathrm{mm}$ and a remaining divergence of 15 mrad. Over the pathlength of 400 mm to the interference filter the diameter increases by 6 mm. In this configuration the aperture of the vapour cells is completely used. Therefore, a uniform magnetic field over the cross-section is necessary.

The tunable narrow-band seeding laser can be coupled into the fiber cable to measure the practical transmission curve of the twin FADOF. A high overall transmission of about 75% is achieved, excluding the interference filter, which has a peak transmission of 68.5%. The remaining losses are mainly transmission losses of the polarizers and the uncoated optical windows of the vapour cells. An example of the measured transmission around the line center is given in Figure 3.16. As shown in the graph, an excellent agreement is achieved with the theoretical filter curve for a field of $B = 1800\,\mathrm{G}$ with a gradient of 200 G/cm and a cell temperature of $\theta_F = 124.6°\mathrm{C}$. The agreement was measured over the full range of ±15 pm (cf. Figure 3.13). These parameter values are determined from the best agreement with the measured curve at different temperatures. While no device was available to us to measure B directly, the values are in good agreement with the specifications for the magnets. The temperatures measured in the two housings are 120°C and 127°C for an identical transmission curve. The absolute calibration of the temperature probes seems to be off by a few degrees but the deviation may also result from the fact that the probes do not measure θ_F directly at the cell but outside the magnets.

In summary, a very high transmission and contrast are achieved with the novel twin FADOF design. Regardless of any possible inaccuracies of the theoretical filter curves, the measurements show that the desired flat K(D_1) transmission curve was realized. The FADOF naturally also allows some transmission at the K(D_2) line (766 nm), but here the interference filter provides full blocking.

3.3.2 Frequency Response and Effective Transmission

All scattering processes used with the K-lidars are usually categorized as *elastic* scattering. Nevertheless, the spectral composition of the backscattered light will deviate significantly from the laser pulse spectrum. To calculated the effect of narrow spectral filtering on the temperature measurements, the optical Doppler effect is considered again. As described in Section 2.3.1, the effective cross-section is broadened because the moving scatterers experience a shifted frequency $\nu_R = \nu_E - \Delta\nu_D$, where ν_E is the frequency measured at the emitter and $\Delta\nu_D = \nu_E\, w/c$ is the Doppler shift. The vertical velocity w is defined positive in upward direction. When the backscattered light is spectrally filtered by the lidar receiver, its frequency has to be calculated. It is given as

$$\nu_R^{\uparrow} = \nu_E^{\uparrow} - \Delta\nu_D^{\uparrow}, \quad \text{and} \qquad \nu_R^{\downarrow} = \nu_E^{\downarrow} - \Delta\nu_D^{\downarrow}. \tag{3.1}$$

In this notation, the arrows denote the beam direction. So $\nu_E^{\uparrow}$ is the lidar emitted and $\nu_R^{\downarrow}$ is the lidar received frequency. For elastic scattering the scattering objects receive and emit at the same frequency, i. e. $\nu_R^{\uparrow} = \nu_E^{\downarrow}$. As required by linear momentum conservation, the velocity of the object practically does not change during the scattering process and the Doppler shift is the same for both directions: $\Delta\nu_D^{\uparrow} = \Delta\nu_D^{\downarrow} \equiv \Delta\nu_D$. Thus, the frequency received by the lidar is shifted by twice this value:

$$\nu_R^{\downarrow} = \nu_E^{\uparrow} - 2\Delta\nu_D\,. \tag{3.2}$$

When light is emitted at a single frequency $\nu_E^{\uparrow}$ and scattered back from the atmosphere, it has a spectral distribution $f(\nu_R^{\downarrow})$ which depends on the scattering process and the velocity distribution of the scatterers. The effective transmission $\mathcal{T}^{\text{eff}}$ of the filter for the backscattered light is the inner product of this spectrum with the filter transmission curve $\mathcal{T}(\nu)$:

$$\mathcal{T}^{\text{eff}}(\nu_E^{\uparrow}) = \int f(\nu_R^{\downarrow})\, \mathcal{T}(\nu_R^{\downarrow})\, d\nu_R^{\downarrow}\,. \tag{3.3}$$

For example, Rayleigh scattering is practically independent of frequency within the Doppler range and the signal from an altitude z has a continuous spectral distribution $f_{\text{Ray}}(\nu_R^{\downarrow})$. It has twice the Doppler width given for the molecular velocity distribution $n(\nu)$ in Eq. 2.12, depending on the local air temperature $T_{\text{Ray}}(z)$ and causes a smoothing of the transmission curve. For relatively heavy aerosol particles, the Doppler broadening is small compared with the filter bandwidth and the effective transmission for the Mie scattered light equals the filter transmission.

FADOF Influence on the Potassium Resonance Signal

Resonant backscattering by K atoms only occurs when the atoms experience the laser frequency as an atomic resonance frequency, i. e. $\nu_R^{\uparrow} = \nu^K$ and, thus, when $\Delta\nu_D = \nu_E^{\uparrow} - \nu^K$. This condition is fulfilled for a portion of atoms given by the Maxwellian distribution $n(\Delta\nu_D)$ in Eq. 2.13. The received light, therefore, has a frequency of $\nu_R^{\downarrow} = \nu^K - (\nu_E^{\uparrow} - \nu^K)$. In other words, for light emitted at $\nu^K + \Delta\nu_D$ the *elastically* backscattered signal is received at $\nu^K - \Delta\nu_D$. For each atomic resonance line only atoms in a distinct portion of the velocity distribution can scatter the light and the received light becomes a composite of differently shifted frequencies. For the four hyperfine structure lines ν^K of the K(D_1) transition (Appendix A), this mechanism results in four different values of $\nu_R^{\downarrow}$.

Furthermore, the emitting frequency of the atom is not necessarily equal to that received. From both excited states ($F' = 0, 1$) of the atom, relaxation is possible into both ground states

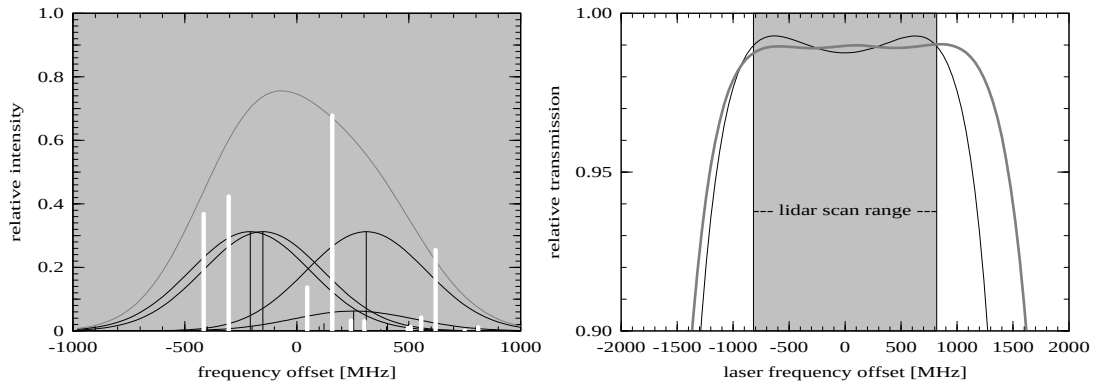

Figure 3.17: Frequency response from the K(D_1) transition for $T_K = 200$ K. Left: for laser light emitted at the center frequency the 12 frequency components and their relative intensities are given as white bars, with the Doppler broadened hfs lines (black) of ^{39}K and the effective cross-section (grey). Right: FADOF transmission $\mathcal{T}$ (black) and effective transmission $\mathcal{T}_K^{\text{eff}}$ for the resonance signal (grey).

($F = 0, 1$). Thus, excitation at $\nu_R^{\uparrow} = \nu_{F=0}^K$ with fluorescence at $\nu_E^{\downarrow} = \nu_{F=1}^K$ (and *vice versa*) are additional scattering pathways. Since these two transitions differ by the same frequency as the corresponding Doppler shifts needed, the received frequencies are equal. Thus, for each excited state, three different frequencies are observed, resulting in a total of six lines per isotope. The effective transmission for the lidar return from the potassium layer, for an emitted $\nu_E^{\uparrow}$, is the sum over the 12 received frequencies $\nu_R^{\downarrow}$:

$$\mathcal{T}_K^{\text{eff}}(\nu_E^{\uparrow}) = \sum \mathcal{T}(\nu_R^{\downarrow})\ f_K(\nu_E^{\uparrow}, \nu_R^{\downarrow})\,. \tag{3.4}$$

The weighting function f_K includes isotopic occurrence, transition line weight, and Maxwellian velocity distribution and, thus, the temperature dependence. As shown in Figure 3.17 (white bars), the spectral response for laser light emitted at the line center is distributed over the range of the broadened cross-section from -416 to 810 MHz. Consequently, the effective filter curve is smoothed over the center of the K(D_1) line and becomes asymmetric (right panel). It is such that the effect of the FADOF on temperature measurements is reduced and can become negligible.

The atmospheric temperature T_K is calculated from the spectral intensity distribution of the detected resonance backscatter signal. Due to the signal being the product of the backscatter cross-section and the effective filter transmission, the calculated temperature may deviate systematically from the true T_K. As the effective filter transmission depends on the unknown temperature T_K in the K layer, it is not possible to correct the measured signal prior to the temperature calculation but the calibration of the temperature calculation has to be corrected, if necessary (*Chen et al.*, 1996). Figure 3.18 shows the influence of the FADOF temperature θ_F on the calculation of the atmospheric temperature for $T_K = 150$ K and 250 K (derived from synthetic data). The calculated value does not deviate from T_K for filter temperatures near $\theta_F = 124°$C. This zero-crossing point depends only marginally on T_K and is one degree below the value for maximum line center transmission. At $\theta_F = 124°$C the filter transmission $\mathcal{T}$ shows a slight dip at the center of less than 1% (cf. Figure 3.14). The temperature deviation is higher for a higher T_K when the broader frequency response causes a reduced $\mathcal{T}_K^{\text{eff}}$ at the wings of the scan range. If a temperature error of up to 1 K was acceptable, the allowed range for FADOF

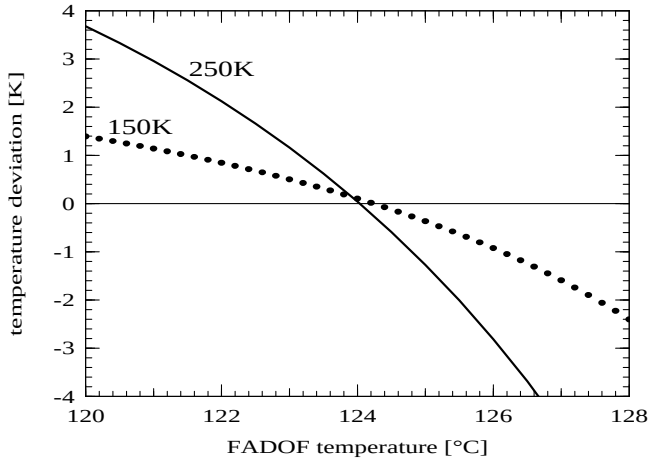

Figure 3.18: The simulated deviation due to the FADOF transmission curve between the atmospheric temperature and the value calculated from the resonance signal for $T_K = 150\,\mathrm{K}$ and 250 K. Positive values denote fit results being too high.

operation would be $\theta_F = 124 \pm 0.8°\mathrm{C}$. The observed stability of the FADOF cells is much higher (±0.2°C) and regular measurements of the filter curve ensure that the correct operation point is used. Thus, no temperature corrections are necessary when the FADOF is used and the additional uncertainty is below 0.3 K. This conclusion was supported by test measurements with and without the daylight filter which showed no detectable temperature difference.

FADOF Influence on the Rayleigh Signal

For air molecules the Rayleigh (or Cabannes) backscatter cross-section is constant over the lidar scan range and the wavelength dependence of the measured Rayleigh signal equals the effective filter transmission. Due to the backscatter signal being Doppler broadened 'twice' (Eq. 3.2), $\mathcal{T}^{\mathrm{eff}}_{\mathrm{Ray}}$ for the Rayleigh signal has a relatively strong wavelength dependence. For a realistic atmospheric temperature of $T_{\mathrm{Ray}} = 250\,\mathrm{K}$ in an altitude of 40 km, $\mathcal{T}^{\mathrm{eff}}_{\mathrm{Ray}}$ at the edges of the lidar scan range is 8% lower than at the center when the filter has the desired temperature of $\theta_F = 124°\mathrm{C}$. The calculated $\mathcal{T}^{\mathrm{eff}}_{\mathrm{Ray}}$ (Figure 3.19, left panel) is in good agreement with the measurements. For $\theta_F = 122°\mathrm{C}$ and 126°C, the decline is changed to about 5% and 13%, respectively. This dependence of $\mathcal{T}^{\mathrm{eff}}_{\mathrm{Ray}}$ on θ_F is stronger than the influence of T_{Ray}. Assuming $T_{\mathrm{Ray}} = 150\,\mathrm{K}$ a decline of 6% for $\theta_F = 124°\mathrm{C}$ is calculated, which is closer to the original 8% than for a two degrees colder filter and $T_{\mathrm{Ray}} = 250\,\mathrm{K}$. Thus, $\mathcal{T}^{\mathrm{eff}}_{\mathrm{Ray}}$, which is always obtained from the data, is rather insensitive to T_{Ray} but can be used to monitor θ_F during the measurement. To this end the second central moment, the variance, of the spectral intensity distribution ($\sum(\lambda_k - \lambda_0)^2\beta_k / N\beta_0$), over the 18 wavelength bins $\lambda_1..\lambda_N$, is calculated and shown in Figure 3.19 (right panel). Even a change in T_{Ray} by 100 K does not cause a stronger change of the variance than that resulting from a warming of the filter cell by 1.3°C. Due to the stratospheric temperature variations being in the order of 10 K, the statistically robust variance is a suitable measure to continuously monitor the filter curve during long-term lidar measurements.

As described before (p. 8), the mesospheric backscatter coefficient is determined through a comparative measurement to the Rayleigh signal from a lower altitude (e. g. 40 km). Hence,

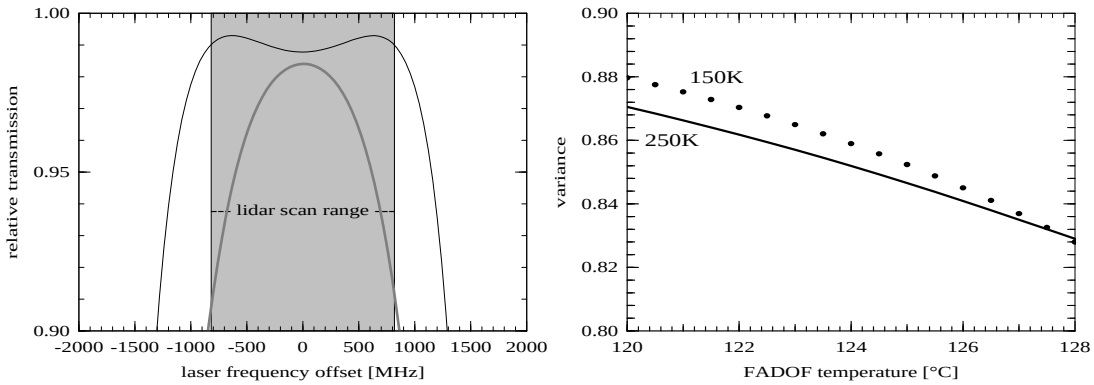

Figure 3.19: FADOF effective transmission for the Rayleigh signal. Left: FADOF transmission $\mathcal{T}$ (black) and effective transmission $\mathcal{T}_{\mathrm{Ray}}^{\mathrm{eff}}$ (grey). Right: The variance of the frequency distribution of the Rayleigh signal due to the FADOF transmission curve for $T_{\mathrm{Ray}} = 150\,\mathrm{K}$ and $250\,\mathrm{K}$.

$\mathcal{T}_{\mathrm{Ray}}^{\mathrm{eff}}(\lambda)$ for the Rayleigh signal could have an erroneous influence on the data evaluation. For the ideal filter temperature of $\theta_F = 124°\mathrm{C}$ and $T_{\mathrm{Ray}} = 250\,\mathrm{K}$, the mean (theoretical) effective transmission is 94% for the Doppler broadened Rayleigh signal while it is 99% for the K resonance signal. Thus, the derived backscatter coefficients have to be corrected by about 5% to yield correct values of the potassium density. If a reference from higher altitudes is used, the lower temperatures cause a reduced density correction which reaches 2% for $T_{\mathrm{Ray}} = 150\,\mathrm{K}$.

The implications of $\mathcal{T}_{\mathrm{Ray}}^{\mathrm{eff}}(\lambda)$ for the temperature measurements are more important. For nighttime operation without a narrow-band filter the signal in each wavelength bin was normalized to its own Rayleigh signal to calculate the $\beta_{\mathrm{K}}(\lambda)$ curve. This procedure avoids erroneous influences of varying laser pulse energy or atmospheric transmission on the temperatures derived. If it would be applied to measurements with the daylight filter, the reduced $\mathcal{T}_{\mathrm{Ray}}^{\mathrm{eff}}$ at the outer wavelengths would lead to apparently broader curves and higher temperatures would be calculated. This effect is quantified in Figure 3.20. The deviation depends on θ_F as well as on T_{K} and T_{Ray} at the altitude from which the Rayleigh signal is used for normalization. For the FADOF operation point $\theta_F = 124°\mathrm{C}$, the induced systematic error would range from 4 K to 16 K, being smaller for lower T_{K} and T_{Ray}. For $T_{\mathrm{Ray}} = 150\,\mathrm{K}$ (grey curves), the effect could be minimized by a FADOF operation at $\theta_F = 122°\mathrm{C}$ at the expense of overall filter transmission and a direct influence on the temperatures, as discussed above. Furthermore, the FADOF temperature cannot be adjusted because T_{Ray} is not known in advance and may change during a measurement. Thus, this correction is not feasible with sufficient accuracy and should be avoided.

The more accurate technique is a normalization to the number of laser shots per wavelength bin and the Rayleigh signal at the line center. This method relies on a constant laser power and a constant receiver efficiency. The latter is assured by using the same detector and electronics for all wavelengths. Due to the higher laser stability in the new IAP setup, its energy is not found to vary with wavelength. Furthermore, it is now possible to measure the laser power during lidar operation simultaneously for each laser pulse. In the vicinity of the $\mathrm{K}(\mathrm{D}_1)$ line the atmospheric transmission does not vary systematically. Statistical fluctuations of the Rayleigh signal, i. e. the laser power inside the FOV, can also be induced by atmospheric turbulence or passing clouds but they are randomly distributed and average out after sufficient integration time. The

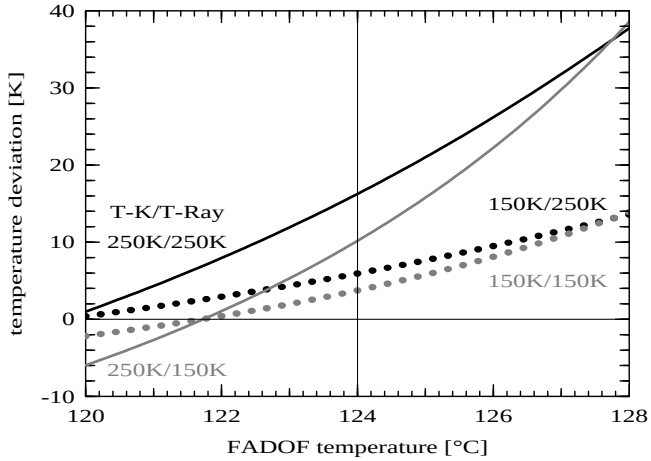

Figure 3.20: The possible erroneous influence of the effective transmission for the Rayleigh signal on the temperature calculation when the signal is normalized independently for each wavelength. The simulation results are given for each combination of temperature T_K in the potassium layer and T_{Ray} in the Rayleigh altitude (solid: $T_K = 250$ K, dotted: $T_K = 150$ K; black: $T_{Ray} = 250$ K, grey: $T_{Ray} = 150$ K).

averaging process is supported by a fast wavelength scan (2 s period) which is possible with the external cavity seeding laser.

3.3.3 Reduction of the Field of View

The background intensity is proportional to the solid angle captured by the telescope mirror and, thus, to the square of the *field of view* (FOV) of the telescope. The (full) FOV is determined by the ratio of fiber aperture diameter d_F and the telescope's focal length. For nighttime measurements with the stationary lidar, fibers with $d_F = 0.6$ mm were used, giving a FOV of 500 µrad. In the transportable lidar, the FOV was 789 µrad. For daylight lidar operation the FOV must be reduced to a minimum. A background reduction by a factor of 10 was aimed at and, thus, a reduction of the FOV to below 200 µrad (the apparent diameter of Jupiter ranges from 150 to 240 µrad).

The possibilities for a reduction of the FOV are limited by the atmospheric *seeing* which denotes wave front distortions due to atmospheric turbulence. Astronomers associate good seeing conditions with a resolution better than 5 µrad (1 arcsec, *Wilson*, 1996). For sunlit conditions the seeing can easily be ten times worse. When the FOV is reduced below 200 µrad, signal fluctuations are observed to increase, especially for a high solar elevation. The induced signal losses are expected to counteract a reduction to below ∼100 µrad.

In addition, the divergence of the laser beam has to be reduced to maintain full overlap between the beam and the FOV. A threefold Galilean beam-widening telescope is used to obtain a beam divergence of 133 µrad. Furthermore, a high pulse-to-pulse pointing stability of the laser is necessary, which was achieved with the new laser setup. The necessary full overlap at all altitudes used (>40 km) limits the FOV reduction due to the bi-static setup of the K-lidars. Another limit is set by the saturation effects which are to be expected when the energy intensity in the potassium layer is increased due to the narrow laser beam (discussed in detail in Section 3.3.4).

With the stationary K lidar in Kühlungsborn, tests have been made to use a bundle of

0.27 mm fibers to get a FOV of about 225 µrad with three of the 0.5-m mirrors. Unfortunately, the optical quality of the machine-turned aluminium mirrors did not provide a focus of that size. Although the laser beam divergence is clearly below the nominal FOV, only between 20% and 50% of the intensity were received. Thus, the insufficient optical quality of these telescopes does not allow daytime operation.

Therefore, the first measurements in full daylight were carried out with the transportable lidar on Tenerife in November 2000. This instrument is equipped with a high quality 0.8-m telescope that has a focal length of 1.9 m and was specified to have a focus spot smaller than 50 µm. It was previously used with a 1.5 mm fiber, i. e. a FOV of 789 µrad. After a d_F =0.365 mm fiber (FOV 192 µrad) was installed, almost the full signal was obtained, while the solar background was reduced by a factor of 17. In combination with the FADOF this was sufficient for measurements in full daylight.

In Kühlungsborn a new 30" (0.762 m) telescope mirror was installed in summer 2002 which provides high optical quality (RMS surface accuracy of $\lambda/24$) and a focal length of 3.227 m. With a d_F =0.6 mm fiber, it has a FOV of 186 µrad and reached background values comparable to the transportable system. A further reduction to 124 µrad is possible using an 0.4 mm fiber. Thereby, the background is halved, but the signal is also reduced by 10–15% because the beam divergence of 133 µrad exceeds the FOV. Additionally, higher signal fluctuations are observed at times of strong convection which are presumably caused by downgraded seeing conditions.

3.3.4 Saturation

Reducing the telescope's FOV implies a reduction of the beam divergence which increases the energy density in the laser beam. When the energy density gets too high the backscatter signal from the potassium layer may no longer be proportional to the laser energy. During one scattering process the excited atom is not available for absorbing and re-emitting following photons. Furthermore, stimulated emission may cause the photon from the excited atom to be emitted coherently with the laser beam, directed upwards and not scattered back to the receiver. These two processes reduce the detected resonance signal rather independent of frequency over the Doppler range of the resonance line. Thus, they will reduce the apparent atom density, while influencing the temperature retrieval only weakly. Due to the different strengths of the possible relaxation pathways, the atoms which have been excited before may deviate from the equilibrium ground state distribution. This optical pumping will influence the following backscatter processes depending on frequency and disturb the temperature derivation. To accurately calculate the saturation effect, exact knowledge of the spectral, temporal and spatial laser energy distribution (and also the atmospheric transmission) is required but usually not available.

A first-order estimation of the saturation can be derived under simplifying assumptions. The total absorption cross-section of an atom is given as (*Fricke and von Zahn*, 1985)

$$\sigma_{\mathrm{tot}} = \int_0^\infty \sigma(\nu)\,d\nu = f\frac{\pi e^2}{m_e c} = f \cdot 2.654 \times 10^{-6}\,\mathrm{m^2 s^{-1}}\,, \tag{3.5}$$

where f is the oscillator strength (0.339 for K(D_1)). The contributions are distributed over the hyperfine components with the natural linewidth. At this point the effective cross-section σ_{eff}, which is due to Doppler broadening, must not be used as it applies only to an ensemble of thermally moving atoms. As the laser bandwidth Γ_{L} is larger than the natural linewidth ($\sim$6 MHz), it is reasonable to assume a mean laser energy per unit frequency of $E_{\mathrm{p}}/\Gamma_{\mathrm{L}}$ constantly over the natural linewidth. The spectral photon density $i = \frac{E_{\mathrm{p}}/h\nu}{A\Gamma_{\mathrm{L}}}$ is about $6.6 \times 10^7\,\mathrm{m^{-2}Hz^{-1}}$ for an

illuminated area of $A = 220\,\mathrm{m}^2$ (in 90 km altitude for 186 µrad divergence) and a pulse energy of 150 mJ. The number of photons per laser pulse which are scattered by one atom excited via a strong K(D_1) hyperfine structure transition (weight $g = 5/16$, $\sigma_{\mathrm{tot}} = 9 \times 10^{-7}\,\mathrm{m}^2\mathrm{s}^{-1}$) at the center of the laser line, is estimated to be

$$p = \int_0^\infty i(\nu)\,\mathcal{T}\,g\,\sigma(\nu)d\nu = i\,\mathcal{T}\,g\,\sigma_{\mathrm{tot}} \approx 9.3\,, \tag{3.6}$$

for an atmospheric transmission of $\mathcal{T} = 0.5$, assuming three times the extinction as for pure Rayleigh scattering. Due to the pulse length of $t_{\mathrm{p}} \approx 250$ ns being scarcely 10 times the natural lifetime of the excited state of $\tau_n = 26.2$ ns, a number of 9.3 scattering processes per atom is hardly possible. Significant saturation can already be expected if $p > 0.1\,t_{\mathrm{p}}/\tau_n$, i. e. the atoms are involved in scattering processes on average during 10% of the pulse duration. To fulfill this condition the energy density would need to be reduced by one order of magnitude.

In the literature the degree of saturation S has been subject to several considerations. It is defined as one minus the ratio of the received saturated and the expected unsaturated signal. Although it should be noted that the process of saturation is highly non-linear, the mean photon flux $\varepsilon = \frac{E_{\mathrm{p}}/h\nu}{At_{\mathrm{p}}}$ is calculated to compare the available results. For the above values (150 mJ, 250 ns, 186 µrad) the flux is $1 \times 10^{22}\,\mathrm{m}^{-2}\mathrm{s}^{-1}$. This flux is used as a reference value $\varepsilon_0 = 10^{22}\,\mathrm{m}^{-2}\mathrm{s}^{-1}$ for comparison in the following.

The first treatment of the K(D_1) transition by *Megie et al.* (1978) gave a saturation of 8% for broadband laser pulses with $\varepsilon = 3\varepsilon_0$ (0.77 J, 30 ns, 0.7 mrad, and 8 pm bandwidth). For the IAP K-lidar, *Eska* (1998) calculated $S = 2\%$ for $\varepsilon = 2.3\varepsilon_0$ (150 mJ, 100 ns and 0.2 mrad pulses). For the reduced photon flux of $\varepsilon = 0.6\varepsilon_0$ for a system comparable to those used here (0.2 mrad, 275 ns, 100 mJ), *von Zahn and Höffner* (1996) predicted about 1% saturation.

The degree of saturation can be estimated experimentally when the energy density is varied. Since a variable attenuator was not available, the adjustment of the 4-fold beam-widening telescope was varied for a constant pulse energy of 150 mJ and a pulse length of 200 ns. The lowest divergence was 133 µrad ($\varepsilon = 2.5\varepsilon_0$). As the Rayleigh signal is not saturated it can be used as a measure of the beam intensity inside the telescope's FOV and it decreases expectedly when the beam divergence exceeds the FOV of 186 µrad (Figure 3.21). The absolute values of the beam divergence are not known due to the high uncertainty of the beam diameter. Assuming 2.5 mm, the additional divergence is varied in multiples of 200 µrad (0, 1, 2, 3, 4, 6, 8). If the K layer would not change, linear backscattering would result in a straight line in the graph. From the two groups at minimum divergence, which were obtained at the beginning and the end of the test, the atmospheric potassium density can be estimated to have varied by a factor of two within the 3 hours. The potassium signal for the lowest divergence is expected to be about 5–10 times higher to give the same ratio as for the lowest intensities. In agreement with the above estimation, it is found that the energy density must be reduced by a factor of 10 to reach the linear region, where the K signal is not saturated. A saturation of $S = 50\%$ is achieved when the Rayleigh signal is decreased by a factor of three with no significant signal losses from the potassium layer. This saturation is higher than the values calculated by *Eska* (1998) and more comparable to the results of *Papen et al.* (1995) who have calculated about 50% saturation of the K(D_2) line for a flux of $\varepsilon = 2.2\varepsilon_0$ (200 µrad, 200 ns, 250 mJ and 30 MHz spectral width). As the K(D_2) oscillator strength is twice that of K(D_1), these calculation may be applicable to the observations with our system, which was operated at half the pulse energy. The lower values derived in other estimations may be due to the use of inaccurate values for the effective cross-section.

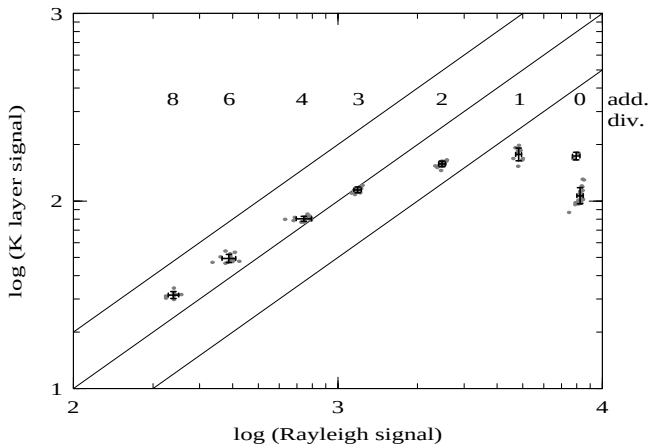

Figure 3.21: Relation between the Rayleigh signal from 40 km altitude and the potassium resonance signal (80–105 km) for different values of additional beam divergence, measured in Kühlungsborn on September 13th, 2002. The spots mark single files (4000 shots) and the error bars give the standard deviations for each beam divergence.

Influence of Saturation on the Temperature Measurements

As saturation occurs at all frequencies within the Doppler broadened resonance line, it influences the absolute backscatter coefficient more than its spectral dependence. Thus, the temperatures derived are influenced less than the densities. For a single transition without hyperfine structure, saturation does not change the observed Doppler-width. For the D_1 transition of potassium, the three strong hfs lines which contribute 93.75% of the cross-section are of equal strength and thus saturated to the same degree. Thereby, the shape of the resonance curve is changed only slightly. Simulations (*von Zahn and Höffner*, 1996) of the wavelength dependence have shown that even a saturation of 10% would change the temperature results only by about 0.2 K. These calculations are supported by the experimental results. Even when the saturation reaches 80% the systematic temperature offset is found to be less than 5 K.

Consequently, the K-lidar temperatures are indeed less effected than the results from a narrow-band Na-lidar for which *von der Gathen* (1990, 1991) calculated an error of about 8 K for 10% saturation. The higher sensitivity is due to the weights of the hyperfine structure components which are less uniform for the Na(D_2) transition compared with K(D_1). The Na(D_2) hyperfine structure is dominated by one of the six lines which constitutes nearly 50% of the cross-section. It is three times stronger than any other and saturated earlier.

Some possible deviation of the K(D_1) spectrum is due to optical pumping occurring during the duration of a laser pulse. Atoms excited from the ground state doublet $F = 1$ (named D_{1b}), which includes the one weaker line, are more probable to cascade into the ground state $F = 2$ than into the original state. In the former case it is not available to absorb another photon at the same frequency. For excitation of the other doublet (D_{1a}) the probability of a relaxation to the $F = 1$ ground state is lower (about on third). Thus, the stronger D_{1a} doublet is less declined by optical pumping than the weaker D_{1b}.

In summary, the useful reduction of the field of view is limited by the maximum achievable luminance of the metal layer. For the IAP K-lidars saturation may occur for beam divergences below about 700 µrad. The influence on temperature measurements depends on the hyperfine

structure of the observed line and is relatively low for K(D_1). Consequently, the laser is operated for daytime measurements at $E_p = 120$ mJ and $t_p = 270$ ns, which reduces the photon flux to 60% compared with the 150 mJ and 200 ns used in the test measurement (Figure 3.21). Furthermore, the beam-widening telescope is adjusted to give an increased beam divergence of about 300 µrad compared with the 133 µrad possible. Depending on atmospheric transmission, this results in a saturation of about $S = 50\%$ which introduces significant uncertainty to the density measurements while the temperatures derived are still reliable.

3.3.5 Avalanche Photodiode

The introduction of the FADOF and reduction of the FOV have reduced the background to a degree where temperature measurements under daylight conditions become possible. The accuracy of the temperatures derived can be doubled for a constant SBR when the statistics are enhanced by a factor of 4 (Figure 3.9). This might be realized in various ways. An extended integration in time and altitude would cause an undesirable resolution reduction. To operate the lidar at higher repetition rates is possible in principle by nearly a factor of two but would imply many changes for the detector electronics. A larger receiving area is relatively costly. In this case, an easier way to increase the photon counts was the introduction of a more efficient detector.

Avalanche photodiodes (APDs) are known to have high efficiencies for wavelengths in the near infrared with a maximum near 700 nm and in the last years single photon counting modules with low noise have become commercially available. The model used (EG&G SPQM-AQR) is specified with a dark count rate of 25 Hz and a photon detection efficiency of 68% at 770 nm. This means a possible improvement by a factor of 4.5 compared with the PMT. The disadvantages are a small sensitive diode area with less than 200 µm diameter (e. g. 192 µm for our S/N 5212-1) and the reduced dynamic range with 10 MHz bandwidth and significant non-linearities above 1 MHz. The correction factor for 5 MHz count rate, typically, exceeds 1.33 and is known with an accuracy of ±5%. Furthermore, the deviations from the linear response can be corrected only for steady signals but as the lidar signal varies rapidly with altitude, time-dependent corrections would be necessary due to signal-induced heating effects of the diode itself. This effect is observed to vary between modules of the same type. When both background and Rayleigh signal are kept low enough, parallel measurements with APD and PMT have proven that no noticeable deviation in the results is induced by the detector.

Using a fiber cable aperture of $d_F = 0.6$ mm the collimated beam on the detection bench attains a diameter of ∼26 mm behind the FADOF (see p. 34). It needs to be imaged with an effective focal length f of less than 13 mm to make the spot fit completely onto the sensitive detector area. This f-number of $f/0.5$ is very small and no suitable lens system was commercially available from series production. Spherical aberration is expected to cause significant losses under these conditions, so a combination of aspherical doublet lenses is used. A series of three available lenses with decreasing diameter and focal length (50, 30, and 14 mm) was found to meet the requirements. A focal diameter of 196 µm was calculated using ray tracing theory, assuming no aberration. When fibers with smaller apertures are used (smaller FOV), the mapping becomes less critical.

The nominal efficiency exceeds the 15% of the PMT by a factor of 4.5. With the described imaging lens system, a signal enhancement by a factor of 4 was reached in lidar measurements. The remaining losses of 10–15% are presumably caused by the multiple surfaces and remaining aberrations of the imaging lens system.

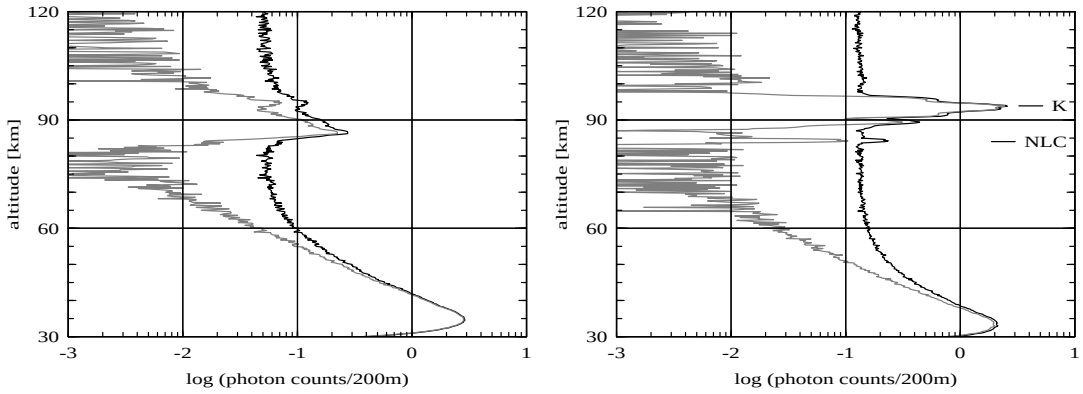

Figure 3.22: Daytime measurement examples: raw data (black) and data after background subtraction (grey). Left: On Tenerife at sunrise (0° solar elevation, 06:44 LT) on December 10th, 2000. Right: On Svalbard on June 18th, 2001 (01:27 LT), at a solar elevation of 12.4°. The photon counts are averaged over 4000 laser pulses (∼2 min) with an altitude resolution of 200 m.

3.3.6 Achieved Daylight Capability

The combination of the FADOF and the decreased FOV has reduced the solar background by about 3 orders of magnitude in comparison with the nighttime configuration. The first measurements with the twin FADOF were carried out with the transportable K-lidar in November 2000 on Tenerife (28°N). Due to good weather conditions and the high altitude of the site it was possible to measure temperatures continuously during night and day, although the PMT was still used (see Section 5.3 for results). The highest solar elevation angle was 42°. The APD has been integrated into the receiver in December 2000. An example for a photon count profile obtained under daylight conditions is given in the left panel of Figure 3.22 showing SBRs of up to 5. Since the solar elevation of 0° does not take atmospheric refraction into account, the data were taken shortly after the apparent sunrise.

These measurements have demonstrated the daylight capability of the new detection system and the instrument was subsequently installed on Svalbard (78°N). A profile of photon counts measured in the Arctic near summer solstice is given in the right panel of Figure 3.22. For a solar elevation of 12.4° a SBR of 20 was obtained at the peak of the potassium layer which extends from 87 to 98 km. A noctilucent cloud (NLC) is also clearly visible causing a strong backscatter signal near 84 km. On Svalbard, mesospheric temperatures have been measured during the Arctic summer when the maximum solar elevation is 35°. At Kühlungsborn, daytime observations have become possible with the installation of the 30” telescope mirror in summer 2002.

The background signal during daytime depends strongly on both the solar elevation and the atmospheric conditions. The dependence on the solar elevation is given in Figure 3.23 as it was observed near summer solstice in Kühlungsborn, when the sun can be up to 59.4° above the horizon. The values shown were measured for a FOV of 186 µrad on June 26th under good weather conditions, except around noon (solar elevation >50°), when some cumulus clouds appeared. Temperatures could still be derived with a statistical uncertainty of ±5 K at the peak of the potassium layer when a smaller FOV (124 µrad) was used.

In addition to Rayleigh scattered sunlight, a dominant part of the background is observed to be caused by Mie scattering. It can become a multiple of the Rayleigh contribution, espe-

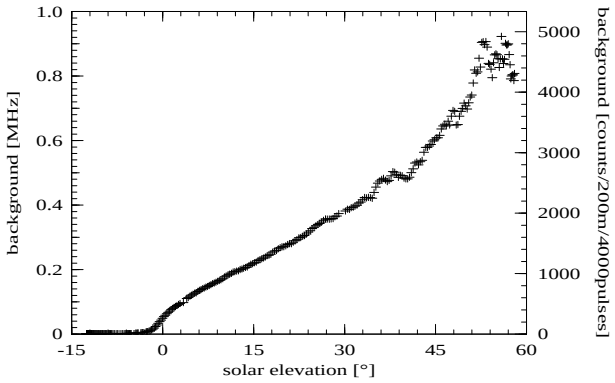

Figure 3.23: The solar background, as a function of solar elevation, as observed with a FOV of 186 µrad in Kühlungsborn on June 26th, 2003. The scatter for angles above 50° is due to clouds.

Table 3.2: Typical receiver properties of the stationary IAP potassium lidar, August 2003.

Telescope	Newtonian, $d = 76.2$ cm, $f = 3227$ mm
Field of view	186 µrad
Broad-band filtering	IF-filter (1 nm, $\mathcal{T}$ =70%)
Narrow-band filtering	Twin K-FADOF (1800 G, 124°C, $\mathcal{T} = 75\%$)
Overall peak transmission	50%
Contrast	1:10,000
Peak width (FWHM)	6.7 pm
Temperature effect	±0 K
Detector	APD
Photon detection efficiency	68% @ 770 nm

cially due to haze, mist or cirrus clouds, even if the signal is attenuated only weakly. When the skylight brightness increases, it can be seen by the naked eye that the contributions of longer wavelengths are increased stronger than that of shorter wavelengths (i. e. the sky turns from blue towards white) and, thus, the K-lidar measurements at 770 nm are strongly effected. In summer, the tropospheric boundary layer is broader than in winter and exhibits an enhanced scatter coefficient (*Schneider and Eixmann*, 2002) as aerosols swell due to the high water vapour content. This can increase the background to a level where temperature measurements in full daylight become impossible. In Kühlungsborn, the atmospheric conditions in summer, especially under stable high-pressure weather conditions, together with the high solar elevation may prevent continuous long-term K-lidar observations. But even when a certain period around noon has to be excluded, measurements over about 20 hours are often possible and they are sufficient to identify most wave perturbations, including diurnal tides.

Finally, the receiver configuration is summarized in Table 3.2. The given overall transmission of 50% includes the complete detection bench between fiber cable and detector. For daytime temperature measurements the overall systematic uncertainty is increased by up to 5 K and depends on the weather conditions. It is mainly due to variations of the background and the laser energy while the laser scans over the different wavelength channels.

3.4 Potassium Lidar: Discussion and Outlook

The resonance lidar technique developed since the work of *Fricke and von Zahn* (1985) has become the standard method to measure atmospheric temperatures in the mesopause region. It does provide vertical profiles of high accuracy and good temporal and spatial resolution. With the daylight capability it can be used to retrieve continuous measurement series on the scale of hours and days as well as long-term observations for months and years at almost any location.

With the described configuration of the IAP potassium lidars, reliable temperature measurements have been carried out under both nighttime and daytime conditions. Continuous measurements have been performed covering periods up to 100 hours and observations were successfully conducted under Arctic summer conditions. While results will be discussed in the following chapters, this section summarizes the technical progress that has been achieved during the work up to this thesis.

Due to the recent developments the alexandrite power laser has become a reliable and easy to use system with ideal spectral purity, high power, long pulses and beam properties which are sufficient for small fields of view as they are necessary for daylight operation. The external cavity diode laser for injection seeding has proven to provide full control over the power laser frequency and is very useful to determine optical properties like filter characteristics. Compared with the systems used in sodium temperature lidars, the transmitter unit of the IAP K-lidars is very compact, all solid-state, and possesses a high long-term stability.

The system has a high potential for automation and is already operated in a semi-automatic mode which is inevitable for long continuous measurements. An increased degree of automation including the reaction to the current weather conditions would enable measurements under rapidly changing conditions and could strongly enlarge the number of measurements.

Lidar Measurements During Daytime

While observations at nighttime have been carried out before, mesospheric temperature measurements with the IAP K-lidars are now possible also in full daylight. Using a FADOF, a narrow field of view and a highly efficient detector, temperatures have been derived with ±5 K statistical accuracy at solar elevations up to 60°. However, the altitude range usable for temperature measurements is reduced during daytime. The demands on the weather conditions are much higher than during nighttime because, beneath a good transmission, also a low capability of scattering sunlight is necessary.

The potential of the IAP K-lidars for daytime operation may be compared with other resonance temperature lidar techniques, although a quantitative discussion is beyond the scope of this work. Sodium lidars are used at Colorado State University with a FADOF (*Chen et al.*, 2000) and at the University of Illinois (*States and Gardner*, 2000a) with an etalon for daytime operation. Using sodium has the advantage of higher densities in the mesosphere (10–100 times that of K). It could result in a much better signal-to-noise ratio than for the K-lidar if the same laser power and filter performance were available. In practise, typical signal-to-background ratios reported for Na-lidars at the peak of the layer and the peak of the resonance line at noon range between 15 (*Chen et al.*, 1996) and 0.5–4.0 (*States and Gardner*, 2000a) which are comparable to the K-lidar values. Furthermore, due to the more complex hyperfine structure the temperature evaluation is much more sensitive to saturation than in the case of potassium.

Iron has about 2–3 times the density of sodium (*Kane and Gardner*, 1993) but only a tenth of its oscillator strength, depending on the transition used, and has also been studied by

lidar before. The Fe-Boltzmann technique has been shown to allow temperature measurements but in daylight only in the presence of very high densities (*Chu et al.*, 2002). It uses one thermally excited lower state which may constitute only 1% of the total occurrence, hence, the signal strength is drastically reduced. The systematic uncertainty is relatively high, induced for example by the spectral energy distribution of the broad-band lasers used. Alternatively, the Doppler broadening of iron can be probed with a narrow-band laser, similar to the technique described here for potassium and first tests at night have been carried out at the IAP with promising results (*Lautenbach and Höffner*, manuscript submitted to *Appl. Optics*).

Spectral Filtering Technique

A fundamental technique for successful daytime lidar measurements is the spectral filtering. The novel twin FADOF provides a high transmission and a good background reduction (*Fricke-Begemann et al.*, 2002a). The flat filter transmission curve in combination with the width of the central peak provides efficient filtering that has no direct effect on the temperature measurements. The flat filter curve is a major improvement compared with all FADOF realizations reported before. Since the FADOF does not affect the measurements negatively, it remains integrated in the instrument during nighttime measurements, thereby providing uniform continuous data sets.

The first FADOF for lidar resonance temperature measurements has been developed by *Chen et al.* (1993) for a sodium lidar. Due to the larger hyperfine structure splitting ($\sim$1.8 GHz for Na(D_2) vs. $\sim$0.5 GHz for K(D_1)) and the narrower filter curve used ($\sim$2 GHz FWHM vs. $\sim$3.4 GHz), the necessary correction for temperature calculations lies above 50 K (*Chen et al.*, 1996). Thus, the exact knowledge of the FADOF transmission curve is very important for the sodium lidar to minimize the uncertainties emerging from this correction. The effective transmission of about 10% reported in their work and also the current value of 20–25% (*She et al.*, 2003) is significantly below our 75%. The difference is partly caused by our twin setup which allows the use of both polarization axes of the received light, whereas only one axis is used in their sodium filter.

The Fabry-Perot Etalon

The more widely used narrow-band filtering technique is the Fabry-Perot etalon. Concurrently to the development of the FADOF, a filter setup with a stabilized etalon (Hovemere ltd.) had been tested as an alternative with the stationary K-lidar. It has a bandwidth of 10 pm FWHM and a finesse of 50 which is relatively high for a single parallel etalon. In order to make this finesse usable the allowed divergence of the beam in the detection bench is about 4 mrad. To attain this value, a 4-fold beam-widening and an aperture of 100 mm had to be used. With light from the seeding laser which has a lower divergence, the specified finesse was verified and a transmission of 70% was achieved. A high contrast of nearly 1000:1 was realized which is still by a factor of 10 less than that of the FADOF. Unfortunately, the stability of the etalon was not sufficient. Thermally induced variations of the center of the transmission band by $\pm$2 pm were observed in a stable laboratory environment. They need to be suppressed before the instrument can be employed for lidar measurements, but even after 2 years of trials, the etalon does not provide the required stability. If the above results could be reproduced in lidar operation, both filtering techniques would have similar values for peak transmission and background equivalent integrated transmission, including the sidebands in the case of the FADOF.

Calculations with synthetic data for the etalon parameters show that the effective transmission for the K(D_1) resonance backscatter signal is less uniform than that of the FADOF. Temperature corrections between 2 K and 5 K are necessary for atmospheric temperatures of 150 K and 250 K, respectively, when the etalon is operated at the line center. Additionally, a shift of the center of the transmission band by 2 pm can influence the temperature calculation by up to 3 K.

In summary, for mesospheric temperature measurements which use the K(D_1) resonance line, the FADOF appears superior to an etalon. It is much more cost efficient, the large acceptance angle sets lower requirements for the incoming light, the spectral stability is assured due to the atomic resonance, and it is very robust. The latter properties are especially important if the instrument is operated under non-ideal conditions such as that found in the Arctic, on board a research vessel or on an aircraft. For other lidar types, the FADOF technique is usable only if suitable vapour cells are available.

Future Developments

The signal-to-background ratio should be improved further to make the potassium lidar daytime measurements more robust. As saturation already limits the reduction of the field of view, a higher pulse energy or spatial filtering is not feasible. Spectrally broader laser pulses would reduce the problem of saturation but enhance systematic uncertainties in the temperature derivation. Temperatures are often calculated with 1 km vertical resolution only but higher resolutions are used for metal layer and aerosol observations. Hence, although longer laser pulses would decrease saturation, a significant further increase of the pulse length is also not desirable and its realizability is questionable. The remaining possibility of spectral filtering is discussed separately below.

Higher accuracy of temperature calculations can also be achieved with enhanced statistics. The overall efficiency of the detector is very high already but an increase in receiver area or in laser power and FOV, simultaneously, would increase the photon counts. But the efforts for a significant increase in photon counts are relatively high and the maximum photon count rate of the detector is already reached.

Possibly, in the future much better statistics can be provided if the pulse repetition rate of the power laser is strongly increased. Thus, a large future improvement would be a substitution of the flashlamps by laser diodes for pumping the alexandrite rods. The pulse repetition rates could be increased to about 1 kHz, thereby reducing the necessary integration time by a factor of 30. Furthermore, a reduced power consumption would simplify the operation at remote places and reduce problems of thermal stability. The operation of a diode-pumped alexandrite laser was first demonstrated by *Scheps et al.* (1990) and its application for a spaceborne Doppler lidar was discussed by *McKay and Wilkerson* (1997). A limiting factor today is the lifetime of high power pumping diodes. Nevertheless, diode-pumped alexandrite lasers have already become commercially available.

Currently, the systematic uncertainty during daytime is increased compared with nighttime measurements but this could largely be avoided. The influence of quickly varying weather conditions, e. g. passing clouds or fog, can be reduced when the measurement regime is changed, away from the sinusoidal wavelength scan to a pulse-to-pulse variation of the wavelength. Furthermore, a more accurate background determination could be achieved by extending the measurement to higher altitudes, measuring it between the laser pulses or simultaneously on a nearby wavelength. The energy of each individual laser pulse needs to be stored together with

its frequency and the photon counts. In any case, major revisions of the data acquisition system will be necessary in the future.

Further Background Reduction With the FADOF Technique

Beyond the background rejection achieved with the FADOF discussed, a higher reduction is possible when a narrower filter curve is realized. This can be achieved with a lower magnetic field. Such filter cells have been developed for the IAP K-lidars which are operated at $B = 800\,\mathrm{G}$ and $\theta_F = 111°\mathrm{C}$ and can be exchanged quickly with the regular cells. While the background (integrated transmission) is further suppressed by a factor of 3 compared with the regular FADOF, the transmission at the line center is still about 90%. Due to the FWHM being reduced to about 2 pm, the lidar is not operated in scanning mode but stabilized to the line center. This mode is used for the detection of aerosols (noctilucent clouds) but not for temperature measurements because temperature corrections of several 10 K would be necessary. While the transmission of 90% is usable for Mie scattering, the effective transmission is reduced to 50% for the K resonance and Rayleigh backscatter signal due to the Doppler broadening.

The main difference between our regular FADOF and an ideal filter, which would have a rectangular filter curve, are the side peaks of the FADOF transmission curve (Figure 3.13). The $\mathcal{T} = 25\%$ plateaus contribute to about 15% of the background while the remaining amount is equally distributed between the central and the side peaks. As only the center peak is needed for the lidar measurements, the background is twice as high as necessary. The side peaks are due to the inherent symmetry of the FADOF and cannot be avoided by changing its parameters. A possibility to suppress them would be the usage of additional absorption cells behind the FADOF. When absorption cells are placed in a transversal magnetic field they can be designed to absorb only the Zeeman shifted lines. This cannot be done with a single cell, because the emerging light is not polarized. A rejection of both the 25% plateaus and the side peaks would be possible and, thus, a further background reduction by more than 50% could be achieved.

Chapter 4

The Nighttime Climatology

A large database of temperature soundings at different locations has been accumulated with the IAP K-lidars. This chapter will first introduce this database. The presentation focusses on mid and low latitudes for which a climatology is derived in this work. The mean properties and the seasonal variation of the potassium layer and the temperature structure of the mesopause region are presented in the following sections. Although temperature soundings are the main topic of this work, it seems natural to present the potassium densities first because the metal occurrence forms the basis for temperature measurements by K-lidars.

4.1 Data Coverage of the Potassium Lidar Measurements

Initial potassium and temperature soundings with the transportable K-lidar were carried out on the German island of Rügen (54°38'N, 13°24'E) in 1995 (*Höffner and von Zahn*, 1995). During a campaign on the research vessel 'Polarstern' between April 24th and June 18th, 1996, nighttime temperature measurements with this instruments were performed while sailing northward from 71°S to 45°N (*von Zahn et al.*, 1996). These observations led to the discovery of the two-level behaviour of the mesopause which exhibited a discontinuity of its altitude at northern low latitudes. The potassium layer and its latitudinal structure, observed during this campaign, have been described in detail by *Eska et al.* (1999).

Since June 26th, 1996, routine potassium lidar measurements have been made at the site of the IAP in Kühlungsborn (54°07'N, 11°46'E, $z_0 = 70$ m) with the transportable system. Since 1999 measurements are continued using the new stationary instrument. The first annual set of temperature data supported the concept of a two-level mesopause (*She and von Zahn*, 1998). The potassium layer exhibited an unexpected seasonal variation that deviates from those of other metals (*Eska et al.*, 1998). The data set from Kühlungsborn has been extended over several years and is therefore presented again in this work.

From March 1999 until December 2000, the lidar container was installed on the Canary island of Tenerife, where the lidar was situated at 2390 m altitude at the Observatorio del Teide (28°18'N, 17°31'W). This astronomical site enjoys excellent weather conditions for lidar observations, especially in the spring and summer months. At this location data were retrieved during five measurement campaigns. Between 2001 and 2003 this lidar was operated at the Arctic archipelago Svalbard (78°14'N, 15°23'E) to study temperatures and noctilucent clouds at this very high latitude (*Höffner et al.*, 2003).

Table 4.1 presents the part of the K-lidar database which is considered in this thesis or has been obtained during the work to it. It gives an overview of the temperature and potassium soundings collected since the beginning of observations in Kühlungsborn in 1996 and shows the accumulated period of K-lidar temperature measurements and the number of nights grouped in seasons. Note that December is added to the winter season of the following year. Originating from pure nighttime observations, the measurements are grouped in terms of *nights*, i. e. periods

Table 4.1: Temperature measurements with the transportable and the stationary IAP K-lidar. For each season, the observation period in hours and the number of *nights* are given (∘, nighttime only; •, including daytime measurements).

Year	Latitude	K-lidar	Dec-Jan-Feb		Mar-Apr-May		Jun-Jul-Aug		Sep-Oct-Nov	
1996	54°N	transp.	—	—	—	—	62 h	19 ∘	125 h	29 ∘
1997	54°N	transp.	131 h	18 ∘	122 h	28 ∘	109 h	32 ∘	70 h	14 ∘
1998	54°N	transp.	41 h	6 ∘	45 h	16 ∘	17 h	10 ∘	47 h	9 ∘
1999	54°N	transp.	30 h	6 ∘	—	—	—	—	—	—
1999	54°N	stat.	—	—	—	—	—	—	25 h	6 ∘
2000	54°N	stat.	12 h	1 ∘	—	—	8 h	4 ∘	—	—
2001	54°N	stat.	—	—	—	—	10 h	2 ∘	—	—
2002	54°N	stat.	9 h	1 •	13 h	2 •	50 h	14 •	79 h	11 •
2003	54°N	stat.	137 h	8 •	58 h	8 •	118 h	22 •	164 h	20 •
1999	28°N	transp.	—	—	165 h	25 ∘	110 h	15 ∘	107 h	15 ∘
2000	28°N	transp.	—	—	—	—	—	—	170 h	10 •
2001	28°N	transp.	36 h	3 •	—	—	—	—	—	—
2001	78°N	transp.	—	—	—	—	224 h	33 •	53 h	17 •
2002	78°N	transp.	9 h	1 ∘	111 h	16 •	—	—	—	—
2003	78°N	transp.	—	—	133 h	19 •	138 h	34 •	—	—

from noon on one day to noon on the following day (in UT, universal time). Seasons which include daytime observations are marked (•). The measurements with the two systems at Kühlungsborn are listed separately. A list with detailed information for each month is given in Appendix D, including data from Rügen and the Polarstern campaign.

The largest portion of daytime data has been obtained at Svalbard. At 78°N in summer, operation of the lidar is possible only when it is capable of daytime measurements due to the continuous daylight conditions for more than 4 months. The evaluation of this unique data set is not within the scope of this work, which concentrates on mid and low latitudes.

Data From Kühlungsborn (54°N)

In Kühlungsborn measurements were carried out most frequently during the first year (until summer 1997). On average between 10 and 20 nights of data from each month of the year were collected before the system was moved to Tenerife. By contrast, in subsequent years the new stationary system was mainly used for instrument development, for measurements on special occasions and to fill remaining gaps in the seasonal coverage. Only since the installation of the new telescope in summer 2002 have high quality daytime measurements become possible and are carried out more regularly. The majority of data still originates from pure nighttime observations. At present, a reliable climatology for the latitude of 54°N can be derived only for nighttime conditions. The inclusion the daytime observations would result in a very inhomogeneous data set because they are irregularly distributed over the year, have higher statistical errors and cover a reduced altitude range. The nighttime climatology is given below from all the data obtained between June 1996 and February 1999. The temporal coverage of the data used is shown in Figure 4.1. The data are well distributed over the year, though some gaps exist in March and in November – December when good weather is rare. The local time coverage changes significantly with the seasons. The period of darkness per day ranges from 4 to

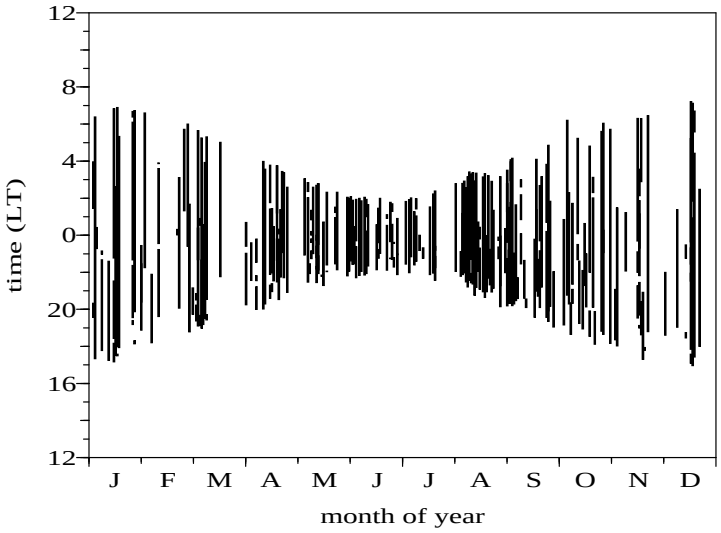

Figure 4.1: Local time coverage of the nighttime K-lidar observations in Kühlungsborn as a composite of measurements made between 1996 and 1999.

14 hours. Thus, especially during summer, the results may be influenced by diurnal variations, while in winter the effects of semi- and terdiurnal tides are almost smoothed out.

The data set consists of about 800 hours from 187 nights from which the first half has been published before. To investigate the seasonal variation of the potassium density *Eska et al.* (1998) used 94 selected nights from one year (June 1996 – June 1997) which did not exhibit sporadic layers. Temperature data from the first 13 months (July 1996 – August 1997) were studied by *She and von Zahn* (1998) in combination with the climatology from 41° and 69°N. From Kühlungsborn the authors used 88 nights with 3 hours or more, plus 2 nights from May 1995 (Rügen). These first 2 nights are excluded from the following analysis due to possible systematic differences to the measurements at Kühlungsborn.

Data From Tenerife (28°N)

On Tenerife measurements were concentrated on five campaigns. Due to the good weather conditions the lidar could usually be operated in 1999 during the entire period of darkness which lasts longer than 8 hours throughout the whole year. With the development of the FADOF, K-lidar daytime measurements became possible and were first successfully carried out during an additional campaign in 2000.

The system was installed in mid-March 1999, followed by four observation campaigns during 1999 with routine operations providing a total of 382 hours of measurement during 55 nights:

- March 28th to April 2nd, plus April 14th, 1999: 6 nights (2 nights with 8–9 h)
- May 1st– 26th, 1999: 19 nights (15 nights with 8–9 h)
- June 19th to July 15th, 1999: 15 nights (13 nights with 8–9 h)
- November 6th– 29th, 1999: 15 nights (9 nights with 9–12 h)

The last campaign was interrupted by a period of bad weather from November 13th to 19th (including the Leonid meteor shower). The reaction of both the K layer and the ambient temperatures to the 1999 Leonid meteor shower has been described by *Höffner et al.* (2000). The authors did not find any outstanding enhancement of potassium or changes of the temperature due to the Leonids.

The campaign with the first K-lidar daytime measurements was carried out from November 12th to December 10th, 2000. A period with good weather (November 19th–26th) enabled nearly uninterrupted measurements for a full week, which provide an exceptional long-term data set.

Although the nighttime data do not cover a full year's cycle, they provide interesting insights into the seasonal variation of the mesospheric potassium layer and temperature structure. The results are presented in the following sections, from which basic parts have already been published (*Fricke-Begemann et al.*, 2002b). The daytime data are restricted to November and December and hence the results from 2000 are analysed separately for diurnal variation (Section 5.3).

4.2 The Mesospheric Potassium Layer

Lidar soundings of the Earth's upper atmosphere metal layers have contributed significantly to our understanding of the mesopause region (80 to 105 km). While the metals are used as tracers to study the dynamics and temperature structure, analysing the occurrence of metal atoms has also provided insight into atmospheric chemistry. Almost all available results are from mid and polar latitudes. For midlatitudes, the seasonal variations of Na, Ca, Fe and K densities are well studied (*Plane et al.*, 1999; *Gerding et al.*, 2000; *Helmer et al.*, 1998; *Eska et al.*, 1999, respectively), both through observation and modelling. Sodium is relatively easy to observe and has been studied most extensively. Although low latitudes are also of considerable interest, data from there are only recently becoming available (*Friedman et al.*, 2002; *Fricke-Begemann et al.*, 2002b; *Raizada and Tepley*, 2003).

4.2.1 Midlatitude Potassium Layer: Kühlungsborn (54°N)

The seasonal variation of the potassium layer above Kühlungsborn, as derived from the nighttime measurements, is shown in Figure 4.2. Density profiles are obtained every ∼2 minutes (4000 laser pulses) with 200 m altitude resolution. The detection limit for nighttime observations is about 0.2 atoms/cm^3 under clear sky conditions. For the evaluation the individual profiles have been pre-averaged to give nightly means. In comparison with the data from the first year's cycle (*Eska et al.*, 1998), the extension of the data base by two more years has statistically improved the results and added some interesting details.

The potassium layer is permanently observed between 80 km and 105 km. The most prominent feature of the K layer is the semi-annual variation of atomic occurrence. Both the density ρ_K at the peak of the layer and the integrated *column density* $C_K = \int \rho_K(z)dz$ are higher at the solstices than at the equinoxes. The column density in winter is even higher than in summer, with about 7 and 5×10^7 cm^{-2}, respectively. In spring and autumn only $C_K \approx 3 \times 10^7$ cm^{-2} is observed.

The peak density has one maximum in January with densities above $\rho_K = 60\,\mathrm{cm}^{-3}$ and another in summer. The latter is much broader, it lasts for about 4 months (May – August)

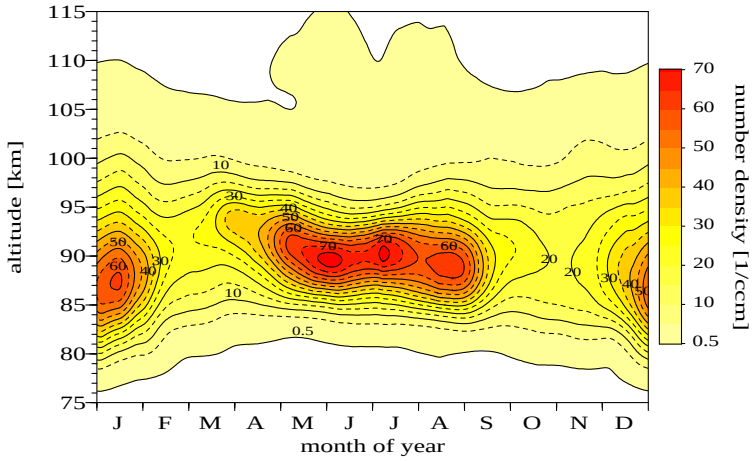

Figure 4.2: Nighttime climatology of the potassium density at 54°N. For smoothing the data a Hanning filter with 21 days and 2 km FWHM is applied. Contours are given each 5 cm^{-3} with the first contour at 0.5 cm^{-3} instead of zero.

and reaches values of up to 70 cm^{-3}. In Figure 4.2 it appears with some substructure of local maxima, which however, is sensitive to the smoothing filter applied. At the minima, peak densities near 20 cm^{-3} are observed.

The altitude of the peak shows a simple annual cycle with a minimum at the beginning of January (∼87 km) and a maximum at the end of March (∼94 km), while being rather uniform throughout summer and autumn. For the centroid altitude a similar variation between 92 km and 89 km was found by *Eska et al.* (1998). The width of the layer exhibits a clear annual variation with root-mean-square (rms) values varying between 3 km and 5 km. The minimum of the width in summer produces the lower column density than in winter. A similar variation is obtained when the outer edges of the permanent layer are considered, except for the upper edge in summer, which is observed at higher altitudes. Whereas the lower edge is well defined due to the sharp gradient at the bottom side of the layer, the altitude of the upper edge depends on the threshold chosen. The sporadic occurrence of separate high layers at altitudes up to 130 km causes a slow decrease with altitude of the average density at the upper edge. In summer, the average potassium mixing ratio (ρ_K/ρ_{air}) is nearly constant with height above 100 km.

4.2.2 Low Latitude Potassium Layer: Tenerife (28°N)

To illustrate the seasonal variation of the potassium layer above Tenerife, all observations in 1999 are grouped into periods of 5 to 9 nights with small temporal separation and a comparable characteristic. For these groups the mean layer properties are given in Table 4.2. Due to the limited number of nights, this analysis is based on the individual 2-minute profiles without pre-averaging. For the eight groups the mean density profiles are shown in Figure 4.3 without any vertical smoothing.

At Tenerife, the overall mean state of the potassium layer is characterized by a peak atom density of 43 atoms/cm^3 at an altitude of 90 km. The mean column density derived from our observations is $C_K = 4.2 \times 10^7$ cm^{-2}. The major part of the potassium layer is constantly located between 85 and 95 km with wings extending from 80 to 105 km. However, under certain

Table 4.2: Mean properties of the potassium layer as observed at 28°N. For the column densities (integrated either over the whole profile or up to 95 km only) the 1σ-standard deviation of the individual 2-minute profiles is given.

#	Period 1999	Nights (with ALE)[1]	Profiles	ColDens [1e7/cm^2]	ColDens<95km [1e7/cm^2]
1	27 Mar. – 14 Apr.	6 (2)	713	2.4 ±0.7	2.1 ±0.7
2	1 May – 15 May	8 (4)	1551	2.4 ±0.8	1.9 ±0.7
3	15 May – 20 May	5 (0)	772	4.7 ±1.4	4.3 ±1.3
4	20 May – 27 May	6 (4)	1229	6.7 ±2.8	5.3 ±1.8
5	20 June – 2 July	8 (3)	1250	6.0 ±2.1	5.3 ±1.9
6	3 July – 15 July	7 (4)	1195	5.6 ±2.5	4.6 ±2.1
7	6 Nov. – 13 Nov.	6 (2)	1188	2.8 ±1.4	2.3 ±1.5
8	18 Nov. – 19 Nov.	9 (5)	1237	2.8 ±1.1	2.4 ±1.0

[1] The number of nights with obvious atomic layer enhancement (ALE) or sporadic layers

#		Peak Density [1/cm^3]	Peak Altitude	Median Altitude	RMS-Width (FWHM)
1	*...vide supra ...*	29.4	89.9 km	90.1 km	4.4 (7.0) km
2	.....	23.2	89.9 km	90.1 km	5.7 (8.9) km
3	.....	50.6	88.3 km	88.9 km	4.7 (8.7) km
4	.....	62.5	89.3 km	90.3 km	5.8 (10.4) km
5	.....	71.1	89.1 km	89.5 km	5.3 (7.8) km
6	.....	53.4	88.7 km	90.9 km	5.2 (9.0) km
7	.....	29.3	90.7 km	90.9 km	4.5 (8.2) km
8	.....	22.6	86.9 km	88.7 km	5.3 (12.6) km

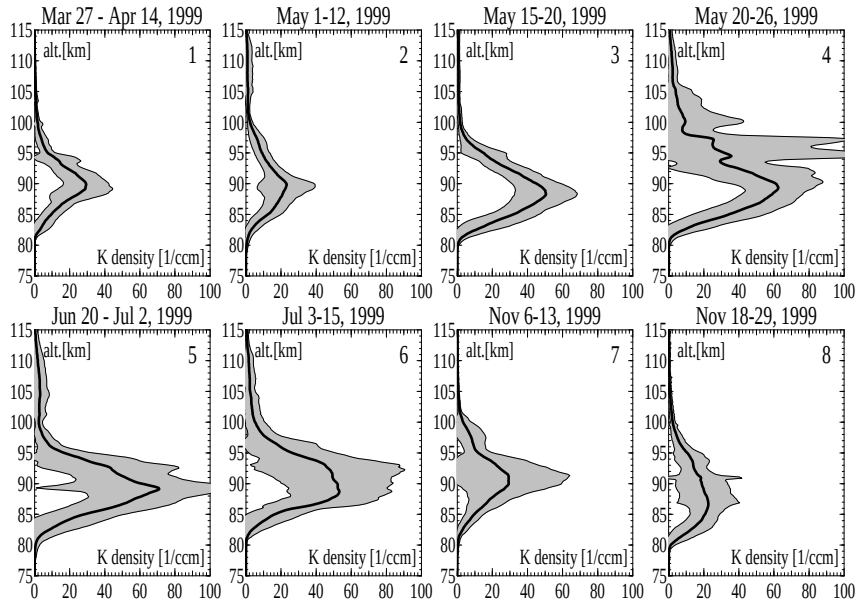

Figure 4.3: Mean potassium density profiles measured at 28°N for the periods given. The grey area represents the 1-σ standard deviation of the individual 2-minute profiles. Further statistics on the profiles are provided in Table 4.2 (from *Fricke-Begemann et al.*, 2002b).

conditions it can reach up to altitudes of 115 km (cf. groups 4, 5 and 6). The high variability is shown by the 1σ-standard deviation which is about 50% at the height of the peak and increases further with altitude. Sporadic layers are observed mainly above 95 km and therefore densities have been integrated up to this altitude also (given in Table 4.2). The occurrence of these layers does not exhibit a clear seasonal dependence. Sporadic layers are apparent from the graphs by an increased standard deviation (e. g. panel 4) but do not affect the seasonal variation of the overall layer parameters.

The most remarkable feature of the seasonal variation is the strong increase in both peak and column density by a factor of about 2.5 within 14 days during May (periods # 2–4). The density remains high during summer and is low again in November. The other parameters of the potassium layer show little systematic variation. The height of the peak seems to decrease during summer from 90 km in April to 89 km in July while the median height remains slightly above 90 km. The width appears to stay relatively constant.

In summary, from 55 nights of lidar observations at 28°N it was possible to derive a seasonal series of mean potassium profiles in the mesopause region. Major features of the seasonal variation have been revealed despite the absence of data from a full year's cycle.

4.2.3 Potassium Layer: Discussion

The potassium layer at 54°N, as obtained from the 3-year data set, corroborates the earlier measurements of the first year and no significant inter-annual variation has been detected. *Eska et al.* (1998) have shown that the mean column density of 4.4×10^7 cm^{-2} at Kühlungsborn lies within the range of values derived from earlier twilight observations at midlatitudes (44–52°N) by various groups.

Seasonal Density Variation at Different Latitudes

The midlatitude measurements with the IAP lidar have identified the previously unknown seasonal variation of the K layer. As the variation is of semi-annual character it is distinct from that of all other mesospheric metal layers which have been observed. This result has stimulated the interest in the behaviour of the K layer at different latitudes.

Prior to our measurements on Tenerife, data from low latitudes were scarcely available. The Polarstern campaign provided data at 24°N during two nights (June 11st–13th, 1996, *Eska et al.*, 1999), with a column density of $C_K = 7.3 \times 10^7$ cm^{-2} (or 5.5 below 95 km) and a peak density of $\rho_K = 60$ cm^{-3}, which complement the data gap between our periods 4 and 5 (Table 4.2).

The Polarstern observations between 30°N and 30°S, showing $C_K \approx 7$–8×10^7 cm^{-2}, have led to the hypothesis that the occurrence at low latitudes might in general be higher than at midlatitudes. Our data from Tenerife show that this is not the case in spring and autumn when C_K is 10–20% less than the value for Kühlungsborn of 3×10^7 cm^{-2}. Instead, this new Tenerife data set suggests a strong semi-annual variation at low latitudes with a second maximum in winter, as observed at midlatitudes. From the nighttime campaigns from 1999 considered above, no data between December and February are available. However, the sparse observations in December 2000 indicate that the K density increased between late November and mid December.

The first potassium detection by lidar (*Felix et al.*, 1973) was reported from Jamaica (18°N), where a high density of $C_K = 9 \times 10^7$ cm^{-2} (±25%) was observed on January 27th. This observation would fit the assumption of a semi-annual variation at low latitudes. With a symmetry

between the hemispheres, the high densities observed during the Polarstern campaign under southern winter conditions would also support this picture.

Recently, *Friedman et al.* (2002) reported potassium lidar measurements from Arecibo, Puerto Rico, (18°N) covering a full year's cycle. Their data set shows a semi-annual variation which seems to be even stronger than at Tenerife with about $C_K = 6$, 5 and 2×10^7 cm^{-2} for summer, winter and the intermediate minima, respectively. The corresponding values for 54°N are 5, 7 and 3×10^7 cm^{-2}. At Arecibo the annual density variation appears more symmetric with a narrower summer maximum compared with Kühlungsborn.

The lidar observations at 44°N of *Megie et al.* (1978) show a decrease in potassium by about 30% throughout June to December. Although the absolute density values must be doubted (see *Eska et al.*, 1998), this variation qualitatively agrees with the other observations.

The quantitative evaluation of the polar latitude measurements with the IAP lidar at Svalbard (78°N) is beyond the scope of this thesis. Nevertheless, it should be noted that a semi-annual character of the potassium layer is also indicated at the Arctic site. While no winter measurements are available, low densities around the equinoxes and higher values in summer agree with mid and low latitude behaviour.

Thus, as no principle difference is expected for the southern hemisphere, the semi-annual variation can be seen as a global phenomenon. High column densities in summer and presumably again in winter, together with minima at the equinoxes, were revealed in various lidar observations. Compared with midlatitudes, the seasonal differences are stronger at low latitudes and lead to higher densities in summer.

Potassium Layer Properties

At Tenerife, the **height** of the K layer peak declines from April towards July slightly by about 1 km and is very non-uniform in November, while no systematic variation was observed in the median height. This finding is in agreement with the observations from Arecibo, where little seasonal variation of the centroid height was found. The annual mean is 91.5 km and only the autumn values appear slightly higher. By contrast, at 54°N the height shows a clear maximum in spring ($\sim$ 92 km) and a minimum in January (88–89 km). Throughout the rest of the year the centroid height is rather constant. This behaviour can be interpreted as a superposition of annual and semi-annual variation. The mean height is 90.5 km which is similar to 28°N.

The **width of the layer** at 28°N has an average rms-value of 5 km and did not exhibit a systematic variation. The mean value is slightly higher (5.5 km) at 18°N where the layer is about 1 km broader in summer than in winter. This broad layer in summer is due to a bimodal vertical structure which is not observed at the other stations. Contrary to the low latitudes, the width at 54°N shows a clear annual cycle with a maximum in winter and ±1 km variation around the mean of 4 km.

Consistent with the constant width, the **peak density** is proportional to the column density at 28°N. By contrast, at 54°N the highest peak density is found in summer and the highest column density in winter while both show the pronounced semi-annual variation. Average peak densities range from 20 to 70 cm^{-3} at mid and low latitudes but individual profiles often exhibit much higher densities.

In conclusion, the potassium layer at low latitudes does not exhibit much seasonal variation of its geometric height and width. While this is in contrast to 54°N, a close agreement between 18° and 28°N is observed. The semi-annual variation of the potassium occurrence, on the other hand, is a feature that is common to all latitudes. The variability of the 2-min profiles about

their monthly mean is generally higher at low latitudes (∼50%) than at midlatitudes (∼30%). The reason for the higher variability is presumably a stronger wave activity.

Mesospheric Layers of Other Metals

The seasonal variation of a number of mesospheric metal atom layers has been studied but the semi-annual character of the potassium layer appears unique.

Kane and Gardner (1993) have compared iron (Fe) and sodium (Na) layers at 40°N. Both have a column density which is more than 100 times higher than that of potassium. The mean values are $C_{\mathrm{Na}} = 530 \times 10^7\ \mathrm{cm}^{-2}$ and $C_{\mathrm{Fe}} = 1060 \times 10^7\ \mathrm{cm}^{-2}$. The column densities are dominated by an annual cycle. The density values are three times higher in winter than during the summer minimum. The layer centroid heights vary semi-annually as it is the case with potassium. While the mean Fe height of 88 km is clearly below the K height, the Na height at 92 km is above it. The maximum layer width of Na occurs in winter and again in summer, whereas Fe and K both show an annual variation with a single minimum in summer. On average, the Fe layer has a rms-width of 3.4 km and is narrower than the K layer by about 1 km. In contrast to K, the Fe density differs significantly between mid and low latitudes (*Raizada and Tepley*, 2003). This supports the assumption that the Fe layer is controlled by different processes than the K layer.

The calcium (Ca) layer at 54°N was studied by *Gerding et al.* (2000). The mean column density of $2.1 \times 10^7\ \mathrm{cm}^{-2}$ is slightly lower than for K. Column and peak density show a mainly annual variation but, in contrast to Na and Fe, with a minimum in spring and a maximum in autumn. Width and height change semi-annually both with a minimum in summer. While the layer width of K, Fe and Ca is out of phase with that of Na, the centroid height is the only parameter that varies similarly for all metals. *Gerding et al.* analysed the calcium layer with a chemical model. The reason for the unusual behaviour of calcium and its observed high night-to-night variability is the small contribution Ca atoms make to the whole family of Ca-species (which is dominated by Ca^+ and $CaCO_3$ in the region of the mesospheric metal layer).

Sodium and iron layers at midlatitudes are found to be highly correlated with the thermal structure of the mesopause region (see Section 4.3), which is dominated by an annual variation. The density of these metals is controlled by the chemical processes which are temperature dependent. In contrast, for potassium the seasonal variation appears to be semi-annual and uncorrelated with temperature. The independence of temperature is supported by the finding that the semi-annual density variation decreases with increasing latitude whereas the temperature variation increases. The chemical reactions of potassium are very similar to those of sodium and have been analysed in a chemical model for the K layer by *Eska et al.* (1999). Not only the temperature, but also chemical reactions, trace gas constituents and transport mechanisms fail to explain the unique seasonal variation of potassium.

The authors proposed the source of the mesospheric metals as the cause for the differences. The majority of meteoroids undergo differential ablation and metals with different volatility ablate at different altitudes depending on mass and velocity of the meteoroids (*von Zahn et al.*, 2002). Thus, the fraction of meteoritic material that can contribute to the permanent metal layers depends strongly on the mass and velocity distribution. The variation of this distribution throughout the year thereby affects the mesospheric layers of different metals in different ways. This interpretation is supported by the observation that the semi-annual character of the K layer is independent of latitude.

4.3 The Temperature Structure of the Mesopause Region

The main objective of the climatological observations of the mesopause region with the IAP K-lidars is the investigation of the vertical temperature structure and its temporal and latitudinal variation. The mesopause, the upper boundary of the mesosphere, is characterized by a pronounced minimum in the temperature profile. It is the horizontal surface with the absolute temperature minimum between mesosphere and thermosphere at each location. When shorter time scales are considered, the mesopause could either be identified by the altitude of the instantaneous temperature minimum or by the altitude of the absolute minimum of the mean temperature profile, after appropriate averaging to smooth out most wave effects. Following *She and von Zahn* (1998), the latter definition is favoured here because it excludes perturbations by small scale atmospheric waves. Considering global and seasonal scales, the mesopause is the altitude which separates two major atmospheric regions with distinct thermal characteristics and energy budgets.

In order to determine the altitude and temperature of the mesopause, temperature profiles obtained from lidar observations would ideally be averaged over 24 hours to smooth out both gravity and tidal waves. Single nighttime measurements can only provide approximate results and even when averaged over multiple nights they may be biased by systematic diurnal variations. These can only be identified by continuous 24-h observations and will be discussed in the next chapter. Nevertheless, the bias is expected to be small when the nighttime observations used cover 8 to 12 hours.

Temperatures used in this section are calculated from the photon count profiles integrated over single nights with a 1-km vertical binning and a 2-km running mean filter. The remaining statistical error is below 1 K at the center of the potassium layer and increases towards its wings. If it exceeds a threshold value, the temperature value is discarded. The profiles from individual nights are then averaged to obtain a climatological mean. The accuracy of the means increases with the number of profiles included in the average and similar maximum uncertainties are desired for both stations. Therefore, the large number of observations in Kühlungsborn allows individual values with up to 20 K statistical uncertainty to be used, while for Tenerife a threshold value of 12 K was applied.

Previous Observations

To explore the thermal structure of the mesopause region, a large number of experiments have been performed over the past decades. Most frequent have been rocket-grenade type experiments and meteorological rocket launches (e. g. *von Zahn*, 1990; *Lübken*, 1999). As pointed out by *von Zahn* (1990), none of these methods were able to yield information on temperatures above $\sim$92 km. Consequently, these measurements have only been able to detect the mesopause when it was located below 90 km. In the interpretation it had been disregarded that the majority of the profiles did not show a temperature minimum, and if it did, that it could have been a local minimum which did not represent the mesopause. Thus, the mesopause was assumed to be located slightly below 90 km (e. g. *USSA*, 1976, see Appendix B). Experiments which determined temperatures to above 100 km, like rocketborne mass spectrometers or active falling spheres, have been too infrequent to provide a consistent global picture.

Only with the advent of groundbased metal resonance lidars with the potential to measure accurate temperature profiles from 80 km to 110 km, has our present notion started to develop. From sodium lidar observations at 69°N, *von Zahn and Neuber* (1987) found the mesopause

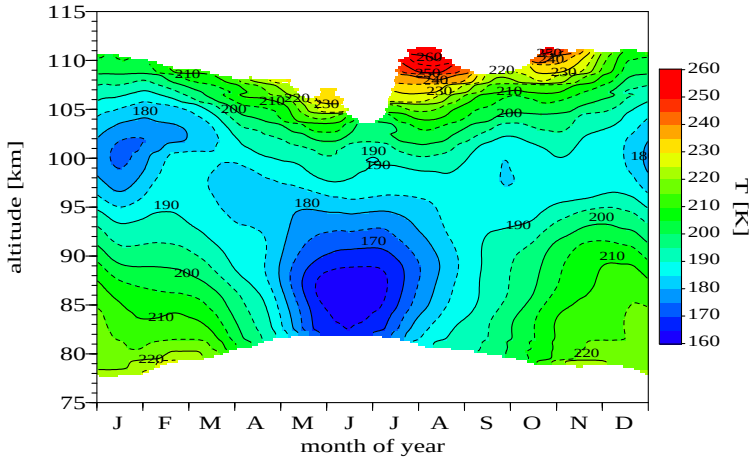

Figure 4.4: Nighttime temperature climatology at Kühlungsborn (54°N). The data has been smoothed using a Hanning filter with 31 days and 2 km FWHM.

to be consistently located at 100 km altitude during winter. Summertime rocket measurement at the same location clearly located the mesopause at 88 km (*von Zahn and Meyer*, 1989). Surprisingly, at midlatitudes (41°N) the same two altitude levels were found for the mesopause in winter and summer, again with the use of a sodium lidar (*She et al.*, 1993). The global two-level character of the mesopause became evident from the potassium lidar measurements by *von Zahn et al.* (1996) onboard the Polarstern. Sailing from 71°S to 45°N in April–June, a distinct jump of the mesopause altitude from 99 km down to 83 km was observed near 24°N in mid June. Both before and after that day, the mesopause altitude had been rather constant around 100 km and 86 km, respectively. On the other hand, the mesopause temperature had continuously decreased with increasing latitude throughout the whole series of measurements.

Taking into account the first year of lidar temperature measurements in Kühlungsborn, *She and von Zahn* (1998) established the concept of the global two-level behaviour of the mesopause. Throughout the winter hemisphere and the tropics the mesopause is in its normal state, i. e. located at 100 km. Only at high and midlatitudes in summer is the mesopause found near 88 km. *She and von Zahn* estimated that at any time and location on Earth, one finds the mesopause only with a frequency of 17% in the lower state but regularly its altitude is 100 km.

4.3.1 Midlatitude Temperature Structure: Kühlungsborn (54°N)

The nighttime temperature climatology of the mesopause region at 54°N is shown in Figure 4.4. It covers the 187 nights of measurements, from 1996 until 1999, performed with the IAP's first generation potassium lidar. Throughout the year temperatures can be derived approximately between 80 km and 105 km, i. e. in the region where potassium densities are above 1 cm^{-3}. The mean temperature of this layer is about 190 K. A filter with 31 days FWHM was applied, which is wider than that for the potassium densities because of strong day-to-day variations.

A cold region in summer below 95 km is the most remarkable feature of the temperature structure. Around solstice and 87 km altitude, the temperatures drop down to nearly 160 K, while in winter temperatures above 200 K are observed at these altitudes. This behaviour is counter-intuitive because during summer the mesosphere experiences the highest energy input

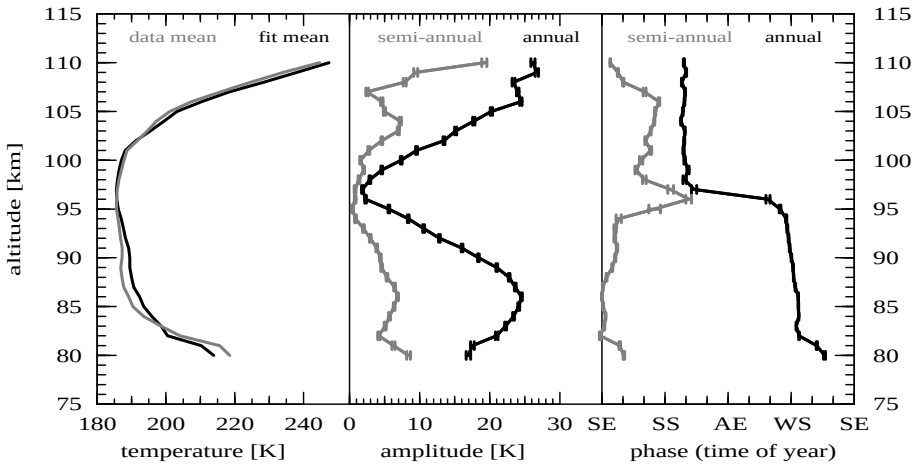

Figure 4.5: Harmonic fit to the seasonal temperatures (Figure 4.4) at 54°N. Left: annual mean temperature of fit and data. Middle: annual and semi-annual amplitudes. Right: phases (SE, spring equinox; SS, summer solstice; AE, autumn equinox; WS, winter solstice)

of solar radiation, but obviously, the mesopause region is not governed by radiative processes alone. In 95–100 km temperatures are relatively constant and only above this level the seasonal variation is found to be in phase with the solar input. This region is also characterized by a strong temperature increase with altitude.

The climatological temperatures in each altitude are analysed by a LMS fit of annual and semi-annual harmonic variation (see Appendix C.1 for details):

$$\tilde{T}(t) = T_0 + T_1 \cos(2\pi(t-\phi_1)/12\,\mathrm{mo}) + T_2 \cos(2\pi(t-\phi_2)/6\,\mathrm{mo})\,. \tag{4.1}$$

It represents the averaged data quite closely and widely agrees with the analysis of *She and von Zahn* (1998) which was carried out for the first year of the current 3-year data set. Significant interannual variations were not observed. The derived fit parameters are displayed in Figure 4.5. The annual component reaches an amplitude of $T_1 = 25\,\mathrm{K}$ at altitudes of 86 km and above 105 km, while it falls below 2 K at 97 km. The semi-annual harmonic similarly has a minimum in this region but the amplitudes are, in general, much smaller than for the 12-month period (typically $T_2 = 5\,\mathrm{K}$). The annual variation at 87 km is in good agreement with observations of OH-nightglow which originates near this altitude and shows a similar amplitude ($\sim$22 K at 51°N, *Bittner et al.*, 2002). The amplitude minimum at 97 km indicates a phase jump of the annual component (right panel). Above 97 km the temperature maximum occurs one month after summer solstice. Below this height it occurs in winter: while at 87 km the maximum is attained at winter solstice, at other heights it varies by about ±10 days around this date with a tendency to occur later at lower altitudes. The maxima of the semi-annual component occur at the equinoxes at 82 km and increasingly later with increasing altitude (near the solstices in 105 km).

A slight deviation ($\sim$2 K) between the annual mean profile of the data and that of the fit functions (T_0) is observed at 88 km (Figure 4.5, left panel). This is mainly caused by the remaining irregularities in the distribution of the observations, which were most frequent in June to August. The measured mean temperature is lowest in 96 km with 185.6 K and a secondary

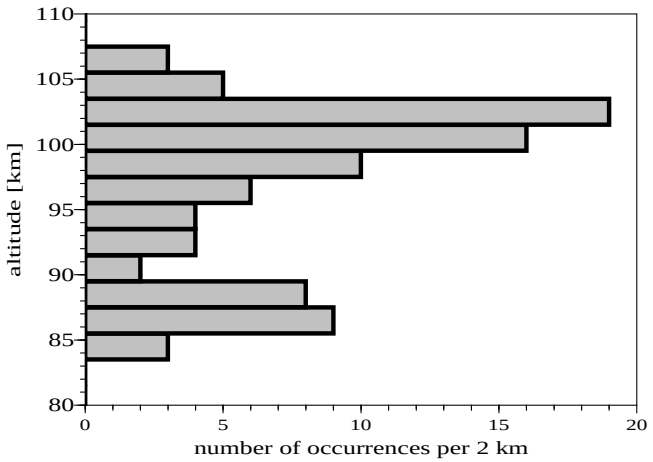

Figure 4.6: Frequency distribution of the height of the mesopause at 54°N, at a vertical resolution of 2 km. Included are all observations which covered more than 4 hours and which showed the mesopause.

minimum of 186.9 K is weakly indicated at 89 km. The fitted mean shows a distinct temperature minimum of 185.6 K at 97 km, while 10 km below it predicts $T_0 = 190$ K.

The relatively isothermal annual mean temperature profile in combination with the odd seasonal variation leads to the formation of the two-level mesopause. The temperature at 97 km is rather constant. In winter a cold region develops above this altitude while in summer it develops below it. Since the temperatures at all lower altitudes vary in phase and the amplitudes increase steadily down to 87 km, the minimum is located at this altitude as soon as the temperature at 97 km exceeds the temperature at all lower altitudes. Hence, the mesopause occurs either above 100 km or near 87 km as apparent from statistics on the occurrence of the mesopause (Figure 4.6). Its altitude is counted for each night which lasted more than 4 hours and which allowed the mesopause to be identified. The frequency distribution peaks around the two altitudes of 102 km and 87 km, which represent the regular and the summer mesopause, respectively. The mesopause was rarely located in the region of 90–95 km. The picture is still disturbed by wave perturbations and becomes clearer when only longer measurements are considered, but due to the short summer nights, this would reduce the number of summer mesopause observations and bias the results.

4.3.2 Low Latitude Temperature Structure: Tenerife (28°N)

No complete year-round cycle of measurements is available from Tenerife. To illustrate the seasonal variation of the temperature profile at this subtropical site, the mean profiles for the four campaigns in 1999 are shown in Figure 4.7. No further vertical smoothing was applied to the data. Values are only shown for altitudes where data can be derived from more than 50% of the nights. The panels also demonstrate the natural night-to-night variability which significantly exceeds the error bars resulting from the statistical uncertainties for the individual nights. The spring profile (1) shows a clear local minimum at 88 km. Another minimum at or above 101 km is not fully delineated because of a lack of potassium. The May (2) and summer (3) profiles both show two distinct minima above 85 km and at 100 km with temperatures of about 185 K. After summer solstice the lower minimum has become just cold enough to form

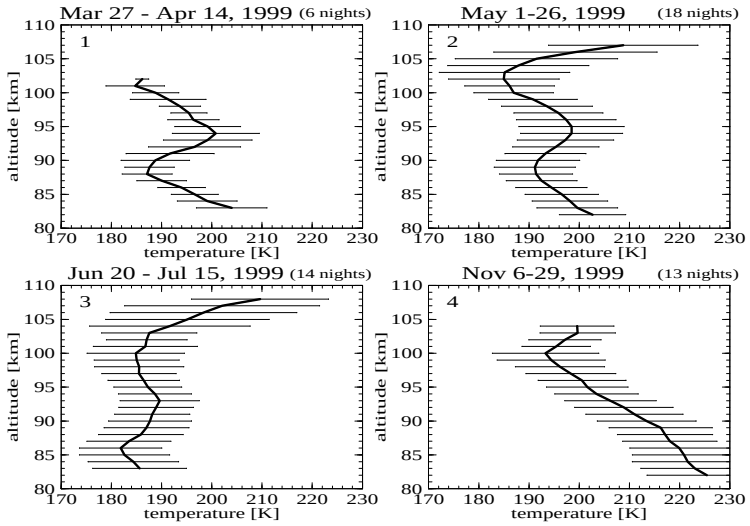

Figure 4.7: The mean temperature profiles at Tenerife (28°N) for the four campaigns in 1999 along with the standard deviation of the nightly means. Values are only shown for altitudes where more than 50% of the nights contribute reliable data (from *Fricke-Begemann et al.*, 2002b).

the mesopause. The November profile (4) represents a typical regular mesopause with an altitude of 100 km and a constant lapse rate below. During all seasons the temperature of the mesopause remains in the range of 180 to 195 K. The observations frequently lasted for more than 8 hours per night, except for (1). Thus, biasing effects of semi- and terdiurnal tides can be expected to be small as well as that of gravity waves.

For the annual variation a maximum amplitude of 18 K at 85 km is derived from a harmonic fit (Eq. 4.1, not shown). Similar to Kühlungsborn it decreases with increasing height to 2 K at 101 km, but no phase shift is observed at this altitude. At all heights available (up to 104 km), temperatures in November were higher than those during any other campaign.

The variability at 28°N is of comparable magnitude to that observed at 54°N. The 1σ-standard deviation of 8–9 K is of the same order as the vertical structure in May and summer. Nevertheless, the *double structure* with two minima is very clear as it occurs in almost every night. A major contribution of the variability is due to the variation of the mean temperature. For example, for May (2) nearly 60% of the variance in each altitude is constituted by the night-to-night variance (σ^2) of the mean, taken between 86 km and 100 km. The upper minimum varies less in altitude than the lower and, hence, the temperature difference between the minimum and the intermediate maximum becomes statistically significant when the mean temperature is subtracted. Except for the 2-km vertical integration in the temperature retrieval, no further smoothing was applied and, thus, the continuity of the profiles further supports that the structure is not due to statistical fluctuations.

For a more detailed look at the mesopause behaviour, the May and summer (June–July) campaigns are split into periods of 3 or 4 subsequent nights and shown in Figure 4.8. During the first half of May the mesopause was still located at the regular high altitude near 100 km. The profiles then became more isothermal with the gradient gradually changing from negative to positive (panels 1 and 2). At the end of May a clear low mesopause state was reached. Analogously at the end of June, low mesopause conditions were still present (panel 3) with the

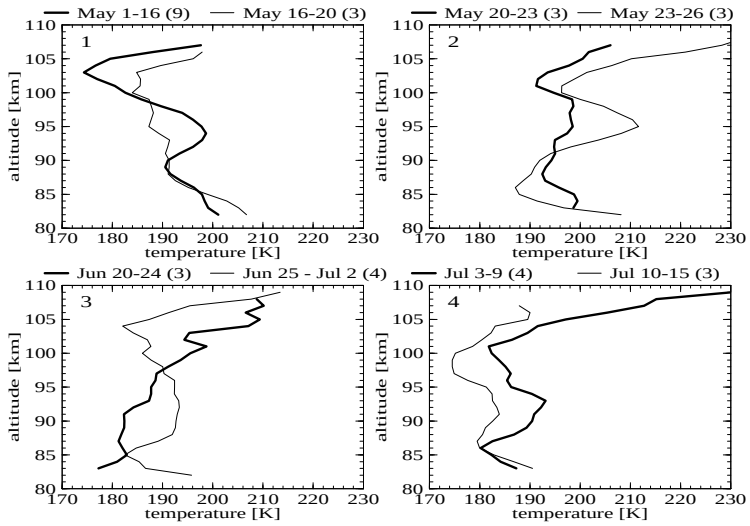

Figure 4.8: Development of the mean temperature profiles at 28°N (the number of nights is given in parentheses) during the campaigns in May (panels 1 and 2) and June–July (3 and 4). The bold line gives the earlier period in each panel. No nights are skipped. Values are only presented for altitudes where more than 50% of the nights contribute reliable data (from *Fricke-Begemann et al.*, 2002b).

upper minimum getting more pronounced and by the mid of July the regular state was reached again (panel 4). Thus, starting at the end of May (Figure 4.8, panel 2), the mesopause attained a low state at 86 km for about four weeks. The mean temperature of the low mesopause was 183 K. The transition periods between the regular and the low mesopause state lasted about two weeks each.

4.3.3 Discussion: Low Latitude Temperatures

In contrast to midlatitudes, there are few data from low latitudes that would be comparable to the measurements presented above. From a southern low latitude site, *Clemesha et al.* (1999) reported a mean temperature profile retrieved by lidar in late winter (July–October, 23° S). The mesopause was observed at 103 km with a temperature of 190 K. Apart from the slightly higher mesopause, this profile is in very good agreement with the winter profile (4) shown in Figure 4.7, suggesting hemispheric symmetry.

From Hawaii (20°N), *Leblanc et al.* (1998) have reported climatological temperatures extending up to 85 km (also at night), as measured by Rayleigh lidar. At this altitude they obtained an annual variation ranging from slightly below 190 K in summer to about 200 K throughout October–March. From Fort Collins (41°N), *She et al.* (2000) have reported monthly mean values at 85 km with annual extrema of 175 and 216 K in June and November, respectively. Also at this altitude, the seasonal variation of 38 K at 28°N, apparent in Figure 4.7, fills the gap quite reasonably and might be smoothed out a little if more extensive data sets would be available.

At the 100-km level, Tenerife sees only small seasonal variation around 190 K, as also similarly observed at midlatitudes. Over the full range of the K layer, all other seasons appear warmer compared with November which is the closest representation of winter conditions available at 28°N. This contrasts with midlatitudes (41° and 54°N), where from 100 km upwards the highest temperatures are observed in summer. Whereas the seasonal variation of UV

absorption by O_2 governs the temperature variation above 98 km at midlatitudes, it seems to be more constant at subtropical latitudes and subordinate to dynamical cooling.

Recently, *Friedman* (2003) has published a temperature climatology measured by potassium lidar at Arecibo (18°N) in 2001–2003. As expected, in summer the mesopause is found at the regular level (99 km). With $T = 176$ K it is about 5 K colder than the low mesopause at Tenerife and in good agreement with the results from the Polarstern. However, the seasonal variation was not expected which does not approve the anticipated year-round winter-like high mesopause. An annual variation by up to ±20 K with low temperatures in summer was found between 95 km and 103 km, i. e. above the altitude range where this type of variation is observed at midlatitudes. While this is in contrast to midlatitudes, a similar variation was observed at 28°N but with much smaller magnitude. In April at 18°N, a clear double structure was observed with relatively low temperatures ($\leq$185 K) at the lower minimum near 86 km. This is in good agreement with the results from our first campaign at 28°N (March–April), when also unexpectedly low values were measured at this level. Similar perturbations near the autumn equinox have been reported by *Taylor et al.* (2001) for 35° and 41°N. Possible reasons for this finding may be the tidal activity or planetary wave perturbations during the *springtime transition* (e. g. *Shepherd et al.*, 2002). Finally, in November the nearly isothermal profile at Arecibo agrees with Tenerife values below 90 km but the mesopause is about 20 K warmer. In summary, it appears that the temperatures above the low latitude sites at 28° and 18°N show a weaker agreement than it was observed for the potassium layer.

Empirical models of the atmosphere are a valuable tool for geophysical research, hence they need to be compared with measured data to check the accuracy of the model perceptions. For the mesopause region two classes of models are widely used. CIRA (COSPAR International Reference Atmosphere) comprises tables based on averages of global data compilations. Mass Spectrometer Incoherent Scatter Radar (MSIS-class) empiric models are described by analytic functions fitted to an extensive database. The MSIS-E-90 model (*Hedin*, 1991) gives, for the location of Tenerife at local midnight in mid November, the values for 200 K, 177 K and 200 K at altitudes of 85 km, 95 km and 105 km, respectively. While the value at the upper level is in agreement with the lidar data, the other model values are lower by about 20 K. Zonal/diurnal means are colder in 105 km (186 K) but unchanged at the lower levels. For July 1st, the model provides 186 K, 180 K and 205 K, respectively. These 0-LT values match our summer data (campaign 3) more closely but at the center altitude of 95 km they are again too low. The zonal mean values deviate at all levels in the direction that increases the differences to the lidar results. The situation in May and April is similar to summer solstice.

Picone et al. (2002) published the updated NRLMSIS-E-00 which does not include new data from the mesopause region but is different due to some changes in the model parameterization. Thus, the general discrepancies with the measurements are conserved. Changes appear mainly in the local time dependence, when compared with the previous version. Throughout the year, the 0-LT temperatures are now lower than the zonal means at 80–100 km for 28°N.

Temperatures in July from CIRA-86 (*Fleming et al.*, 1990) are a few degrees lower between 85 and 95 km and higher at lower altitudes, when compared with the MSIS-E-90 zonal mean. The values near 90–95 km of $\sim$180 K are again lower than the lidar results. For November CIRA-86 gives higher temperatures than MSIS-E-90 by up to 15 K between 90 and 105 km. Consequently, they are closer to the lidar measurements around 100 km (187 K) but again much too low around 90 km (191 K). In contrast to these discrepancies, it should be mentioned that below 80 km the empirical models are in much better agreement with the mean temperature profile (e. g. *She et al.*, 1995).

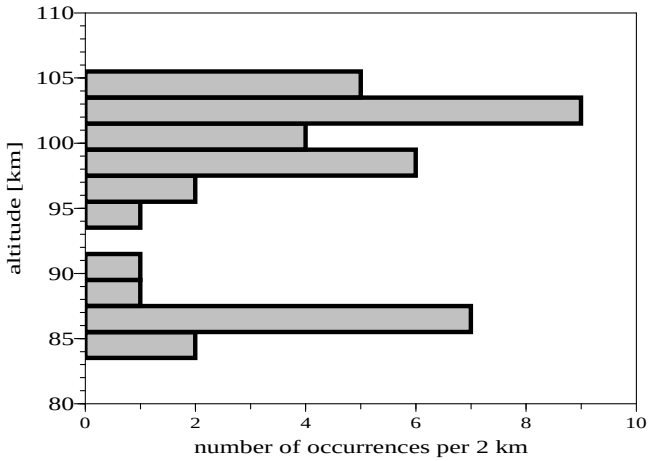

Figure 4.9: Similar to Figure 4.6 but for 28°N. Included are all observations from 1999 which covered more than 3 hours and showed the mesopause. From *Fricke-Begemann et al.* (2002b).

4.3.4 Discussion: The Two-Level Mesopause

Alongside the absolute temperatures, much attention has been attracted by the vertical temperature structure and the behaviour of the mesopause altitude. The seasonal and latitudinal two-level structure has been described above. At midlatitudes the mesopause occurs regularly near 100 km but for some period in summer it is located at 87 km.

For an overview of the mesopause altitudes above Tenerife, Figure 4.9 shows the occurrence frequency of the mesopause at each height. The altitude of the mesopause has been counted for 40 nights with observations lasting more than 3 hours. The mesopause is clearly appearing at two distinct levels only: a regular (high) level and a low level. Even though the bar chart in Figure 4.9 includes the observations from the transition periods, the mesopause is nearly never found in the intermediate range between the two levels. The histogram is in perfect agreement with that for Kühlungsborn (Figure 4.6), showing peaks near 101 km and 87 km. However, the relative occurrence at the upper altitude would be increased if the observations at Tenerife were distributed more evenly over the year. The agreement strongly supports the concept of the mesopause occurring worldwide at two altitude levels only. The mesopause altitudes at 28°N also agree with the observations at 41°N, where the mean altitudes were 101 km for August–April and 86.5 km for May–July (*She et al.*, 2000). The mean mesopause temperature for the lower state was ∼180 K. In November, the regular mesopause had a mean temperature of 192 K, which was only 2 K below our low latitude value.

As discussed by *She and von Zahn* (1998), the same two-level mesopause behaviour is observed for all latitudes away from the tropics, with a regular altitude around 100 km. The appearance of the low mesopause is summarized in Table 4.3. The low mesopause in summer was observed at Tenerife for about 4 weeks at 86 km. At 41°N *She et al.* (2000) observed the summer state for more than 3 months (early May to mid August) at 86.5 km. At Kühlungsborn (54°N) it occurs for the 4-month period May–August at 87 km. Numerous rocket measurements near 69°N, between late April and mid September, showed a low mesopause at 88 km from early May to early September, with temperatures as low as 129 K (*von Zahn and Meyer*, 1989; *Lübken*, 1999). Even at Svalbard (78°N) the same behaviour is apparent. While

Table 4.3: Low mesopause state in summer at selected northern latitudes, given are values for the averaged minimum temperature and the duration of the low mesopause state. Taken from tabulated monthly means (single stations) or contour plots (HRDI satellite data).

Latitude	z [km]	T [K]	Period	Day/Night	Reference
78°N	89	115	4½ mo.	• / •	*Höffner*, private communication
69°N	88	129	4 mo.	• / •	*Lübken* (1999)
54°N	87	162	4 mo.	– / •	this work
41°N	86	178	3 mo.	– / •	*She et al.* (2000)
41°N	87	173	2 mo.	• / •	*Chen et al.* (2000)
40°N	87.5	187	2 mo.	• / •	*States and Gardner* (2000a)
28°N	86	183	1 mo.	– / •	this work
18°N	(99)	—	—	– / •	*Friedman* (2003)
≥45°N	≥82	≤175	1 mo.	• / –	*Ortland et al.* (1998)
≥45°N	≥84	≤175	4 mo.	• / –	*Thulasiraman and Nee* (2002)

the temperatures there fall to nearly 115 K, the period with a low mesopause is of similar extent with 4½ months from the beginning of May until mid September. The altitude of the summer mesopause appears to be higher than 88 km, thereby continuing the weak increase of summer mesopause altitudes with latitude. As a minor difference to the idealized picture by *She and von Zahn* (their Figure 1), the period of existence of the summer mesopause increases only slowly from midlatitudes towards the pole.

At the tropical site of Arecibo (18°N) the mesopause is at its regular level during the whole summer (*Friedman*, 2003). However, the lowest temperatures were not always found near 100 km, but instead, around 93 km in February and 90 km in October.

The first temperature climatology based on diurnal mean lidar temperature profiles has been given by *States and Gardner* (2000a) for 40°N, thereby confirming the two-level behaviour with transitions lasting not more than a week. The low summer mesopause was found only in May and June with 186.6 K at 87–88 km but not in the July mean when the transition to the regular state occurred. Thus, the summer period was not symmetric to summer solstice. This agrees with the IAP measurements on Tenerife. The existence of the low mesopause state at 41°N is also found for 2 monthly means when daytime observations are included (*Chen et al.*, 2000), in comparison with 3 months for pure nighttime data (*She et al.*, 2000). On the other hand, the diurnal mean temperature of the low mesopause clearly deviates between the measurements at 40° and 41°N.

The worldwide appearance of two altitude levels is closely related to the double structure which appears with great regularity in the (nighttime) temperature profiles measured by lidar at mid and low latitudes. It has been linked in the literature to tidal variations, breaking gravity waves and chemical heating. The climatology at 54°N, given in Figure 4.4, does not exhibit a double structure due to the smoothing filter applied but it is weakly indicated even in the annual means. By contrast, a double structure is very prominent in many nights, especially in spring and autumn, as in the example from August given in Figure 3.8. Two minima at the altitudes of the regular and the summer mesopause are observed. The intermediate maximum in the height range 90–95 km is 30–40 K warmer than the minima in this example. At 41°N the double structure, by up to 5 K, is apparent in monthly means from spring and autumn (*Yu*

and She, 1995; *She et al.*, 2000). At 28°N it is clearly visible from all campaigns except for November (Figure 4.7). At 18°N a persistent double structure is observed from mid April until mid August. The persistence of this phenomenon provides that the mesopause rarely occurs in this intermediate altitude region between 90 and 95 km.

Satellite Measurements

Instruments onboard the Upper Atmosphere Research Satellite (UARS) have been used to derive temperatures from the MLT region. The High Resolution Doppler Imager (HRDI) measures the brightness of two rotational lines in the O_2 atmospheric band. *Ortland et al.* (1998) derived preliminary daytime mean temperatures from HRDI data for July 1993/94, with an estimated error of ±7 K. Their Figure 12 is reproduced here (Figure 4.10). The two-level structure is evident and between ∼10° and 45°N, a vertical double structure is observed. Contrary to our lidar measurements, the upper altitude minimum stays colder than the lower minimum until 40°N. At 30°N they show two minima at 98 km (173 K) and 81 km (187 K). The altitudes are lower than measured by lidar and the temperature of the upper minimum seems too low compared with our nighttime results (185 K). Towards polar latitudes the mesopause altitude increases in agreement with lidar and rocket measurements but at 69°N the mesopause temperature is too high by ∼15 K. Recently published data from the same instrument (*Thulasiraman and Nee*, 2002) have basically confirmed the earlier (preliminary) results. A low mesopause is apparent only poleward of 45° in the temperatures which are averaged over 4 months (May–August 1993). Near 30°N a constant temperature of 190 K is reported for 80–90 km and a mesopause with slightly less than 180 K at 97 km. The absolute values have come closer to the K-lidar. On the other hand, the newer data do not show the double structure which appeared in the July data (Figure 4.10), presumably due to the 4-month average. However, *Thulasiraman and Nee* also published equinoctial results, which show two local minima at various latitudes. The September values are especially close to the IAP lidar's spring profile, although the lower minimum is located further down at 80 km.

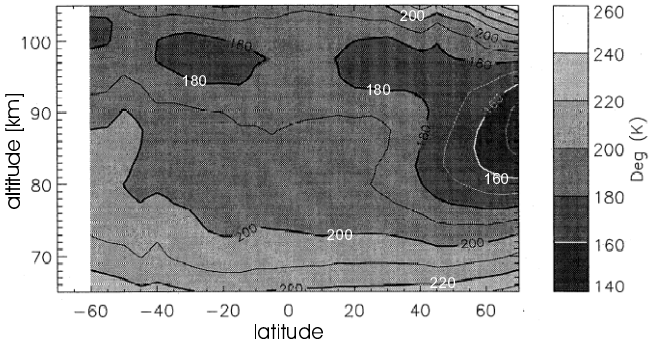

Figure 4.10: MLT temperatures at daytime for July from UARS/HRDI, taken from *Ortland et al.* (1998).

From the Wind Imaging Interferometer (WINDII) on UARS, *Shepherd et al.* (2001) derived temperature profiles up to 90 km. Data were retrieved in the latitudinal range of 25–35°N in July 1992/93 during the morning and afternoon hours. The temperature profile shows a minimum at 83 km of about 190 K (±10 K), which is slightly closer in height to the lidar-observed summer mesopause (86 km, 183 K) than the HRDI results.

The SME spacecraft measured temperatures up to 92 km at 14:00–15:00 LT (*Clancy et al.*, 1994). In November and April minima at 80 km with 200 K between 25° and 30°N were derived which deviate significantly from both lidar or UARS data. However, for July a minimum with 192 K at 84 km is reported which closely matches the lidar data.

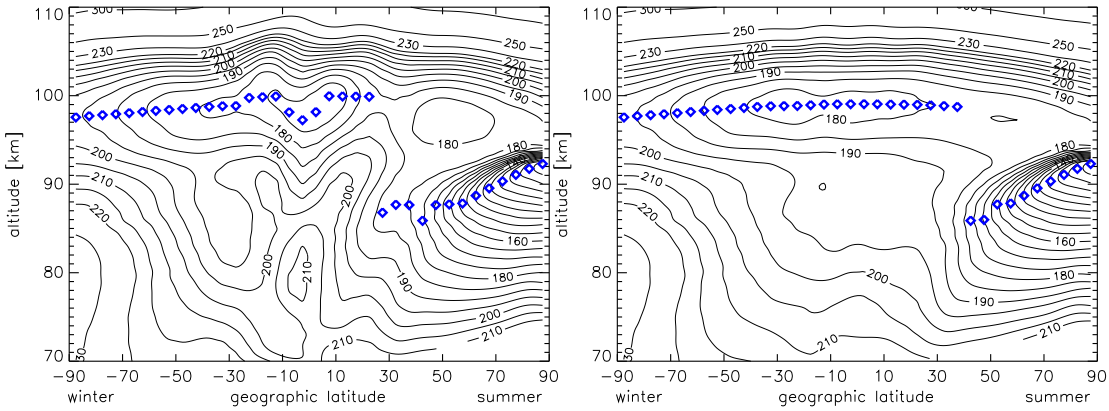

Figure 4.11: Mesopause temperature structure from the COMMA-IAP model (from *Berger and von Zahn*, 1999). Results are for June 21st, the mesopause is marked. Left: nighttime, right: diurnal mean.

Model Atmospheres

It has been pointed out in several works before that semi-empirical models do not include the observed global two-level structure of the mesopause. For subtropical latitudes, CIRA-86 gives a mesopause altitude that varies smoothly between 97 km in winter and 93 km in summer, thus, in a region where it is never observed. At midlatitudes in summer the mesopause is indicated lower and, hence, closer to the observations but the variation is again continuous in contrast to the abrupt transition measured. The recent MSIS version (*Picone et al.*, 2002, NRLMSIS-E-00) is similar to CIRA for 28°N when the zonal mean is considered and it predicts a nearly constant mesopause altitude of ∼97 km at midnight. The vertical double structure is also not represented for the mid and low latitudes at which it is observed. On the other hand, for 54°N the seasonal pattern is nicely reproduced, especially when nighttime (00:00 LT) values are considered. The mesopause is at ∼99 km in winter and ∼88 km in summer with transitions lasting only 4 weeks each in April and September–October. Even the local minimum in January–February is reproduced closely. The mesopause temperature values are not as close to the lidar climatology since they decrease to below 150 K on July 1st.

The first accurate representation of the mesopause region with a 3-dimensional general circulation model was achieved by *Berger and von Zahn* (1999) with the COMMA-IAP (COlogne Model of the Middle Atmosphere[1] at the IAP). Their results are reproduced here in Figure 4.11 showing the diurnal and a nighttime (22:00–04:00 LT) mean for better comparison with the lidar measurements. The authors were able to reproduce the mesopause behaviour at midlatitudes and predicted two nearly equivalent nighttime minima of ∼185 K at 87 and 99 km for June 21st and 28°N. This is in almost perfect agreement with our finding. At night the low summer mesopause is apparent at 30°N and higher latitudes, while for the diurnal mean, a regular mesopause is predicted until 40°N. This is in correspondence with both the UARS/HRDI and our lidar observations. Furthermore, the model exhibits an increase of mesopause altitude towards the summer pole which agrees also with the measurements. The representation of polar latitudes has been improved further in more recent versions of the model (*Berger and von Zahn*, 2002).

[1] For details on COMMA see also *Berger* (1994) and *Ebel et al.* (1995)

The causative mechanisms of the mesopause formation were studied by *Berger and von Zahn* (1999) in detail. They concluded that the dominance of IR cooling processes, in combination with the chemical heat release by the major reactions involving O, H, and O_3 in the 90 to 95-km region, is primarily responsible for the regular high-level mesopause. The low-level mesopause in summer is due to the momentum deposition by breaking gravity waves. The global two-level feature of the mesopause is mainly due to photochemical heating processes while diurnal tides play an important role in the formation of the double structure at low latitudes.

4.3.5 Concluding Remarks

It can be concluded that measurements by means of resonance lidars have provided an entirely new view of the temperature structure of the altitude region between 80 and 105 km. Lidar observations at locations from subtropical to very high latitudes have established the worldwide two-level characteristic of the mesopause. The results are partly supported by satellite measurements, but deviating findings also exist. The temperature data derived by lidar have stimulated new modelling efforts which have increased our understanding of the physical processes in the middle and upper atmosphere.

The main results derived during the work to this thesis can be summarized as follows. From three years of routine nighttime K-lidar measurements at Kühlungsborn (54°N) the low mesopause state is determined to exist for about 4 months around summer solstice when minimum temperatures of nearly 160 K are reached at 87 km. The IAP K-lidar measurements at Tenerife (28°N) in 1999 have revealed a seasonal two-level behaviour as seen at higher latitudes which is consistent with the earlier Polarstern results. In our nocturnal lidar observations the low mesopause state is characterized by an altitude of 86 km and a temperature of 183 K. This is similar in altitude and slightly warmer than at 41°N. The low mesopause state existed for about 4 weeks from the end of May until the end of June. In November we observed a regular mesopause with 194 K at 100 km.

The weak temperature gradient at low latitudes in summer, if combined with strong tidal wave activity, would allow for local time dependencies of the mesopause behaviour. Differences which concern the mesopause altitude and temperature have been identified between nighttime lidar and daytime satellite measurements. If the discrepancies are partly caused by diurnal variations remains to be evaluated. Hence, continuous observations over complete diurnal cycles are needed to derive the *true* (diurnal) mean temperature structure and its variations (cf. Chapter 5).

First 24-h lidar observations near 40°N (*Chen et al.*, 2000; *States and Gardner*, 2000a) have shown that the mean temperature of the low mesopause in summer might be underestimated by up to 5 K due to a lack of daytime measurements and that the double structure is less pronounced in diurnal mean profiles (see Section 5.4.2). Thus, the period of existence of the low mesopause state is restricted on a diurnal average but the altitude is unchanged. On the other hand, there is a large discrepancy between the two data sets giving annual temperature variations at 86 km of 21 K and of 9.5 K at 41° and 40°N, respectively. These values are smaller than the amplitudes derived at the same locations from the nighttime data, 24 K and 13.5 K, respectively.

With the COMMA-IAP model *Berger and von Zahn* (1999) were first able to represent the mesopause temperature structure at summer solstice conditions in agreement with the lidar observations, while empirical models are still unable to show the observed double structure.

Picone et al. (2002) were aware of the fact that the vertical double structure is not well represented in their MSIS model, although its formulation is sufficiently flexible to capture such structures. As they noted, the model provides primarily a smooth connection between the lower thermosphere and the region below 62.5 km due to a lack of data from the upper mesosphere. They explicitly called for a comprehensive database of 24-h observations of the mesopause region. Those can be provided increasingly in the near future by metal resonance lidars to improve the quality of the widely used empirical models.

Long-term variations of the mesopause temperature, including solar-cycle influences or general trends, could not be addressed so far. *She et al.* (2002b) observed a temperature increase at 98.5 km over Fort Collins (41°N) until December 2000 which they attributed to the 11-yr solar cycle. Especially after April 2000 they reported temperatures which exceeded the climatological mean by about 15 K. Although, in a more recent assessment of the data the increase was determined to be only about 8 K (*She*, private communication). A similar variation of the mesopause region temperature over Kühlungsborn should be observable with the IAP K-lidars also. The K-lidar measurements began after the solar minimum in June 1996 and no significant interannual variation has been observed since March 1999. As operation of the new instrument was sparse in 1999–2001, a temperature change during this period would barely be detectable. However, it has been noted that observations in 2002 and 2003 with the stationary lidar yielded, on average, higher temperatures than those from the late 1990s. This effect could partly be caused by a systematical difference between the two instruments. To allow a conclusive analysis a direct comparison of the two K-lidars after the return of the transportable system from Svalbard would be valuable.

Chapter 5

Diurnal Temperature Variations and Tides

The mean state of the mesopause has been discussed in the previous chapter together with its seasonal variation. However, the atmosphere is in a state of permanent perturbation by various waves. As the climatology given in Chapter 4 is based on nighttime observations only, it is necessary to understand the nature of diurnal temperature variations. Solar tides are the most profound and persistent perturbations of the large scale dynamics in the mesosphere and lower thermosphere. Due to their diurnal periodicity (periods of 24 h, 12 h, etc.), they may also cause a systematic difference of the atmosphere's state between night and day.

The topic of this chapter is the effect of tides on the temperature field of the mesopause region. The theory of tides has been discussed in detail in the literature (*Chapman and Lindzen*, 1970; *Forbes*, 1982a,b, 1995; *Lindzen*, 1990) and only the major characteristics are summarized below. In the following sections, different approaches to derive tidal information from lidar observations are assessed in case studies, exemplifying the importance and the potential of continuous measurements covering full diurnal cycles. Finally, the results are discussed in relation to other measurements and current state-of-the-art model predictions.

Tides

Atmospheric tides are global-scale waves with periods that are harmonics of a solar or lunar day. This work focusses on solar thermal tides, which are periodically forced by solar UV and IR radiation. In contrast to oceanic tides, solar and lunar gravitational tides are of minor importance in the atmosphere. The main excitation of thermal tides is due to absorption of solar radiation by H_2O in the troposphere, by O_3 in the stratosphere (and also at the secondary ozone maximum in the mesopause region) and by O_2 above 90 km.

Gravity is the restoring force of tidal waves and, thus, tides can be classified as a special group of gravity waves, with the distinctive feature that they are affected by the Earth's sphericity and rotation. Like other gravity waves, tides can propagate vertically and, if their energy is conserved, their amplitudes grow with increasing altitude as atmospheric density decreases. The dispersion relation of gravity waves provides that the vertical components of phase and wave (energy) propagation are of opposite sign.

The *classical* tidal theory (*Chapman and Lindzen*, 1970) describes atmospheric tides as eigenmodes of the Earth's atmosphere which are excited by periodic forcing. The tidal equation is separable for vertical and horizontal structure. For each period that is a subharmonic of a solar day, the eigenvalues determine the vertical wavelength and the eigenfunctions, known as Hough modes, describe the latitudinal structure (e. g. *Forbes*, 1995). The vertical wavelengths of the first three symmetric modes are $\lambda_{z,1} \approx 28$, 11 and 7 km for diurnal tides, and $\lambda_{z,2} \approx 311$, 54 and 33 km for semidiurnal tides. The actual values depend on the background temperature profile and the values given are for an isothermal atmosphere at 256 K (*Forbes*, 1995). In addition, for diurnal oscillations, *trapped* (or *evanescent*) modes exist, which cannot propagate vertically and appear with an infinite vertical wavelength. Coriolis forces inhibit vertical prop-

agation if the relevant wave frequency is less than the Coriolis parameter $f = 2\Omega\sin\phi$ (where Ω is the Earth's angular rotation rate and ϕ is latitude).

Propagating diurnal tides maximize at low latitudes. They are strong below 20° and near 30–40° whereas there are also nodes at 25–30° for the first four Hough modes. In contrast, trapped modes are concentrated at higher latitudes (above ∼50°). Semidiurnal modes, on the other hand, attain their maximum at middle to high latitudes. The degree to which the atmospheric response falls into either of these modes is determined by how well the horizontal and vertical structure of these modes match that of the forcing. The expansion of solar forcing via O_3 and H_2O into Hough modes shows that most of the diurnal forcing goes into trapped modes, while the semidiurnal proportion can effectively be stored in a single global mode (*Lindzen*, 1990). This yields an explanation for the dominance of the semidiurnal tide as it was measured in surface pressure oscillations, which were the first atmospheric tides to be observed in the late eighteenth century (e. g. *Cartwright*, 1999).

The classical tidal modes describe *migrating* tides which propagate westward with the apparent motion of the sun and, thus, occur with a constant phase in local time at every location on a circle of latitude. In addition, so-called *non-migrating* tides exist whose horizontal (westward) wavenumbers deviate from their frequencies in cycles per day. The term non-migrating tides may be misleading as they can be standing or propagating around the Earth, eastward or westward, but distinct from the apparent motion of the sun. Thus, they are also called non-classical or not sun-synchronous. Since the tropospheric forcing is to a high degree not zonally symmetric, it is believed to be the major source for latitudinal differences and non-migrating tides. Other sources, like non-linear interactions between migrating tides and stationary planetary waves in the middle atmosphere, are also discussed in the literature (e. g. *Forbes et al.*, 2003).

Observations and Modelling

Groundbased remote sensing instruments measure temporal fluctuations of atmospheric parameters, which are caused by the full spectrum of atmospheric waves. Variations which are coherent over a sufficiently long time interval and exhibit periods of 24, 12, 8, or 6 hours are associated with tides. They represent the local superposition of migrating and non-migrating tides. These are distinguishable only by their longitudinal structure which can be obtained from networks of groundbased instruments or spaceborne experiments. In contrast, satellites provide a limited local time coverage and, hence, a combination of both techniques is desirable.

Tides have to a large extent been studied with mechanistic and general circulation models (GCMs) since the development of the classical theory (see *Forbes*, 1995; *Cartwright*, 1999; *Hagan*, 2000). Modelling the tidal structure of the mesopause region at midlatitudes is especially complicated as propagating and trapped modes are of comparable importance (*Forbes*, 1982a). The tidal components of horizontal wind oscillations in the MLT region have been studied experimentally for decades using radars. Additionally, spaceborne wind observations have increased in recent years and provide tidal information. Subsequently, models have been improved and tested on the representation of tidal winds and, today, they are found to give increasingly reasonable predictions of the wind observations (e. g. *Manson et al.*, 2002; *Pancheva et al.*, 2002; *Forbes et al.*, 2003). As horizontal winds are controlled by different modes than temperature and vertical wind, no close correlation between their amplitudes and phases is expected. Therefore, tidal perturbations of the temperature have to be considered independently.

Compared with wind observations, only very limited temperature data from the MLT region

are available. Groundbased airglow and lidar studies have long been restricted to nighttime and did not allow complete sampling of tidal structures. Thus, diurnal tides had to be excluded from the analysis. Since metal resonance lidars have first been upgraded for daylight operation, a few initial studies using diurnal observations have been carried out (*States and Gardner*, 2000b; *She et al.*, 2002a). Correspondingly, the following analysis begins with the nighttime lidar measurements for which a large database exists at the IAP before cases of daytime observations are discussed. Monthly mean nighttime temperature variations at 54° and 28°N have been analysed by *Oldag* (2001) to investigate the seasonal variation of tidal activity. In this work, parts of the data are evaluated again with an extended methodology in preparation for the assessment of diurnal variations.

5.1 Tidal Analysis of Nighttime Measurements

5.1.1 Derivation of Tidal Parameters

In the previous chapter only nightly mean temperature profiles have been used but, in fact, the atmosphere is far from adopting a constant temperature profile. The potassium lidars detect strong perturbations in almost every measurement. Temperature values used below are derived at intervals of 15 min and 1 km from photon count profiles which are integrated over 1 h and 2 km. An example for the observed variations is shown in Figure 5.1 (panel 1). The colour contour plot shows the deviations from the mean temperature profile for the night of the $10^{\text{th}}/11^{\text{th}}$ of November, 1999, at Tenerife (28°N). Deviations up to ±25 K are observed with regular patterns progressing downwards. Such strong variations are not exceptional in the mesopause region and are also seen at other lidar stations. Even variations over twice this range have been observed on single occasions at low and midlatitudes (*Oldag*, 2001; *Williams et al.*, 2002).

Perturbations can be caused by various wave phenomena. Solar tides can be extracted as they have constant phases, i. e. the temperature maximum appears on every day at the same local time in a given altitude. Thus, by averaging over a number of nights with respect to local time (LT), most incoherent gravity wave effects are smoothed out and the tidal signature remains. This is exemplified in panel 2 of Figure 5.1 using all 12 nights with more than 2 hours of measurements from November 1999 at Tenerife. The temperatures at each height and local time are averaged and the altitudinal means are subtracted to derive the *mean LT variation.* A wave structure becomes clear with a separation of about 6 h between minima and maxima. Deviations of nearly 20 K are still present. Due to varying potassium occurrence and weather conditions, only a few nights contribute to the composite at the upper and lower edges, causing a large scatter in the mean variation.

To derive tidal parameters a series of harmonic functions is fitted in a LMS sense to the mean LT variation in each altitude (see Appendix C.1 for details):

$$\tilde{T}(t) = A_0 + \sum A_i \cos(\omega_i (t - \phi_i)) \,, \qquad \text{with} \quad \omega_i = 2\pi i / 24\,\text{h} \,. \tag{5.1}$$

For the constant periods $2\pi/\omega_i$, the fit provides amplitude A_i and phase ϕ_i, which is the local time when the maximum temperature occurs. The LT values are weighted with the inverse square root of the number of contributing nights and used only when at least 25% of the nights provide data.

For nighttime measurements covering about 12 hours, only semidiurnal (SD) and terdiurnal (TD) harmonics can be fitted reliably but the diurnal harmonic has to be excluded. The different

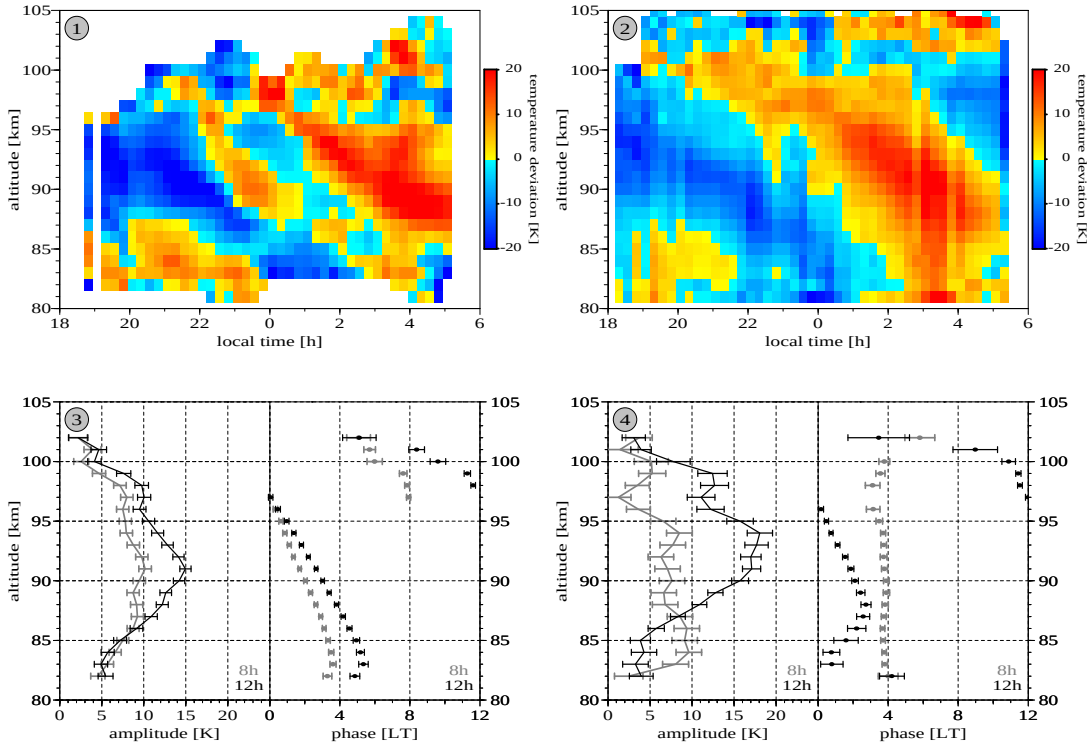

Figure 5.1: Temperature variations at Tenerife (28°N) in November 1999: (1) Deviation from the mean profile during a single night (Nov. 10th/11th). (2) Mean LT variation for all nights with $\geq$2 h of observations. (3) Amplitudes and phases from two separate harmonic fits, and (4) from a combined fit of 12-h and 8-h harmonics.

harmonics are not independent from each other and, hence, combined fits in the sense of Eq. 5.1 will deviate from separate fits of the individual harmonics (see Appendix C.1). The significance of the results from different harmonic analyses is briefly considered below. The results of separate fits of single cosine functions, with either an 8-h or 12-h period, to the mean variation are shown in panel 3 of Figure 5.1 and resemble closely the results of *Oldag* (2001). The parameters from the two fits exhibit a strong similarity, although the SD amplitude reaches 15 K and the TD amplitude reaches only 10 K. The phases of both harmonics follow the downward propagating pattern which is obvious from the contour plot over the whole altitude range. At midnight a maximum is displayed at 97 km and a minimum at 83 km (panel 2). Each of the separate fits represents a vertical wavelength of $\sim$30 km, causing different phase propagations. An inspection of the residual temperature variations after subtraction of the fitted harmonic (not shown), reveals remaining systematic structures. Thus, a single harmonic cannot represent the complete mean LT variation. This is in agreement with the results of *Oldag* (2001) who analysed monthly mean variations from the IAP K-lidars at Tenerife and Kühlungsborn and found that single tidal harmonics can explain about half the variation observed.

To extend the analysis, a combined fit of a sum of SD and TD harmonics (as in Eq. 5.1) is applied to the mean deviation and the results are given in panel 4. The enlargement of the error bars reflects the added degrees of freedom of the fit algorithm. Phase information is given only when the amplitude deviates significantly from zero. The SD component remains

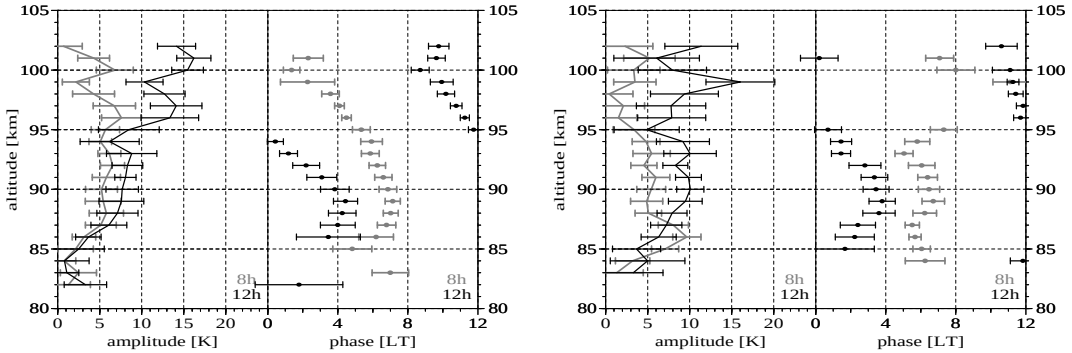

Figure 5.2: Amplitude and phase profiles from a combined fit of 12-h and 8-h harmonics to the mean nighttime temperature variation at Tenerife in May 1999 (left) and June/July 1999 (right).

similar as before though its amplitude is further increased above 90 km. The TD component becomes dominant below 87 km and decreases towards higher altitudes. Surprisingly, the TD phase is constant over the full altitude range while the SD tide turns out to be responsible for the apparent downward phase propagation above 87 km, where it is the stronger component. The SD wave (energy) propagates upward with a vertical wavelength $\lambda_{z,2} \approx 35$ km, denoting a forcing at lower altitudes.

How closely the fit represents the data can be described by the standard deviation σ_{dT} of the residuals after subtracting the fit function. Averaged over the altitude range 85–100 km, the SD oscillations fit the data reasonably well and reduce σ_{dT} to 3.7 K from an original value of 8.6 K for the data. The TD fit alone is clearly a worse representation of the measurements with $\sigma_{dT} = 6.7$ K, whereas the combination deviates only by $\sigma_{dT} = 2.5$ K, which is mainly due to non-systematic fluctuations. Including an additional 24-h or 6-h harmonic into the fit function $\tilde{T}$ does not lead to a closer representation of the data. Nevertheless, there may be contributions of other harmonics which would bias the results. Using a combined 24-h and 12-h fit (not shown) and accepting the very large error bars, the results are very similar to those shown in panel 4 with A_1 replacing A_3, a diurnal phase of $\phi_1 \approx 0$ h for all altitudes and a slightly reduced wavelength of $\lambda_{z,2} \approx 30$ km. The phase opposition between ϕ_1 and ϕ_3 agrees with the simulation discussed in the appendix (Figure C.1).

In summary, the results given in panel 4 show the stability of the fit function with 2 harmonics. Whereas separate fits interpret the same variation in two different ways, the combined fit can be expected to give the most reliable results when about 12 hours of data are available. The fit values, especially for the TD harmonic, may be influenced by a diurnal tide, though.

5.1.2 Tidal Parameters at Tenerife for Different Seasons

From Tenerife, sufficient data to derive the nightly mean LT variation are also available from the two campaigns of nearly 4 weeks in May and June/July 1999. While the period of darkness lasts about 11 hours in November, it is 8 hours near summer solstice. While this is enough for a separate fitting of individual harmonics, the combined fit of SD and TD components is vulnerable to producing artificial results and has to be inspected carefully.

The results for the two campaigns are shown in Figure 5.2 and exhibit major similarities,

which are presumably characteristic for the time around summer solstice. The SD component is dominant over the whole altitude range. Its amplitude increases from $A_2 < 5$ K below 86 km to 10–15 K near 100 km. The SD phase ϕ_2 shows a downward propagation only above 90 km, being slightly slower than −2 km/h, which is equivalent to a vertical wavelength of $\lambda_{z,2} =$ 20–25 km. For the TD component, the fit gives $A_3 \approx 5$ K in the range of 85–95 km and less below and above. The TD phase behaviour is clear only in May with a downward propagation of about −2.5 km/h above 90 km. The higher phase velocity is associated with the same wavelength as for the SD.

When the results for November (Figure 5.1, panel 4) are compared with those for May–July, the higher amplitudes of up to $A_2 = 20$ K and $A_3 = 10$ K are noticeable. The SD amplitude A_2 decreases above 95 km in November while it increases with altitude of the whole range in May–July. The phase speed of both components tends to be lower in summer than in winter and the maximum occurs at a later local time around 90 km. The enlarged error bars reflect the shorter observation periods in summer which complicate the combined 12-h and 8-h fit. Compared with the separate fits (see *Oldag*, 2001), the surprisingly close agreement between the SD and TD components is reduced. The increase of the TD amplitude with height is no longer present, while the SD amplitude remains relatively unchanged.

5.1.3 Tidal Parameters at Kühlungsborn in Winter

In Kühlungsborn (54°N), temperature measurements are possible for up to 14 hours without daylight capability in winter. The temporal coverage is drastically reduced during other seasons (cf. Figure 4.1) and does not allow reliable simultaneous fits of SD and TD components. During winter, data from individual months are rather sparse and unevenly distributed. Due to the high variability of the atmosphere, a reduction to coherent tidal signals is not assured and single nights could have a large influence on the fit results. As discussed by *Oldag* (2001), a similar phase characteristic is observed for the winter months. This finding is consistent with that for semidiurnal wind tides at this latitude (*Jacobi et al.*, 1999). Hence, from the winters of 1997 to 1999 all nights with more than one hour of observation from December, January and February (DJF) are combined. This DJF mean includes 7, 12 and 7 nights, respectively, from the individual months. On average, these nights contain nearly 8 hours of observation.

The mean LT variation of the temperature and the results from combined SD and TD fits are given in Figure 5.3. As in the previous case, a warm period is clearly visible which propagates downward during the night (located at 90 km near local midnight). Below 90 km, positive temperature deviations from the mean profile are also found at the beginning and the end of the average night. The cold-to-warm transition before midnight and the warm-to-cold transition after midnight exhibit different propagation rates. Consequently, the TD component dominates the fit results in the lower part of altitude range while the SD component is stronger above it. Thus, the downward progression of the warm period is reflected mainly by the TD harmonic in the lower part and by the SD harmonic in the upper part of the altitude range. The resulting phase speed of the dominant component is about 5–6 km/h in each height range and the phases connect smoothly at 23 h at 92–93 km. Thus, above 91 km the SD wavelength is $\lambda_{z,2} =$ 60–72 km. The SD harmonic shows a phase jump at 91 km and the TD harmonic shows one at 95 km. The phase behaviour indicates the influence of another wave and simulations have shown that a propagating diurnal tide could have caused it.

The DJF mean smoothes out intraseasonal variability. When compared with the fit results for individual months and periods (*Oldag*, 2001), the SD component in the DJF mean is in rela-

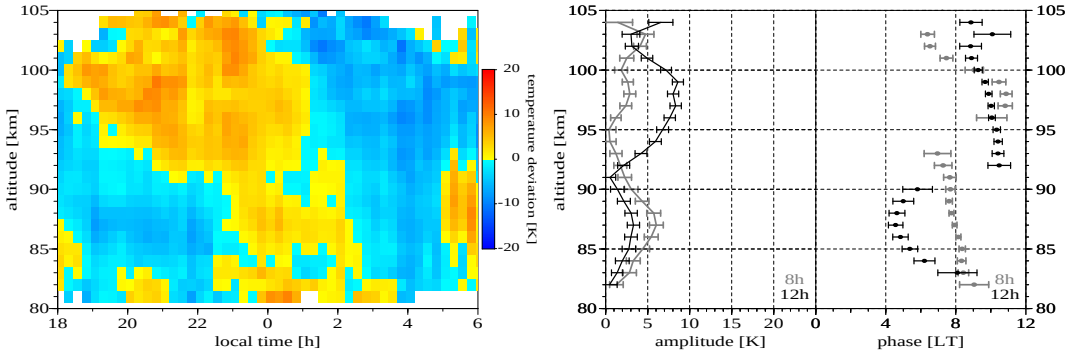

Figure 5.3: Mean temperature variation (left) and results from a combined fit of 12-h and 8-h harmonics (right) for nighttime observations at Kühlungsborn in winter (DJF97–99).

tively close agreement with the results for December and January, although in January slightly lower amplitudes are found at 95–100 km. In February, between 85 and 90 km, SD amplitudes reach 10 K which is the threefold value compared with those shown in Figure 5.3. The longest vertical SD wavelength during this period was observed in December with $\lambda_{z,2} = 44$ km, which is still less than the DJF result. The TD component tends to be weaker in the combined DJF fit than in the individual analyses. For all months, in the individual fits the behaviour of the SD and TD phase is very similar and it is resembled in the combined calculation (Figure 5.3) by the stronger component in each altitude.

5.1.4 Discussion

Pure nighttime results from the lidar measurements have been used to derive tidal parameters in this section. While the results are assessed only briefly below, a detailed discussion follows in Section 5.4. Due to the limited observation period, the diurnal tide cannot be determined but it may cause spurious effects on the higher harmonics, as exemplified in Figure C.1, and indications for such an influence have been found. Although results from combined fits should be considered carefully, it has been demonstrated that individual fits cannot provide reliable tidal information. This is because they are not independent from each other but both of them tend to reproduce the dominating wave pattern.

In general, reduced magnitudes of the temperature variations in winter at 54°N (DJF) in comparison with 28°N (November) are evident. The relation between the SD and TD components is similar at both latitudes. The TD is stronger below 90 km than the SD in all data sets, except for May at 28°N, when both were equally as small. The appearance of the temperature maximum was a few hours later at Tenerife and its propagation speed was similar at both locations.

Autumn transitions between summer and winter tidal patterns can occur as late as November at midlatitudes (e. g. *Gille et al.*, 1991; *Williams et al.*, 1998; *Jacobi et al.*, 1999). The transition periods are associated with small SD tides of horizontal winds. Since a strong SD tide was observed at Tenerife in November 1999, it can be assumed that the observations were carried out after the autumn transition and that the winter tidal pattern was observed.

Lidar temperature measurements at night in Fort Collins (41°N) were analysed by *Williams*

et al. (1998). In agreement with the results from 54°N they found similar behaviour for the winter months and provided results for a mean data set from November to March. Fits of SD harmonics determined increasing amplitude with height, with $A_2 = 8$–9 K between 90 and 100 km, i. e. a magnitude which ranges between those for 28° and 54°N. With a downward propagating phase yielding $\lambda_{z,2} = 30$ km and $\phi_2 = 0$ h at 97 km, the phasing is in perfect agreement with our results from Tenerife. For summer (May–August) at 40°N, reduced amplitudes ($A_2 \leq 5$ K) below 100 km and a similar phasing with $\lambda_{z,2} = 35$ km were found which is also in agreement with our results from 28°N.

In summary, a clear downward propagating SD tide (with $\lambda_{z,2} = 30$–35 km in winter) is observed in the mesopause region temperatures at all stations. It decreases with latitude and is weaker in summer than in winter when A_2 can exceed 10 K.

The terdiurnal tide has been deduced with considerable amplitude from potassium and sodium lidar measurements. The existence of a TD wind tide has been shown by *Smith* (2000), and 8-h temperature oscillations have also been identified in nighttime airglow measurements at midlatitudes (*Wiens et al.*, 1995; *Pendleton et al.*, 2000). From the Tenerife data, TD phases with no vertical propagation are derived but classical tidal theory predicts trapped modes only for the 24-h components. Thus, the TD parameters are possibly influenced by the diurnal tide which cannot be identified on the basis of pure nighttime measurements.

5.2 Combination with WINDII Measurements

Temperature measurements in the mesopause region at daytime are possible with spaceborne experiments. The Wind Imaging Interferometer (WINDII) onboard the Upper Atmosphere Research Satellite (UARS) can measure temperatures at altitudes between 65 and 90 km (*Shepherd et al.*, 2001). To derive temperature variations over complete diurnal cycles WINDII data can be combined with the potassium lidar results. This approach has been discussed in detail by *Shepherd and Fricke-Begemann* (2004) and is represented here in summarized form only.

WINDII derives mesospheric temperatures from Rayleigh scattered sunlight via the density scale height. Observations on a latitude circle change in local time by $\sim$20 min for consecutive days. Daily zonal means provide single local time values and a period of 36 observation days is required to achieve full local daytime coverage (06:00–18:00 LT). Hence, day-to-day variations in background temperature will appear as changes with respect to local time. Successional 36-day periods are usually not obtained due to the observation schedule and, in practise, composites of several months or years have to be used. Even then, gaps in local time remain and the data associated with different local times originate from different periods of observation. This may cause a spurious local time dependence and a large scatter of the data when compared with a groundbased system which covers the complete range of local times during each night. To reduce influences from year-to-year variations, the annual mean is subtracted from the WINDII data and the residuals are averaged in local time. WINDII temperature data were available from the years 1991 to 1997. For comparison with the lidar measurements, latitude ranges of 10° centered at 28°N and 55°N were used. Due to the small vertical overlap, no combined profile could be retrieved and the study was restricted to the altitude of 89 km.

A geophysical difference between lidar and satellite observations lies in the representation of non-migrating tides. While the lidar, at a fixed longitude, measures the local tidal activity without distinction between migrating and non-migrating tides, the satellite provides zonal averages which represent only the migrating components. The magnitude of non-migrating

Table 5.1: Semi- and terdiurnal fit results for 89 km at 28°N derived separately for K-lidar and WINDII data. Also given are the number of observations and the mean temperature T_0 for each data set.

Month	Instrum.	Obs.	A_2 [K]	ϕ_2 [h]	A_3 [K]	ϕ_3 [h]	T_0 [K]
Nov.	K-lidar	12	13.0 ±0.9	2.4 ±0.2	7.1 ±1.5	4.0 ±0.2	219.5
	WINDII	38	7.4 ±2.5	1.2 ±0.0	3.8 ±0.3	6.1 ±0.9	210.0
May	K-lidar	18	7.8 ±4.3	4.6 ±1.0	5.8 ±3.3	7.3 ±0.6	194.5
	WINDII	60	5.4 ±0.3	9.7 ±0.4	8.5 ±1.1	4.2 ±0.1	199.1

components and their influence on the lidar data is not known. Model simulations (discussed in Section 5.4.5) have estimated significantly lower amplitudes for the non-migrating than for the migrating components, but data are scarcely available. *Pancheva et al.* (2002) combined wind measurements in the 90 to 95-km region from 22 radar instruments. For northern midlatitudes in summer they derived a longitudinal amplitude variation of ±30% and 35% for diurnal and semidiurnal tides, respectively. From HRDI daytime data, *Talaat and Lieberman* (1999) deduced that non-migrating temperature tides in the mesopause region possess significant amplitudes, e. g. at 27°N in November the strongest diurnal mode peaks at 85 km with 4 K.

Though being aware of these complications arising from the combination of data from two totally different instruments, it is believed that the following approach is justified by the scarcity of measurements covering complete diurnal cycles. Before measurements are combined they are considered independently to assess their comparability.

Low Latitude Measurements

Temperatures from WINDII between 23° and 33°N were obtained between 1992 and 1996. Thus, no simultaneous observations with the K-lidar at 28°N are available. K-lidar and WINDII results from combined fits of 12-h and 8-h harmonics are given in Table 5.1. The lidar data reproduce the results from the previous section for 89 km. Marginal deviations are due to the different binning in local time which was changed to match the 30-min grid of the WINDII data.

In November both instruments see a dominantly strong semidiurnal and a weaker terdiurnal oscillation. Both amplitudes are significantly weaker for the satellite data, while relatively small deviations are found for the phases. This suggests that amplitudes are reduced in the satellite data by smoothing out latitudinal differences, year-to-year variations or non-migrating components.

In contrast, diverging parameters for May are derived from the two data sets with almost opposite phases. While the amplitudes deviate by 2–3 K, it should be noted that they agree within the relatively large uncertainties and that the sum of the two amplitudes is nearly identical for both instruments. Large amplitude errors show that the temperature variation cannot be attributed unambiguously to either of the two harmonics. This could result from the short period of darkness in summer or the presence of another oscillation like a diurnal tide. The semidiurnal tide is found to be less prevalent in May than in November. The mean temperatures T_0 of the individual data sets deviate by 5–10 K. It is not possible to decide if this is due to instrumental bias, day-night difference or geophysical variation of the background temperature.

Table 5.2: Semi- and terdiurnal fit results, as in Table 5.1, but for winter (DJF) at 55°N.

Instrument	Years	Obs.	A_2 [K]	ϕ_2 [h]	A_3 [K]	ϕ_3 [h]	T_0 [K]
K-lidar	97–99	26	2.2 ±0.8	5.1 ±0.6	4.3 ±0.8	7.7 ±0.2	207.7
WINDII	96–97	56	6.7 ±2.0	9.6 ±1.4	0.4 ±4.1	5.4 ±4.7	206.9

Midlatitude Measurements

For the winter months from 50° to 60°N, WINDII data have been analysed in the work of *Shepherd and Fricke-Begemann* (2004) building three consecutive 2-year composites from 1992 to 1997. The derived harmonic fit parameters exhibit a large variability with amplitude ranges of $A_2 = 3.5$–6.7 K and $A_3 = 0.4$–4.6 K. For the last data set (DJF96–97), which overlaps in time with the lidar measurements, the strongest SD component is derived with an almost opposite phase to the previous years, while the weak TD is insignificant (Table 5.2).

The K-lidar measurements at Kühlungsborn (54°N) in winter have provided a 3-year and 3-month composite (Section 5.1.3). In comparison with the lidar observations of a single month and year at Tenerife, this composite is presumably less influenced by non-migrating components, because these are expected to vary strongly from year to year and average out. In the lidar data the TD is stronger than the SD contribution, both with small uncertainties, and ϕ_2 is also significantly different from the satellite results for DJF96–97. It is interesting to note that the added amplitudes are again practically the same for WINDII and K-lidar data. The different contributions to the harmonics may be due to a diurnal component which cannot be accounted for here. Inspection of the data shows, that 46% of the lidar observations are from January, whereas WINDII measurements were mostly carried out in February (52%). Since the lidar results from the individual months have shown the strongest SD and the weakest TD harmonic in February, this yields another possible explanation for the difference.

In comparison with the low latitude data, the agreement of the individual tidal fits is not superior in this case in spite of the temporal overlap between WINDII and lidar data. Some parameters even agree better with the results from other 2-year data sets. On the other hand, the mean temperatures T_0 are nearly identical in this case. The T_0 differences between lidar and satellite at 28°N are within the variability range which is given by the WINDII 2-year data sets at midlatitudes, suggesting that they cannot be interpreted as systematic day-night differences.

5.2.1 Approach to Diurnal Tidal Components

Separate analyses of the temperature measurements from the two different instruments have shown certain agreements and differences. Their cause cannot be addressed unless the influence of the diurnal tide is considered. The diurnal tide can be deduced only from temperature data covering almost full diurnal cycles, as has been discussed earlier. This possibility is offered by the combination of lidar data from the nighttime and satellite data from the daytime.

For this combination, the residual temperatures (deviations from the mean) from each instrument have to be used to prevent the differences in absolute temperature causing an alias in the diurnal behaviour. Possible causes for such differences are numerous, including instrumental offsets, geophysical year-to-year variations or longitudinal dependencies, but also, systematic day-night differences. The joined data are fitted with a combination of the first three diurnal harmonics (24-, 12-, and 8-h periods). The resulting fit functions are shown together

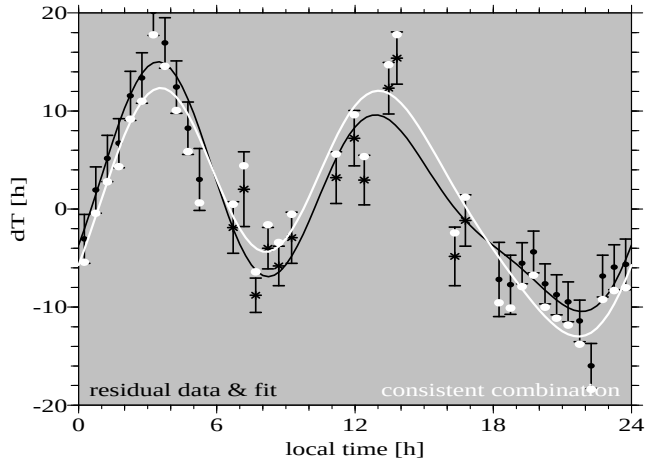

Nov, 28°N

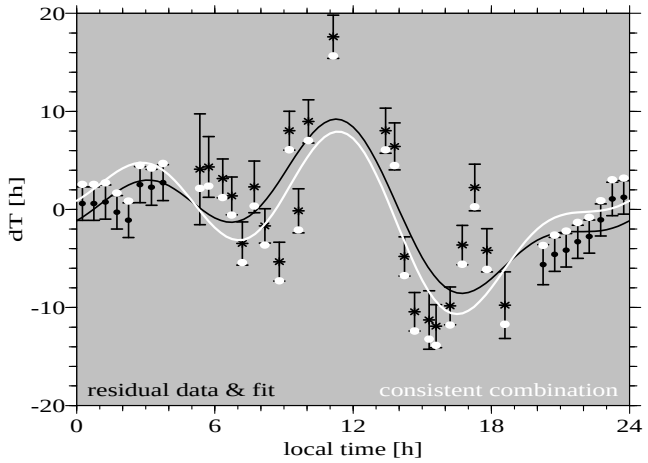

May, 28°N

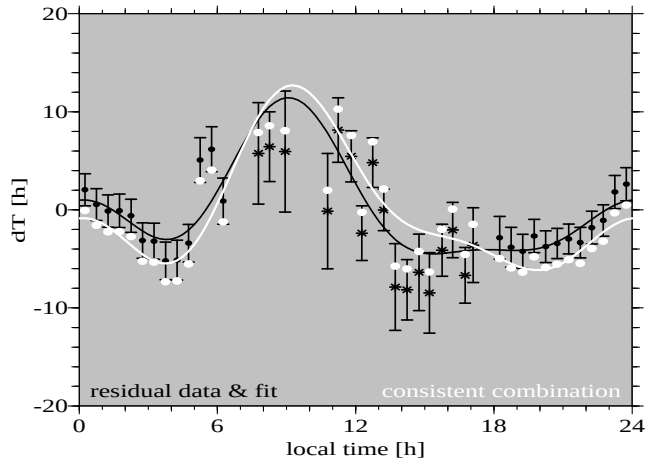

DJF, 54°N

Figure 5.4: Combined residuals (black) of K-lidar (circles) and WINDII (stars) temperatures at 89 km with tidal fit (solid). For the consistent combination (white) error bars are omitted for clarity. Fit parameters are given in Table 5.3.

Table 5.3: Tidal fit results for the first three diurnal harmonics of the combined data at 89 km from Tenerife (November and May) and Kühlungsborn (DJF). The lower part gives the result for the consistent combination with the total offset $\Delta T = \Delta T^N - \Delta T^D$ between the residuals (see text for details).

		A_1 [K]	ϕ_1 [h]	A_2 [K]	ϕ_2 [h]	A_3 [K]	ϕ_3 [h]	ΔT [K]
Nov.	28°N	4.5 ±0.4	7.6 ±0.5	8.8 ±0.6	2.7 ±0.2	4.1 ±0.8	3.7 ±0.1	
May	28°N	4.5 ±0.3	7.8 ±0.5	3.9 ±0.5	11.6 ±0.2	2.9 ±0.3	3.6 ±0.3	
DJF	54°N	5.2 ±0.4	8.1 ±0.6	4.2 ±0.5	9.7 ±0.5	2.3 ±0.7	0.8 ±0.1	
Nov.	28°N	6.5 ±0.4	9.3 ±0.7	8.8 ±0.8	2.7 ±0.1	3.2 ±0.4	3.8 ±0.3	-4.8
May	28°N	4.0 ±0.3	5.8 ±0.5	4.6 ±0.5	11.7 ±0.2	3.5 ±0.3	3.7 ±0.3	+3.9
DJF	54°N	6.5 ±0.3	9.5 ±0.6	4.1 ±0.4	10.0 ±0.2	2.6 ±0.8	0.7 ±0.1	-4.3

with the data in Figure 5.4 (black). A good local time coverage is achieved with the joined data sets and the fits give a close reproduction of the systematic variations. One also notes the relative large scatter in the WINDII daytime data that has been discussed above. The transition between the individual data sets is remarkably unobtrusive, considering the range of variations in the data. The fit parameters are listed in Table 5.3, now including amplitude A_1 and phase ϕ_1 of a 24-h harmonic. In all three cases, the diurnal amplitudes lie in the same range as the components considered previously. Although the number of fit parameters is increased, they are derived with much less uncertainty (below 1 K and 1 h, respectively) than in the fits of the individual data sets.

The November data from 28°N show two clear temperature maxima in the early morning and afternoon hours, resulting from a strong semidiurnal oscillation. Its amplitude ($A_2 = 8.8$ K) lies between the values derived separately from lidar and WINDII data, and the same holds for the terdiurnal component. While the amplitudes are closer to the smaller WINDII values, the phases are closer to the lidar results. The diurnal component is about equal in strength to the terdiurnal and has its maximum in the morning ($\phi_1 = 8$ h). For May, the diurnal fit parameters are very close to those from November. The higher harmonics in this case have a reduced magnitude compared with those derived before with considerable uncertainty. The phases from the joined data are closer to those from WINDII data alone. For the time around winter solstice and 50–60°N, the diurnal tide is derived from the joined data with surprising similarity to the low latitude cases. The parameters of the higher harmonics are close to the mean values of the individual analysis.

Consistent Combination

Although the data combinations look reasonable, one needs to consider a disadvantage of the usage of residual temperatures. The residuals have been calculated separately for both instruments. Combining them into one data set inevitably includes the assumption that the mean background temperatures are equal for both observations. This is not necessarily true when systematic differences between day- and nighttime exist. Diurnal variations are determined in the fit procedure and, thereby, the result may become inconsistent with the implicit assumption of the combination. As discussed in detail in Appendix C.1, with the so-called *consistency test*, a novel method was developed which provides an offset between the two data sets and fit parameters which are consistent with each other. In an iterative procedure, the offset is derived

from the fit results and the fit is recalculated. The terdiurnal component is of minor importance for the offset but it was found to be very sensitive to a large scatter of the data and the relative uncertainties assigned. Thereby in one case, results which are considered unrealistic were derived and, thus, the TD component is not included in the consistency test. The test is performed with 24-h and 12-h components only and afterwards all three harmonics are fitted to the derived combination.

Offsets up to 5 K are calculated and amplitudes have changed by up to 2 K in the consistent combination, as shown in Figure 5.4 (white). As apparent from the fit results given in Table 5.3, the SD components are basically conserved as was expected. The TD components are slightly varied in their strength but not in their phase. It has been expected that the combination of residuals partly smoothes out the diurnal oscillation and, in fact, the diurnal tide is estimated to be stronger in the autumn–winter months, whereas for May (28°N) mainly ϕ_1 has changed. Interestingly, the November (28°N) and DJF (54°N) diurnal tides are again estimated to be identical. The diurnal tide is found to dominate at midlatitudes while the semidiurnal does so at low latitudes. For May at 28°N, the three harmonics are of almost equal magnitude.

The total offset ΔT of the nighttime lidar temperatures relative to the daytime WINDII results is derived from the consistency test and gives an initial hint to the day-night differences at 89 km. In the cases of November (28°N) and DJF (54°N), the night is colder than the day. These differences are derived for the calculated means of the data sets which may be influenced by the remaining gaps in local time coverage. When means from the consistent fit functions are calculated for the 12-h intervals, centered at local noon and midnight, the values change but the tendency is conserved. For November (28°N), the night is estimated to be 2.6 K colder than the diurnal mean, while for May (28°N) it is slightly warmer by 0.8 K. For May, the diurnal phase is close to 6 h and, hence, only small differences are calculated, although a significant amplitude A_1 was found. In the DJF (54°N) case, the night is 3.8 K colder, which is even more than in November at the lower latitude.

5.2.2 Discussion

The combination of K-lidar and WINDII temperature measurements provides three diurnal data sets. They have been reproduced with good agreement by regression analyses including 24-, 12- and 8-h harmonics. This provided initial information about the diurnal temperature tide which was not available before for these latitudes in the mesopause region. It shows that from the combination of complementary data sets, as from daytime and nighttime observations, further and more accurate information can be successfully deduced than from the individual data sets. On the other hand, it was also demonstrated that the fundamental differences of the two databases give rise to uncertainties. Geophysical variability from year to year, and within WINDII's 10° latitude band, are possible causes for discrepancies in the analyses. Such variability within a narrow latitude band has been observed in radar wind tides by *Jacobi et al.* (1999). Better results could be expected from more correlated observations and the contribution of non-migrating components can be addressed if at least one of the instruments provides diurnal coverage.

In a comparable approach, *Drob et al.* (2000) combined data from HRDI, sodium lidar and nightglow spectrometer which were obtained at 41°N during the same period. They derived temperature variations at 87 km by fitting the data with a multi-dimensional Fourier model. While SD parameters are generally consistent with those derived from lidar measurements alone (*Williams et al.*, 1998; *States and Gardner*, 2000b), the results for the diurnal tide vitally

depend on the bias correction of the instruments. The determined bias corrections of ±10 K exceed the offsets ΔT derived for our combination. Diurnal amplitudes of about 5 K ($\phi_1 \approx 14$ h) were derived for DJF with notable year-to-year variation. Similar amplitudes were calculated for summer while transition periods in October/November and around April exhibited strongly reduced diurnal tides. At this point only the comparability of the outcome with our study is noted. A more detailed discussion of the results follows in Section 5.4.

5.3 Daytime Lidar Measurements

Studies of the diurnal variability of temperatures in the mesopause region have been drastically improved since the daytime upgrade of the IAP potassium lidars. Since November 2000, a large number of measurements which include daytime observations have been carried out. Though, at mid and low latitudes they are still sparse and irregularly distributed. Therefore, the analysis in this work concentrates on the study of two outstanding measurements from Tenerife and Kühlungsborn which continuously cover several days.

5.3.1 Measurements at Tenerife, November 2000

As described in Section 4.1 the first measurements under daylight conditions were carried out with the transportable K-lidar on Tenerife during a campaign in November and December 2000. The first temperature measurement was performed successfully on November 17$^{\text{th}}$. A period of good weather enabled continuous lidar operation from November 19$^{\text{th}}$, 22:00 UT to November 26$^{\text{th}}$, 08:30 UT which was interrupted only on the 21$^{\text{st}}$ (ca. 13:00–18:00 UT) and on the 22$^{\text{nd}}$ for less than one hour. Ignoring the latter, a period of about 106 hours of continuous measurements was obtained.

The temperatures obtained during the 7-day run are shown in Figure 5.5. During the day the altitude range of the temperature profiles is restricted to regions of high potassium density due to the skylight background. Condensation clouds over the mountain ridge around noon caused an increased background on two days (22$^{\text{nd}}$ and 23$^{\text{rd}}$). As the photomultiplier was still used as a detector in this measurement (cf. Section 3.3.6), the integration intervals for temperature calculation are increased to 3 km and 2 h. Uncertainties up to 20 K are accepted, although values above 10 K are usually reached only for one altitude bin at the edge of the profiles. The highest temperatures occur at 85–90 km, where in November the atmosphere is ∼20 K warmer than near the mesopause at 100 km (cf. Figure 4.7). Downward progressing structures are visible during the whole 7-day period. For example, cold phases are seen to propagate down from 105 km after midnight on each day. On the other hand, Figure 5.5 demonstrates that the mesopause region is far from showing one monochromatic wave or only coherent tidal perturbation. For example, high temperatures exceeding 230 K are observed to a larger extent on only two days (20$^{\text{th}}$ and 23$^{\text{rd}}$). Before the full spectrum of variations is considered, the analysis will first be restricted to tidal signatures.

Harmonic Analysis

As in the previous sections, the measured temperatures are averaged with respect to local time. The resulting deviation from the diurnal mean profile is shown in Figure 5.6 (panel 1). A strong similarity to the data from November 1999 (Figure 5.1, panel 2) can be seen when the changed time axis is noted. Analogous downward propagating (ca. −2 km/h) structures appear with a

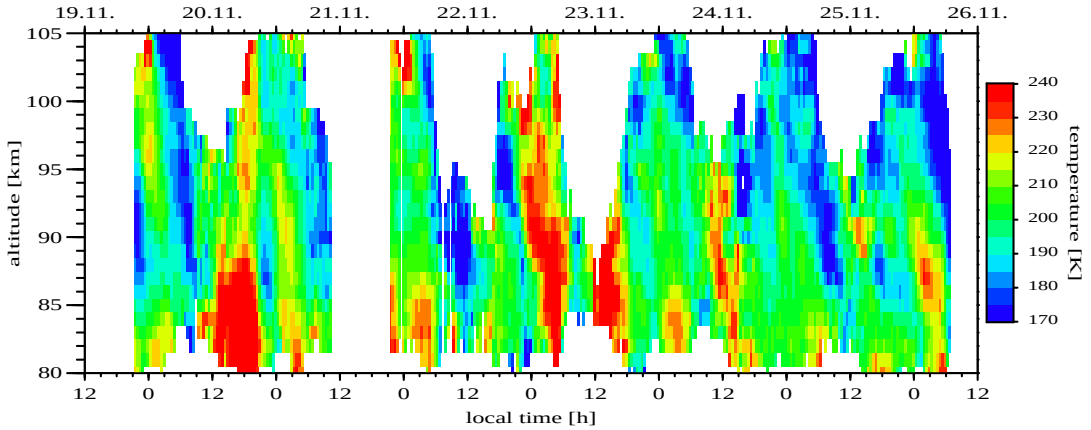

Figure 5.5: The 7-day run of temperature measurements at Tenerife in November 2000, calculated with a 1-km and 30-min resolution from 3-km and 2-h integration intervals. On occasion profiles reach up to 109 km and down to 78 km.

similar phasing (e. g. at 90 km a warm period begins close to local midnight). To examine the comparability with the results from the previous year, a combined 12-h and 8-h fit was applied to the subset of nighttime data (18:00–06:00 LT). The fit results for 2000 (panel 2) show some agreement with those for 1999. The SD component is again dominating, although with lower amplitudes especially between 90 and 95 km. An identical phasing with a phase velocity of about −3 km/h is derived. The highest TD amplitudes occur again in the lower part of the height range, but like the SD amplitudes, they are lower than in 1999. The TD phasing is also different from the previous year and now shows a downward propagation similar to that of the SD component.

The complete diurnal data set from November 2000 allows to be fitted with a harmonic series including the first 4 harmonics of the solar day, i. e. 24-, 12-, 8-, and 6-h cosine functions. The fit reproduces the observed temperature variations very well as shown in panel 3 of Figure 5.6. The residual deviation σ_{dT} is about 2-3 K over the height range with full diurnal coverage and due to short-scale fluctuations. The tidal parameters derived by the harmonic fit are given in panel 4. Above 97 km the data do not cover the whole diurnal cycle. Consequently, the results of the multi-parameter fit have a high uncertainty as indicated by the enlarged error bars (±5 K), and they change when the 6-h harmonic is excluded.

Below 97 km, amplitudes in the order of $A_1 = 3$–5 K are constantly derived for the diurnal (D) component (white). The D phase shows an unusual upward propagation, with a speed of about 2.5 km/h, indicating a forcing in the thermosphere. However, the results are also consistent with two regions of non-propagating oscillations (divided at 91 km). As expected from the contour plot, the SD component (black) is dominating the temperature variation. Compared with the nighttime data (panel 2), its amplitude is increased between 85 and 95 km to above 10 K, which is closer to the values for November 1999. The SD phase remains unchanged compared with the nighttime results from both years, with $\lambda_{z,2} = 33$ km. The TD amplitude (grey) is reduced to below 3 K and, hence, weaker than the D component. The D amplitude profile is very similar to that of the TD component from the nighttime subset (panel 2). Thus, when using nighttime data only, the unresolved diurnal component evidently has a large influence on the results for the higher harmonics. The TD phase is constantly near 4 h for all altitudes, as it

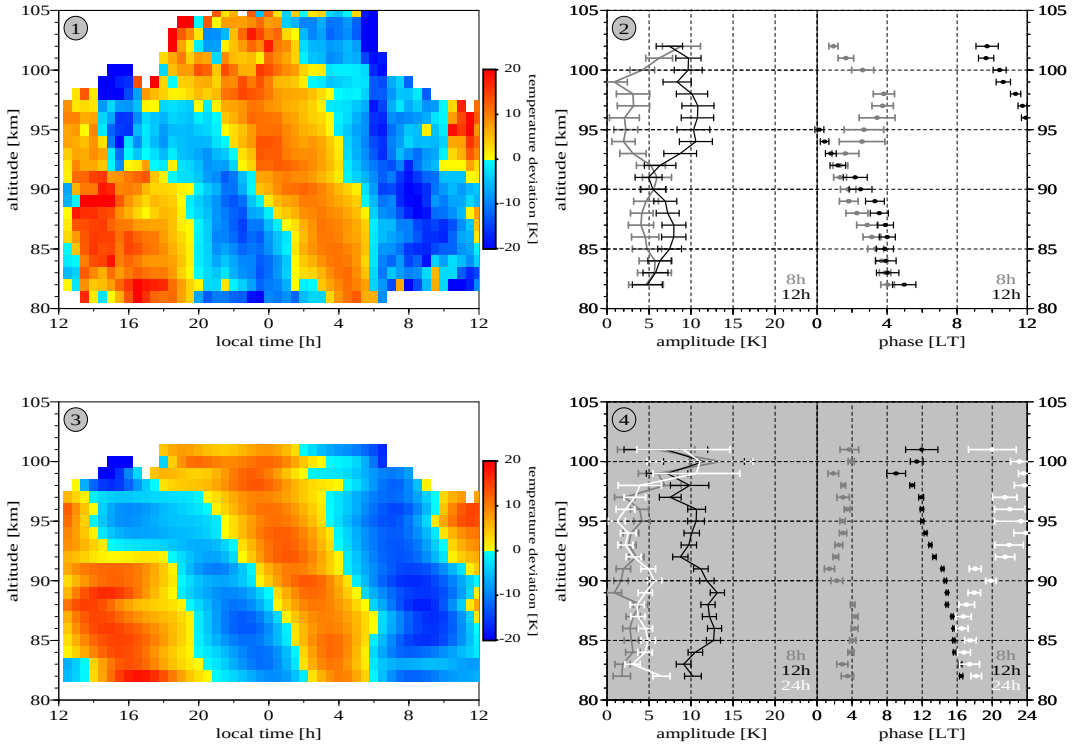

Figure 5.6: Temperature variations at Tenerife in November 2000: (1) Mean LT variation for all seven nights. (2) Amplitudes and phases from a harmonic fit to nighttime data only. (3) Variation as reproduced by the harmonic fit (incl. 24 h), and (4) parameters from the fit (D, white; SD, black; TD, grey).

was for November 1999. Shifting the phase values below 90 km to around 20 h shows that ϕ_3 is at all altitudes about 3 h behind ϕ_1. The 6-h harmonic is not shown although it was included in the fit. Its amplitude is about 1–2 K (except above 97 km) and the effect of including it into the fit on the other components is negligible.

For comparison with the WINDII/K-lidar combination (W/K) the results for 89 km are gathered in Table 5.4. Comparison with the W/K November data (Table 5.3) yields good agreement concerning the dominant SD component, although it is even stronger in November 2000. The TD phase ϕ_3 is also in agreement but the amplitude A_3 has practically vanished in this case. The D amplitude in 2000 agrees with that from the direct combination, while it was larger after applying the consistency test ($A_1 = 6.5$ K). The D phase ϕ_1 shows the largest deviation (9–10 h) from the W/K results and will be reconsidered below.

Table 5.4: Fit parameters for 89 km, November 2000, Tenerife.

Period	A_i [K]	ϕ_i [h]
24 h	4.6 ±0.8	18.0 ±0.7
12 h	13.1±0.9	2.9 ±0.1
8 h	0.9 ±0.9	3.9 ±1.2

Spectral Analysis

In the previous sections temperature variations in the mesopause region were analysed with regard to their content of diurnal harmonics which were derived after averaging the measurements with respect to local time. Nevertheless, it has been noted that many fluctuations in the temperature field do not exhibit a 24-h periodicity. They can be caused by waves of arbitrary periods which can be close to those of tides.

The study of gravity and planetary waves is a topic of its own and beyond the scope of this work. Apart from demonstrating the new data quality that has become available with daytime measurements, this section is dedicated to show that relevant information can be gained for the study of tides from spectral analysis of data sets covering multiple diurnal cycles. Long continuous lidar runs allow the frequency spectrum of the temperature perturbations to be determined by standard methods of spectral analysis (summarized in Appendix C.2).

For comparison with the previous results, the analysis is again concentrated on the altitude of 89 km since the mean features are very similar at adjacent heights. Periodograms for temperature variations during the 7-day lidar run in November 2000 on Tenerife are displayed in Figure 5.7 (upper row). The power spectrum is estimated with both the windowed fast Fourier transform (FFT) and the maximum entropy method (MEM) using zero padding to fill data gaps. Since the temperatures were derived from 2-h integrated photon counts, only periods longer than 4 h are considered. The FFT spectrum provides a salient broad feature for periods near 12 h, which is consistent with the strong semidiurnal tide described before. On the other hand, additional diurnal harmonics such as 24-, 8- or 6-h oscillations are not apparent. Instead, contributions from periods longer than 24 h and at low values are found. The general finding is confirmed by the MEM periodogram. By contrast to the FFT it can determine exact frequency values for the spectral features. The semidiurnal component is accurately identified with a period of 11.9 h. The low frequency contributions are associated with periods of 31.7 and 79 h, and power peaks at high frequencies with periods of 9.9, 4.8, 6.9 and 4.1 h, respectively, in the order of their power. All of them indicate incoherent gravity or planetary waves rather than tidal activity. Whereas the absence of 8-h and 6-h periods is in agreement with the harmonic analysis, a significant 24-h component would have been expected but is not found. Some wave features can be identified directly in Figure 5.5 like the 79 h period which corresponds to the high temperatures on November 20$^{\text{th}}$ and 23$^{\text{th}}$.

The power spectrum estimations above assume constant period and phase over the time stretch observed. The temporal development of the spectral distribution can be assessed with the aid of a wavelet transformation. The derived amplitude spectrum is given in the lower row of Figure 5.7. It should be noted (see Appendix C.2) that the amplitudes are only approximate values which tend to be underestimated for about one period at the beginning and the end of the time stretch covered and to a lower degree around the data gap on the second day (November 21$^{\text{st}}$). The largest amplitudes are again derived for the 12-h oscillation but with significant changes in magnitude. While its maximum on the forth day (November 23$^{\text{rd}}$) exceeds 20 K, it drops to nearly 5 K only one day later. On average it agrees with $A_2 = 13.1$ K from the harmonic fit. Three 12-h maxima occur which are separated by 48–60 h. On November 21$^{\text{st}}$ the maximum amplitude appears with a period of 10 h according to the secondary peak in the MEM power spectrum. A combination of 10-h and 12-h oscillations presumably occurred, which is not resolvable. Periods between 12 and 24 h are not observed but a contribution with more than 24 h is found. Its center period varies from below to above 32 h in agreement with a mean of 31.7 h from the MEM analysis. Periods well above 48 h cannot be investigated in this

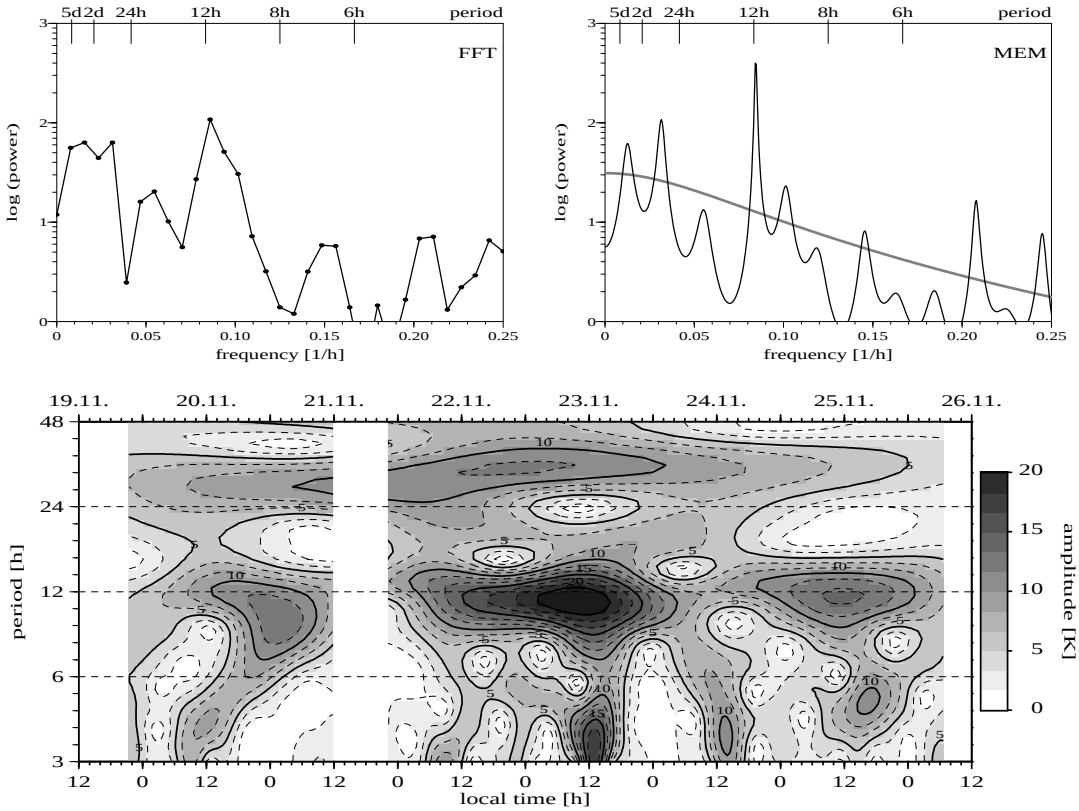

Figure 5.7: Spectral analysis of the temperatures at 89 km above Tenerife measured during the 7-day lidar run on November 19th–26th, 2000. Top left: FFT periodogram, certain periods are given at the upper axis. Top right: MEM periodogram, the grey line gives a noise level estimation. The power scale is logarithmic in arbitrary units. Bottom: Wavelet amplitude spectrum for the full period of measurements. Solid isolines are given every 5 K.

wavelet analysis due to the limited period of continuous observation. The 32-h wave of varying amplitude gives rise to a significant D amplitude value of 3–4 K in the harmonic analysis. Thus, it has a large erroneous influence on the diurnal harmonic.

Towards shorter periods, there is again a range of few spectral power at 6–8 h and a more active band at 4–5 h, in agreement with the periodograms. These waves are displayed to be very short-lived, lasting only one or two periods. Since the Morlet wavelet itself has a half-width of nearly two periods, the spectral features could have been even shorter. In that case the period identified in the wavelet spectrum can deviate significantly from the intrinsic frequency of the oscillation and that in the periodogram. Alternatively, the pattern of recurring oscillations may be generated not by individual wave packets but by the beating of two independent waves with similar frequencies or a modulated wave amplitude. It is remarkable that these oscillations maximize always around 12:00 LT which may be due to a 48-h modulation of the short period wave. These oscillations have their strongest peak simultaneously with the 12-h component. This suggests a coupling between the semidiurnal component and waves of shorter periods.

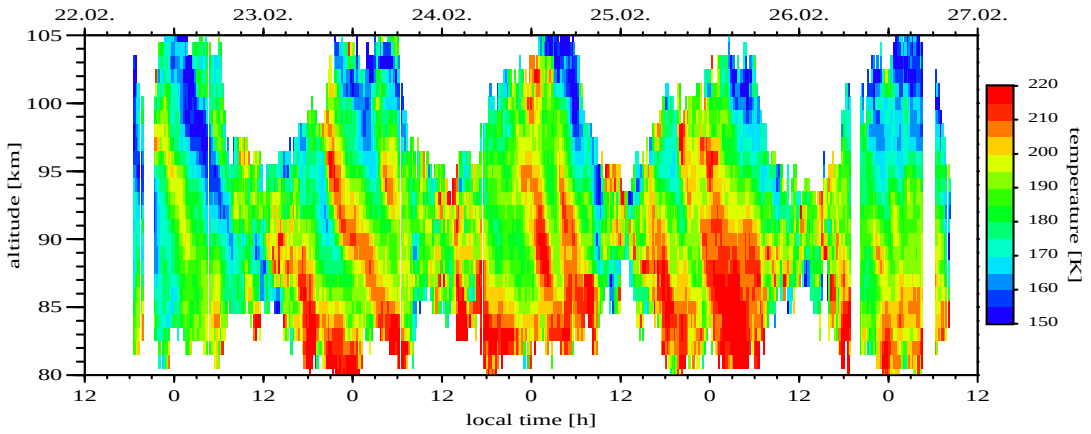

Figure 5.8: The 5-day run of temperature measurements at Kühlungsborn in February 2003, calculated with a 1-km and 15-min resolution from 2-km and 1-h integration intervals. On occasion profiles reach up to 106 km and down to 79 km.

5.3.2 Measurements at Kühlungsborn, February 2003

One similarly long continuous set of temperature measurements with the K-lidar in Kühlungsborn exists. Apart from three data gaps of about 1 h, a period of good weather in February 2003 permitted continuous temperature measurements for nearly 113 hours (February 22nd, 17:33 UT to February 27th, 10:26 UT). The temperatures during the 5-day run are derived after 2-km and 1-h integration and shown in Figure 5.8. Noting the generally lower temperatures, the plot resembles many features of its analogue from Tenerife (Figure 5.5). Again, strong temperature variations over a range of about 50 K are observed in every height with downward propagating structures. Higher temperatures occur around 85 km than around 100 km, reflecting the high (regular) mesopause state at this time of year.

Harmonic Analysis

The proportion of regular diurnal temperature perturbations is shown by the mean LT variation in Figure 5.9. The contour plot is surprisingly similar to that from 28°N for November (Figure 5.6), showing mainly semidiurnal variation. Again, at 90 km a warm period begins just before local midnight and this transition propagates downward at about 2 km/h.

Fitting the data with diurnal harmonics yields a decrease of all amplitudes with increasing height from 85 to 95 km. Due to lack of data around noon above 95 km, the results are considered to be partially artificial which is also reflected by the increasing error bars. The SD component dominates with amplitudes up to 10 K, while the others are weaker by more a factor of 2. The D component is about equal to the TD harmonic and shows no clear phase propagation with the maximum occurring around local midnight. For the higher harmonics, equal phase velocities of about −1.7 to −1.8 km/h are derived, corresponding to $\lambda_{z,2} = 21$ km and $\lambda_{z,3} = 14$ km.

For this case the tidal analysis for the nighttime (18:00–06:00 LT) subset of the data is not displayed. Since the diurnal component is relatively weak, SD and TD fit parameters are similar to those from the complete diurnal analysis, except for the TD amplitude A_3 which is

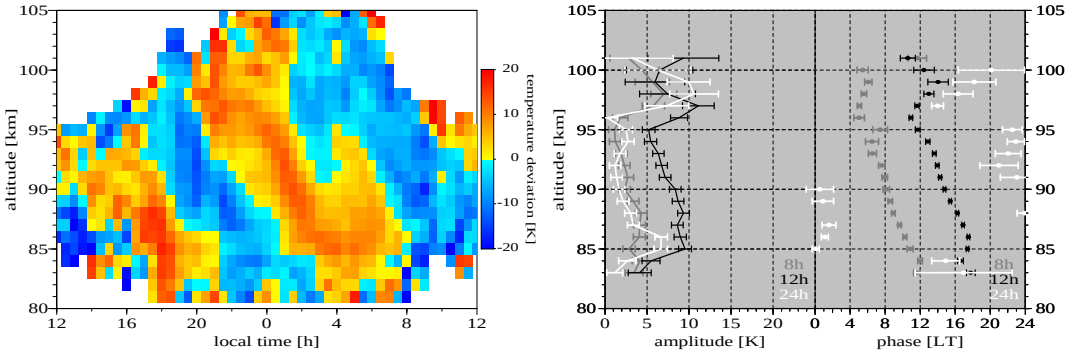

Figure 5.9: Temperature variations at Kühlungsborn in February 2003. Left: Mean LT variation for all five nights. Right: Parameters from the fit to mean LT variation (D, white; SD, black; TD, grey).

increased in the pure nighttime calculation.

Compared with the DJF mean winter data (Figure 5.3), the dominant SD component is stronger here in the range 85–95 km. Its phase exhibits a continuous phase propagation and is close to the former values below the phase jump. A_3 has a similar altitude dependence with a maximum of about 6 K between 85 and 90 km. The downward phase propagation was, with −6 km/h, relatively fast in the DJF mean and was adopted partially by the SD and the TD component. A comparable phase velocity is not identified here for any of the harmonics, but it would be consistent with the D phase ϕ_1 in 85–95 km.

The fit values for 89 km are gathered in Table 5.5. Significant differences appear in comparison with the DJF results obtained from the WINDII/K-lidar combination (W/K). In the 5-day lidar run the dominating SD component has twice the amplitude and almost the opposite phase. The diurnal tide, which was estimated as the dominant component with more than 5 K in the W/K combination, appears to be much weaker in this case and the phases differ by ∼8 h. Only the terdiurnal tidal parameters are in close agreement.

Table 5.5: Fit parameters for 89 km, February 2003, Kühlungsborn.

Period	A_i [K]	ϕ_i [h]
24 h	2.2 ±0.7	0.9 ±1.2
12 h	8.7 ±0.7	3.4 ±0.2
8 h	3.3 ±0.7	0.6 ±0.3

In contrast, the fits of single SD and TD harmonics to the nighttime data from February 1997–99 (*Oldag*, 2001) are in surprisingly good agreement with the results from the diurnal lidar data. For the amplitudes at 89 km, $A_2 = 6$ K and $A_3 = 4$ K were derived and both phases are near 1 h. Thus, the differences between the W/K combination and the 5-day run may partly result from the different periods covered by the data. Most of the WINDII data originate from February, whereas the largest portion of DJF lidar observations have been carried out in January. As the semidiurnal tide was determined to be stronger in February than in the two previous months, A_2 was larger in the WINDII data, which are accordingly in better agreement with the lidar results from February 2003. However, it is noted that the SD phase is in relatively close agreement between the two lidar data sets, while the WINDII results deviate.

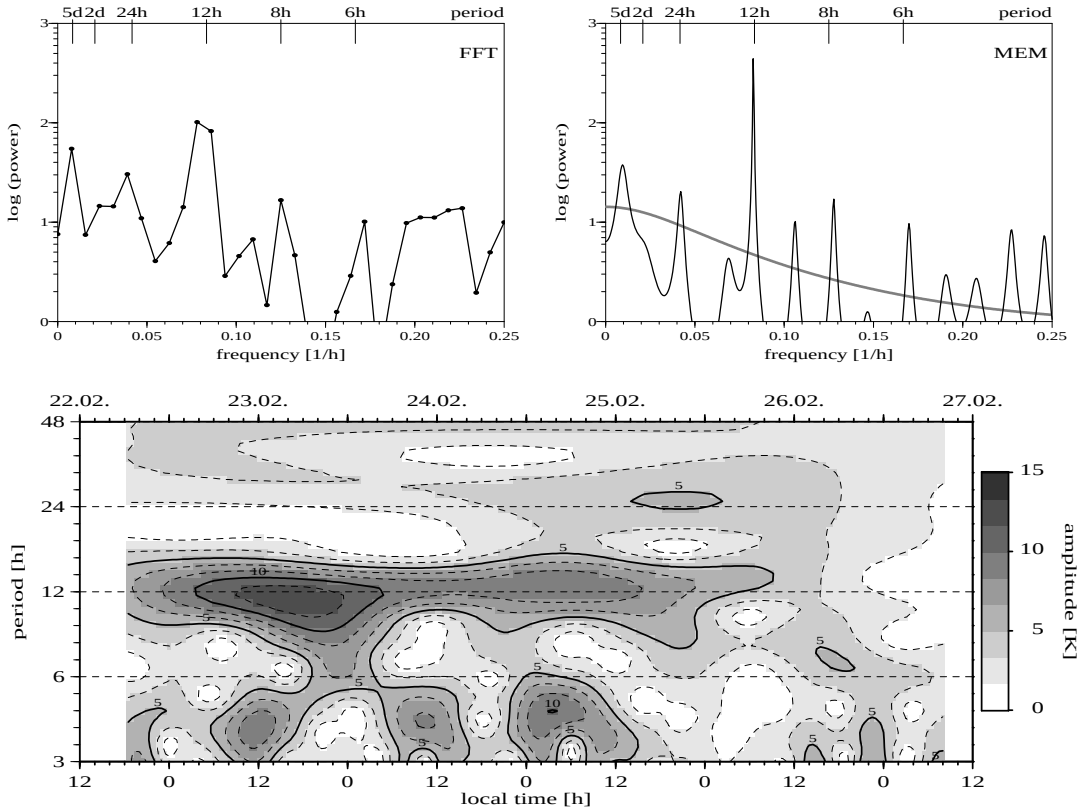

Figure 5.10: Same as Figure 5.7 but at Kühlungsborn during the 5-day lidar run on February 22nd–27th, 2003. Note the changed amplitude range in the wavelet spectrum.

Spectral Analysis

The 5-day lidar run at Kühlungsborn on February 22nd to 27th is spectrally analysed in the same way as the 7-day run at Tenerife and the results are displayed in Figure 5.10. As for the data from Tenerife, the FFT periodogram shows a striking peak at periods around 12 h. The contributions from the other diurnal harmonics are different because they show some enhancement of spectral power in this case. A long period feature near 5 days and some relatively continuous contribution with frequencies above 0.2 h^{-1} are also observed. In the MEM power spectrum, the diurnal harmonics are very closely represented with maxima at periods of 23.8, 12.1, 7.8 and 5.9 h, respectively, where the semidiurnal oscillation is about one order of magnitude stronger than any other. The long term variation is associated with a period of 105 h or 4.4 days. Periods of 9.4, 4.4 and 4.1 h are calculated for the strongest of the remaining features.

The wavelet analysis confirms the dominance of the semidiurnal component. Its initial increase is partly an edge effect of the wavelet analysis, the so-called *cone of influence.* An amplitude of about 12 K is indicated for the second day and it gradually decreases during the measurement to below 5 K, which is in good agreement with the mean $A_2 = 8.7$ K from the harmonic analysis (Table 5.5). During the same time the diurnal component increases to 5 K on the forth night (February 25th) and decreases again afterwards. The contributions of the 6-h and 8-h harmonics are not clearly resolved in the wavelet spectrum. Except for one peak

near the end, the main contributions originate from the second night when the 12-h wave also exhibits its maximum. This observation agrees with the finding in the tidal analysis that the TD tide always shows a behaviour related to the 24-h and/or the 12-h oscillation, indicating mode coupling. The wavelet analysis can also be used to examine the phase development of the semidiurnal component (not shown). In this case it is very stable near 3 h, while it was slightly more variable at Tenerife, varying from 4 h at the beginning to 2 h at the end of the 7-day period.

A relative quite band exists for periods between 12 and 24 h, whereas stronger wave activity is found for periods below 6 h, which is similar to Tenerife. On the third night an amplitude of 10 K is reached by a short period wave which corresponds to the 4.4-h peak in the MEM periodogram. The average power content of this wave is relatively low, because it exists for only about two periods. Like at Tenerife in November, the oscillations of higher frequency tend to maximize near local noon, thereby indicating a coupling to long-period waves. One could assume that the semidiurnal tide is the most probable candidate. It is the only component detected at Tenerife with 24-h periodicity and by far the strongest in this case. Furthermore, it has the same phase in both cases which applies also to the modulation of the 4–5-h oscillations.

5.3.3 Measurements at Kühlungsborn, June 2003

Before the above results are discussed, an additional example is presented briefly. No tidal information could be derived earlier from Kühlungsborn in summer, due to the short nights of about 4 hours and a lack of daytime measurements. Although these have recently become possible, no continuous lidar run of several days was permitted by the weather conditions in summer 2003. However, shorter observations are still useful to investigate wave activity. An 18-h measurement on June 26th/27th shows variations of ±20 K around 90 km, which is only slightly weaker than in winter. The periodogram has to be calculated with a reduced spectral resolution when compared with the longer measurements and hence no usable FFT analysis can be obtained. Though not very sharp due to noise and the short observation, the MEM in Figure 5.11 shows two distinct peaks corresponding to periods of 18.8 and 4.6 h, which is in good agreement with the data. From the half-width of the peaks, uncertainties of ±2 h and ±1 h can be assigned to the low and high frequency maximum, respectively. The short period contribution is similar to those observed in the cases discussed above. A remarkable difference is the absence of any tidal periods, especially the semidiurnal component that was most dominant both in the data from Tenerife and from Kühlungsborn in winter. Even if the degrees of freedom of the MEM calculation are increased, such that spurious peaks appear, still no 12-h or 24-h contribution is found. To some degree this is in agreement with the finding at 28°N that the semidiurnal tide is weaker in summer than in winter.

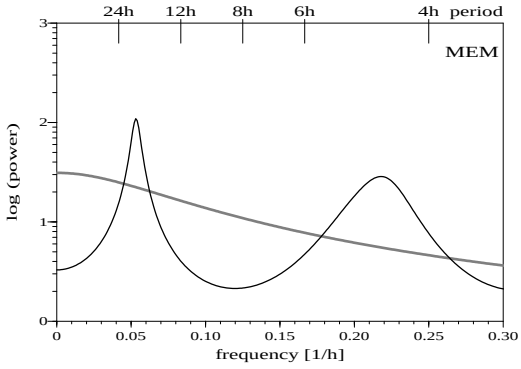

Figure 5.11: MEM periodogram as in Figure 5.7, but for June 26th/27th, 2003, at Kühlungsborn.

5.3.4 Discussion of Spectral Analyses

The daytime capability of the IAP K-lidars provides a full diurnal coverage and enables continuous temperature measurements over several days. Spectral analyses of this series allow the frequency of perturbations to be determined and distinguish to some degree tidal and other wave activity. Thereby, they provide further information in addition to harmonic analyses. Two cases from different locations and times have been analysed above and they show both similarities and differences. While the results which concern tides are discussed in detail in Section 5.4, a brief assessment of the spectral analyses is given here.

Observations of upper mesosphere temperatures, which continuously cover several nights and days, have not been available without the daylight capability of metal resonance lidars. Rayleigh lidar temperature measurements at daytime are typically limited to below 60 km. Nevertheless, measurements at 44°N over several consecutive nights were spectrally analysed by *Gille et al.* (1991). They found clear diurnal and semidiurnal signatures in January between 60 and 70 km. In contrast, in their data from November both these harmonics were absent and instead periods of 22 and 26 h appeared, inducing a spurious diurnal amplitude in a harmonic analysis. This is in general agreement with the results from the mesopause region presented above which also show a high variability of the perturbations, strong oscillations with periods that deviate from 24 and 12 h and the absence of a 24-h wave in November (28°N).

She et al. (2003) reported results from an initial 80-h continuous lidar measurement at Fort Collins (41°N) in April 2002. They identified temperature oscillations in 89 km with periods of about 10 and 21 h, while the zonal wind measured simultaneously exhibited contributions with ca. 16, 24 and 40 h. The 10-h component, especially, is in good agreement with our measurements.

Some of these spectral features can be attributed to non-linear interactions between the semidiurnal tide and a quasi-two-day planetary wave (e. g. *Palo et al.*, 1999). Amplitude modulation can result in difference and sum frequency excitation as

$$2 \cdot \cos(\omega_a t) \cdot \cos(\omega_b t) = \cos(\omega_a t + \omega_b t) + \cos(\omega_a t - \omega_b t)\,. \tag{5.2}$$

Thus, the interaction of 12- and 48-h period waves results in 16- and 9.6-h periods, which have been observed in wind measurements before (e. g. *Manson and Meek*, 1990). Quasi-two-day waves (QTDWs), typically with periods between 44 and 56 h, are not detected in our measurements but the secondary waves may be generated at lower heights and propagate up into the region of observation. Furthermore, QTDWs are more often observed around solstice in the summer hemisphere (e. g. *Shepherd et al.*, 1999) but they can penetrate across the equator and have also been observed in winter at midlatitudes (for 55°N, see *Hoffmann et al.*, 2002). The 9.6-h wave was found to be the strongest secondary wave which is excited by non-linear interaction of migrating tides with the QTDW in numerical simulations by *Palo et al.* (1999). It can be associated with the periods of 9.4 and 9.9 h in the two long-term lidar observations, whereas no 16-h wave has been detected.

The wavelet spectra give further support to this interpretation. For an amplitude modulation in the sense of Eq. 5.2, the spectrum will show both sum and difference frequency, as long as their separation exceeds the wavelet resolution. The two mixed frequencies ($\omega_a \pm \omega_b$) are not resolved when $\omega_a \geq 4\omega_b$ and mode beating with $2\omega_b$ appears in the spectrum instead. Thus, 24-h modulations, as observed for periods below 6 h, may also originate from a QTDW. Our observations agree with radar measurements of MLT winds, which show that 12-h, 24-h and

48-h modulations dominate the variability of oscillations with periods below 6 h (*Manson et al.*, 1998).

Measurements of the meridional wind were made daily in February 2003 near Kühlungsborn at the IAP radar station on Rügen (55°N, 13°E; e. g. *Hoffmann et al.*, 2002). Beneath the tidal components[1], fluctuations with periods of about 10 and 16 h, as well as 2–3, 6 and 16 days were identified at 86 km (*Hoffmann*, private communication). This result is in good agreement with the lidar observations and the additional periods support the interpretation given above.

The temperature perturbations of shorter periods ($<$8 h) could be caused by short-lived gravity waves. Alternatively, one might follow the line of the argument above and speculate about the periods derived in the MEM periodograms. Surprisingly, all derived periods are obtained by this approach. Mixing the hypothetical QTDW with a TD tide also results in a 9.6-h wave additionally in a 6.8-h wave, which compares well with the period of 6.9 h observed in November 2000. A period of 4.8 h is obtained mixing 24- and 6-h waves or alternatively 12- and 8-h waves. A 4-h period would result from the interaction of a 6-h wave with a semidiurnal tide and 4.1 h were derived from both lidar observations.

Considering the low frequency part of the spectrum for November, one finds that the observed 79- and 32-h periods could originate from a QTDW and a 4–5-day planetary wave. Such planetary waves are consistent with the amplitude modulation of the SD tide in the November observation. A corresponding period is derived directly from our February case with 105 h. The so-called *5-day wave* has frequently been observed in radar wind measurements and is identified as the first symmetric Rossby wave (e. g. *Forbes*, 1995; *Jacobi et al.*, 1998).

5.3.5 Conclusions of Spectral Analyses

To summarize, spectral analysis of long continuous lidar runs has been demonstrated to enable better understanding of harmonic tidal analyses, in addition to exploring waves with arbitrary periods. While large spectral power for 12-h oscillations was found, in agreement with the harmonic analyses, the absence of an exact 24-h oscillation might explain the difficulties to identify a clear phase pattern for the diurnal tide for Tenerife in November 2000. The diurnal fit results are strongly influenced by the 32-h wave. Such single continuous measurements over several days are possibly not sufficient to separate coherent tidal components from other waves. A strong day-to-day variability of the tidal components is found for both cases considered. Amplitudes were observed to vary by a factor of 4–5 within a few days even for the strong and persistent semidiurnal tide. The most constant parameter was the phase of the semidiurnal tide. Thus, a relatively large database is required to eventually determine the mean tidal pattern.

Apart from the tidal periods, strong perturbations are observed with periods above 24 h and below 6 h, which are associated with planetary and gravity waves, respectively. Intermediate periods may be connected with non-linear wave-wave interaction and also the gravity waves appearance suggests such interactions.

For future studies, it will be helpful to extend the spectral analysis spatially. It is possible over a limited height range with the data presented and further improvements of the lidar daylight capability should provide an extension of the usable height range. At the IAP in Kühlungsborn, a Rayleigh/Mie/Raman lidar system is operated which gives, in combination with the K-lidar, continuous temperature profiles from 100 down to 1 km at nighttime with a temporal resolution of 1 h (*Alpers et al.*, 2004). These measurements allow to analyse the full

[1]The MF radar measurements were made during daytime only what may have spurious effects in the analysis especially on the diurnal harmonics (e. g. *Hernandez*, 1999).

vertical propagation of the waves. Additional information about the horizontal structure can be obtained by two or more instruments located at a suitable distance or in combination with spaceborne experiments when simultaneous measurements with high resolution are available.

5.4 Discussion of Tidal Analyses

The IAP potassium lidars reveal strong systematic temperature variations in almost every observation of the mesopause region. A large proportion of the fluctuations can be explained in terms of regular coherent oscillations with periods that are subharmonics of a solar day. They can be interpreted as atmospheric tides when the data are based on sufficiently long periods of observation. Significant tidal amplitudes have been observed and tides are confirmed to have a large influence on the temperature field in the mesopause region. As discussed above, fluctuations with other periods also occur and a single groundbased instrument cannot definitely distinguish tides from other waves. The amount of data required for a reliable classification depends on the actual periods, duration and occurrence rate of waves with near-tidal periods.

Lidar observations from different months, years and latitudes have been analysed. In all cases, the mean local time variation exhibits prominent downward phase propagation denoting upward wave (energy) propagation. The conditions for vertical propagation and wave-wave interactions between the mesopause region, where the oscillations are observed, and the stratosphere and troposphere, where the strongest forcing due to ozone and water vapour occurs, are highly variable. This causes the high variability of the tidal pattern that is observed on all time scales: interannual, intraseasonal and day-to-day. While the shortest time scales have become evident by the spectral analyses of continuous lidar measurements, year-to-year variations are apparent in the lidar observations from November on Tenerife (Figure 5.1 and 5.6) as well as in the WINDII data.

Tidal parameters have been derived using different methods and the main results are summarized below. While a large amount of nighttime lidar observations are available, they have to be interpreted carefully. An unresolved 24-h wave can strongly influence the analysis as has been demonstrated using diurnal measurements. In particular, the determination of the weaker component becomes uncertain which mostly concerns the terdiurnal tide. Two cases of important continuous long-term measurements have been presented and further technical development is expected to provide them more regularly in the future in Kühlungsborn. The combination with the spaceborne WINDII daytime measurements has provided diurnal data that has not been available at these locations before. Although, it also incorporates considerable uncertainties caused by the different methods and periods of observation. In comparison with the continuous lidar runs, certain differences occurred and it is not clear if they are completely due to geophysical variability or partly of systematic origin. Further information could be obtained from simultaneous 24-h lidar and satellite measurements.

5.4.1 Results

Among the possible modes of tides it is the **semidiurnal tides** that show on average the largest amplitudes. Semidiurnal tides with amplitudes up to $A_2 = 15\,\mathrm{K}$ have regularly been observed at low and midlatitudes during the months around winter solstice (November–February). Near summer solstice strong 12-h oscillations were also present at 28°N but a single example from 54°N has shown that conditions with no detectable 12-h wave also occur. This is in agreement

with observations of horizontal winds, for which the dominance of the semidiurnal tide at midlatitudes in winter is a well-known fact (*Forbes*, 1995).

At Tenerife (28°N) in November 1999 and 2000, upward propagating semidiurnal tides with vertical wavelengths of $\lambda_{z,2} = 30$–35 km have been observed, which correspond to the third symmetric Hough mode, $H(2,6)$. In February 2003 at 54°N, a shorter wavelength of $\lambda_{z,2} = 21$ km was deduced from the observations. This would correspond to a Hough mode of high order, $H(2,9)$, which is expected to be subjected to large fluctuations, depending on propagation and forcing conditions. In spite of the large amplitude variations, a very stable phase of the SD wave was derived during the 5 days. A similar phase propagation was obtained from the DJF97–99 nighttime composite only around 85 km, where the SD component is weak and subordinate to the TD component. Between 95 and 100 km, above the phase shift, the SD tide was stronger in the mean DJF nighttime data than in the 5-day run and exhibited a vertical wavelength of about 60 km, which can be identified with the more stable second symmetric mode, $H(2,4)$. The SD phase at 89 km is constantly near 3 h during winter. Only the W/K combination for DJF at 54°N has provided a different value, which is determined by the WINDII observations that have shown a large year-to-year variability and a value near 3 h has also been observed in previous years.

Diurnal tides have become detectable with observations covering full diurnal cycles and they were found to have significant amplitudes in the order of $A_1 = 2$–6 K. The W/K combination determined similar amplitudes for 28°N in November and 54°N in winter, whereas no detectable D tide was observed in the 7-day lidar run in November 2000. The tidal analysis of this data is strongly hampered by the strong influence of a 32-h wave.

Propagating diurnal Hough modes have vertical wavelengths of less than 27 km, but corresponding phase velocities of 1 km/h or less were not observed in the continuous lidar runs. In contrast to the SD tide, the D tide at 54°N in February 2003 did not exhibit a clear phase propagation but was relatively constant with altitude. This behaviour can be caused by a superposition of various modes and also by a trapped mode without vertical propagation, which is excited in the MLT region. This interpretation would be consistent with the lidar measurements in autumn by *States and Gardner* (1998) and with the modelling results by *Forbes* (1982a). Non-propagating modes are expected to peak near 18:00 LT since they are forced by *in-situ* absorption of solar radiation. The observed phase at local midnight could also result from chemical heating, which is known to be stronger during the night than during the day and predicted to peak around 90 km (*Mlynczak*, 2000). In this region it can be stronger than the absorption of solar radiation and could explain at least parts of the observations. However, recent modelling has predicted the effect of chemical heating to be small (*Smith et al.*, 2003).

The third harmonic, the **terdiurnal tide**, appeared with significant amplitudes in the measurements, except for November 2000 at 28°N. As the vertical wavelengths were short (as small as 14 km), they do not agree with any modes expected from the classical tidal theory. It has been noted that the vertical profiles of the TD parameters (A_3, ϕ_3) were always in close relation to those of the SD, the D, or both components. This suggests that they do not occur as individual modes but are coupled to the other tides. Hence, they could be generated by non-linear interaction of diurnal and semidiurnal tides with each other or with planetary waves as discussed by *Smith and Ortland* (2001). For oscillations with periods of 6 h, negligible amplitudes of less than 1–2 K have been derived in the continuous lidar runs.

The results presented need to be assessed in the light of other work on this topic. To focus the following comparisons the tidal amplitudes derived from the continuous lidar runs for 89 km and those from WINDII/K-lidar combination, after applying the consistency test,

Table 5.6: Overview of tidal amplitudes near 89 km. Values best matching the continuous K-lidar observations are shown (K-lidar day/night-runs; W/K, WINDII/K-lidar combination; Na-lidar measurements; GSWM, COMMA, and DNM model results). See text for details and references.

	K-lidar	W/K	Na-lidar		GSWM-00/02	COMMA	DNM
Month(s)	Nov.	Nov.	NDJ	ASON	Nov.	Dec.	Nov.
Latitude	28°N	23–33°N	40°N	41°N	27°N	28°N	28°N
A_1 [K]	[4.6]	6.5	4.5	5.2	3.1 / 5.0	6.6	5.5
A_2 [K]	13.1	8.8	7.0	4.5	4.1 / 4.7	6.0	0.5
A_3 [K]	[0.9]	3.2	2.6	—	—	1.9	1.1
Month(s)	Feb.	DJF	FMA	DJF	Feb.	Dec.	Jan.
Latitude	54°N	50–60°N	40°N	41°N	54°N	53°N	56°N
A_1 [K]	2.2	6.5	8.5	5.3	0.8 / 1.7	1.7	0.3
A_2 [K]	8.7	4.1	3.7	9.0	2.4 / 2.1	6.6	0.5
A_3 [K]	3.3	2.6	4.4	—	—	0.8	0.4

are given in Table 5.6 together with comparable measurements and model results. Error bars are omitted for clarity. The corresponding phases are gathered in Table 5.7 below. Listed are Na-lidar measurements at 40°N and 41°N. In addition, model predictions are shown from the GSWM (Global-Scale Wave Model), the COMMA-IAP and the RAS-DNM GCM (Russian Academy of Science - Department of Numerical Mathematics General Circulation Model), which is also used at the IAP. Values are given for the time period, altitude and location with the closest temporal and spatial agreement to the continuous K-lidar measurements. The K-lidar values from November 2000 which are not clearly caused by tidal activity are given in brackets. The available results are discussed in detail below.

5.4.2 Lidar Measurements at Other Latitudes

Prior to this work there existed no data of temperature measurements in the mesopause region covering full diurnal cycles at latitudes near 28° and 54°N. However, groundbased Na-lidar observations have been carried out at an intermediate latitude. Results are available for differently defined seasons from Urbana, Illinois and Fort Collins, Colorado and those closest to our measurements are listed in Table 5.6 and 5.7.

For **Urbana** (40°N, 88°W), annual variations of tidal parameters from continuous lidar measurements were calculated by *States and Gardner* (2000b). The authors noted strong diurnal variations below 92 km (and weaker in 92–100 km) throughout the year, with exceptions in late November, December, early January and May showing weaker activity. The low amplitude in November is in agreement with the insignificant D component in the 7-day K-lidar run at 28°N. Seasonal 3-month averages of the derived parameters were calculated, centered at the equinoxes and solstices.[2] For NDJ (winter season, ca. November–January) the diurnal amplitude A_1 reaches a maximum of 5 K near 90 km and a minimum of 2 K at 98 km, which is comparable to the W/K results for 28°N in November and also with the results (Figure 5.9)

[2]Monthly averages including a minimum of 3 nights were fitted with the diurnal harmonics. While arithmetic mean amplitudes are given, vector averages are used for the phases. This procedure possibly generates larger amplitudes than the fit of a 3-month temperature average which we have used in the W/K combination.

Table 5.7: As Table 5.6 but for the tidal phases (in local time).

	K-lidar	W/K	Na-lidar		GSWM-00/02	COMMA	DNM
Month(s)	Nov.	Nov.	NDJ	ASON	Nov.	Dec.	Nov.
Latitude	28°N	23–33°N	40°N	41°N	27°N	28°N	28°N
ϕ_1 [h]	[18.0]	9.3	1.5	4	22.9 / 23.2	7.3	5.0
ϕ_2 [h]	2.9	2.7	2.7	4.5	3.3 / 3.3	8.2	8.7
ϕ_3 [h]	[3.9]	3.8	2.4	—	—	5.3	6.3
Month(s)	Feb.	DJF	FMA	DJF	Feb.	Dec.	Jan.
Latitude	54°N	50–60°N	40°N	41°N	54°N	53°N	56°N
ϕ_1 [h]	0.9	9.5	11	3	1.8 / 2.6	17.2	15.7
ϕ_2 [h]	3.4	10.0	3.5	2.7	2.4 / 2.5	7.8	6.6
ϕ_3 [h]	0.6	0.7	1	—	—	6.6	3.2

for February at 54°N. On the other hand, the D phase shows a clear downward propagation at 40°N which was not observed at the other latitudes. The SD harmonic exhibits a continuous increase with height at 40°N, reaching the strength of the SD tide at 28°N only above 97 km. At 89 km, A_2 is closer to the results from the W/K combination.

In FMA (spring season, ca. February–April) at 40°N, A_1 exceeds 8 K between 85 and 90 km and adopts a minimum of 4 K at 95 km. At 54°N in February, A_1 was clearly smaller in the 5-day lidar run but had comparable altitude dependence. In contrast, A_2 was stronger in the K-lidar observation. Thus, the K-lidar data from late February (54°N) are in better agreement with the Na-lidar results at 40°N from around winter solstice (NDF), although they fall into the later period. This finding is further supported by the excellent agreement of both ϕ_1 and ϕ_2 in 89 km with the NDF mean. For autumn, winter and spring, downward propagating phases with $\lambda_{z,2} \approx 30$–33 km are reported from 40°N, also being in perfect agreement with 28°N. The W/K combination from DJF 54°N has a larger temporal overlap with the NDJ period but shows a better agreement in D and SD amplitude and phase with the FMA results at 89 km. Finally, for the seasonal average from May to July, results at 40°N are relatively close to the values inferred from the W/K combination for May at 28°N. The TD harmonics at 40°N show amplitudes of $A_3 = 2$–3 K at all seasons and altitudes below 97 km, except for FMA when it reaches 5 K at 93 km, thus largely supporting our results. Like in our observations, the 6-h component is weaker than the 8-h component and is negligible.

For **Fort Collins** (41°N, 105°W), *She et al.* (2002a) derived seasonal tidal parameters from eighteen diurnal lidar observations. By inspection of the tidal signature, observations were grouped to give autumn (ASON, Aug.–Nov.), winter (DJF), spring (Mar.–Apr.) and summer (May and July) means. Thus, the seasons are defined differently to those discussed above. All seasons exhibit downward phase propagation of diurnal ($\lambda_{z,1} \approx 20$ km) and semidiurnal ($\lambda_{z,2} \approx 35$ km) components, except for the SD phase in ASON which is nearly constant with altitude. This $\lambda_{z,2}$ is identical with that derived at 28°N in November. While the phase profiles are in good agreement between 40° and 41°N, the amplitudes exhibit certain differences. The sharp diurnal amplitude minima observed at 97 km in the Urbana data for all four seasons are not seen at Fort Collins. Instead, the height profiles from DJF (41°N) show a distinct minimum of tidal variation (D and SD) at 85 km. The diurnal amplitudes below 90 km are generally smaller

at Fort Collins than at Urbana by ∼4 K in both spring and autumn and by ∼2 K in winter.

For ASON, tidal amplitudes at 89 km of $A_1 = 5.2$ K and $A_2 = 4.5$ K were found. In relation to our data from November (28°N), the diurnal component is comparable in magnitude but the semidiurnal amplitude is significantly smaller. The DJF data from 41°N show a similar diurnal amplitude but a stronger SD tide of 9 K. This is more similar to the results from November at 28°N, supporting the argument that our results should be considered as representing a winter state. Compared with the results from 54°N, A_1 agrees with the W/K combination while A_2 is close to the result from the continuous lidar run. Finally, in summer, the diurnal tide is again of equal strength (5.3 K) while the semidiurnal is much weaker (3 K) than in winter, both being comparable to our May W/K results from 28°N. Higher harmonics are reported again to be of minor influence with amplitudes below 4 K at all heights mapped above Fort Collins.

In general, between the autumn and spring transitions (ca. November–February), the SD tide appears to be dominating in the 85–95 km range at all mid and low latitudes considered. During the rest of the year, semidiurnal and diurnal tides are of comparable magnitude. Amplitudes range around 5 K, except for the winter SD tide, which can be twice as strong. The deviation of the W/K DJF case from this finding may be explained by the multi-year and multi-month averaging of the data, the fact that the lidar data mostly originate from January when the SD tide was weakest, and the SD phase difference in the individual data sets. In contrast to the K-lidar observations at 28° and 54°N, a clear downward propagating D phase with about $\lambda_{z,1} =$ 25–30 km is observed at both 40° and 41°N in winter, indicating the first symmetric propagating diurnal mode $H(1,1)$. From tidal theory, the diurnal modes are expected to maximize near 40°N, suggesting that a single prevalent mode is found at this latitude rather than at 28° or 54°N and that the amplitude might be overestimated in the W/K combination. On the other hand, there are also considerable differences between the two lidar stations at Fort Collins and Urbana which are not yet explained. Possible sources include those of geophysical (e. g. year-to-year variations, longitude dependent non-migrating tides), statistical (e. g. insufficient data to average out incoherent wave effects) and data-processing origin (e. g. definition of seasons, averaging procedure). Both *She et al.* (2002a) and *States and Gardner* (2000a) have reported large month-to-month variability. Hence, the grouping into seasons is problematic as long as sufficient data from the individual months are not available.

5.4.3 Bias of Nighttime Mean Temperatures

Most climatological temperature data derived by optical methods, using groundbased lidar and airglow techniques (or spaceborne methods), originate from either nighttime or daytime observations. While semidiurnal tides will almost smooth out in nighttime lidar observations of sufficient length in winter, this is not necessarily true for diurnal tides. Therefore, the possible bias of the climatologies derived in comparison with diurnal mean temperatures needs to be assessed.

Fit functions obtained by harmonic analyses allow to calculate nighttime (18:00–06:00 LT) means, which are compared with diurnal mean temperatures. A tendency towards a negative nighttime bias, i. e. a lower temperature at night than at daytime, was found in November 2000 at 28°N over the whole altitude range but with large uncertainty due to the major influence of the 32-h wave on the fit results. A stronger negative nighttime bias of −2.6 K for 89 km has been deduced by the consistency test from the joined W/K data in which the D tide was more prominent than in the 7-day lidar run.

In February 2003 at 54°N, the diurnal phase ϕ_1 lies near midnight for almost all altitudes

up to 95 km. Hence, in this case the night is warmer than the mean day in 84–95 km. The differences range below 2 K (except for 85–86 km) and decrease with increasing altitude (cf. Figure 5.9). Thus, the nocturnal temperature profile has a stronger gradient than the diurnal mean. On the contrary, from the W/K combination a nighttime bias to lower temperatures (−3.8 K) was derived for 89 km and DJF at 54°N. A significant D tide was observed in May at 28°N but due to its phasing the nighttime bias is negligible (+0.8 K). A small nighttime bias is also expected for 54°N in summer, although only short periods of darkness occur, if the single observation with no significant D and SD tidal contribution is representative.

In contrast to our measurements, a clear upward propagating D tide is observed both at Fort Collins (41°N) and Urbana (40°N) with $A_1 \approx 4$ K and $\lambda_{z,1} = 20$–25 km. It causes an annual mean nighttime bias towards higher temperatures between about 90 and 100 km, and towards lower temperatures below and above these tidal nodes. Thus, the mean temperature profile is systematically biased when it is derived from pure nighttime observations. However, the bias at 89 km is mostly small and its sign varies with the altitude of the tidal node.

The diurnal tide appears to be weaker at both K-lidar stations considered than at 40°N and also more variable or dominated by non-propagating modes. Thus, the influence on the nighttime mean temperature profile and especially on its gradient is expected to be smaller at 28° and 54°N than at the intermediate latitude.

5.4.4 Other Observations

While lidar observations rely on good weather conditions, meteor radars can be used for continuous diurnal observations of the mesopause region. The derivation of temperatures depends on *a-priori* knowledge of atmospheric pressure or the mean temperature gradient. Whereas the absolute calibration is problematic, temperature variations can be detected on a basis of about 30 h of data, using monthly mean composite days. The temperatures calculated for 88 km depend on the varying vertical temperature gradient. As discussed by *Hocking and Hocking* (2002), this dependence can be accounted for when the vertical wavelength of the dominating tidal pattern is used, which is derived from simultaneously measured wind perturbations. The authors reported a large variability of tidal parameters from year-to-year and month-to-month. During the winter months (DJF97–99) diurnal amplitudes and phases at 43°N ranged within $A_1 = 3$–12 K and $\phi_1 = 19$–5 h, respectively. The corresponding semidiurnal results were $A_2 =$ 5–10 K and $\phi_2 = 2$–6 h. This broad spread includes the parameters derived from the lidar run in February 2003. By contrast, from the W/K combination for DJF at 54°N only the D amplitude lies well within the range and the SD amplitude at the lower edge, while the phases are clearly different with values of about 10 h. The W/K combination for November at 28°N mainly differs with respect to ϕ_1 while the other parameters lie within the range given by *Hocking and Hocking* for 43°N. On the other hand, the W/K May (28°N) results agree excellently with radar results for both spring and summer.

In conclusion, the meteor radar supports the observation of large interannual and intraseasonal variability and the agreement with the results in this work is deemed fair. The agreement of the radar observations (43°N) with the Na-lidar results from 40°N is closer than with ours from 28° and 54°N. A possible cause for deviations, apart from latitudinal and temporal differences, is the assumption of identical vertical wavelengths for wind and temperature tides. This is not confirmed by recent simultaneous measurements of wind and temperature variations (*She et al.*, 2003).

Spaceborne observations have considerable difficulties to identify migrating tides due to

their restricted local time coverage. Some studies used values near the equator differing in local time by 12 h and attributed differences to the migrating 24-h tide, often neglecting the possible influence of an 8-h tide. On the other hand, satellites can infer the longitudinal structure of temperature variations and can distinguish between migrating and non-migrating components. *Shepherd et al.* (1999) used WINDII daytime measurements to study migrating diurnal tides in December/January. The D tides maximize with amplitudes of 6 K at the equator in 75–80 km and tend to decrease towards the tropics and higher altitudes ($\sim$3 K at 20°N and 90 km). This observation supported the semi-empirical study by *Khattatov et al.* (1997) who used tidal wind oscillations, derived from HRDI data, to calculate diurnal temperature tides. Temperature oscillations are predicted to minimize near 20° and maximize near 40° throughout the year, in agreement with classical tidal theory. For 28°N in November and May, amplitudes of about $A_1 = 5$ K were calculated for 89 km, and $A_1 = 5$–10 K for the altitude range of 90–115 km. This agrees with the W/K combinations for 28°N for which similar amplitudes of 4.0–6.5 K have been observed. On the other hand, the increase towards 40°N is consistent with the fact that diurnal tides clearly appeared in lidar observations at 40° but not at 28°N in November 2000.

The amplitude values for 7.5°N derived in November during the CRISTA1 mission (*Oberheide and Gusev*, 2002) are similar to the WINDII study. In addition, the authors derived non-migrating diurnal tides and found them to be equivalent to the migrating modes. Comparable importance was assigned to the non-migrating diurnal components by *Talaat and Lieberman* (1999) using HRDI daytime observations. At 27°N the gravest non-migrating mode peaks with 4 K amplitude at 85 km. Thus, the deviations between WINDII and lidar data could be partly caused by non-migrating tides.

The **terdiurnal tide** has experienced considerably less interest than the lower harmonics. Its global structure in the zonal wind field at 95 km has been derived by *Smith* (2000) who found that at midlatitudes near solstice the TD amplitude can reach one third of the prevalent semi-diurnal tide and also considered tidal interaction as a possible source, which is in agreement with our results.

In particular cases, large 8-h temperature oscillations exceeding 10 K have been derived at 42°N from observations of nighttime airglow originating from near 90 km (*Wiens et al.*, 1995; *Pendleton et al.*, 2000). The TD amplitudes in our lidar observations were much lower. Although increased TD activity near equinox is in agreement with the results from 40°N (Section 5.4.2), only 50% smaller amplitudes were found in the Na-lidar data. Due to the high variability of tides, events with strong TD tides are not unreasonable, but on the other hand, spurious results due to the observation periods of 8 or 10 h are also possible.

5.4.5 Model Predictions

A widely used model for the study of atmospheric tides is the **Global Scale Wave Model** (GSWM). Monthly results for migrating diurnal and semidiurnal tides from the GSWM-00 (*Hagan et al.*, 1999, 2001) are available and those corresponding to the two long-term lidar measurements are given in Figure 5.12. Terdiurnal tides are not considered in the GSWM. The altitude level nearest to the height used in the W/K combination is 90.6 km which is used in Table 5.6 and 5.7.

The model describes an upward propagating diurnal tide ($\lambda_{z,1} \approx 30$ km) at 27°N in November. The predicted D amplitude is smaller than in the W/K combination (3.1 vs. 6.1 K) whereas in the 7-day lidar run a 24-h oscillation of this strength was not detected. With $\phi_1 = 22.9$ h

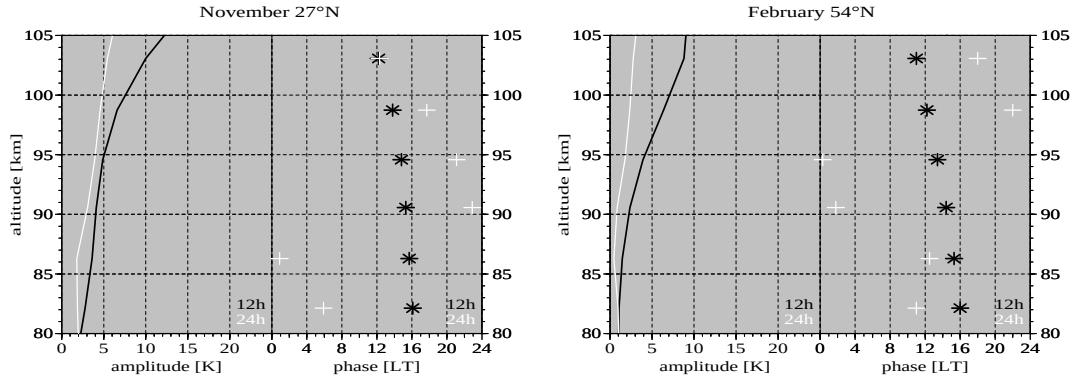

Figure 5.12: Tidal parameters from the GSWM-00, for Tenerife in November (left) and for Kühlungsborn in February (right). Amplitudes and phases of diurnal (white) and semidiurnal (black) migrating tides are given.

at 90.6 km, the phase is opposite to the W/K data. The SD tide is strongly underestimated in the model in comparison with the lidar measurement ($A_2 = 4.1$ K vs. 13.1 K), while there is close agreement for the phase ($\phi_2 = 3.3$ h vs. 2.9 h) which is also confirmed by the W/K combination. The GSWM predicts a general increase in tidal amplitude above 90 km which is not observed in the measurement up to 98 km. Compared with the lidar observation, the SD vertical wavelength ($\lambda_{z,2} > 50$ km) is overestimated by 15 km.

The GSWM results for February at 54°N are very similar to those for November at 27°N. The amplitudes are reduced but the SD tide remains the stronger component and its phasing is practically unchanged. At 90.6 km both components are much weaker than in the lidar measurements ($A_1 = 2.2$ K vs. 0.8 K and $A_2 = 8.7$ K vs. 2.4 K) but the phases agree within 1 h. A propagation of the D phase was not detectable but the phase jump (at 85 km in the lidar data) is remarkably similar to the discontinuity at 86 km in the GSWM. The model results do not change much during the winter months, although the phases are shifted in January. Compared with the DJF case of the W/K combination, the amplitudes are again too low and also the phases are significantly different.

The most recent model version GSWM-02 (*Hagan and Forbes*, 2002, 2003) includes non-migrating tidal components forced by tropospheric H_2O insolation absorption and convective latent heat release. The tidal amplitudes for 90.6 km vary with longitude by ±20–40% while the phases are almost unchanged. In November near Tenerife (27°N, 20°W), $A_1 = 5.0$ K was calculated which is in good agreement with the W/K combination. The SD tide adopts its highest amplitude at this longitude ($A_2 = 4.7$ K), thereby slightly reducing the difference to the measured values. For February near Kühlungsborn, nearly the lowest values within the latitudinal range are calculated ($A_1 = 1.7$ K, $A_2 = 2.1$ K). Nevertheless, the inclusion of non-migrating components improves the agreement with the continuous lidar measurements for the diurnal tide in all cases.

General circulation models often include the calculation of tidal oscillations. From the **COMMA-IAP** (see also p. 70), tidal results for winter solstice conditions are available (*Berger, private communication*). In the model version used, non-migrating components contribute only to about 10% of the tidal amplitudes (*Berger*, 1994) and, hence, the results can be interpreted as migrating tides. The nearest grid points to the lidar stations are 27.5°and 52.5°N, and the

results for 89 km are listed in the tables above. For the low latitude, the diurnal tide is in good agreement with the combined W/K measurements, including the phase. The semidiurnal tide, although quite strong, is still weaker than determined in both measurements and of opposite phase, while the TD component is reasonably small. At midlatitudes, the model predicts a prevalent SD tide and a weak D tide, what seems to be correct in comparison with the 5-day lidar run. On the other hand, the 8-h tide is underestimated and the phase agreement is poor, also in relation to the DJF results for the W/K combination.

The **RAS-DNM GCM** (*Grieger et al.*, 2002) includes longitudinal dependence of the tropospheric forcing of solar thermal tides and migrating and non-migrating components have been analysed separately. Temperature tides for 86 km near Tenerife (28°N, 20°W) are given in Table 5.6 and 5.7 (*Grieger, private communication*). For November, the diurnal amplitude has a maximum at this altitude with 5.5 K whereas the semidiurnal is weak (0.5 K). For the local D tide, migrating (4.7 K) and non-migrating (1.3 K) components add constructively, while they partly annihilate for the SD tide, being 1 K and 0.7 K, respectively. For January near Kühlungsborn (56°N, 20°E), all amplitudes are below 1 K at this altitude. The D and SD tides remain small over the whole altitude range up to 105 km and only the TD non-migrating component reaches 3.5 K near 100 km. Thus, with the exception of the diurnal tide at 28°N, all tidal components are clearly underestimated. While the absolute values of the phases deviate from the lidar measurements, their vertical structure is closely related. The vertical wavelength of the SD tide is in perfect agreement with the measured values: 32 km in November at 28°N and 21 km in January at 56°N. The D phase at low latitudes indicates a clear upward propagating tide in the model which was not observed in November. By contrast, a phase jump is predicted for the D tide near 90 km at 56°N, similar to the measurements at 85 km. The TD phase propagates at the same velocity as the SD phase near 90 km in the RAS-DNM GCM in both cases. This supports the interpretation of our observations that the TD tide is often closely coupled to the D or SD tide.

In summary, it is noted that the comparisons with model results yield relatively few agreements. In the models, the semidiurnal tide is mostly underestimated and the phases often differ significantly from the measurements. The GSWM gives a good approximation of the diurnal amplitude due to the inclusion of non-migrating components and represents closely the observed phase of the semidiurnal tide. However, due to the longer vertical wavelength than in the lidar observations this agreement is found near 90 km only. On the other hand, the COMMA-IAP provides the most reasonable semidiurnal amplitudes, especially at 54°N, and the RAS-DNM GCM correctly predicts the vertical wavelengths for the SD tides.

Similar results were achieved concerning the tidal amplitudes for 40°N in winter which are also underestimated in the GSWM in comparison with the Na-lidar results (*States and Gardner*, 2000b). The amplitudes at 41°N are slightly larger and thus the differences to the model greater (*She et al.*, 2002a). On the other hand, D and SD phases are in relatively good agreement with the Na-lidar measurements at both stations, in cases when these show a clear upward propagation.

Models seem to suggest (*Hagan et al.*, 1999) that maximum tidal amplitudes around 90 km should not exceed 6–8 K but they are observed to be larger. Models widely assume temperature tides as being caused by adiabatic compression and expansion, and propagating upwards into the mesopause region. Other possibilities need to be examined further, including diabatic processes like chemical heating which could also introduce temperature fluctuations and may account for the fact that today models represent wind tides much better than temperature tides.

5.5 Conclusions

Solar thermal tides play an important role among the perturbations of the temperature structure of the mesopause region as they cause the strongest and most persistent variations. The derivation of tidal parameters from lidar observations has been demonstrated and discussed using different approaches. While providing quantitative information the measurements also reveal a large variability of the tides on all time scales.

For both diurnal and semidiurnal tides 5 K are a typical amplitude at low and midlatitudes in this altitude region. The cases considered between November and February were identified with winter conditions. They exhibit a strong prevailing semidiurnal tide with amplitudes which regularly exceed 10 K and which are mostly underestimated by models. The most constant parameter seems to be the phase of the semidiurnal tide which is almost unchanged even between different latitudes. The clear phase propagation denotes a single upward propagating mode with vertical wavelengths between 20 and 35 km in winter.

In contrast, the diurnal tide appeared with a highly variable phase and no distinct vertical structure at 28° and 54°N. It is presumably a superposition of various propagating and trapped modes and, additionally, it may be influenced by non-migrating tides. The classical diurnal modes are expected to peak near 40°N and the diurnal tide appears more clearly structured there. On occasion, however, downward propagating, trapped, and/or multiple modes for diurnal tides are also observed at this latitude (*States and Gardner*, 1998; *She et al.*, 2003). This is in general agreement with classical theory which predicts that semidiurnal forcing goes mainly into one single global mode, whereas much of the diurnal forcing is bound in trapped modes and the remainder distributed over several modes (*Lindzen*, 1990; *Berger*, 1994, p. 129). During the 7-day lidar run at 28°N in November 2000, no detectable 24-h oscillation occurred while the tidal analysis was influenced by a 32-h wave. The absence of a significant amplitude in this case is in agreement with observations near 40°N which also showed periods with only weak diurnal tides in late November (*Drob et al.*, 2000; *States and Gardner*, 2000b).

Terdiurnal oscillations are observed with notable amplitudes and are often closely correlated to the diurnal and semidiurnal tides which suggests that a coupling mechanism exists between them. TD tides are usually not the dominant component and, thus, they cannot be derived accurately from lidar observations unless D and SD oscillations are also deduced which requires measurements covering complete diurnal cycles.

The nighttime mean temperature tends to be biased towards higher temperatures from 84 to 95 km at 54°N in February. On the contrary, a negative bias was deduced from the W/K combination for 89 km at 28° and 54°N in winter. Since the diurnal tides are relatively weak and do not exhibit a clear propagating structure, the bias of the nighttime mean temperatures, and especially of the temperature gradient, are expected to be smaller at 28° and 54°N than near 40°N.

The observations discussed have provided valuable and in many respects initial information about tidal temperature perturbations. Nevertheless, it has become evident that more climatological measurements over complete diurnal cycles are necessary to clarify the role of tides in the mesopause region in detail. Continuously measuring groundbased instruments should be combined with satellites which simultaneously observe the horizontal temperature structure with high temporal resolution. Hence, metal resonance temperature lidars with daylight capability can contribute largely to the future exploration of tides in the middle atmosphere.

Chapter 6

Summary

Lidar measurements of the temperature structure and potassium layer in the mesopause region (80–105 km) have been reported in this work. Based on existing potassium temperature lidar technology, a new lidar system has been set up at the Leibniz-Institute of Atmospheric Physics in Kühlungsborn. A multitude of technical developments have improved the emitter and the receiver unit of the potassium lidar. Measurements have successfully been performed at different locations. Parts of the extensive data set have been analysed with respect to seasonal and latitudinal variations, as well as tidal signatures. The main results of this work can be summarized as follows.

- Determining the Doppler broadening of the potassium resonance line with a narrow-band laser has proven to be an appropriate technique to measure temperature profiles of the mesopause region with high resolution and high accuracy.

- With the recent developments, the tunable all solid-state laser system has become a reliable and stable high power emitter for continuous long-period observation of the mesopause region.

- The development of the Faraday Anomalous Dispersion Optical Filter (FADOF) together with a narrow field of view and a highly efficient detector has enabled temperature measurements in full daylight. The filter curve is almost ideal with efficient background reduction, high transmission and no temperature bias implied.

- Measurements at Tenerife (28°N), Kühlungsborn (54°N) and Svalbard (78°N) have provided climatological data sets. The potassium layer and temperature structure at mid and low latitudes have been analysed and revealed seasonal variations and latitudinal differences, though the Tenerife data do not cover a full year's cycle. Comparisons with other observations and model calculations were presented.

- An outstanding feature of the potassium layer is its semi-annual variation with high peak and column densities around the solstices. The seasonal differences between summer and equinox increase towards lower latitudes in spite of the decrease in temperature variation: $C_K = 3$ to 5×10^7 cm^{-2} at Kühlungsborn and 2.5 to 6×10^7 cm^{-2} at Tenerife.

- The temperature structure of the mesopause region exhibits worldwide a two-level characteristic which has been established by lidar measurements from the subtropics to polar latitudes.

- At Kühlungsborn, the three year nighttime data set confirms the results deduced from the first year of measurements, showing a maximum annual variation of ±25 K at 86 km and less than ±2 K at 97 km.

- At Tenerife, the nighttime mean temperature structure exhibited a low mesopause state for about 4 weeks in summer, characterized by an altitude of 86 km and a temperature of 183 K. Thereby the mesopause is similar in altitude and slightly warmer than at midlatitudes. In November a regular mesopause with 194 K at 100 km was observed.
- The nighttime lidar measurements have shown the presence of strong tidal perturbations, presumably with a dominant upward propagating semidiurnal tide but the analysis is obstructed by the limited local time coverage. At Tenerife the semidiurnal activity was found to be weaker in summer than in November.
- The combination of nighttime lidar measurements with daytime satellite data (WINDII) provides diurnal temperature data at 89 km, from which diurnal tides with amplitudes of about 5 K were estimated for low and midlatitudes.
- Two continuous lidar runs over several days give an excellent possibility to study the temporal development of the temperature. The diurnal tidal component in winter was estimated weaker than that from the lidar/satellite combination. No detectable diurnal tide was present in the observation at 28°N. The diurnal tide was significant at 54°N but no single propagating tidal mode was apparent. The nighttime temperature bias was towards higher temperatures between 84 and 95 km.
- The semidiurnal tide is the prevailing component in the 85 to 95-km region with amplitudes around 10 K in winter at low and midlatitudes. The amplitude is regularly underestimated in current tidal models. The terdiurnal tide appears to be strongly coupled to the 24-h and 12-h oscillations.
- The spectral analyses have confirmed the existence of a permanent semidiurnal tide. It exhibited strong day-to-day variations in amplitude but a relatively constant phase. The variability of the tidal amplitudes is similarly high as observed on interannual and intraseasonal scales.
- Additional oscillations with periods above 24 h and below 12 h were identified. Coupling between different tidal, gravity and planetary waves has been suggested by the results.

Possible Fields of Work for Future Research

The nighttime data sets obtained have provided valuable information about the thermal structure of the mesopause region. With respect to the climatology, some open questions remain which concern for example the possible nighttime bias or long-term temperature variation. The potassium lidars are now capable of long continuous temperature measurements, though the background sensitivity needs to be reduced further. This opens a wide range of possibilities to explore the temperature fluctuations, especially those caused by waves and tides. The strong variability of the tidal parameters on the scale of years, months and days has shown that a large database of well-distributed measurements is necessary to obtain a consistent climatological picture of the temperature tides. In order to take the horizontal structure into account and distinguish between migrating and non-migrating tides, it would be desirable to combine continuous diurnal lidar measurements with simultaneous satellite data. Additional information could also be obtained by the simultaneous operation of two lidars at a certain horizontal distance. Merging the potassium lidar data with that from other lidar systems operated at the same site allows to study waves over a large vertical range.

Acknowledgements

I wish to thank everybody who has supported me during the work to this thesis and contributed to its accomplishment.

Firstly, Professor von Zahn deserves my gratitude for the opportunity to perform this work at the IAP in Kühlungsborn. His support and stimulations have enabled a versatile and interesting work. I am also indebted to Professor Lübken for the continuing support since his appointment as the new director of the IAP.

I thank Josef Höffner for the good cooperation in daily and nightly work as well as on special occasions like during the campaigns at Mount Teide. I have greatly benefitted from his profound knowledge on technical and computational means.

My gratitude is expressed to the lidar group of Professor She at Colorado State University for their initial help with the development of the Faraday filter. The theoretical calculations were largely facilitated by the support by Biff Williams and the computer program originally written by Steven Tomczyk.

For the good collaboration concerning the analysis of the combination of WINDII and lidar data I am thankful to Marianna Shepherd. From her and our work I have learned much about tides as well as about satellite data.

I am thankful to U. Berger, N. Grieger, M. Hagan and P. Hoffmann for providing unpublished model and radar data.

Parts of the work to this thesis were funded by the Kultusministerium des Landes Mecklenburg-Vorpommern under grant IAP 89 001 70 - 1998, (‘Entwicklung eines extern stabilisierten und durchstimmbaren Seederlasers für ein Kalium-Lidar’) and by the Deutsche Forschugsgemeinschaft under grant AL 458/3-1 (‘Thermische Gezeiten und Tagesmittel von Temperaturprofilen in der Mesopausenregion’).

I acknowledge the time and efforts spent by numerous people from the IAP during the time consuming acquisition of the lidar data used in this work. I wish to thank the optics group and all the other people at the IAP. I have enjoyed and greatly benefitted from working with you.

For proof-reading and corrections of the manuscript I am especially grateful to Matthias Alpers, Eiko Nemitz, Michael Gerding and Howard Canning.

Zu guter letzt, aber sicher nicht am wenigsten, möchte ich mich bei denjenigen lieben Menschen bedanken, die mich begleitet haben und ohne deren Rückhalt und Zuversicht diese Arbeit so nicht möglich gewesen wäre. Für viel Kraft und Liebe danke ich Birgit von Herzen. Ein besonderes Dankeschön geht an meine Eltern und Familie für die nie versiegende Unterstützung.

Appendix A

Atomic Data on Potassium

The most important atomic data used in this work are collected in this appendix. General data are taken from the CRC Handbook (*Lide*, 1999) and the physical reference database (http://physics.nist.gov/PhysRefData) of the NIST (National Institute of Standards and Technology).

The alkali metal potassium is characterized by:

Atomic number	^{19}K
Standard atomic weight	39.0983(1)
First ionization energy	4.3407 eV
Ground state level	$^2S_{1/2}$
Ground state configuration	[Ar:1s^{2}2s^{2}2p^{6}3s^{2}3p^6] 4s

Its natural isotopic composition is:

Isotope	Atomic mass	Abundance	Nuclear spin	K(D_1) line shift
39	38.963 706 9(3)	0.932 581(44)	$I = 3/2$	0
40	39.963 998 67(29)	0.000 117(1)	$I = 4$	125.58 MHz
41	40.961 825 97(28)	0.067 302(44)	$I = 3/2$	235.28 MHz

The naturally occurring radioactive ^{40}K decays slowly ($\tau = 1.26 \times 10^9$ y). Due to its low abundance it is not considered in the calculations. The isotopes 42 and 43 have half-life periods of several hours.

The ground state resonance lines K(D_1) and K(D_2) together are known as the Fraunhofer A′ line and given below. The index of refraction used is $n_{\text{air}} = 1.000275$. The oscillator strength f is related to the transition coefficient A_{ik} by $f = A_{ik}\frac{g_k}{g_i}\lambda^2 \cdot 1.4992 \times 10^{-16}$, where A_{ik} is given in s^{-1} and λ in Å. The lower (g_i) and upper (g_k) statistical weights are given by the total electronic angular momentum as $g = 2J + 1$.

Transition	K(D_1)	K(D_2)
Wavelength air [nm]	769.8974	766.4911
Wavelength vacuum [nm]	770.1093	766.7021
Rel. intensity	24	25
A_{ik} [$10^8 s^{-1}$]	0.382 (±10%)	0.387 (±10%)
f-value	0.340	0.682
Terms $^{2S+1}L_J$	$^2S_{1/2} - {}^2P^o_{1/2}$	$^2S_{1/2} - {}^2P^o_{3/2}$
$g_i - g_k$	2-2	2-4

The K(D_1) Transition

The most recent accurate measurements of the values for the K(D_1) transition by *Saloman* (1993) are used for this work (uncertainties were not given):

Center resonance level	$\bar{\lambda} = 12985.170\,\mathrm{cm}^{-1}$
Oscillator strength	$f = 0.339$
Lifetime (≈relaxation time)	$\tau = 26.2\,\mathrm{ns}$

The lifetime gives a natural transition linewidth of $\nu_N = (2\pi\tau)^{-1} = 6.1\,\mathrm{MHz}$ (FWHM). Using the internationally recommended values of the fundamental constants (CODATA1998) the line center can be expressed in different units:

Unit	K(D_1) line	Conversion factor
$\bar{\lambda}$ [cm^{-1}]	12985.170 (1)	
λ_{vac} [nm]	770.109 286 (59)	
ν [Hz]	3.892 856 03 (30) $\times 10^{14}$	$c = 299792458\,\mathrm{m/s}$
E [J]	2.579 433 17 (29) $\times 10^{-19}$	$h * c = 1.98644544(16) \times 10^{-25}$ Jm
E [eV]	1.609 955 73 (14)	$hc/e = 1.239841857(49) \times 10^{-6}$ Jm/As
λ_{air} [nm]	769.897 387	$n_{air} = 1.00027523$ (CRC99)
λ_{air} [nm]	769.884 480	$n_{air} = 1.000292$
λ_{air} [nm]	769.898 334	$n_{air} = 1.000274$

At 770 nm the refractive index of standard air (15°C, 101.325 kPa, 0.03 Vol-% CO_2) is given by the CRC Handbook as $n_{air} = 1 + 27523 \times 10^{-8}$. Different values are used in different works and often not stated explicitly. The actual value can result in a change of λ_{air} by more than 0.01 nm. A difference in wavelength of $\Delta\lambda_{air} = 1\,\mathrm{pm}$ equals 505.84 MHz and 16.86×10^{-3} cm^{-1}.

The hyperfine structure (hfs) splitting is caused by the interaction of the magnetic field originating from the electronic shell with the magnetic moment of the nucleus, in the case of a non-vanishing nuclear spin. J and I couple to a total angular momentum $F = I - J, \ldots, I + J$. For K(D_1) the quadrupole interaction constant is zero and the dipole constant was measured by *Saloman*. It is 230.86 MHz for the ground and 28.0 MHz for the upper state of ^{39}K. The values for ^{41}K are 127.01 MHz and 15.2 MHz, respectively. This results in the following total offsets of the hfs components from the line's center of mass:

$^2S_{1/2}$	$^2P_{1/2}$	^{39}K		^{41}K		Line strength
		[MHz]	[pm]	[MHz]	[pm]	relative
F=1	F'=2	310	-0.61	405	0.80	5
	F'=1	254	-0.50	375	0.74	1
F=2	F'=2	-152	0.30	151	0.30	5
	F'=1	-208	0.41	121	0.24	5

For a discussion on the effective line intensities see, for example, *Windholz and Musso* (1988). For a thorough discussion of the effective backscatter cross-section, I refer to the comparable lineshape of sodium which has been treated more extensively in the literature (e. g. *Chamberlain et al.*, 1958; *Fricke and von Zahn*, 1985).

Appendix B

U. S. Standard Atmosphere, 1976

The U. S. Standard Atmosphere *USSA* (1976) gives mean values for the Earth's atmosphere. It attempts to depict idealized year-round midlatitude vertical profiles for the following values:

Geometric altitude	z	$[10^3\,\mathrm{m}]$
Geopotential altitude	H	$[10^3\,\mathrm{m}]$
Kinetic temperature	T	[K]
Pressure	p	$[10^2\,\mathrm{Pa}]$
Mass density	ρ_m	$[\mathrm{kg/m^3}]$
Number density	ρ_n	$[\mathrm{m^{-3}}]$
Acceleration due to gravity	g	$[\mathrm{m/s^2}]$
Pressure scale height	H_p	[m]
Particle speed	v	[m/s]
Collision frequency	ν	[1/s]
Mean free path	L	[m]
Molecular weight	M	[kg/kmol]

In Table B.1, values at some altitudes are extracted to give a guideline for estimating atmospheric properties. The stratopause is located at 49 km ($T = 270.65$ K) and an isothermal mesopause range 86–91 km is given with 186.87 K.

Table B.1: *USSA* (1976): values are reproduced with at least 4 significant digits when possible.

z	0 km	10 km	30 km	60 km	90 km	120 km
H	0	9.984	29.86	59.44	88.74	117.8
T	288.15	223.25	226.5	247.0	186.9	360.0
p	1013.25	264.99	11.97	0.2196	1.836 e-3	2.538 e-5
ρ_m	1.2250	0.4135	1.841 e-2	3.097 e-4	3.416 e-6	2.222 e-8
ρ_n	2.547 e+25	8.598 e+24	3.828 e+23	6.439 e+21	7.116 e+19	5.107e+17
g	9.8066	9.776	9.715	9.624	9.535	9.447
H_p	8434	6555	6693	7368	5636	12091
v	458.9	404.0	406.9	424.9	369.9	539.3
ν	6.919 e+9	2.056 e+9	9.219 e+7	1.620 e+6	1.56 e+4	163
L	6.633 e-8	1.965 e-7	4.414 e-6	2.624 e-4	2.37e-2	3.31
M	28.964	28.964	28.964	28.964	28.91	26.2

Appendix C

Data Analysis

The most important mathematical methods used in this work to analyse the data, from the received signal to the obtained time series, are summarized in this appendix. With the exception of the *consistency test*, they have been discussed in detail in the literature.

The numerical evaluation is realized using the programming environment DELPHI (Borland, Inc.) with a shared object library and database developed by the IAP lidar group to match its specific requirements. Many mathematical routines are based on the *Numerical Recipes in Pascal* (*Press et al.*, 1989).

Error Bars

Continuous variables like atmospheric parameters are assumed to follow the *Gaussian* (or *normal*) distribution, which is characterized by the probability density function

$$f(y) = \frac{1}{\sigma\sqrt{2\pi}} e^{-\frac{(y-\mu)^2}{2\sigma^2}}, \tag{C.1}$$

where μ is the expectation value of the continuous variable y. Unless stated otherwise, the uncertainty of a value is given throughout this work as its standard deviation σ which equals the square root of the variance of its distribution.

For discrete distributions, e. g. counting processes, *Poisson statistics* have to be applied to describe the probability that a number $y = 0, 1, 2, \ldots$ is realized:

$$P(y) = \frac{\lambda^y}{y!} e^{-\lambda}. \tag{C.2}$$

The parameter λ equals both the expectation value and the variance. If it has an integer value, the probability of $y = \lambda$ and $y = \lambda - 1$ is the same. For large values of λ the Poisson distribution converges towards the Gaussian.

If the variance has to be calculated from the mean $\bar{y}$ of a data set y_i ($i = 1, .., N$), the degrees of freedom are reduced to $N - 1$ and the variance is calculated to be $\sigma^2 = \sum(y_i - \bar{y})^2/(N-1)$. Mean values calculated from independent sets of N data points are distributed with a reduced variance of σ^2/N. The mean $\bar{y} \pm \frac{\sigma}{\sqrt{N}}$ has an error probability of $\beta = 31.7\%$.

Fitting of Model Functions

If a model function $\tilde{f}_a(t)$ is to be fitted to a series of data points (t_i, y_i), with $i = 1..N$, measured with respect to t, the most *likely* set of parameters a is sought. It is taken to be the model with the highest probability of the given data set as a realization. Assuming normal (Gaussian) distributions around the *true* model with individual standard deviations σ_i, the best fit is the

parameter set which gives a minimum for the function

$$\chi^2 = \frac{1}{N}\sum_i \left(\frac{y_i - \tilde{f}_a(t_i)}{\sigma_i}\right)^2 . \tag{C.3}$$

This is called a *least mean square* (LMS) fit and is usually realized in this work by employing the *Levenberg-Marquardt* algorithm (*Press et al.*, 1989), which is suitable for linear and non-linear functions. In the case of counting processes, the LMS approach is not ideal because the Poisson distribution deviates from the Gaussian. The convergence towards the normal distribution is relatively slowly out on the tail of the distribution what leads to the fact that outliers are overestimated in the LMS fit. Instead, a *robust estimation* (*Press et al.*, 1989) can be applied. It is used for example to derive the temperature from the measured photon counts (Section 3.2.4).

C.1 Harmonic Analysis

The measured temporal variation of the temperature or other atmospheric parameters is analysed to identify the inherent contribution of periodic processes (e. g. waves or seasonal variations). In some cases the calculation is naturally limited to a few frequencies, as for the tidal analysis. In this case, the most direct method is an LMS fit of the expected function $\tilde{f}(t)$ to the data. For harmonic analysis the fitting function is chosen as a superposition of sinusoids:

$$\tilde{f}(t) = A_0 + \sum_{i=1}^{m} A_i \cos(\omega_i(t-\phi_i)) \ . \tag{C.4}$$

Here, A_0 is a constant offset, the m amplitudes of the individual periods $T_i = 2\pi/\omega_i$ are A_i, and the phases ϕ_i denote the time of the maximum value in the interval $[0, T_i]$. Usually the periods are fixed values (e. g. $T_1 = 24\,\mathrm{h}$, $T_2 = 12\,\mathrm{h}$) but they can also be fitted as free parameters.

The harmonic fit in the sense of Eq. C.4 can produce valuable results only if the parameters are chosen in a sensible way according to the problem, and sometimes it relies on a good approximation for the starting values of the parameters. For example, if the temperature is measured for many days and then averaged in bins with respect to local time, a time series is achieved on the interval of $[0, 24\,\mathrm{h}]$, as in Chapter 5. To this series any period can be fitted but only harmonics of 24 h are sensible because for others the function does not correspond to the local times the data were measured at, except for one certain day.

In general, the results for the individual harmonics are not independent from each other, except for one special case. Only if the time series is sampled at equally spaced intervals t_i and with equal uncertainties σ_i over a period T_{tot} the fitting results for harmonics of the sampling period (i. e., $T_i = T_{\mathrm{tot}}/i$) do not influence each other. This is usually not the case for measured data. It means that, e. g., the amplitude of a 12-h component will change if a 24-h or 8-h component is included in the fitting function $\tilde{f}$. A simultaneous fit of m periods will differ from the results of m individual fits of the single periods.

The following example represents typical conditions for nighttime lidar operation where it occurs that $f(t)$ has been sampled over much less than the full period of 24 h. In this case the diurnal harmonic cannot be fitted with reliable results, as has been discussed in the literature (e. g. *Crary and Forbes*, 1983; *Gille et al.*, 1991). On the other hand, an existing 24-h oscillation can have an erroneous influence on the results for the higher harmonics as shown

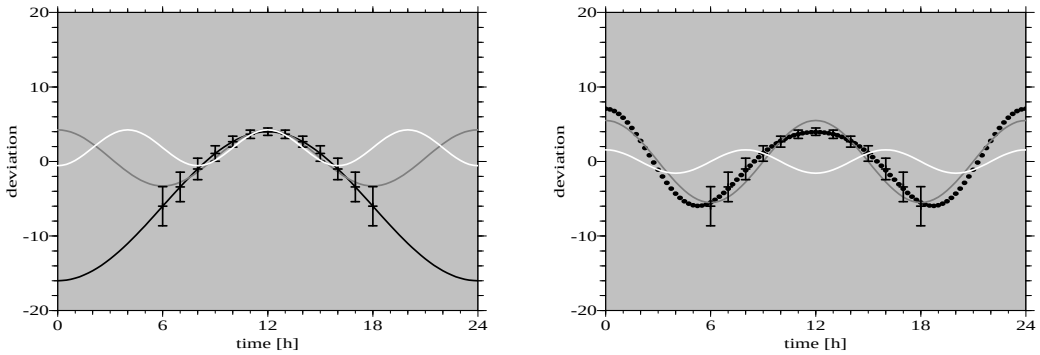

Figure C.1: Example for the fit results of hypothetical data representing a partially sampled 24-h oscillation (error bars). Left: individual fits of 24-h (black), 12-h (grey) and 8-h (white) oscillations. Right: a combined fit (dotted) of 8-h and 12-h oscillations with the components shown separately (grey, white).

in Figure C.1. It represents a pure 24-h oscillation with $A_1 = 10$ and $A_2 = A_3 = 0$, which is sampled during its positive half only, i. e. daytime. While the 24-h harmonic function provides the true waveform, individual 8-h and 12-h harmonics reproduce the hypothetical data to some degree with amplitudes of $A_2 = 3.8$ and $A_3 = 2.4$ (left panel). A combined fit (right panel) with both periods represents the data astonishingly well with amplitudes of $A_2 = 5.5$ and $A_3 = 1.6$. However, it is far off the true behaviour at times when the oscillation was not sampled. At $t = 0$ h the prediction is off by 23 units from the correct value. The two components of the combined function are shown also and it is found that the 8-h phase is opposite to the individual fit. For the error bars given, all these results are statistically highly significant, whereas for combination of 24-h, 12-h and 8-h harmonics the results are insignificant though they are correct due to the absence of noise ($A_1 = 10 \pm 23$).

The false amplitude results can even be doubled when the phase of the 24-h oscillation is shifted relative to the period of data sampling. The erroneous results are reduced only slowly when the sampling interval is extended. Thus, in order to achieve reliable results concerning all tidal oscillations, a sampling interval of nearly 24 h is required.

The Consistency Test

A novel method is applied in Section 5.2 for the tidal analysis when the diurnal harmonics are to be determined from a combined data set of lidar and satellite obtained temperatures (*Shepherd and Fricke-Begemann*, 2004). The temperatures are measured by WINDII during daytime by the lidar during nighttime. The two data sets can be fitted separately for the series of harmonics but they will not reveal the 24-h component. To identify this the complementary data sets $(T_i, t_i)^D$ and $(T_i, t_i)^N$ are combined. The mean temperatures have to be subtracted from each data set to avoid influences from instrumental bias, period and location of observation. The usage of residuals, however, implies that the real mean temperatures during both observation periods were identical. This is usually not the case due to the influence of the diurnal tide which is to be determined.

The harmonic series $\tilde{T}$ is first fitted to the combined zero-mean data set. From this fitted $\tilde{T}$ the predicted ensemble means for the two data sets are calculated separately, e. g. $\Delta T^D = \langle \tilde{T}(t_i) - T_i \rangle^D$. Typically ΔT^D and ΔT^N will not be identical but differ, mainly due to the 24-h

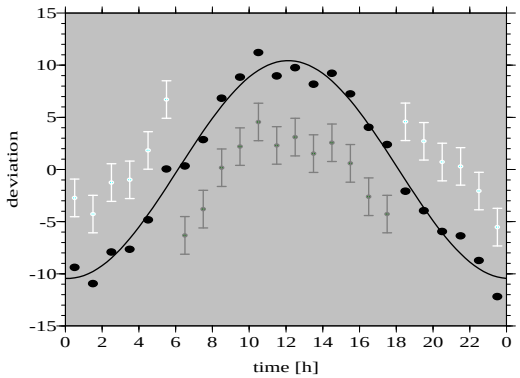

Figure C.2: Example for the consistent combination of two synthetic residual data sets for night- (white) and daytime (grey) obtained from a 24-h harmonic oscillation with an amplitude of 10 plus artificial noise. The consistency test restores the original offset to the data (dotted) and gives the correct fit result (black line).

component. This result is in turn not consistent with the implicate assumption of an identical mean which was made when combining the residual data sets. For correction, the calculated mean is added as an offset to the data sets giving $(T_i + \Delta T^D, t_i)^D$ and $(T_i + \Delta T^N, t_i)^N$. To the corrected data the series is fitted again and the means are re-calculated. This procedure is repeated until the means calculated from the fit agree with those of the data sets, i. e. fit function and offset are consistent. It can be shown that the recursion is converging. A number of simulations have shown that the true offsets are calculated, provided that the model function agrees with the 'true' course of the data (plus unsystematic scattering). As a simulation example, Figure C.2 shows the residual data sets with their mean subtracted (white and grey) together with the consistent data and the final fit (black). The initial fit (not shown) to the simply combined data gives an amplitude of less than 20%.

One expects the diurnal amplitude to increase during this procedure as its effect is partly cancelled out by the use of the residuals. Even if applied to the absolute temperatures the method can only provide the correct relative offset, but naturally not the correct mean value.

C.2 Spectral Analysis

The temporal development of a physical variable often needs to be analysed with respect to its frequency content. Correctly speaking there is a systematic difference between *harmonic analysis*, the detection of regular periodic signals, and *spectral analysis*, the description of how variance is distributed as a function of time scale in non-periodic processes. Nevertheless, they have some common properties and a number of mathematical tools exist which serve both purposes depending on the conditions. Here a short introduction to the methods used in this work shall be given, more details can be found in a number of textbooks and reviews (e. g. *Taubenheim*, 1969; *Press et al.*, 1989; *von Storch and Zwiers*, 1999; *Ghil et al.*, 2002). In contrast to the harmonic fits, the results for different frequencies do not influence each other but the uncertainties of the sampled data points are not taken into account. Spectral analyses are useful only for long time series where the observation period is a multiple of the signal periodicity.

The most common method is to describe a function $f(t)$ by a trigonometric expansion, the *continuous Fourier transformation*:

$$f(t) = \int_{-\infty}^{\infty} F(\nu) e^{2\pi i \nu t} d\nu \,. \tag{C.5}$$

The Fourier transform function $F(\nu)$ is calculated by inner product of the base function with the variable $f(t)$:

$$F(\nu) = \int_{-\infty}^{\infty} f(t) e^{-2\pi i \nu t} dt \,. \tag{C.6}$$

For the practise of real functions, the Fourier transform is symmetrically equal to its complex conjugate ($F(-\nu) = F^*(\nu)$).

In many situations the value of $f(t)$ is recorded at evenly spaced time intervals. The N discretely sampled values at intervals of Δt are

$$f_n = f(t_n), \quad t_n = n\Delta t, \quad n = 0, 1, 2, \ldots, N-1 \,. \tag{C.7}$$

The function $f(t)$ is completely determined by the series f_n if it is bandwidth limited to frequencies smaller in magnitude than the *Nyquist critical frequency* $\nu_c = 1/(2\Delta t)$. Higher frequencies are aliased into the frequency range $[-\nu_c, \nu_c]$ and produce false results. The *discrete Fourier transform* is represented by a set of N discrete *natural* frequencies over the range $-\nu_c$ to ν_c

$$\nu_k = \frac{k}{N\Delta t}, \qquad k = -\frac{N}{2}+1, \ldots, \frac{N}{2} \,, \tag{C.8}$$

where N is assumed to be even. The discrete form of the Fourier transform is the mapping from the summable time series to a set of functions defined over the Nyquist interval by

$$\begin{aligned} F(\nu_k) = F_k \Delta t &= \sum_{n=0}^{N-1} f_n e^{-2\pi i \nu_k t_n} \Delta t \\ f_n &= \frac{1}{N\Delta t} \sum_k F(\nu_k) e^{2\pi i \nu_k t_n} \,. \end{aligned} \tag{C.9}$$

The complex Fourier coefficients $F_k = \sum f_n e^{2\pi i kn/N}$ are independent of the length of the sampling interval. In order to simplify the numerical calculation of the Fourier transform, the

measured values are often provided in a set of $N = 2^m$ samples, what allows the application of the *Fast Fourier Transform* (FFT) algorithm.

As can be seen from the given set of frequencies (Eq. C.8) there is very little information in the low frequency range and the sampling interval should be chosen appropriately to provide information for all frequencies of interest. For example, the positive natural frequencies of a $T = 12$ h sampling period with intervals of $\Delta t = 1$ h correspond to periods of 2, 2.4, 3, 4, 6, and 12 h. A longer sampling interval will enhance the spectral resolution while a smaller Δt will extend the range to higher frequencies. However, the transform $F(\nu)$ can be calculated for any frequency with the disadvantage of loosing many properties of the full Fourier transform which is based on a complete set of base functions.

The Power Spectrum

The total power of the function $f(t)$ is defined as the integral over its total squared amplitude and can equivalently be calculated in the frequency domain (*Parseval's theorem*):

$$\text{total power} = \int_{-\infty}^{\infty} |f(t)|^2 dt = \int_{-\infty}^{\infty} |F(\nu)|^2 d\nu \tag{C.10}$$

If the question is addressed how much power is contained in the frequency interval between ν and $\nu + d\nu$, it is convenient to define the (one-sided) *power spectral density* (PSD) of the function $f(t)$ as

$$P_f(\nu) = |F(\nu)|^2 + |F(-\nu)|^2, \qquad 0 \le \nu < \infty. \tag{C.11}$$

It is equal for a real function to $P_f(\nu) = 2|F(\nu)|^2$. For infinite functions the amplitude of the Fourier transform may not be finite (the Fourier transform of a cosine is the sum of two delta functions), thus the PSD per unit time $P(\nu)$ may be considered. It is calculated by taking a finite representative stretch of $f(t)$ (by setting it equal to zero outside the range $[0, T]$), calculating its PSD (C.11) and dividing it by the length T of the time stretch used. Following Parseval's theorem its integral equals the mean squared amplitude of the signal:

$$\int_0^{\infty} P(\nu) d\nu = \frac{1}{T} \int_0^T |f(t)|^2 dt\,. \tag{C.12}$$

For a cosine function $f(t) = A\cos(\omega t)$ the time stretch is taken as a multiple of its period and the above calculation yields the value $A^2/2$. It is noted that for a cosine $P(\nu)$ is not converging but becomes a delta function for $T \to \infty$ while its area is conserved.

After the *Wiener-Khinchin theorem* it is equivalent to define the power spectrum as the Fourier transform of the auto-covariance of the time series. But as the auto-covariance is well defined only over a short range of the time range covered by the data, this is not the best way to calculate the power spectrum of a short time series.

Power Spectrum Estimation

For a certain stochastic process the continuous power spectrum is a well-defined parameter, but for the case of a discretely sampled function f_n the PSD has to be estimated from the data. This can be done in a number of ways, that go under a variety of names in the literature (*Press et al.*, 1989). There are also different normalizations for the total power, from which the *mean squared amplitude* is used here, which is equal to the variance of the sample:

$$\text{total power} = \frac{1}{N} \sum_n |f_n|^2 \approx \frac{1}{T} \int_0^T |f(t)|^2 dt\,. \tag{C.13}$$

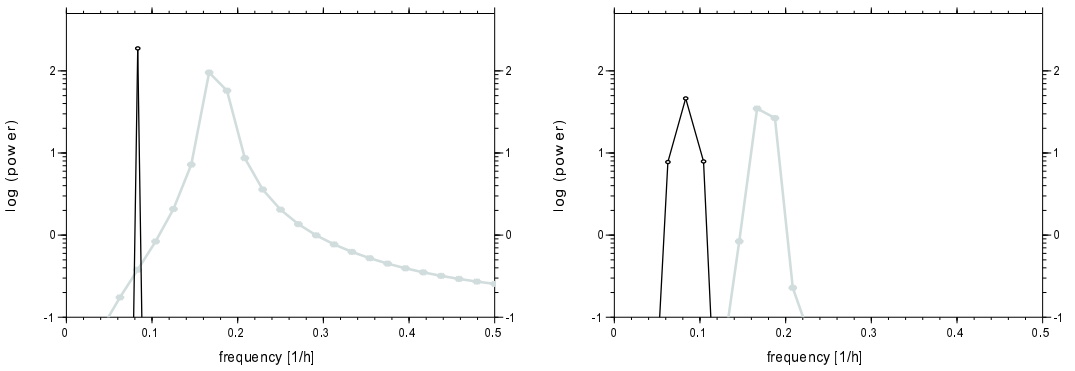

Figure C.3: FFT periodograms of a cosine function with $f = 1/12\,\mathrm{h}$ (black) and $f = 1/5.7\,\mathrm{h}$ (grey) demonstrating the leakage. Left: full FFT; right: windowed FFT.

The classic estimation of the PSD is the *periodogram* using the discrete Fourier transform coefficients (Eq. C.9):

$$\begin{aligned} P(0) &= \frac{1}{N^2}|F_0|^2 \\ P(\nu_k) &= \frac{1}{N^2}\left[|F_k|^2 + |F_{-k}|^2\right] \qquad k = 1, 2, \ldots, \frac{N}{2} - 1 \\ P(\nu_c) &= \frac{1}{N^2}|F_{N/2}|^2 . \end{aligned} \tag{C.14}$$

The expectation value of the $P(\nu_k)$ is some average of the continuous PSD over the frequency range around ν_k extending halfway to its neighbour frequencies. Although, it can be shown that a significant *leakage* from one frequency bin to the neighbouring bins occurs in the Fourier periodogram, i. e. the estimated PSD is smeared out. Only for a pure sine wave of a frequency equal to one of the natural frequencies ν_k there will be no leakage to adjacent ν_k's. The leakage can be reduced by *data windowing* where the stretch of data used is multiplied with a window function that equals one at the center and falls off towards the edges of the interval (see Eq. C.16 below). This effect is demonstrated in Figure C.3 where the periodograms of two different cosine functions with the same amplitude are shown. 64 data points over a period of $T = 48\,\mathrm{h}$ are calculated. The cosine with $f = 1/12\,\mathrm{h}$ (black) matches a natural frequency of the FFT and gives a sharp peak, while the other frequency ($1/5.7\,\mathrm{h}$, grey) lies about halfway between two FFT values ($1/6\,\mathrm{h}$ and $1/5.33\,\mathrm{h}$) and produces a relatively broad periodogram due to the leakage. The window function produces a similar result for both cases (right panel), which is preferable unless the occurring frequencies are exactly known. For the significance of periodograms, see for example *Hernandez* (1999).

A second unpleasant fact about the simple periodogram is its variance which is always 100% (i. e. equal to the square of its expectation value), independent of N. For long data sets or short sampling intervals Δt, the variance can be reduced by averaging the calculated $P(\nu_k)$ either over a number of data segments or a number of calculated frequencies. For the first option it turns out to be optimal to use segments which overlap by one half of their length.

There are some advantages in a different approximation whose free parameters a_k lie in the

denominator, namely,

$$P(\nu) \approx \frac{a_0}{\left|1+\sum_{k=1}^{M} a_k z^{k/M}\right|^2}, \qquad \text{with} \quad z = e^{2\pi i \nu \Delta t}. \tag{C.15}$$

This model is called the *all-poles* or *maximum entropy method* (MEM) and can be calculated with the use of the FFT of the autocorrelation of the f_n. The MEM can possibly have poles in the complex z-plane, i. e., infinite spectral density at real frequencies in the Nyquist interval. This is an advantage compared with the FFT periodogram, making the MEM useful to analyse sharp spectral features, corresponding to discrete frequencies. On the other hand it has to be used carefully as it may produce spurious peaks from data including noise. Whereas $P(\nu)$ can always be evaluated on a very fine frequency grid, the number of parameters M has to be chosen carefully. Necessarily it is $M \leq N$, but usually it is a few times the number of expected sharp spectral features in the data. In the example of Figure C.4 the MEM is calculated with $M = 3$ for the two different cosine functions used in Figure C.3. Other than the FFT it can produce sharp spectral features at the exact frequencies of underlying functions.

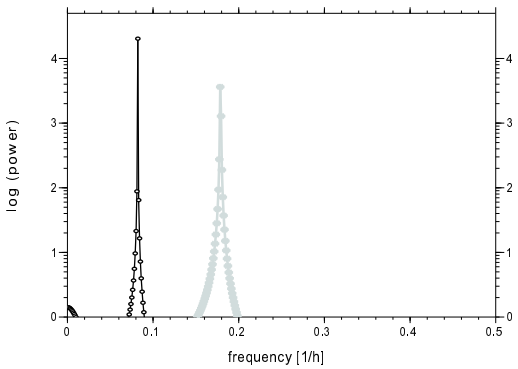

Figure C.4: MEM power estimation for the same functions as in Figure C.3.

Time Dependent Power Estimation: Wavelets

The Fourier transform methods are suitable to analyse homogenous or indefinite periodic functions. For short lived oscillations they do not provide information *at which time* a frequency portion was present. When atmospheric observations are analysed the case of a uniform oscillation is rather seldom (see Section 5.3). In order to deduce temporal information about the intensity of a frequency portion the *windowed Fourier transform* can be used,

$$F^{win}(\omega, t_0) = \int_{-\infty}^{\infty} g(t-t_0)\, f(t) e^{-i\omega t}\, dt\,. \tag{C.16}$$

The window function $g(t-t_0)$ is chosen to be finite near $t = t_0$ and zero for $t \to \pm\infty$. Here it serves to localize the amplitude information in time, while, as mentioned above, it is also useful to correct the spectral leakage of the peridogram power estimation. The accuracy of the localization depends on the window function g but not on the angular frequency $\omega = 2\pi\nu$. In general, a wider window function provides more accuracy in the frequency range while a narrower window gives better temporal resolution. The localization in the frequency domain can be derived from the Fourier transform of the window function $G(\nu)$, using the variances σ_g^2 and σ_G^2 of $g(t)$ and $G(\nu)$, respectively. Owing to the uncertainty principle, their relation satisfies $\sigma_g^2 \sigma_G^2 \geq \pi/2$, where the equality is achieved only when $g(t)$ is a Gaussian.

Under some circumstances it is considered unfavourable that the relative localization in the frequency domain (σ_G/ω) is not constant but becomes worse if longer periods are analysed. Especially for the geophysical analysis of waves this is inconvenient. To overcome

this dependence of the relative localization properties on the frequency the *continuous wavelet transformation* is defined analogously to the Fourier transform (e. g. *Foufoula-Georgiou and Kumar*, 1994):

$$F^{\Psi}(\lambda, t_0) = \frac{1}{\sqrt{\lambda}} \int_{-\infty}^{\infty} f(t) \psi_{\lambda}^{*}(t - t_0) dt \,. \tag{C.17}$$

The function $f(t)$ is projected onto a series of functions

$$\psi_{\lambda}(\delta t) = \frac{1}{\sqrt{\lambda}} \psi_0 \left(\frac{\delta t}{\lambda} \right), \tag{C.18}$$

derived from a *mother wavelet* ψ_0. The parameter λ describes the dilation and δt the time offset. The normalization factor $1/\sqrt{\lambda}$ ensures that $\int |\psi_{\lambda}|^2$ is constant. There are mathematical conditions for a wavelet function leading to the request that it converges to zero for $\delta t \to \infty$ and its Fourier transform does so for $\omega \to 0$.

The main properties of the wavelet functions can be understood when their Fourier transforms $\hat{\psi}_0, \hat{\psi}_{\lambda}$ are calculated. By defining the center of passing band $\omega^0_{\hat{\psi}}$ as the center of mass and the standard deviation $\sigma_{\hat{\psi}}$ over the positive frequency range only, and also σ_{ψ} in the time domain, the following relationships are obtained:

$$\begin{aligned}
\sigma_{\psi,\lambda} &= \lambda \, \sigma_{\psi,0} \quad \text{for the time localization,} \\
\sigma_{\hat{\psi},\lambda} &= \frac{1}{\lambda} \, \sigma_{\hat{\psi},0} \quad \text{for the frequency localization, and} \\
\omega^0_{\hat{\psi},\lambda} &= \frac{1}{\lambda} \, \omega^0_{\hat{\psi},0} \quad \text{for the frequency passing band.}
\end{aligned} \tag{C.19}$$

Thus, the desired feature is obtained that the relative frequency localization $\sigma_{\hat{\psi}}/\omega^0_{\hat{\psi}}$ of the passing band is conserved for all values of the dilation parameter λ.

There is a large number of real and complex mother wavelets (e. g. *Mexican hat, Haar*). From those that one must be chosen which is most appropriate for the application at hand. The different wavelets and their properties are discussed in various textbooks (e. g. *Foufoula-Georgiou and Kumar*, 1994). For oscillatory processes like they are observed in the atmosphere the *Morlet wavelet* is applied, which is defined very similarly to a Fourier transform with a Gaussian window (Eq. C.16):

$$\psi_0(\tau) = \pi^{-\frac{1}{4}} \, e^{-\frac{\tau^2}{2}} \, e^{-i w_0 \tau} \,. \tag{C.20}$$

The dimensionless parameter w_0 determines the number of oscillations ($4w_0/2\pi$) included between the points where the amplitude has fallen to e^{-2}. It is often chosen as the smallest value allowed by the admissibility condition $w_0 \geq 5$. The full half-width of the $w_0 = 5$ Morlet wavelet is $\sim$1.9 periods. Other than for the windowed Fourier transform, the number of oscillations in the window is kept constant for all frequencies. The Fourier transform of the Morlet wavelet ψ is given by

$$\hat{\psi}(w) = \pi^{-\frac{1}{4}} \, e^{-(w - w_0)^2/2} \,. \tag{C.21}$$

The center of its passing band is w_0 and the spreads σ_{ψ} and $\sigma_{\hat{\psi}}$ both equal unity. The wavelet transform is calculated by either the use of Eq. C.17 or the Fourier transform to obtain the amplitude F^{Ψ} as a function of time t and center angular frequency $\omega = w_0/\lambda$ (or period $2\pi\lambda/w_0$). In Figure C.5 (left panel) the Morlet wavelet is shown with a period of 24 h. This mother wavelet is the only one used in this work.

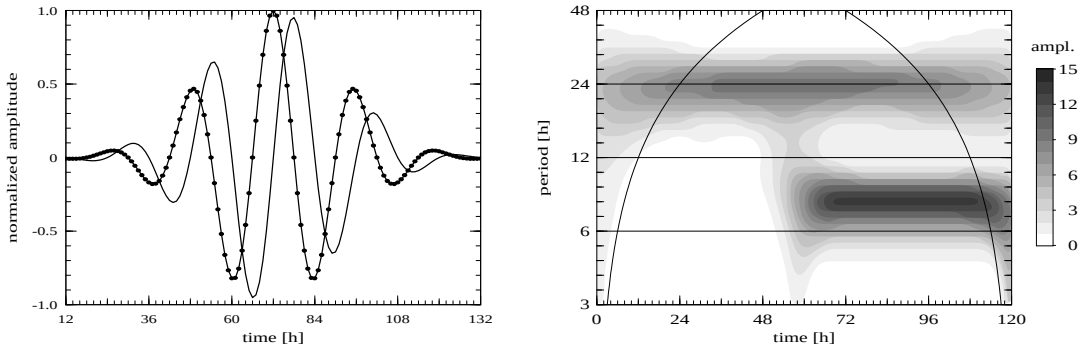

Figure C.5: Left: The Morlet wavelet with a period of 24 h and $w_0 = 5$. The real part (with dots) and the imaginary part are shown, with the real part scaled to unity. Right: The wavelet amplitude spectrum $|F^\Psi|$ of an analytic function in colour contours. The lines mark the cone of influence.

For the discretely sampled data set f_n with $n = 0, \ldots, N-1$ the wavelet transform is defined as

$$F^\Psi(\lambda, t_n) = \frac{\Delta t}{\sqrt{\lambda}} \sum_{n'=0}^{N-1} f_{n'} \psi^* \left(\frac{(n'-n)\Delta t}{\lambda} \right) . \tag{C.22}$$

When a complex wavelet is used the analysis provides in addition to the intensity also phase information about $f(t)$. The phase ϕ_n can be calculated from the complex $F^\Psi(\lambda, t_n)$ using $tan\phi_n = \mathrm{Im}(F^\Psi)/\mathrm{Re}(F^\Psi)$. The phase function $\phi(\lambda, t_n)$ equals one at times when the component with dilation λ is at its maximum value. The wavelet power spectrum is defined as $P^\Psi(\lambda, t_n) = |F^\Psi(\lambda, t_n)|^2$.

A simulated application of the wavelet analysis is shown in the right panel of Figure C.5. Sampled over 120 h are two harmonics with periods of 24 h and 8 h. The first is continuous with an amplitude of 10 and the second has a 50% larger amplitude and starts at half-time. The wavelet spectrum correctly shows both components with their amplitude, time of occurrence and period (on the logarithmic scale given, the periods of 4, 8, 16, and 32 h are at about 2/5 of the major intervals). Also shown is the *cone of influence* denoting the range where edge-effects become important. For about one period from the outside the amplitudes are reduced and the period is less well localized. For introduction to significance tests of wavelet analysis, see *Torrence and Compo* (1998). In one-dimensional power spectra as described in the last section, the 8-h harmonic would simply appear with a lower amplitude.

Appendix D

Monthly Observation Statistics

The monthly observation statistics for the IAP K-lidars is given in the following tables. Separate tables list (D.1) the initial observations on Rügen, (D.2) the Polarstern campaign, (D.3) observations in Kühlungsborn with the transportable K-lidar, (D.4) on Tenerife, (D.5) on Svalbard, and (D.6) observations in Kühlungsborn with the new stationary K-lidar. All data sets since 1996 comprise more than 500 hours of temperature observations from a total of 563 nights (and days). Therefore, no complete listing of the individual observations is given.

All values in the tables include only those observations where the lidar was operated in regular scanning mode on the K(D_1) line allowing temperature calculation, except for the column 'No T', where other files are counted separately. Individual files regularly include 4000 laser shots ($\sim$2 minutes). The total measurement time includes both day and nighttime, while the daylight periods are accumulated separately again. As 'nights' the periods between noon and noon (UT) are counted and the portion including daytime observations is given in addition as 'days'. All measurements until December 31st, 2003, are included.

In addition to J. Höffner who accomplished all the campaigns, a number of other people were involved in the measurements: U. von Zahn, M. Alpers (until 2000), V. Eska (until 1997), C. Fricke-Begemann (1997–2003), T. Köpnick, J. Oldag (1998–1999), J. Lautenbach (since 2001), P. Menzel (since 2001), M. Gerding (since 2003), M. Rauthe (since 2003), and many others who have assisted.

Table D.1: K-lidar temperature measurements at Juliusruh, Rügen (55°N).

Month	Year	T-files	No T	Total time	Daylight	Nights	Days
1	1995	0	205	0 h	–	3	–
2	1995	0	724	0 h	–	5	–
3	1995	—	–	—	–	—	–
4	1995	66	76	5 h	–	4	–
5	1995	28	160	12 h	–	3	–
6	1995	18	12	1 h	–	1	–
total		112		18 h	0 h	16	0

Table D.2: K-lidar temperature measurements during the Polarstern campaign between 70°S and 45°N.

Month	Year	T-files	No T	Total time	Daylight	Nights	Days
3	1996	0	5	0 h	–	1	–
4	1996	219	60	10 h	–	9	–
5	1996	1615	54	82 h	–	13	–
6	1996	881	17	51 h	–	12	–
total		2715		143 h	0 h	35	0

Table D.3: Temperature measurements in Kühlungsborn (54°N) with the transportable K-lidar.

Month	Year	T-files	No T	Total time	Daylight	Nights	Days
6	1996	15	4	1 h	–	1	–
7	1996	427	15	20 h	–	6	–
8	1996	858	87	41 h	–	12	–
9	1996	1151	–	57 h	–	14	–
10	1996	886	6	43 h	–	10	–
11	1996	565	17	26 h	–	5	–
12	1996	127	13	6 h	–	1	–
1	1997	2124	17	94 h	–	12	–
2	1997	695	18	31 h	–	5	–
3	1997	1178	2	43 h	–	7	–
4	1997	1402	6	50 h	–	12	–
5	1997	709	2	28 h	–	10	–
6	1997	1046	34	41 h	–	14	–
7	1997	207	16	9 h	–	5	–
8	1997	1345	8	60 h	–	13	–
9	1997	685	4	29 h	–	6	–
10	1997	713	7	31 h	–	5	–
11	1997	233	–	10 h	–	3	–
12	1997	939	8	40 h	–	5	–
1	1998	5	–	0 h	–	1	–
2	1998	7	–	0 h	–	1	–
3	1998	392	3	20 h	–	6	–
4	1998	226	98	11 h	–	4	–
5	1998	287	18	14 h	–	6	–
6	1998	140	13	6 h	–	6	–
7	1998	80	–	4 h	–	2	–
8	1998	152	–	7 h	–	3	–
9	1998	345	–	17 h	–	4	–
10	1998	402	–	17 h	–	3	–
11	1998	312	–	13 h	–	2	–
12	1998	367	–	15 h	–	3	–
1	1999	76	–	3 h	–	1	–
2	1999	294	–	12 h	–	2	–
total		18390		799 h	0 h	190	0

Table D.4: K-lidar temperature measurements on Tenerife (28°N).

Month	Year	T-files	No T	Total time	Daylight	Nights	Days
3	1999	376	–	15 h	–	2	–
4	1999	337	–	15 h	–	4	–
5	1999	3552	–	136 h	–	19	–
6	1999	1046	96	49 h	–	7	–
7	1999	1399	–	61 h	–	8	–
8	1999	—	–	—	–	—	–
9	1999	—	–	—	–	—	–
10	1999	—	–	—	–	—	–
11	1999	2425	1	107 h	–	15	–
12	1999	—	–	—	–	—	–
11	2000	4203	81	170 h	129 h	14	10
12	2000	848	58	36 h	22 h	9	3
total		14186		588 h	151 h	78	13

Table D.5: K-lidar temperature measurements on Svalbard (78°N).

Month	Year	T-files	No T	Total time	Daylight	Nights	Days
6	2001	1030	16	32 h	32 h	9	9
7	2001	2412	31	75 h	75 h	11	11
8	2001	3640	18	118 h	110 h	14	14
9	2001	981	–	36 h	23 h	11	9
10	2001	459	1	15 h	6 h	5	3
2	2002	265	2	9 h	–	1	–
3	2002	3284	70	111 h	6 h	16	8
4	2003	1635	18	56 h	42 h	6	6
5	2003	2216	6	77 h	77 h	13	13
6	2003	1181	14	43 h	43 h	13	13
7	2003	1448	3	58 h	58 h	11	11
8	2003	1105	2	37 h	37 h	10	10
total		19656		666	509	120	107

Table D.6: Temperature measurements in Kühlungsborn (54°N) with the stationary K-lidar.

Month	Year	T-files	No T	Total time	Daylight	Nights	Days
6	1999	0	58	0 h	–	3	–
9	1999	0	7	0 h	–	1	–
10	1999	70	19	2 h	–	2	–
11	1999	593	58	22 h	–	7	–
1	2000	351	4	12 h	–	1	–
6	2000	88	10	3 h	–	2	–
7	2000	64	–	3 h	–	1	–
8	2000	50	–	2 h	–	1	–
10	2000	0	112	0 h	–	3	–
6	2001	0	22	0 h	–	3	–
7	2001	0	81	0 h	–	1	–
8	2001	283	–	10 h	–	2	–
1	2002	—	–	—	–	—	–
2	2002	262	–	9 h	3 h	1	1
3	2002	245	–	8 h	5 h	1	1
4	2002	142	–	5 h	3 h	1	1
5	2002	—	–	—	–	—	–
6	2002	811	25	28 h	18 h	10	5
7	2002	255	14	9 h	–	4	–
8	2002	368	128	13 h	–	8	–
9	2002	599	–	20 h	2 h	3	1
10	2002	332	5	12 h	2 h	3	3
11	2002	1337	11	47 h	17 h	5	4
12	2002	855	1	29 h	7 h	3	2
1	2003	—	–	—	–	—	–
2	2003	2742	37	108 h	45 h	5	5
3	2003	182	16	7 h	7 h	3	3
4	2003	1328	12	51 h	12 h	5	3
5	2003	—	–	—	–	—	–
6	2003	1661	78	61 h	33 h	10	9
7	2003	426	2	15 h	9 h	4	3
8	2003	1162	6	42 h	3 h	8	2
9	2003	1826	118	62 h	2 h	10	2
10	2003	1641	389	58 h	–	8	–
11	2003	938	5	32 h	3 h	2	1
12	2003	974	11	33 h	–	3	–
total		19585		705	173	124	46

Bibliography

Alpers, M., R. Eixmann, C. Fricke-Begemann, M. Gerding, and J. Höffner, Temperature lidar measurements from 1 to 105 km altitude using resonance, Rayleigh, and Rotational Raman scattering, *Atmos. Chem. Phys.*, *4*, 793–800, 2004.

Baldwin, M. P., and T. J. Dunkerton, Stratospheric harbingers of anomalous weather regimes, *Science*, *294*, 581–584, 2001.

Becker, E., and G. Schmitz, Climatological effects of orography and land-sea heating contrasts on the gravity wave-driven circulation of the mesosphere, *J. Atmos. Sci.*, *60*, 103–118, 2003.

Beckers, J. M., The profiles of Fraunhofer lines in the presence of Zeeman splitting. I: the Zeeman triplet, *Sol. Phys.*, *9*, 372–386, 1969.

Beig, G., P. Keckhut, R. P. Lowe, R. G. Roble, M. G. Mlynczak, J. Scheer, V. I. Fomichev, D. Offermann, W. J. R. French, M. G. Shepherd, A. I. Semenov, E. E. Remsberg, C. Y. She, F. J. Lübken, J. Bremer, B. R. Clemesha, J. Stegman, F. Sigernes, and S. Fadnavis, Review of mesospheric temperature trends, *Rev. Geophys.*, *41*, 1015, doi:10.1029/2002RG000121, 2003.

Berger, U., Numerische Simulation klimatologischer Prozesse und thermischer Gezeiten in der mittleren Atmosphäre, Ph.D. thesis, Institut für Geophysik und Meteorologie der Universität zu Köln, 1994.

Berger, U., and U. von Zahn, The two-level structure of the mesopause: A model study, *J. Geophys. Res.*, *104*, 22,083–22,093, 1999.

Berger, U., and U. von Zahn, Icy particles in the summer mesopause region: Three-dimensional modeling of their environment and two-dimensional modeling of their transport, *J. Geophys. Res.*, *107(A11)*, doi:10.1029/2001JA000316, 2002.

Bittner, M., D. Offermann, H.-H. Graef, M. Donner, and K. Hamilton, An 18-year time series of OH rotational temperatures and middle atmosphere decadal variations, *J. Atmos. Solar Terr. Phys.*, *64*, 1147–1166, 2002.

Blamont, J. E., M. L. Chanin, and G. Megie, Vertical distribution and temperature profile of the night time atmospheric sodium layer obtained by laser backscatter, *Ann. Géophys.*, *28*, 833–838, 1972.

Brasseur, G. P., A. K. Smith, R. Khosravi, T. Huang, S. Walters, S. Chabrillat, and G. Kockarts, Natural and human-induced perturbatons in the middle atmosphere: a short tutorial, in *Atmospheric Science Across the Stratopause*, edited by D. E. Siskind, S. D. Eckermann, and M. E. Summers, vol. 123 of *Geophys. Monogr. Ser.*, pp. 7–20, AGU, Washington, D. C., 2000.

Bucholtz, A., Rayleigh-scattering calculations for the terrestrial atmosphere, *Appl. Optics*, *34*, 2765–2773, 1995.

Cartwright, D. E., *Tides: a scientific history*, Cambridge University Press, 1999.

Chamberlain, J. W., and D. M. Hunten, *Theory of Planetary Atmospheres*, vol. 36 of *International Geophysics Series*, 2nd ed., Academic Press, Inc., 1987.

Chamberlain, J. W., D. M. Hunten, and J. E. Mack, Resonance backscattering by atmospheric sodium – IV, Abundance of sodium in twilight, *J. Atmos. Terr. Phys.*, *12*, 153–165, 1958.

Chapman, S., and R. S. Lindzen, *Atmospheric tides*, Reidel, Dordrecht, Holland, 1970.

Chen, H., C. Y. She, P. Searcy, and E. Korevaar, Sodium-vapor dispersive Faraday filter, *Opt. Lett.*, *18*, 1019–1021, 1993.

Chen, H., M. A. White, D. A. Krueger, and C. Y. She, Daytime mesopause temperature measurements with a sodium-vapor dispersive Faraday filter in a lidar receiver, *Opt. Lett.*, *21*, 1093–1095, 1996.

Chen, S., Z. Hu, M. A. White, H. Chen, D. A. Krueger, and C. Y. She, Lidar observations of seasonal variation of diurnal mean temperature in the mesopause region over Fort Collins, Colorado (41°N, 105°W), *J. Geophys. Res.*, *105*, 12,371–12,380, 2000.

Chu, X., W. Pan, G. C. Papen, C. S. Gardner, and J. A. Gelbwachs, Fe Boltzmann temperature lidar: design, error analysis, and initial results at the North and South Poles, *Appl. Optics*, *41*, 4400–4410, 2002.

Clancy, R. T., D. W. Rusch, and M. T. Callan, Temperature minima in the average thermal structure of the middle mesosphere (70-80 km) from analysis of 40- to 92-km SME global temperature profiles, *J. Geophys. Res.*, *99*, 19,001–19,020, 1994.

Clemesha, B. R., I. Veselovskii, P. P. Batista, M. P. P. M. Jorge, and D. M. Simonich, First mesopause temperature profiles from a fixed Southern Hemisphere site, *Geophys. Res. Lett.*, *26*, 1681–1684, 1999.

Crary, D. J., and J. M. Forbes, On the extraction of tidal information from measurements covering a fraction of a day, *Geophys. Res. Lett.*, *7*, 580–582, 1983.

Dick, D. J., and T. M. Shay, Ultrahigh-noise rejection optical filter, *Opt. Lett.*, *16*, 867–869, 1991.

Dressler, E. T., A. E. Laux, and R. I. Billmers, Theory and experiment for the anomalous Faraday effect in potassium, *J. Opt. Soc. Am. B*, *13*, 1849–1858, 1996.

Drob, D. P., J. M. Picone, S. D. Eckermann, C. Y. She, J. F. Kafkalidis, D. A. Ortland, R. J. Niciejewski, and T. L. Killeen, Mid-latitude Temperatures at 87 km: Results From Multi-instrument Fourier Analysis, *Geophys. Res. Lett.*, *27*, 2109–2112, 2000.

Duarte, F. J., *Tunable lasers handbook*, Academic Press, Inc., 1995.

Ebel, A., Contributions of gravity waves to the momentum, heat and turbulent energy budget of the upper mesosphere and lower thermosphere, *J. Atmos. Terr. Phys.*, *46*, 727–737, 1984.

Ebel, A., U. Berger, and B. C. Krueger, Numerical Simulations with COMMA, a Global Model of the Middle Atmosphere, *STEP Simpo Newslett.*, *4*, 22–32, 1995.

Eska, V., Die Kaliumschicht in der oberen Atmosphäre (75–110 km): Beobachtungen, Analysen, Modellierung, PhD thesis, Universität Rostock, 1998.

Eska, V., J. Höffner, and U. von Zahn, The upper atmosphere potassium layer and its seasonal variations at 54°N, *J. Geophys. Res.*, *103*, 29,207–29,214, 1998.

Eska, V., U. von Zahn, and J. M. C. Plane, The terrestrial potassium layer (75–110 km) between 71°S and 54°N: Observations and modelling, *J. Geophys. Res.*, *104*, 17,173–17,186, 1999.

Felix, F., W. Keenliside, G. Kent, and M. C. W. Sandford, Laser radar observation of atmospheric potassium, *Nature*, *246*, 345–346, 1973.

Fleming, E. L., S. Chandra, J. J. Barnett, and M. Corney, Zonal mean temperature, pressure, zonal wind, and geopotential height as functions of latitude, *Adv. Space Res.*, *10(12)*, 11–59, 1990.

Forbes, J. M., Atmospheric tides 1. model description and results for the solar diurnal component, *J. Geophys. Res.*, *87*, 5222–5240, 1982a.

Forbes, J. M., Atmospheric tides 2. the solar and lunar semidiurnal components, *J. Geophys. Res.*, *87*, 5241–5252, 1982b.

Forbes, J. M., Tidal and planetary waves, in *The Upper Mesosphere and Lower Thermosphere: A Review of Experiment and Theory*, edited by R. M. Johnson and T. L. Killeen, vol. 87 of *Geophys. Monogr. Ser.*, pp. 67–87, AGU, Washington, D. C., 1995.

Forbes, J. M., X. Zhang, E. R. Talaat, and W. Ward, Nonmigrating diurnal tides in the thermosphere, *J. Geophys. Res.*, *108*, 1033, doi:10.1029/2002JA009262, 2003.

Foufoula-Georgiou, E., and P. Kumar, *Wavelets in Geophysics*, vol. 4 of *Wavelet analysis and its applications*, Academic Press, Inc., San Diego, 1994.

Fricke, K., and U. von Zahn, Mesopause temperatures derived from probing the hyperfine structure of the D_2 resonance line of sodium by lidar, *J. Atmos. Terr. Phys.*, *47*, 499–512, 1985.

Fricke-Begemann, C., M. Alpers, and J. Höffner, Daylight rejection with a new receiver for potassium resonance temperature lidars, *Opt. Lett.*, *27(21)*, 1932–1934, 2002a.

Fricke-Begemann, C., J. Höffner, and U. von Zahn, The potassium density and temperature structure in the mesopause region (80–105 km) at a low latitude (28°N), *Geophys. Res. Lett.*, *29(22)*, 2067, doi:10.1029/2002GL015578, 2002b.

Friedman, J. S., Tropical mesopause climatology over the Arecibo Observatory, *Geophys. Res. Lett.*, *30*, 1642, doi:10.1029/2003GL016966, 2003.

Friedman, J. S., S. C. Collins, R. Delgado, and P. A. Castleberg, Mesospheric potassium layer over the Arecibo Observatory, 18.3°N 66.75°W, *Geophys. Res. Lett.*, *29*, 1071, doi:10.1029/2001GL013542, 2002.

Fry, E. S., H. Qiquan, and L. Xingfu, Single frequency operation of an injection-seeded Nd:YAG laser in high noise environments, *Appl. Optics*, *30*, 1015–1017, 1991.

Gadsden, M., and W. Schröder, *Noctilucent Clouds*, vol. 18 of *Physics and Chemistry in Space*, Springer-Verlag, 1989.

Gardner, C. S., G. C. Papen, X. Chu, and W. Pan, First Lidar Observations of Middle Atmosphere Temperatures, Fe Densities, and Polar Mesospheric Clouds Over the North and South Poles, *Geophys. Res. Lett.*, *28*, 1199–1202, 2001.

Gerding, M., M. Alpers, U. von Zahn, R. J. Rollason, and J. M. C. Plane, Atmospheric Ca and Ca^+ layers: Mid-latitude observations and modeling, *J. Geophys. Res.*, *105*, 27,131–27,146, 2000.

Ghil, M., M. R. Allen, M. D. Dettinger, K. Ide, D. Kondrashov, M. E. Mann, A. W. Robertson, A. Saunders, Y. Tian, F. Varadi, and P. Yiou, Advanced spectral methods for climatic time series, *Rev. Geophys.*, *40*, 1003, doi:10.1029/2000RG000092, 2002.

Gille, S. T., H. A., and M.-L. Chanin, Semidiurnal and diurnal tidal effects in the middle atmosphere as seen by Rayleigh lidar, *J. Geophys. Res.*, *96*, 7579–7587, 1991.

Goody, R. M., and Y. L. Yung, *Atmospheric radiation; theoretical basis*, 2nd ed., Oxford University Press, 1989.

Gray, D. F., *The observation and analysis of stellar photospheres*, 2nd ed., Cambridge University Press, 1992.

Grieger, N., E. M. Volodin, G. Schmitz, P. Hoffmann, D. C. F. A. H. Manson, K. Igarashi, and W. Singer, General circulation model results on migrating and nonmigrating tides in the mesosphere and lower thermosphere. Part I: comparison with observations, *J. Atmos. Solar Terr. Phys.*, *64*, 897–911, 2002.

Hagan, M. E., Modeling atmospheric tidal propagation across the stratopause, in *Atmospheric Science Across the Stratopause*, edited by D. E. Siskind, S. D. Eckermann, and M. E. Summers, vol. 123 of *Geophys. Monogr. Ser.*, pp. 177–190, AGU, Washington, D. C., 2000.

Hagan, M. E., and J. M. Forbes, Migrating and nonmigrating diurnal tides in the middle and upper atmosphere excited by tropospheric latent heat release, *J. Geophys. Res.*, *107*, 4754, doi:10.1029/2001JD001236, 2002.

Hagan, M. E., and J. M. Forbes, Migrating and nonmigrating semidiurnal tides in the upper atmosphere excited by tropospheric latent heat release, *J. Geophys. Res.*, *108*, 1062, doi:10.1029/2002JA009466, 2003.

Hagan, M. E., M. D. Burrage, J. M. Forbes, J. Hackney, W. J. Randel, and X. Zhang, GSWM-98: Results for migrating solar tides, *J. Geophys. Res.*, *104*, 6813–6828, 1999.

Hagan, M. E., R. G. Roble, and J. Hackney, Migrating thermospheric tides, *J. Geophys. Res.*, *106*, 12,739–12,752, 2001.

Hedin, A. E., Extension of the MSIS thermosphere model into the middle and lower atmosphere, *J. Geophys. Res.*, *96*, 1159–1172, 1991.

Helmer, M., J. M. C. Plane, J. Qian, and C. S. Gardner, A model of meteoric iron in the upper atmosphere, *J. Geophys. Res.*, *103*, 10,913–10,926, 1998.

Henderson, S. W., E. H. Yuen, and E. S. Fry, Fast resonance-detection technique for single frequency operation of injection-seeded Nd:YAG lasers, *Opt. Lett.*, *11*, 715–717, 1986.

Hernandez, G., Time series, periodograms, and significance, *J. Geophys. Res.*, *104*, 10,355–10,368, 1999.

Hocking, W. K., and A. Hocking, Temperature tides determined with meteor radar, *Ann. Geophys.*, *20*, 1447–1467, 2002.

Hoffmann, P., W. Singer, and D. Keuer, Variability of the mesospheric wind field at middle and Arctic latitudes in winter and its relation to stratospheric circulation disturbances, *J. Atmos. Solar Terr. Phys.*, *64*, 1229–1240, 2002.

Höffner, J., and U. von Zahn, Mesopause temperature profiling by potassium lidar: recent progress and outlook for ALOMAR, in *Proceedings of the 12th ESA Symposium on European Rocket and Balloon Programmes and Related Research, Lillehammer, Norway (ESA SP)*, pp. 403–407, 1995.

Höffner, J., C. Fricke-Begemann, and U. von Zahn, Note on the reaction of the upper atmosphere potassium layer to the 1999 Leonid meteor storm, *Earth, Moon and Planets*, *82–83*, 555–564, 2000.

Höffner, J., C. Fricke-Begemann, and F.-J. Lübken, First observations of noctilucent clouds by lidar at Svalbard, 78°N, *Atmos. Chem. Phys.*, *3*, 1101–1111, 2003.

Holton, J. R., and M. J. Alexander, The role of waves in the transport circulation of the middle atmosphere, in *Atmospheric Science Across the Stratopause*, edited by D. E. Siskind, S. D. Eckermann, and M. E. Summers, vol. 123 of *Geophys. Monogr. Ser.*, pp. 21–35, AGU, Washington, D. C., 2000.

Humayun, M., and R. N. Clayton, Precise determination of the isotopic composition of potassium: Application to terrestrial rocks and lunar soils, *Geochim. Cosmochim. Acta*, *59*, 2115–2130, 1995a.

Humayun, M., and R. N. Clayton, Potassium isotope cosmochemistry: Genetic implications of volatile element depletion, *Geochim. Cosmochim. Acta*, *59*, 2131–2148, 1995b.

Jacobi, C., R. Schminder, and D. Kürschner, Planetary wave activity obtained from long-period (2–18 days) variations of mesopause region winds over Central Europe (52°N, 15°E), *J. Atmos. Solar Terr. Phys.*, *60*, 81–93, 1998.

Jacobi, C. H., Y. I. Portnyagin, T. V. Solovjova, P. Hoffmann, W. Singer, A. N. Fahrutdinova, R. A. Ishmuratov, A. G. Beard, N. J. Mitchell, H. G. Muller, R. Schminder, D. Kürschner, A. H. Manson, and C. E. Meek, Climatology of the semidiurnal tide at 52–56°N from ground-based radar wind measuremends 1985–1995, *J. Atmos. Solar Terr. Phys.*, *61*, 975–991, 1999.

Jeys, T. H., A. A. Brailove, and A. Mooradian, Sum frequency generation of sodium resonance radiation, *Appl. Optics*, *28*, 2588–2591, 1989.

Kane, T. J., and C. S. Gardner, Structure and Seasonal Variability of the Nighttime Mesospheric Fe Layer at Midlatitdues, *J. Geophys. Res.*, *98*, 16,875–16,886, 1993.

Khattatov, B. V., M. A. Geller, V. A. Yudin, and P. B. Hays, Diurnal migrating tide as seen by the high resolution Doppler imager/UARS 2. Monthly mean global zonal and vertical velocities, pressure, temperature, and inferred dissipation, *J. Geophys. Res.*, *102*, 4423–4435, 1997.

Koechner, W., *Solid-state laser engineering*, vol. 1 of *Optical Sciences*, 3rd ed., Springer-Verlag, 1992.

Kogelnik, H., and T. Li, Laser beams and resonators, *Appl. Optics*, *5*, 1550–1567, 1966.

Lautenbach, J., Aufbau einer Doppler-freien Polarisationsspektroskopie als Wellenlängenstandard anhand der Kalium (D1)-Linie, Diploma thesis, Technische Fachhochschule Wildau, 2001.

Leblanc, T., I. S. McDermid, P. Keckhut, A. Hauchecorne, C. She, and D. A. Krueger, Temperature climatology of the middle atmosphere from long-term lidar measurements at middle and low latitudes, *J. Geophys. Res.*, *103*, 17,191–17,204, 1998.

Lide, D. R., *CRC Handbook of chemistry and physics: a ready-reference book of chemical and physical data*, 80th ed., CRC Press LLC, 1999.

Lindzen, R. S., *dynamics in atmospheric physics*, Cambridge University Press, 1990.

Love, S. G., and D. E. Brownlee, A direct measurement of the terrestrial mass accretion rate of cosmic dust, *Science*, *262*, 550–553, 1993.

Lübken, F.-J., Seasonal variation of turbulent energy dissipation rates at high latitudes as determined by in situ measurements of neutral density fluctuations, *J. Geophys. Res.*, *102*, 13,441–13,456, 1997.

Lübken, F.-J., Thermal structure of the Arctic summer mesosphere, *J. Geophys. Res.*, *104*, 9135–9149, 1999.

Magni, V., Resonators for solid-state lasers with fundamental mode and high alignment stability, *Appl. Optics*, *25*, 107–117, 1986.

Manson, A. H., and C. E. Meek, Long period (8-20h) wind oscillations in the upper middle atmosphere at Saskatoon (52°N): evidence for non-linear tidal effects, *Planet. Space Sci.*, *38*, 1431–1441, 1990.

Manson, A. H., C. E. Meek, and G. E. Hall, Correlations of gravity waves and tides in the mesosphere over Saskatoon, *J. Atmos. Solar Terr. Phys.*, *60*, 1089–1107, 1998.

Manson, A. H., Y. Luo, and C. Meek, Global distributions of diurnal and semi-diurnal tides: observations from HRDI-UARS of the MLT region, *Ann. Geophys.*, *20*, 1877–1890, 2002.

McKay, J. A., Single and tandem Fabry-Perot etalons as solar background filters for lidar, *Appl. Optics*, *38*, 5851–5858, 1999.

McKay, J. A., and T. D. Wilkerson, Diode-pumped alexandrite laser for DIAL and Doppler lidar, in *Proc. SPIE, Application of Lidar to Current Atmospheric Topics II*, edited by A. J. Sedlacek and K. W. Fischer, vol. 3127, pp. 124–132, 1997.

Megie, G., F. Bos, J. E. Blamont, and M. L. Chanin, Simultaneous nighttime lidar measurements of atmospheric sodium and potassium, *Planet. Space Sci.*, *26*, 27–35, 1978.

Mlynczak, M. G., A contemporary assessment of the mesospheric energy budget, in *Atmospheric Science Across the Stratopause*, edited by D. E. Siskind, S. D. Eckermann, and M. E. Summers, vol. 123 of *Geophys. Monogr. Ser.*, pp. 37–52, AGU, Washington, D. C., 2000.

Müller, H., and H. Quenzel, Information content of multispectral lidar measurements with respect to the aerosol size distribution, *Appl. Optics*, *24*, 648–654, 1985.

Oberheide, J., and O. A. Gusev, Observation of migration and nonmigrating tides in the equatorial lower thermosphere, *Geophys. Res. Lett.*, *29*, 2167, doi:10.1029GL016213, 2002.

Oldag, J., Gezeiteneffekte in der Mesopausenregion aus Lidarbeobachtungen über Kühlungsborn und Teneriffa, PhD thesis, Universität Rostock, 2001.

Ortland, D. A., P. B. Hays, W. R. Skinner, and J.-H. Yee, Remote sensing of mesospheric temperature and $O_2(^1\Sigma)$ band volume emission rates with the high-resolution Doppler imager, *J. Geophys. Res.*, *103*, 1821–1835, 1998.

Palo, S. E., R. G. Roble, and M. E. Hagan, Middle atmosphere effects of the quasi-two-day wave determined from a General Circulation Model, *Earth Plan. Space*, *51*, 629–647, 1999.

Pancheva, D., J. Mitchell, M. E. Hagan, A. H. Manson, C. E. Meek, Y. Luo, C. Jacobi, D. Kürschner, R. R. Clark, W. K. Hocking, J. MacDougall, G. O. L. Jones, R. A. Vincent, I. M. Reid, W. Singer, K. Igarashi, G. I. Fraser, T. Nakamura, T. Tsuda, Y. Portnyagin, E. Merzlyakov, A. N. Fahrutdinova, A. M. Stepanov, L. M. G. Poole, S. B. Malinga, B. L. Kashcheyev, and A. N. Oleynikov, Global-scale tidal structure in the mesosphere and lower thermosphere during the PSMOS campaign of June–August 1999 and comparisons with the global-scale wave model, *J. Atmos. Solar Terr. Phys.*, *64*, 1011–1035, 2002.

Papen, G. C., C. S. Gardner, and W. M. Pfenninger, Analysis of a potassium lidar system for upper-atmospheric wind-temperature measurements, *Appl. Optics*, *34*, 6950–6958, 1995.

Pendleton, W. R., M. J. Taylor, and L. C. Gardner, Terdiurnal oscillations in OH Meinel rotational temperatures for fall conditions at northern mid-latitude sites, *Geophys. Res. Lett.*, *27*, 1799–1802, 2000.

Picone, J. M., A. E. Hedin, D. P. Drob, and A. C. Aikin, NRLMSISE-00 empirical model of the atmosphere: Statistical comparison and scientific issues, *J. Geophys. Res.*, *107*, 1468, doi:10.1029/2002JA009430, 2002.

Plane, J. M. C., C. S. Gardner, J. Yu, C. Y. She, R. R. Garcia, and H. C. Pumphrey, Mesosperic Na layer at 40°N: Modeling and observations, *J. Geophys. Res.*, *104*, 3773–3788, 1999.

Press, W. H., B. P. Flannery, S. A. Teukolsky, and W. T. Vetterling, *Numerical Recipes in Pascal*, Cambridge University Press, 1989.

Preuss, D. R., and J. L. Gole, Three-stage birefringent filter tuning smoothly over the visible region: theoretical treatment and experimental design, *Appl. Optics*, *19*, 702–710, 1980.

Raizada, S., and C. A. Tepley, Seasonal variation of iron layers at Arecibo: First results from low-latitudes, *Geophys. Res. Lett.*, *30*, 1082, doi:10.1029/2002GL016537, 2003.

Roble, R. G., Energetics of the mesosphere and thermosphere, in *The Upper Mesosphere and Lower Thermosphere: A Review of Experiment and Theory*, edited by R. M. Johnson and T. L. Killeen, vol. 87 of *Geophys. Monogr. Ser.*, pp. 1–21, AGU, Washington, D. C., 1995.

Saloman, E. B., A resonance ionization spectroscopy/resonance ionization mass spectrometry data service. IV–Data sheets for Be, In, Li, K, Rb, Ag, Ti and V and an update of the data sheet for Ni, *Spectrochimica Acta*, *48B*, 1139–1203, 1993.

Scheps, R., B. M. Gately, J. F. Myers, D. F. Heller, and J. S. Krasinski, Alexandrite laser pumped by semiconductor lasers, *Appl. Phys. Lett.*, *56*, 2288–2290, 1990.

Schmitz, S., Entwicklung eines schmalbandigen und durchstimmbaren Alexandrit Lasers für ein mobiles Na-Temperature-Lidar, PhD thesis, Universität Bonn, 1994.

Schmitz, S., U. von Zahn, J. C. Walling, and D. Heller, Alexandrite lasers for temperature sounding of the sodium layer, in *Proceedings of the 12th ESA Symposium on European Rocket and Balloon Programmes and Related Research, Lillehammer, Norway (ESA SP)*, pp. 395–402, 1995.

Schneider, J., and R. Eixmann, Three years of routine raman lidar measurements of tropospheric aerosols: Backscattering, extinction, and residual layer height, *Atmos. Chem. Phys.*, *2*, 313–323, 2002.

Schwemmer, G. K., H. S. Lee, and C. R. Prasad, Narrowband alexandrite laser injection seeded with frequency dithered diode laser, in *Proc. SPIE, Earth and Atmospheric remote sensing*, edited by R. Curran, vol. 1492, pp. 52–62, 1991.

She, C.-Y., Spectral structure of laser light scattering revisited: bandwidths of nonresonant scattering lidars, *Appl. Optics*, *40*, 4875–4884, 2001.

She, C. Y., and U. von Zahn, Concept of a two-level mesopause: Support through new lidar observations, *J. Geophys. Res.*, *103*, 5855–5863, 1998.

She, C. Y., and J. R. Yu, Simultaneous three-frequency Na lidar measurements of radial wind and temperature in the mesopause region, *Geophys. Res. Lett.*, *21*, 1771–1774, 1994.

She, C. Y., H. Latifi, J. R. Yu, R. J. Alvarez II, R. Bills, and C. Gardner, Two-frequency lidar technique for mesospheric Na temperature measurements, *Geophys. Res. Lett.*, *17*, 929–932, 1990.

She, C. Y., J. R. Yu, and H. Chen, Observed thermal structure of a midlatitude mesopause, *Geophys. Res. Lett.*, *20*, 567–570, 1993.

She, C. Y., J. R. Yu, D. A. Krueger, R. Roble, P. Keckhut, A. Hauchecorne, and M.-L. Chanin, Vertical structure of the midlatitude temperature from stratosphere to mesopause (30-105 km), *Geophys. Res. Lett.*, *22*, 377–380, 1995.

She, C. Y., S. Chen, Z. Hu, J. Sherman, J. D. Vance, V. Vasoli, M. A. White, J. Yu, and D. W. Krueger, Eight-year climatology of nocturnal temperature and sodium density in the mesopause region (80 to 105 km) over Fort Collins, CO (41°N, 105°W), *Geophys. Res. Lett.*, *27*, 3289–3292, 2000.

She, C. Y., S. Chen, B. P. Williams, Z. Hu, and D. A. Krueger, Tides in the mesopause region over Fort Collins, Colorado (41°N, 105°W) based on lidar temperature observations covering full diurnal cycles, *J. Geophys. Res.*, *107*, 4350, doi:10.1029/2001JD001189, 2002a.

She, C. Y., J. Sherman, J. D. Vance, T. Yuan, Z. Hu, B. P. Williams, K. Arnold, P. Acott, and D. A. Krueger, Evidence of solar cycle effect in the mesopause region: observed temperatures in 1999 and 2000 at 98.5 km over Fort Collins, CO (41°N, 105°W), *J. Atmos. Solar Terr. Phys.*, *64*, 1651–1657, 2002b.

She, C. Y., J. D. Vance, B. P. Williams, D. A. Krueger, H. Moosmüller, D. Gibson-Wilde, and D. Fritts, Lidar Studies of Atmospheric Dynamics Near Polar Mesopause, *Eos, Trans. AGU*, *83*, 289–293, 2002c.

She, C. Y., J. Sherman, T. Yuan, B. P. Williams, K. Arnold, T. D. Kawahara, T. Li, L. F. Xu, J. D. Vance, P. Acott, and D. A. Krueger, The first 80-hour continous lidar campaign for simultaneous observation of mesopause region temperature and wind, *Geophys. Res. Lett.*, *108*, 1319, doi:10.1029/2002GL016412, 2003.

Shepherd, M. G., and C. Fricke-Begemann, Study of the tidal variations in mesosperic temperature at low and midlatitude from WINDII and potassium lidar observations, *Ann. Geophys.*, *22*, 1513–1528, 2004.

Shepherd, M. G., W. E. Ward, B. Prawirosoehardjo, S. P. Zhang, and D. Y. Wang, Planetary scale and tidal perturbations in mesospheric temperature observed by WINDII, *Earth Plan. Space*, *51*, 593–610, 1999.

Shepherd, M. G., B. Reid, S. Zhang, B. H. Solheim, and G. G. Shepherd, Retrieval and validation of mesospheric temperatures from Wind Imaging Interferometer observations, *J. Geophys. Res.*, *106*, 24,813–24,829, 2001.

Shepherd, M. G., P. J. Espy, C. Y. She, W. Hocking, P. Keckhut, G. Gavrilyeva, G. G. Shepherd, and B. Naujokat, Springtime transition in upper mesospheric temperature in the northern hemisphere, *J. Atmos. Solar Terr. Phys.*, *64*, 1183–1199, 2002.

Smith, A. K., Structure of the terdiurnal tide at 95 km, *Geophys. Res. Lett.*, *27*, 177–180, 2000.

Smith, A. K., and D. A. Ortland, Modeling and analysis of the structure and generation of the terdiurnal tide, *J. Atmos. Sci.*, *58*, 3116–3134, 2001.

Smith, A. K., D. R. Marsh, and A. C. Szymczak, Interaction of chemical heating and the diurnal tide in the mesosphere, *J. Geophys. Res.*, *108*, 4164, doi:10.1029/2002JD002664, 2003.

States, R. J., and C. S. Gardner, Influence of the diurnal tide and thermospheric heat sources on the formation of mesospheric temperature inversion layer, *Geophys. Res. Lett.*, *25*, 1483–1486, 1998.

States, R. J., and C. S. Gardner, Thermal structure of the mesopause region (80–105 km) at 40°N latitude. Part I: seasonal variations, *J. Atmos. Sci.*, *57*, 66–77, 2000a.

States, R. J., and C. S. Gardner, Thermal structure of the mesopause region (80–105 km) at 40°N latitude. Part II: diurnal variations, *J. Atmos. Sci.*, *57*, 78–92, 2000b.

Summers, M. E., Vertical couplings, *Science*, *284*, 1783–1784, 1999.

Talaat, E. R., and R. S. Lieberman, Nonmigrating diurnal tides in mesospheric and lower-thermospheric winds and temperatures, *J. Atmos. Sci.*, *56*, 4073–4087, 1999.

Taubenheim, J., *Statistische Auswertung geophysikalischer und meteorologischer Daten*, vol. 5 of *Geophysikalische Monographien*, Geest & Portig, Leipzig, 1969.

Taylor, M. J., W. R. Pendleton, H.-L. Liu, C. Y. She, L. C. Gardner, R. G. Roble, and V. Vasoli, Large amplitude perturbations in mesospheric OH Meinel and 87-km Na lidar temperatures around the autumnal equinox, *Geophys. Res. Lett.*, *28*, 1899–1902, 2001.

Thulasiraman, S., and J. B. Nee, Further evidence of a two-level mesopause and its variation from UARS high-resolution Doppler imager temperature data, *J. Geophys. Res.*, *107*, 4355, doi:10.1029/2002JD000118, 2002.

Tomczyk, S., K. Streander, G. Card, D. Elmore, H. Hull, and A. Cacciani, An instrument to observe low-degree solar oscillations, *Sol. Phys.*, *159*, 1–21, 1995.

Torrence, C., and G. P. Compo, A practical guide to wavelet analysis, *Bull. Amer. Meteor. Soc.*, *79*, 61–78, 1998.

USSA, *U. S. Standard Atmosphere, 1976*, vol. S/T 76-1562, NOAA, U. S. Government Printing Office, Washington D. C., 1976.

Vance, J. D., C. She, and H. Moosmüller, Continuous-wave, all-solid-state, single-frequency 400-mW source at 589 nm based on doubly resonant sum-frequency mixing in a monolithic lithium niobate resonator, *Appl. Optics*, *37*, 4891–4896, 1998.

von der Gathen, P., Das Na-Temperatur-Lidar: Berechnung von Sättigungseffekten, Beobachtung von Temperaturprofilen und Ableitung spektraler Leistungsdichten, PhD thesis, Universität Bonn, 1990.

von der Gathen, P., Saturation Effects in Na Lidar Temperature Measurements, *J. Geophys. Res.*, *96*, 3679–3690, 1991.

von Storch, H., and F. W. Zwiers, *Statistical Analysis in Climate Research*, Cambridge University Press, 1999.

von Zahn, U., Temperature and altitude of the polar mesopause in summer, *Adv. Space Res.*, *10*, 223–231, 1990.

von Zahn, U., and J. Höffner, Mesopause temperature profiling by potassium lidar, *Geophys. Res. Lett.*, *23*, 141–144, 1996.

von Zahn, U., and W. Meyer, Mesopause temperatures in polar summer, *J. Geophys. Res.*, *94*, 14,647–14,651, 1989.

von Zahn, U., and R. Neuber, Thermal structure of the high latitude mesopause region in winter, *Beitr. Phys. Atmosph.*, *60*, 93–104, 1987.

von Zahn, U., J. Höffner, V. Eska, and M. Alpers, The mesopause altitude: Only two distinctive levels worldwide ?, *Geophys. Res. Lett.*, *23*, 3231–3234, 1996.

von Zahn, U., M. Gerding, J. Höffner, W. J. McNeil, and E. Murad, Iron, calcium, and potassium atom densities in the trails of Leonids and other meteors: Strong evidence for differential ablation, *Meteorit. & Planet. Sci.*, *34*, 1017–1027, 1999.

von Zahn, U., J. Höffner, and W. J. McNeil, Meteor trails as studied by ground-based lidar, in *Meteors in the Earth's atmosphere*, edited by I. P. Williams and E. Murad, chap. 7, pp. 149–187, Cambridge University Press, 2002.

Walling, J. C., Tunable Paramagnetic-Ion Solid-State Lasers, in *Tunable Lasers*, edited by L. F. Mollenauer and J. C. White, vol. 59 of *Topics in Applied Physics*, pp. 331–398, Springer-Verlag, 1987.

Walling, J. C., H. P. Jenssen, R. C. Morris, E. W. O'Dell, and O. G. Peterson, Tunable-laser performance in $BeAl_2O_4 : Cr^{3+}$, *Opt. Lett.*, *4*, 182–184, 1979.

Wiens, R. H., S. P. Zhang, R. N. Peterson, and G. G. Shepherd, Tides in emission rate and temperature from the O_2 nightglow over Bear Lake Observatory, *Geophys. Res. Lett.*, *22*, 2637–2640, 1995.

Williams, B. P., C. Y. She, and R. G. Roble, Seasonal climatology of the nighttime tidal perturbation of temperature in the midlatitude mesopause region, *Geophys. Res. Lett.*, *25*, 3301–3304, 1998.

Williams, B. P., M. A. White, D. A. Krueger, and C. Y. She, Observations of a large amplitude wave and inversion layer leading to convective instability in the mesopause region over Fort Collins, CO (41°N, 105°W), *Geophys. Res. Lett.*, *29*, 1850, doi:10.1029/2001GL014514, 2002.

Wilson, R. N., *Reflecting telescope optics I*, Astronomy and astrophysics library, Springer-Verlag, 1996.

Windholz, L., and M. Musso, Zeeman- and Paschen-Back-effect of the hyperfine structure of the sodium D_2-line, *Z. Phys. (D)*, *8*, 239–249, 1988.

Wulfmeyer, V., DIAL-Messungen von vertikalen Wasserdampfverteilungen, PhD thesis, Universität Hamburg (MPI für Meteorologie), 1995.

Wulfmeyer, V., Ground-based differential absorption lidar for water-vapor and temperature profiling: development and specifications of a high-performance laser transmitter, *Appl. Optics*, *37*, 3804–3824, 1998.

Yeh, P., Dispersive magnetooptic filters, *Appl. Optics*, *21*, 2069–2075, 1982.

Yin, B., and T. M. Shay, Theoretical model for a Faraday anomalous dispersion optical filter, *Opt. Lett.*, *16*, 1617–1619, 1991.

Yin, B., and T. M. Shay, A potassium Faraday anomalous dispersion optical filter, in *Proc. SPIE, Free-space laser communication technologies IV*, vol. 1635, pp. 128–134, 1992.

Young, A. T., Rayleigh scattering, *Appl. Optics*, *20*, 533–535, 1981.

Yu, J. R., and C. Y. She, Lidar-observed temperature structures and gravity-wave perturbations of the mesopause region in the springs of 1990-1992 over Fort Collins, CO, *Appl. Phys. B*, *57*, 231–238, 1993.

Yu, J. R., and C. Y. She, Climatology of a midlatitude mesopause region observed by a lidar at Fort Collins, Colorado (40.6°N, 105°W), *J. Geophys. Res.*, *100*, 7441–7452, 1995.

Zimmermann, D., Determination of the lifetime of the $4P_{1/2}$ of potassium by Hanle-effect, *Z. Phys. (A)*, *275*, 5–10, 1975.

List of Figures

1.1 General temperature profile, CIRA 2

2.1 Lidar return signal 8
2.2 Theoretical potassium D_1 resonance line 11

3.1 K-lidar schematic 13
3.2 Alexandrite laser setup 16
3.3 Laser pulse length 18
3.4 Seeding interference 20
3.5 Seeding laser setup 21
3.6 Laser frequency spectrum 22
3.7 Laser pulse energy variation 23
3.8 Temperature measurement example 27
3.9 Simulated temperature uncertainty 28
3.10 Seeder induced background 29
3.11 FADOF: Operation schematic 30
3.12 FADOF: Anomalous dispersion 31
3.13 FADOF: Theoretical rotation and transmission 32
3.14 FADOF: Temperature dependent transmission 32
3.15 FADOF: Twin filter setup 33
3.16 FADOF: Measured transmission 34
3.17 FADOF: Effective transmission 36
3.18 FADOF: Influence on temperature measurement 37
3.19 FADOF: Variance of Rayleigh signal transmission 38
3.20 FADOF: Rayleigh transmission influence on temperature 39
3.21 Saturation of K layer signal 42
3.22 Solar background, examples 44
3.23 Solar background dependence on solar elevation 45

4.1 Local time coverage, Kühlungsborn 53
4.2 Potassium layer, Kühlungsborn 55
4.3 Potassium layer, Tenerife 56
4.4 Seasonal temperatures, Kühlungsborn 61
4.5 Seasonal temperature fit, Kühlungsborn 62
4.6 Mesopause occurrence, Kühlungsborn 63
4.7 Seasonal temperatures, Tenerife 64
4.8 Summer mesopause transitions, Tenerife 65
4.9 Mesopause occurrence, Tenerife 67
4.10 Mesopause region temperatures, HRDI 69
4.11 Mesopause region temperatures, COMMA-IAP 70

5.1 Nighttime tidal variations, Tenerife, November 1999 76
5.2 Nighttime tidal parameters, Tenerife, May–July 1999 77
5.3 Nighttime tidal variations, Kühlungsborn, winter 79
5.4 Combination with WINDII data 83
5.5 Temperatures, Tenerife, November 2000 87
5.6 Tidal variations, Tenerife, November 2000 88
5.7 Wave analysis, Tenerife, November 2000 90
5.8 Temperatures, Kühlungsborn, February 2003 91
5.9 Tidal variations, Kühlungsborn, February 2003 92
5.10 Wave analysis, Kühlungsborn, February 2003 93
5.11 Wave analysis, Kühlungsborn, June 2003 94
5.12 Modelled tides: GSWM 104

C.1 Fitting nighttime data, example 117
C.2 Consistency test, example 118
C.3 FFT periodogram example 121
C.4 MEM periodogram example 122
C.5 Wavelet analysis, example 124

List of Tables

3.1 Alexandrite laser properties 24
3.2 K-lidar receiver properties 45

4.1 K-lidar temperature database 52
4.2 Potassium layer, Tenerife 56
4.3 Summer mesopause 68

5.1 WINDII versus K-lidar data, Tenerife 81
5.2 WINDII versus K-lidar data, Kühlungsborn 82
5.3 Tidal parameters from combination with WINDII data 84
5.4 Tidal parameters, Tenerife, November 2000 88
5.5 Tidal parameters, Kühlungsborn, February 2003 92
5.6 Overview: tidal amplitudes in winter 99
5.7 Overview: tidal phases in winter 100

B.1 USSA 1976 113

D.1 Monthly K-lidar observations, Rügen 125
D.2 Monthly K-lidar observations, Polarstern 126
D.3 Monthly K-lidar observations, Kühlungsborn 126
D.4 Monthly K-lidar observations, Tenerife 127
D.5 Monthly K-lidar observations, Svalbard 127
D.6 Monthly observations with stationary K-lidar, Kühlungsborn 128